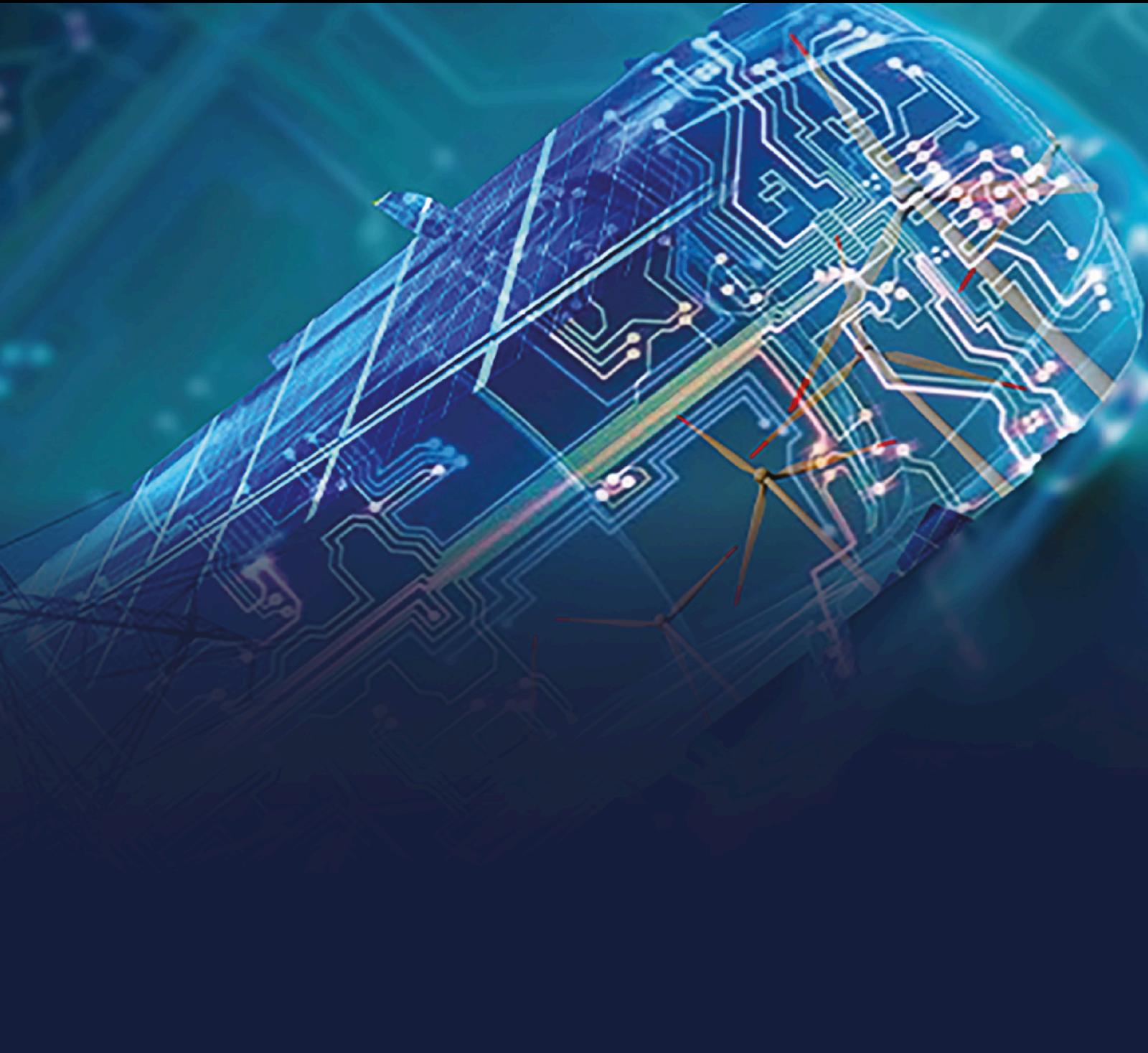


International Transactions on Electrical Energy Systems

# Zero Carbon Energy Systems

Lead Guest Editor: Qiuye Sun

Guest Editors: Li Zhang and Yonghao Gui





---

# **Zero Carbon Energy Systems**

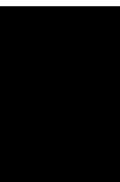
International Transactions on Electrical Energy Systems

---

## **Zero Carbon Energy Systems**

Lead Guest Editor: Qiuye Sun

Guest Editors: Li Zhang and Yonghao Gui



---

Copyright © 2022 Hindawi Limited. All rights reserved.

This is a special issue published in “International Transactions on Electrical Energy Systems.” All articles are open access articles distributed under the Creative Commons Attribution License, which permits unrestricted use, distribution, and reproduction in any medium, provided the original work is properly cited.



## Associate Editors

Chitti Babu Baladhandautham , India  
Antonio Bracale , Italy  
Tomislav Capuder , Croatia  
Chia Chi Chu , Taiwan  
Gilsoo Jang , Republic of Korea  
Dusmanta K. Mohanta , India  
Daniela Proto, Italy  
Ahmet Mete Vural , Turkey

## Academic Editors

JAGABAR SATHIK M MOHAMED ALI,  
India  
Sobhy M. Abdelkader, United Kingdom  
Johny Renoald Albert , India  
Rodolfo Araneo, Italy  
Enrique Rosales Asensio, Spain  
Faroque Azam, India  
Hamed Badihi , Finland  
Ajay Kumar Bansal , India  
Ajay Kumar Bansal, India  
Ramesh Chand Bansal , Australia  
Yukun Bao , China  
Prasenjit Basak , India  
Dr. CH Hussaian Basha, India  
Youcef Belkhier, France  
Jaouher Ben Ali, Tunisia  
Sujin Bureerat , Thailand  
Dhanamjayulu C , India  
Murthy Cherukuri , India  
Paulo Costa , Portugal  
Michele De Santis , Italy  
Mouloud Azzedine Denai , United Kingdom  
Harsh Dhiman , India  
Sheng Du , China  
Youssef Errami , Morocco  
Davide Falabretti , Italy  
Salvatore Favuzza , Italy  
Aymen Flah , Tunisia  
Ci-Wei Gao , China  
Samuele Grillo , Italy





Yueshi Guan, China  
Zhitao Guan, China  
Nitin K. Gupta , India  
Reza Jalilzadeh Hamidi, USA  
Santoshkumar Hampannavar , India  
Tianqi Hong , USA  
Wei-tzer Huang , Taiwan  
Kyeon Hur, Republic of Korea  
Kamran Iqbal , USA  
Hamed Jafari Kaleybar, Italy  
Jyotheeswara Reddy Kalvakurthi, India  
Kangli Liu, China  
Shaofeng Lu , China  
Ibrahim Mahariq, Kuwait  
Anjaneer Kumar Mishra , India  
Manohar Mishra, India  
Adel Oubelaid, Algeria  
Dr. Narendra Babu P , India  
Gayadhar Panda, India  
Dr. N. Prabakaran , India  
Santi A. Rizzo, Italy  
Julio Rosas-Caro , Mexico  
Mohammad Sadi , USA  
Akshay Kumar Saha , South Africa  
Lalit Chandra Saikia , India  
Irfan Sami, Republic of Korea  
Subrata kumar Sarker, Bangladesh  
Gulshan Sharma , South Africa  
Pawan Sharma, Norway  
Yiming Shen , China  
Dr. Arvind R. Singh , South Africa  
Sudhakar babu T , India  
Shafaat Ullah, Pakistan  
Jesus Valdez-Resendiz , Mexico  
Kusum Verma , India  
Yu-Chi Wu , Taiwan  
Rui Yao, China

## Contents





### **Multi-Time Scale Rolling Optimization Scheduling of “Nealy-Zero Carbon Park” Based on Stepped Carbon Allowance Trading**

Tieyan Zhang , Zongjun Yao , Jingwei Hu, and Jinfeng Huang  
Research Article (12 pages), Article ID 4449515, Volume 2022 (2022)





### **An Assessment and Design of a Distributed Hybrid Energy System for Rural Electrification: The Case for Jamataka Village, Botswana**

Ravi Samikannu , Moses Tunde Oladiran , Gladys Gamariel , Patricia Makepe , Ketshephaone Keisang , and Nyagong Santino David Ladu   
Research Article (12 pages), Article ID 4841241, Volume 2022 (2022)

### **A Consensus-Based Distributed Two-Layer Control Strategy with Predictive Compensation for Islanded Microgrid CPS against DoS Attack**

Xinrui Liu , Min Hou , Jianjun Yang , and Yufei Sun   
Research Article (15 pages), Article ID 1348667, Volume 2022 (2022)

### **Techno-Economic Feasibility Analysis of a Solar Photovoltaic Hybrid System for Rural Electrification in Sierra Leone for Zero Carbon Emission**

Martin Sankoh , Bakary Diarra , Ravi Samikannu , and Nyagong Santino David Ladu   
Research Article (14 pages), Article ID 6349229, Volume 2022 (2022)

### **Distributed Energy Management for Zero-Carbon Port Microgrid**

Jing Song , Qihe Shan , Tao Zou , Jingwei Hu , and Fei Teng   
Research Article (14 pages), Article ID 2752802, Volume 2022 (2022)

### **A Novel Short-Term Power Load Forecasting Method Based on TSNE-EEMD-LSTM**

Mingkun Jiang, He Jiang , Yan Zhao , Chenjia Hu, and Jian Xu  
Research Article (11 pages), Article ID 4802633, Volume 2022 (2022)


### **Annular Directed Distributed Algorithm for Energy Internet**

Jiaming Tan  and Hongyou Li   
Research Article (19 pages), Article ID 7717605, Volume 2022 (2022)


### **Situation Awareness of Electric Vehicle Charging Load Based on Random Forest Algorithm**

Wen Bo, Donglai Wang , Yan Zhao, Quanzheng Li, and Zhen Zhang  
Research Article (9 pages), Article ID 2821495, Volume 2022 (2022)





### **Energy Performance Contracting in a Supply Chain under Cap-and-Trade Regulation and Carbon Tax Policy**

Chengzhen Meng, Rong Zhang, and Bin Liu   
Research Article (10 pages), Article ID 1716380, Volume 2022 (2022)

### **Wearable Mixed Energy Management System Based on Power Trajectory Tracking**

Shijun Shen, Chaofan Wang, Chuan Lu, Wei Zheng, and Dawei Gong   
Research Article (15 pages), Article ID 4332766, Volume 2022 (2022)

**Robust Low-Carbon Discrete Berth Allocation under Uncertainty**

Feifei Yu , Qihe Shan , Yang Xiao , and Fei Teng 

Research Article (9 pages), Article ID 5310004, Volume 2022 (2022)

**Resilience Assessment for Microgrid with Pre-Position and Reconfiguration of Emergency Distribution Generations under Natural Hazard**

Hongtao Lei , Shengjun Huang , Yajie Liu , and Tao Zhang 

Research Article (12 pages), Article ID 3970536, Volume 2022 (2022)

## Research Article

# Multi-Time Scale Rolling Optimization Scheduling of “Nearly-Zero Carbon Park” Based on Stepped Carbon Allowance Trading

Tieyan Zhang <sup>1</sup>, Zongjun Yao <sup>1</sup>, Jingwei Hu,<sup>2</sup> and Jinfeng Huang<sup>3</sup>

<sup>1</sup>School of Electrical Engineering, Shenyang University of Technology, Shenyang 110870, China

<sup>2</sup>State Grid Liaoning Power Company Limited Economic Research Institute, Shenyang 110870, China

<sup>3</sup>State Grid Shenyang Electric Power Supply Company, Shenyang 110811, China

Correspondence should be addressed to Zongjun Yao; zjyao@smail.sut.edu.cn

Received 29 June 2022; Revised 3 August 2022; Accepted 5 August 2022; Published 10 September 2022

Academic Editor: Qiuye Sun

Copyright © 2022 Tieyan Zhang et al. This is an open access article distributed under the Creative Commons Attribution License, which permits unrestricted use, distribution, and reproduction in any medium, provided the original work is properly cited.

Aiming at the self-government capacity and multi-time scale energy regulation requirements of “Nearly-zero Carbon Park” (NZCP) under the background of “dual carbon goals” and energy Internet, a day-ahead-intraday rolling optimization scheduling method for NZCP based on stepped carbon allowance trading is proposed. First, the energy supply and demand characteristics of liquid-storage Carbon Capture Gas-fired Power Plants (CCGPP) and Power-to-Gas (P2G) equipment are studied, and a combined system model of CCGPP and P2G is established that takes into account the low-carbon emission requirements of NZCP, and waste pyrolysis power generation facilities and manure treatment facilities are introduced to form a Waste Utilization system (WU) to provide energy support for the power grid and gas network. Second, the carbon allowance offset and low-carbon benefit gains of NZCP are considered, a compensation coefficient is introduced to guide the low-carbon behavior of carbon emitters, and a ladder carbon allowance trading model is established. Then, the influence of the source-load prediction error on the optimal scheduling at different time scales is considered, and a two-stage unit output plan is established. Then, the influence of the source-load prediction error on the optimal scheduling at different time scales is considered, and a two-stage unit output adjustment plan is established. The calculation example results verify that the proposed day-ahead-intraday rolling optimization scheduling model for NZCP can effectively reduce system carbon emissions while reducing system operating costs, and the efficient integration of economic and environmental benefits is achieved.

## 1. Introduction

In recent years, with the aggravation of the energy crisis and the greenhouse effect, it has become a global consensus to seek a clean, low-carbon, efficient, and sustainable energy supply method [1–4]. The “14th Five-Year Plan” for the development of bio-economy pointed out to build biomass utilization technology, production, and consumption system [5]. However, with the high proportion of renewable energy access, the multiple uncertainties of source and load and forecast errors have brought severe challenges to the stable operation of NZCP. At the same time, the energy production devices, conversion devices, and energy storage devices in the system have different response times [6–9]. Therefore,

the establishment of a flexible operation mode with the ability to adjust at multiple time scales is an important means to deal with the uncertainty caused by the source-load prediction error and ensure the stable operation of the system.

The research on the carbon emission allowance trading mechanism at home and abroad is still in the development stage. Reference [10] studied the fairness of low-carbon economic dispatch in the power system, and proposes an initial allocation method for carbon emission rights based on the idea of a cooperative game. Reference [11] proposed an energy hub model based on carbon allowance trading, and calculates the tiered carbon allowance trading cost according to the carbon emission interval. Reference [12] introduced a

carbon allowance trading mechanism in the comprehensive energy system optimization planning problem, established a reward and punishment ladder-type carbon allowance transaction cost model, and restricted the carbon emission level in the planning area. Most of the above studies focus on using the carbon allowance trading mechanism to control the carbon emission level of the Integrated Energy System. NZCP offsets some carbon emissions through the stepped carbon allowance trading mechanism, so that the difference between carbon sources and carbon allowances is close to zero, and near-zero carbon emissions are achieved while taking into account the benefits brought by the trading mechanism.

At present, some studies have been carried out at home and abroad on the application of biomass utilization technology in integrated energy systems. Reference [13] introduced waste incineration power generation into the urban Integrated Energy System, which improved the adjustment capacity of the power grid and gas grid. Reference [14] proposed the topological structure of the rural multi-energy complex, and established a model of the coordination relationship between the waste stockpile and energy supply. Reference [15] studied the synergistic energy supply characteristics of waste pyrolysis and waste incineration and proposed an urban comprehensive energy system optimization model with waste treatment units. The current research has a relatively simple coupling form for the waste treatment system and has not deeply analyzed the synergistic relationship between the waste treatment system and other energy supply systems.

In order to reduce the power fluctuation caused by the high proportion of renewable energy connected to the new power system and the inconsistent scheduling time scale of each unit in the multi-source energy storage system, a lot of research has been carried out on the day-ahead-intraday multi-time-scale scheduling method in China. Reference [16] established a two-stage predictive optimal scheduling model for the park's comprehensive energy system based on rolling optimization and dynamic adjustment to meet the energy demand of multi-energy users. Reference [17] introduced smart buildings into microgrids to form a virtual energy storage system, and proposed an intraday rolling correction method based on model prediction, which corrects the output deviation of microgrids caused by forecast errors through rolling optimization in different time domains. Reference [18] proposed a multi-time-scale optimal scheduling method for integrated energy systems based on the responsiveness of electric and thermal energy on different time scales to smooth out power fluctuations caused by the uncertainty of renewable energy output.

Through the above analysis, the economic benefits and environmental benefits of tiered carbon allowance trading on NZCP are considered, and a day-ahead-intraday rolling optimization scheduling method is proposed. Day-ahead economic optimal scheduling and intra-day rolling optimal scheduling models were established respectively. Day-ahead economic optimal scheduling determined the optimal output structure, and intra-day rolling optimal scheduling determined the optimal time scale. A power adjustment penalty term is introduced to limit carbon emissions while

compensating for carbon emissions, and NZCP's multi-time-scale source-load optimization scheduling is realized. Finally, the simulation verification is carried out via the operation data of the integrated energy system of a park in a certain area in northern China. The calculation example results verify the positive effect of the NZCP multi-time-scale rolling optimization scheduling method proposed in this paper in economic operation and carbon capture.

## 2. Operational Characteristics and Carbon Cycle Model of NZCP

The NZCP based on tiered carbon allowance trading gives full play to the low-carbon characteristics of zero-carbon resources such as liquid-storage CCGPP and waste utilization systems in the system. At the same time, taking into account the self-regulation level of the load in the system, and controlling the operation status of fixed loads, interruptible loads, and transferable loads through compensation and contracting mechanisms, the energy regulation level of the system can be further improved. However, due to the technical limitations of the carbon capture system, the complete capture of carbon emissions cannot be achieved. Therefore, the carbon allowance offset mechanism is used to achieve near-zero carbon operating characteristics while taking into account the economy. The energy coupling and interaction mode of NZCP is shown in Figure 1.

*2.1. CCGPP-P2G System Model.* Different from the traditional carbon capture of coal-fired power generating units, the flue gas emitted by gas generating units has higher oxygen content and lower carbon content [19]. Meanwhile, carbon capture systems have high energy consumption characteristics [20]. Therefore, the solution storage CCGPP is adopted, and the carbon capture process is decoupled from the power generation process of the gas power plant by introducing the solution storage carbon capture system, and the energy consumption required for carbon capture is shifted in time and space, thereby improving the consumption capacity of renewable energy while ensuring the energy supply efficiency.

The carbon capture system of solution storage CCGPP consists of a CO<sub>2</sub> capture device and a CO<sub>2</sub> liquefaction device. The flue gas in the absorption tower realizes CO<sub>2</sub> capture through the reverse transmission process with the lean and rich liquid [21]. The electro-carbon characteristics and energy coupling method of carbon capture system are referenced in [22].

It is considered that P2G equipment has good energy space-time transfer characteristics, and P2G equipment is introduced into NZCP and participates in CCGPP joint operation. The CO<sub>2</sub> captured by the carbon capture equipment is used to produce methane, thus providing a good carbon source for CCGPP. The recycling of CO<sub>2</sub> and the improvement of the level of renewable energy consumption are realized, which provides a good margin for the optimal scheduling of the system at multiple time scales [23, 24].

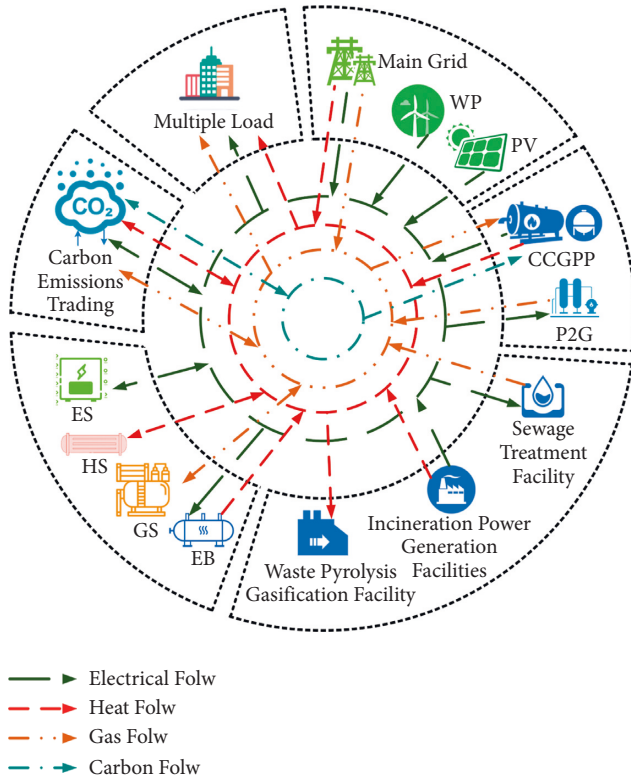


FIGURE 1: "Nearly-zero carbon park" energy interaction mode.

The energy consumption characteristics of the CCGPP-P2G system can be expressed as:

$$P_{C,CCGPP-P2G,t} = P_{C,CCGPP,t} + P_{C,P2G,t} + P_F, \quad (1)$$

where  $P_{C,CCGPP,t}$  is the CCGPP energy consumption at time  $t$ ,  $P_{C,P2G,t}$  is the P2G energy consumption at time  $t$ , and  $P_F$  is the fixed operating energy consumption of the system.

The total amount of  $CO_2$  captured by CCGPP-P2G at time  $t$  is  $Q_{CCGPP-CO_2,t}^\Sigma$ , and the total amount of  $CO_2$  consumed in the process of synthesizing methane by P2G is:

$$\begin{aligned} Q_{CCGPP-CO_2,t}^\Sigma &= \theta_{CO_2,t} \eta_{CO_2,t} P_{CCGPP,t}, \\ Q_{P2G-CO_2,t}^\Sigma &= \chi_{CO_2,t} \eta_{P2G} P_{C,P2G,t}, \end{aligned} \quad (2)$$

where  $\theta_{CO_2,t}$  is the carbon emission intensity of processing at time  $t$ ,  $\eta_{CO_2,t}$  is the carbon capture rate at time  $t$ ,  $P_{CCGPP,t}$  is the total CCGPP output at time  $t$ ,  $\chi_{CO_2,t}$  is the amount of  $CO_2$  required to generate unit capacity of natural gas, and  $\eta_{P2G}$  is the gas production efficiency of P2G.

The natural gas production of the CCGPP-P2G system at time  $t$  is:

$$P_{CCGPP-P2G,G,t}^\Sigma = \frac{3.6 \eta_{P2G} P_{C,P2G,t}}{H_g}, \quad (3)$$

where  $H_g$  is the calorific value of natural gas.

Due to the high energy consumption characteristics of carbon capture, CCGPP with flue gas diversion is used to control the energy consumption of carbon capture by actively emitting  $CO_2$ . The  $CO_2$  discharged into the atmosphere by flue gas diversion is:

$$C_{DE,t} = C_{\Sigma,t} - C_{CCGPP,\Sigma,t}. \quad (4)$$

In the formula,  $C_{\Sigma,t}$  is the total amount of  $CO_2$  emitted by all units in the system at time  $t$ , and  $C_{CCGPP,\Sigma,t}$  is the amount of  $CO_2$  captured by CCGPP at time  $t$ .

**2.2. Waste Utilization System Model.** The biomass utilization potential in NZCP is considered, and the WU is proposed to fully dispatch zero-carbon and negative-carbon resources in the NZCP. WU includes waste pyrolysis gasification power generation facilities and manure treatment gas generation facilities.

The waste pyrolysis gasification power generation facility heats and decomposes the sorted organic waste into combustible gas mixed with natural gas by using a high temperature above  $800^\circ C$  [25]. Then, the combustible gas mixed with natural gas is burned to drive the internal combustion engine to generate electricity. The energy supply relationship with waste can be expressed as:

$$P_{WPG,t} = m_{R,t} g_R \eta_P H_F \eta_{F,E}, \quad (5)$$

where  $m_{R,t}$  is the input amount of gasifiable waste,  $g_R$  is the gasification coefficient,  $\eta_P$  is the calorific value of the gasifiable waste,  $H_F$  is the calorific value of the gasified fuel, and  $\eta_{F,E}$  is the power generation efficiency of the gas turbine.

The heat energy provided by waste pyrolysis can be expressed as:

$$P_{WPG,H,t} = \frac{P_{WPG,t} (1 - \eta_{F,E} - \eta_1)}{\eta_{F,E}} \eta_r, \quad (6)$$

where  $\eta_1$  is the heat dissipation loss rate, and  $\eta_r$  is the flue gas recovery rate.

The manure treatment facility makes full use of the sewage and manure resources in the system and uses anaerobic fermentation technology to electrically heat the manure resources and purify them into natural gas, which can be used as a good gas source for CCGPP [26]. For the characteristics of high nitrogen content in manure waste, an appropriate proportion of wet waste is used to adjust the carbon-nitrogen ratio to improve the degree of anaerobic fermentation reaction, thereby increasing gas production [27].

The biogas model for manure treatment facilities can be expressed as:

$$P_{FS,B,t} = m_{FW,t} \eta_{FW,B} \eta_{F,B} + m_{SG,t} \eta_{SG,B} \eta_{S,B}, \quad (7)$$

where  $P_{FS,B}$  is the amount of biogas produced by manure treatment,  $\eta_{FW,B}$  and  $\eta_{SG,B}$  are the treatment efficiency of manure treatment facilities and the treatment efficiency of sewage treatment facilities, respectively,  $\eta_{F,B}$  and  $\eta_{S,B}$  are the conversion coefficients of manure waste and sewage waste into biogas, and  $m_{FW,t}$  and  $m_{SG,t}$  are the input amount of manure and sewage, respectively.

After desulfurization and decarbonization, the biogas can be made into natural gas with a purity of more than 90%. Biogas purification of natural gas can be expressed as:

$$P_{FS,G,t} = P_{FS,B,t} a_{F,G}, \quad (8)$$

where  $a_{F,G}$  is the purification efficiency of biogas.

**2.3. Energy Storage Unit Model.** The loss characteristics of electrochemical energy storage, hot water tank, and gas storage tank are considered, and the models of Electricity Storage device (ES), Heat Storage device (HS), and Gas Storage device (GS) can be expressed as:

$$\begin{aligned} P_{ES,t} &= (1 - \ell_{ES})P_{ES,t-1} + \eta_{ES}^{ch} P_{ES,t}^{ch} - \frac{P_{ES,t}^{dis}}{\eta_{ES}^{dis}}, \\ P_{HS,t} &= (1 - \ell_{HS})P_{HS,t-1} + \eta_{HS}^{ch} P_{HS,t}^{ch} - \frac{P_{HS,t}^{dis}}{\eta_{HS}^{dis}}, \\ P_{GS,t} &= (1 - \ell_{GS})P_{GS,t-1} + \eta_{GS}^{ch} P_{GS,t}^{ch} - \frac{P_{GS,t}^{dis}}{\eta_{GS}^{dis}}, \end{aligned} \quad (9)$$

where,  $P_{ES,t}$ ,  $P_{HS,t}$ , and  $P_{GS,t}$  are the electricity, heat, and gas energy storage capacity at the end of time  $t$ , respectively;  $\ell_{ES}$ ,  $\ell_{HS}$ , and  $\ell_{GS}$  are the loss rates of the electricity, heat, and gas energy storage devices themselves;  $P_{ES,t-1}$ ,  $P_{HS,t-1}$ , and  $P_{GS,t-1}$  are the electricity, heat, and gas energy storage at time  $t - 1$ , respectively, the power storage, heat storage, and gas storage;  $\eta_{ES}^{ch}$ ,  $\eta_{ES}^{dis}$  are the charging and discharging efficiency of the power storage device;  $P_{ES,t}^{ch}$ ,  $P_{ES,t}^{dis}$  are the charging and discharging power of the power storage device at time  $t$ ;  $\eta_{HS}^{ch}$ ,  $\eta_{HS}^{dis}$  are the charging and discharging efficiency of the heat storage device;  $P_{HS,t}^{ch}$ ,  $P_{HS,t}^{dis}$  are the charging and discharging power of the heat storage device at time  $t$ ;  $\eta_{GS}^{ch}$ ,  $\eta_{GS}^{dis}$  are the charging and degassing efficiency of the gas storage device; and  $P_{GS,t}^{ch}$ ,  $P_{GS,t}^{dis}$  are the charging and degassing power of the gas storage device at time  $a$ .

**2.4. Multi-Energy Coupling Energy Flow Model.** NZCP includes a variety of energy production and transportation forms, and the multi-source coordination method is described by the coupling matrix as:

$$\begin{aligned} \begin{bmatrix} P_{EL,t} \\ P_{HL,t} \\ P_{GL,t} \end{bmatrix} &= \begin{bmatrix} P_{EW,t} \\ P_{HW,t} \\ P_{GW,t} \end{bmatrix} + \begin{bmatrix} P_{ES,t} \\ P_{HS,t} \\ P_{GS,t} \end{bmatrix} \\ + \begin{bmatrix} 1 - \alpha_1 - \alpha_2 & g_R \eta_P H_F \eta_{F,E} & 0 & 0 & \eta_{CCGPP} \\ \alpha_1 \eta_{EB} & g_R \eta_P H_F \eta_{F,E} \frac{(1 - \eta_{F,E} - \eta_1) \eta_t}{\eta_{F,E}} & 0 & 0 & \eta_{CCGPP,H} \\ \alpha_2 \eta_{P2G} & 0 & \eta_{FW,B} \eta_{F,B} a_{F,G} & \eta_{SG,B} \eta_{S,B} a_{F,G} & 0 \end{bmatrix} \begin{bmatrix} P_{WP,t} + P_{PV,t} \\ m_{R,t} \\ m_{FW,t} \\ m_{SG,t} \\ P_{CCGPP,t} \end{bmatrix}, \end{aligned} \quad (10)$$

where  $P_{EL,t}$ ,  $P_{HL,t}$ , and  $P_{GL,t}$  are the loads of electricity, heat and gas, respectively;  $P_{EW,t}$ ,  $P_{HW,t}$ , and  $P_{GW,t}$  are the electricity, heat, and gas power purchased from the main network, respectively;  $P_{WP,t}$  and  $P_{PV,t}$  are the on-grid power of wind power and the on-grid power of photovoltaics, respectively; and  $\eta_{CCGPP}$ ,  $\eta_{CCGPP,H}$ ,  $\eta_{EB}$ , and  $\eta_{P2G}$  are the CCGPP power supply efficiency, CCGPP thermoelectric ratio, EB heating efficiency, and P2G gas supply efficiency, respectively.

### 3. Ladder Carbon Allowance Trading Model

Carbon emission allowance trading is a legal carbon emission allowance allocated to each energy producer or integrated energy body under the premise of environmental and market factors. If the actual carbon emission of the

energy producer is higher than the carbon emission allowance in the production process, it needs to purchase the corresponding amount of carbon emission allowance from the carbon emission trading market. Conversely, if the actual carbon emission of the energy producer is higher than the carbon emission allowance in the production process, the corresponding allowance can be sold in the carbon emission rights trading market to obtain low-carbon benefits. The NZCP can offset carbon emissions with appropriate carbon emission rights allowances, so that the carbon emission level in the system is within a constraint range to achieve near-zero carbon emissions.

The management department allocates the initial carbon emission right pre-allowance based on the carbon emissions of each energy-producing entity or integrated energy body in the previous year, and then determines the actual initial



allowance based on the actual energy supply after accounting. In this paper, carbon emissions and carbon emission allowances are liquidated on an hourly time scale.

The carbon emission rights participating in the carbon allowance trading market is:

$$\begin{aligned} P_{T,t} &= P_{DE,t} - P_{EMI,t}, \\ P_{DE,t} &= \omega_{CCGPP} P_{CCGPP,t} + \omega_{WPG} P_{WPG,t} \\ &\quad - \theta_{CO_2} P_{CCGPP-P2G,G,t}^{\Sigma}, \\ P_{EMI,t} &= \partial_1 P_{CCGPP,t} + \partial_2 P_{WPG,t} + \partial_3 P_{WPG,H,t}, \end{aligned} \quad (11)$$

where  $P_{DE,t}$  and  $P_{EMI,t}$  are the system CO<sub>2</sub> net carbon emissions and free carbon emission rights, respectively;  $\omega_{CCGPP}$ ,  $\omega_{CCGPP}$  and  $\omega_{WPG}$  are the carbon emission intensity corresponding to the unit natural gas consumed by CCGPP, and the carbon emission intensity corresponding to the incineration power generation per unit of waste pyrolysis gasification;  $\theta_{CO_2}$  is the CO<sub>2</sub> density;  $\partial_1$ ,  $\partial_2$ , and  $\partial_3$  are the carbon emission rights allocation quota corresponding to the unit power supply of CCGPP, power supply after waste pyrolysis and gasification, and heating power, respectively.

Different from the traditional unified reward and punishment carbon allowance trading mechanism, the tiered price trading mechanism is introduced in this paper, which is analogous to the time-of-use energy price and establishes a transaction cost calculation method based on the carbon emission range. When the carbon emissions of energy producers exceed the constraint range, the price of carbon allowances rises in stages. At the same time, a compensation coefficient is introduced to motivate the low-carbon behavior compensation of energy-producing subjects [10].

The tiered carbon allowance transaction costs are:

$$C_{CO_2} = \begin{cases} p_B P_{T,t}, & L \leq P_{T,t}, \\ p_B L + p_B (P_{T,t} - L)(1 + \phi), & L < P_{T,t} \leq 2L, \\ p_B (2 + \phi)L + p_B (P_{T,t} - L)(1 + 2\phi), & 2L < P_{T,t} \leq 3L, \\ p_B (3 + 3\phi)L + p_B (P_{T,t} - L)(1 + 3\phi), & 3L < P_{T,t} \leq 4L, \\ p_B (4 + 6\phi)L + p_B (P_{T,t} - L)(1 + 4\phi), & P_{T,t} > 4L, \end{cases} \quad (12)$$

where  $p_B$  is the base price of carbon allowance trading;  $L$  is the length of the carbon emission range; and  $\phi$  is the compensation factor. When  $P_{T,t} > 0$ , it means that the actual carbon emission of the system is lower than the free carbon emission, and the remaining part of the allowance can participate in the trading market to obtain benefits.

#### 4. NZCP Multi-Time Scale Rolling Optimization Scheduling Strategy

The traditional day-ahead scheduling method is difficult to effectively deal with the source-load forecast error and multiple uncertainties of NZCP. Tiered carbon allowance trading and various equipment operation constraints are considered, and a multi-time scale rolling optimization model is established. The hour-level time resolution is

selected, and the optimization goal is to minimize the daily operating cost of the system, and formulate the optimal output and adjustment plan of the unit throughout the day.

Intraday scheduling is to formulate the unit output plan according to the previous scheduling stage, select 15 min as the time scale for rolling optimization, based on the results of renewable energy generation and short-term multi-load forecasting. Through continuous rolling optimization to ensure the accuracy and effectiveness of the dispatch plan, the optimal state adjustment of the source, load, and output is realized.

The day-ahead-intraday rolling optimization strategy framework is shown in Figure 2. Among them,  $t$  is the scheduling period,  $\Delta t$  is the scheduling time interval,  $H$  is the rolling time domain, and  $n$  is the total number of time periods in the rolling time domain.

**4.1. Day-Ahead Optimization.** The objective function of the day-ahead scheduling phase is:

$$\begin{aligned} \min & (C_{buy} + C_{WP,PV} + C_{P2G} + C_{WU} + C_{CCGPP} \\ & + C_{EB} + C_{CSE} + C_{CO_2} + C_{L,DR}), \\ C_{buy} &= \sum_{t=1}^T \partial_{E,t} P_{EW} + \sum_{t=1}^T \partial_{H,t} P_{HW} + \sum_{t=1}^T \partial_{G,t} P_{GW}, \\ C_{WP,PV} &= \sum_{t=1}^T \gamma_{WP,t} P_{WP} + \sum_{t=1}^T \gamma_{PV,t} P_{PV}, \\ C_{P2G} &= \sum_{t=1}^T \gamma_{P2G,t} P_{C,P2G,t}, \\ C_{WU} &= \sum_{t=1}^T [a_1 + b_1 (m_{R,t} + m_{FW} + m_{SG}) \\ & + c_1 (m_{R,t} + m_{FW} + m_{SG})^2], \\ C_{CCGPP} &= \sum_{t=1}^T \gamma_{CCGPP,t} P_{CCGPP,t}, \\ C_{EB} &= \sum_{t=1}^T \gamma_{EB,t} P_{EB,t}, \\ C_{CSE} &= \sum_{t=1}^T \gamma_{CSE,t} Q_{CSE,CO_2,t}, \\ C_{L,DR} &= \sum_{t=1}^T \sum_k^K b_{k,int,t} P_{k,DR,t}^{int} + \sum_{t=1}^T b_{shi,t} P_{DR,t}^{shi}, \end{aligned} \quad (13)$$

where  $C_{buy}$ ,  $C_{WP,PV}$ ,  $C_{P2G}$ ,  $C_{WU}$ ,  $C_{CCGPP}$ ,  $C_{EB}$ ,  $C_{CSE}$ ,  $C_{CO_2}$ , and  $C_{L,DR}$  are the energy purchase cost, operation and maintenance cost of renewable energy power generation equipment, P2G unit operation cost, waste utilization system operation cost, CCGPP operation cost, EB unit operation cost, carbon sequestration cost, tiered carbon allowance transaction cost, and demand-side response load compensation cost, respectively;  $\partial_{E,t}$ ,  $\partial_{H,t}$ , and  $\partial_{G,t}$  are the electricity price, heat price, and natural gas price at the moment;  $\gamma_{WP,t}$ ,



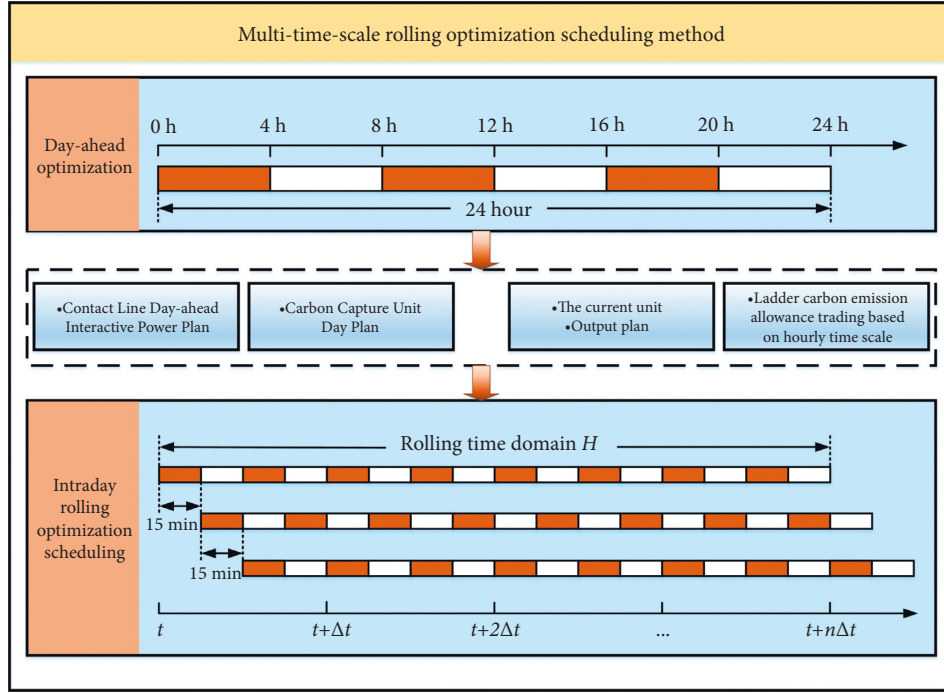


FIGURE 2: Multi-time scale rolling optimization scheduling framework.

$\gamma_{PV,t}$  are the unit operation and maintenance costs of wind power and photovoltaics at the moment, respectively;  $\gamma_{P2G,t}$ ,  $\gamma_{EB,t}$  are the operating cost coefficients of P2G units and EB units, respectively;  $a_1$ ,  $b_1$ ,  $c_1$  are the operating cost coefficients of the waste utilization system;  $\gamma_{CCGPP,t}$  is the CCGPP operating cost coefficient;  $\gamma_{CSE,t}$  is the unit cost of carbon sequestration;  $Q_{CSE,CO_2,t}$  is the amount of  $CO_2$  sequestered by the carbon sequestration device;  $k$  is the number of interruption levels;  $P_{k,DR,t}^{int}$  and  $b_{k,int,t}$  are respectively the  $k$ -th level of interruption load and the interruption compensation price;  $P_{DR,t}^{shi}$  and  $b_{shi,t}$  are respectively the transferable load and the transferable load compensation price.

#### 4.2. Constraints

(1) Power balance constraints:

$$\begin{aligned}
 & P_{EW,t} + P_{WP,t} + P_{PV,t} + P_{WPG,t} + P_{CCGPP,E,t} - P_{C,CCGPP-P2G,t} - \\
 & P_{P2G,t} + P_{ES,t}^{dis} - P_{FS,E,t} - P_{EB,t} = P_{ES,t}^{ch} + P_{EL,t}, \\
 & P_{HW,t} + P_{WPG,H,t} + P_{CCGPP,H,t} + P_{EB,t}^H + P_{HS,t}^{dis} = P_{HS,t}^{ch} + P_{HL,t}, \\
 & P_{GW,t} + P_{FS,G,t} + P_{P2G,H,t} + P_{CCGPP-P2G,G,t}^{\Sigma} - P_{CCGPP,t} + P_{GS,t}^{dis} \\
 & = P_{GS,t}^{ch} + P_{GL,t},
 \end{aligned} \tag{14}$$

where  $P_{EW,t}$ ,  $P_{HW,t}$ , and  $P_{GW,t}$  are the electricity, heat, and gas power purchased from the main grid, respectively;  $P_{WP,t}$ ,  $P_{PV,t}$  are the wind power on-grid power and photovoltaic on-grid power, respectively;  $P_{EL,t}$ ,  $P_{HL,t}$ , and  $P_{GL,t}$  are the electricity, heat, and gas loads, respectively.

(2) CCGPP operating constraints:

$$0 \leq P_{CCGPP,t} \leq P_{CCGPP,max}, \tag{15}$$

where  $P_{CCGPP,max}$  is the upper limit of CCGPP output.

(3) Operational constraints of Waste Utilization system: The operational constraints of waste pyrolysis gasification power generation facilities can be expressed as:

$$P_{WPG,t}^{min} \leq P_{WPG,t} \leq P_{WPG,t}^{max}, \tag{16}$$

where  $P_{WPG,t}^{max}$  and  $P_{WPG,t}^{min}$  are the upper limit and lower limit of power supply power for waste pyrolysis and gasification, respectively.

The operation constraints of manure treatment equipment can be expressed as:

$$\begin{aligned}
 & \Delta P_{FS,G,min} \leq P_{FS,G,t} - P_{FS,G,t-1} \leq \Delta P_{FS,G,max}, \\
 & P_{FS,G,t}^{min} \leq P_{FS,G,t} \leq P_{FS,G,t}^{max},
 \end{aligned} \tag{17}$$

where  $P_{FS,G,t}^{max}$  and  $P_{FS,G,t}^{min}$  are the upper and lower limits of the manure treatment power, respectively;  $\Delta P_{FS,G,max}$  and  $\Delta P_{FS,G,min}$  are the upper and lower limits of the climbing rate of the manure treatment equipment, respectively.

(4) P2G operation constraints:

$$\begin{aligned}
 & 0 \leq P_{C,P2G,t} \leq P_{P2G,max}, \\
 & \Delta P_{P2G,min} \leq P_{P2G,t+1} - P_{P2G,t} \leq \Delta P_{P2G,max},
 \end{aligned} \tag{18}$$

where  $P_{P2G,max}$  is the upper limit of the P2G output;  $\Delta P_{P2G,max}$  and  $\Delta P_{P2G,min}$  are the upper and lower limits of the P2G ramp rate, respectively.

(5) Electric Boiler operation constraints:

$$\begin{aligned} 0 &\leq P_{EB,t} \leq P_{EB,max}, \\ \Delta P_{EB,min} &\leq P_{EB,t+1} - P_{EB,t} \leq \Delta P_{EB,max}, \end{aligned} \quad (19)$$

where  $P_{EB,max}$  is the upper limit of EB output;  $\Delta P_{EB,max}$  and  $\Delta P_{EB,min}$  are the upper limit and lower limit of the EB ramp rate constraint, respectively.

(6) Energy storage devices operation constraints:

$$\begin{aligned} 0 &\leq P_{ES,t}^{ch} \leq P_{ES,t}^{ch,max} o_{ES,t}^{ch}, \\ 0 &\leq P_{ES,t}^{dis} \leq P_{ES,t}^{dis,max} o_{ES,t}^{dis}, \\ 0 &\leq o_{ES,t}^{ch} + o_{ES,t}^{dis} \leq 1, \\ P_{ES,t}^{min} &\leq P_{ES,t} \leq P_{ES,t}^{max}, \end{aligned} \quad (20)$$

where  $P_{ES,t}^{ch,max}$  and  $P_{ES,t}^{dis,max}$  are the maximum value of the charging and discharging power of the power storage device, respectively;  $o_{ES,t}^{ch}$  and  $o_{ES,t}^{dis}$  are the charging and discharging states of the power storage device, respectively. In case of  $o_{ES,t}^{ch} = 0$ ,  $o_{ES,t}^{dis} = 1$ , the

system is in a state of discharge, and in case of  $o_{ES,t}^{ch} = 1$ ,  $o_{ES,t}^{dis} = 0$ , the system is in a state of charge;  $P_{ES,t}^{max}$  and  $P_{ES,t}^{min}$  are the maximum and minimum storage capacity of the power storage device, respectively. The heat storage device and the gas storage device are the same.

(7) Tie line power constraints:

$$\begin{aligned} P_{EW,t,min} &\leq P_{EW,t} \leq P_{EW,t,max}, \\ P_{HW,t,min} &\leq P_{HW,t} \leq P_{HW,t,max}, \\ P_{GW,t,min} &\leq P_{GW,t} \leq P_{GW,t,max}. \end{aligned} \quad (21)$$

In the formula,  $P_{EW,t,max}$  and  $P_{EW,t,min}$  are the maximum and minimum power of the tie line between the system and the power grid, respectively;  $P_{HW,t,max}$  and  $P_{HW,t,min}$  are the maximum and minimum power of the tie line between the system and the heat grid, respectively;  $P_{GW,t,max}$ ,  $P_{GW,t,min}$  are the maximum and minimum power of the tie line between the system and the gas network, respectively.

#### 4.3. Intraday Rolling Optimization

$$\begin{aligned} &\min(C_{buy,roll} + C_{WU,roll} + C_{CCGPP,roll} C_{ES,roll} + C_{HS,roll} + C_{GS,roll}), \\ C_{buy,roll} &= \sum_{t=1}^T \partial_{E,t} (P_{EW,\Theta,t} + \Delta P_{EW,t}) + \partial_{E,pu,t} (\Delta P_{EW,t})^2 \\ &\quad + \sum_{t=1}^T \partial_{H,t} (P_{HW,\Theta,t} + \Delta P_{HW,t}) + \partial_{H,pu,t} (\Delta P_{HW,t})^2 + \sum_{t=1}^T \partial_{G,t} (P_{GW,\Theta,t} + \Delta P_{GW,t}) + \partial_{G,pu,t} (\Delta P_{GW,t})^2, \\ C_{WU,roll} &= \sum_{t=1}^T \left[ a_1 + b_1 (m_{R,\Theta,t} + m_{FW,\Theta} + m_{SG,\Theta} + \Delta m_{R,t} + \Delta m_{FW} + \Delta m_{SG}) \right] \\ &\quad + c_1 (m_{R,\Theta,t} + m_{FW,\Theta} + m_{SG,\Theta} + \Delta m_{R,t} + \Delta m_{FW} + \Delta m_{SG})^2, \\ C_{CCGPP,roll} &= \sum_{t=1}^T \gamma_{CCGPP,t} (P_{CCGPP,t} + \Delta P_{CCGPP,t}), \\ C_{ES,roll} &= \sum_{t=1}^T \partial_{E,t} (\Delta P_{ES,t}^{ch})^2 + \partial_{E,t} (\Delta P_{ES,t}^{dis})^2, \\ C_{HS,roll} &= \sum_{t=1}^T \partial_{H,t} (\Delta P_{HS,t}^{ch})^2 + \partial_{H,t} (\Delta P_{HS,t}^{dis})^2, \\ C_{GS,roll} &= \sum_{t=1}^T \partial_{G,t} (\Delta P_{GS,t}^{ch})^2 + \partial_{G,t} (\Delta P_{GS,t}^{dis})^2, \end{aligned} \quad (22)$$

where  $C_{buy,roll}$ ,  $C_{WU,roll}$ ,  $C_{CCGPP,roll}$ ,  $C_{ES,roll}$ ,  $C_{HS,roll}$ , and  $C_{GS,roll}$  are the cost of purchasing energy from the main network during rolling optimization, the operating cost of the waste utilization system, the operating cost of CCGPP, penalty cost of charging and discharging power change of electric storage device, penalty cost of charging and

discharging power fluctuation of heat storage device, and penalty cost of charging and discharging power fluctuation of gas storage device, respectively;  $P_{EW,\Theta,t}$ ,  $P_{HW,\Theta,t}$ , and  $P_{GW,\Theta,t}$  are the power, heat, and gas purchased from the main network a few days ago, respectively;  $\Delta P_{EW,t}$ ,  $\Delta P_{HW,t}$ , and  $\Delta P_{GW,t}$  are the power, heat, and gas adjustment power

purchased within the day, respectively;  $m_{R,\Theta,t}$ ,  $m_{FW,\Theta}$ , and  $m_{SG,\Theta}$  are the input amount of organic waste, feces, and sewage after the previous classification, respectively;  $\Delta m_{R,t}$ ,  $\Delta m_{FW}$ , and  $\Delta m_{SG}$  are the adjusted amount of organic waste, feces, and sewage after the classification within the day, respectively;  $\Delta P_{CCGPP,t}$  is the daily adjustment power of CCGPP, respectively;  $\Delta P_{ES,t}^{ch}$  and  $\Delta P_{ES,t}^{dis}$  are the adjustment amounts of the charging and discharging power of the power storage device, respectively;  $\Delta P_{HS,t}^{ch}$  and  $\Delta P_{HS,t}^{dis}$  are the adjustment amounts of the charging and discharging power of the heat storage device, respectively;  $\Delta P_{GS,t}^{ch}$ ,  $\Delta P_{GS,t}^{dis}$  are the adjustment amounts of the gas storage device charging and discharging power, respectively.

## 5. Case Analysis

The NZCP multi-time-scale optimization model based on stepped carbon allowance trading established in this study is a typical mixed integer linear programming problem, the Yalmip + Cplex solver is used to solve the problem based on the MATLAB platform.

In this paper, an example simulation is carried out by taking a Park-level Integrated Energy System in northern my country as an example. Renewable energy power generation and multiple load forecast curves are shown in Figure 3. The parameters of each device are shown in Table 1.

In order to verify the economy and low-carbon characteristics of the NZCP multi-time-scale rolling optimization scheduling method based on the ladder carbon allowance trading mechanism proposed in this study, the following three scenarios are used to compare and analyze NZCP. In Scenario 1, the carbon allowance trading mechanism is not considered, and the conventional day-ahead scheduling method is adopted. In Scenario 2, a unified carbon allowance trading mechanism is introduced, and the conventional day-ahead scheduling method is adopted. In Scenario 3, the stepped carbon allowance trading mechanism proposed in this paper is introduced, and the multi-time-scale rolling optimization scheduling method proposed in this paper is adopted. The basic parameters of carbon allowance trading are set: the base price is 250 yuan/t, the compensation coefficient is 0.25, the carbon emission interval length  $L = 50$  t, and the carbon allowance price growth rate is 25%. The scheduling results and carbon emissions under the three scenarios are shown in Table 2.

It can be seen that the introduction of unified carbon allowance trading in Scenario 2 effectively restrains the CO<sub>2</sub> emission level of production enterprises, and the CO<sub>2</sub> emission is reduced by 711.56 t compared with Scenario 1. However, due to the lack of effective output adjustment methods and optimal scheduling mechanisms for the high energy consumption characteristics of carbon capture equipment in Scenario 2, the cost of energy purchase and carbon sequestration will increase, and the unified carbon allowance trading lacks effective reward, punishment and incentive policies, the cost of Scenario 2 increases by 6.39% compared to Scenario 1.

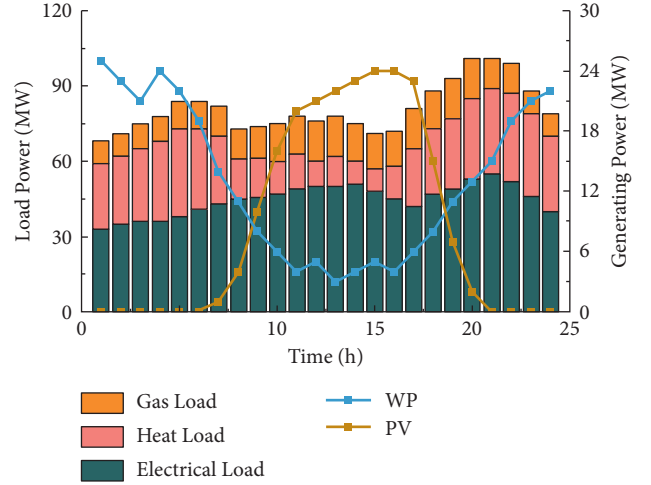


FIGURE 3: Renewable energy generation and load forecast curve.

The tiered carbon allowance trading further constrains the CO<sub>2</sub> emission level of production enterprises. Compared with Scenario 2, the CO<sub>2</sub> emission of Scenario 3 is reduced by 4.76 t, achieving near-zero carbon emissions in the NZCP system. At the same time, the step-by-step allowance price mechanism adopted in Scenario 3 encourages production enterprises to obtain low-carbon behavior benefits, which reduces operating costs by 21.51% and 26.23%, respectively, compared with Scenario 1 and Scenario 2. Benefiting from the tiered carbon allowance trading mechanism, the revenue is greater than the expenditure brought by carbon capture and storage, which verifies that the scheduling method proposed in this study takes into account the reduction of carbon emissions and the reduction of operating costs.

**5.1. Day-Ahead Scheduling Result Analysis.** Figures 4–6 show the optimal scheduling results of the proposed operation mode for the power grid, heat grid, and gas grid based on Scenario 3. The load peak period is 18 h–22 h and 8 h–9 h. At this time, CCGPP is mainly responsible for providing energy consumption for the load. At the same time, the waste pyrolysis and gasification power generation facilities provide active support for the power grid, the carbon emissions at this time are transferred into the liquid storage device through the flue gas bypass. During the period of 10 h–16 h and 22 h–4 h, the electrical load is in low period, and renewable energy is mainly used to generate electricity to meet the energy consumption of carbon capture in the liquid storage equipment. It can be seen that CCGPP and waste utilization system smooth the peak-to-valley curve of electrical load, and liquid storage CCGPP provides a good way for renewable energy consumption.

During the period of 11 h–14 h and 17 h–20 h, it is in the peak period of gas consumption. At this time, the manure gas production facilities in the waste utilization system increase the output, which not only increases the peak shaving capacity of the gas network, but also provides a stable gas source for CCGPP. It can be seen that the waste utilization system can provide peak shaving capability for the gas

TABLE 1: The operating parameters of each equipment.

Equipment	Parameter	Numerical value
Waste pyrolysis gasification power generation facility	Amount of garbage handled	40
	Rated power	30
Manure treatment facility	The amount of manure treated	40
	Electric to gas efficiency	0.7
P2G	Output climbing upper and lower limit	10/0
	Electricity to heat efficiency	0.6
EB	Output climbing upper and lower limit	10/0
	Maximum charge and discharge power	25/25
Electricity storage device	Charge/discharge factor	0.9/0.9
	Maximum charge and discharge power	10/10
Heat storage device	Charge/discharge factor	0.9/0.9
	Maximum charge and discharge power	4/4
Gas storage device	Charge/discharge factor	0.9/0.9

TABLE 2: Optimization results in each scenario and carbon emissions after allowance offset.

Type	Scenario 1	Scenario 2	Scenario 3
Energy purchase cost	6.77	7.32	6.63
Operation and maintenance costs of renewable energy power generation equipment	1.51	1.78	1.35
Waste utilization system operating costs	3.23	3.23	3.23
CCGPP operating cost	4.72	5.13	5.41
P2G unit operating cost	0.72	0.93	0.95
Carbon sequestration cost	0.11	0.25	0.33
Carbon allowance transaction cost	0	-0.51	-4.51
CO <sub>2</sub> emissions after allowance offset	752.14	40.58	8.99
Total operating cost	17.06	18.15	13.39

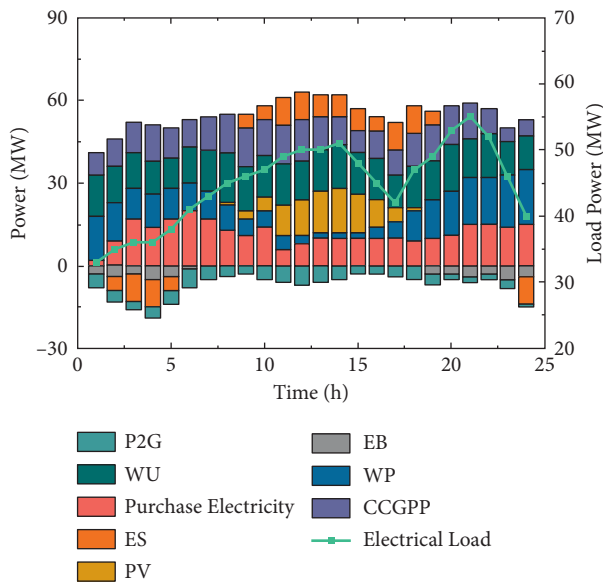
Unit:  $10^4$  ¥.

FIGURE 4: Electricity dispatch results.

network, and the operating cost is low. It provides a good adjustment capability for the gas network and effectively reduces the operating cost of the system.

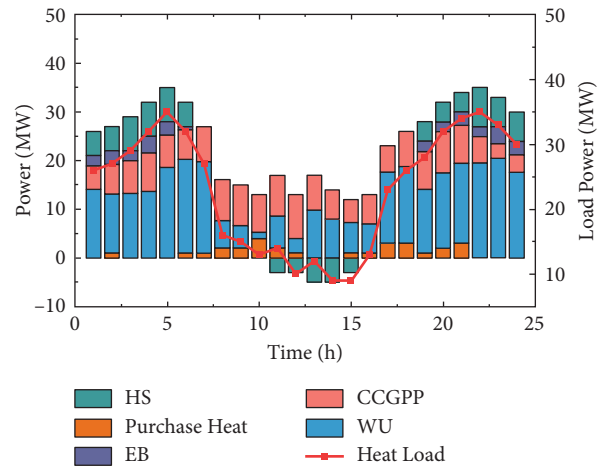


FIGURE 5: Heat dispatch results.

**5.2. Analysis of Intraday Scheduling Results.** The optimal rolling optimization duration within the day is determined based on the operation method proposed in Scenario 3. The system operating costs under different rolling optimization durations are shown in Figure 7.

It can be seen that when the rolling optimization time is increased from 1 h to 3 h, the operating cost is increased from  $16.97 \times 10^4$  ¥ to  $27.74 \times 10^4$  ¥; when the rolling optimization time is increased from 3 h to 4 h, the operating cost

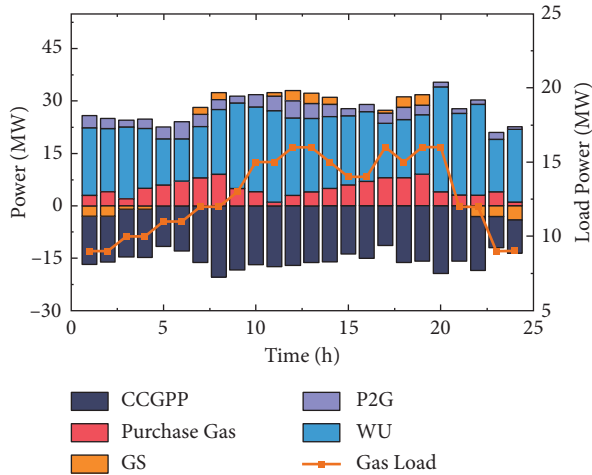


FIGURE 6: Gas dispatch results.

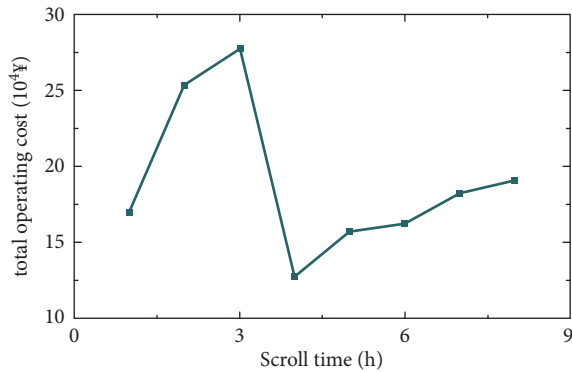


FIGURE 7: The total operating cost curve of the system under different rolling optimization durations.

is reduced from  $27.74 \times 10^4 \text{ ¥}$  to  $12.74 \times 10^4 \text{ ¥}$ ; when the rolling optimization time is increased from 5 h to 8 h, the operating cost increases from  $15.69 \times 10^4 \text{ ¥}$  to  $19.07 \times 10^4 \text{ ¥}$ . According to the above optimization operation results, when the rolling optimization time is 4 h, the system operating cost is reduced by 4.85% compared with the previous total operating cost, and the goal of minimum operating cost is achieved. It can be seen that the optimal rolling optimization time  $H$  is 4 h, and take 15 minutes as the time scale to take 16 sampling points for rolling optimization.

In order to verify the superiority of the multi-time-scale rolling optimal scheduling method, the multi-time-scale rolling optimal scheduling method for this problem is compared with the day-ahead scheduling results. The comparison of the daily output rolling optimization and adjustment effects of the power grid, the heat grid, and the gas grid is shown in Figures 8–10, respectively. In order to cope with the load fluctuation caused by the forecast error of the ultra-short-term time scale of renewable energy within the day, the day-ahead dispatch optimization method mainly purchases energy from the external main network, Intraday rolling optimization scheduling mainly uses energy storage equipment and the low response time characteristics of CCGPP to provide active support for the intraday demand

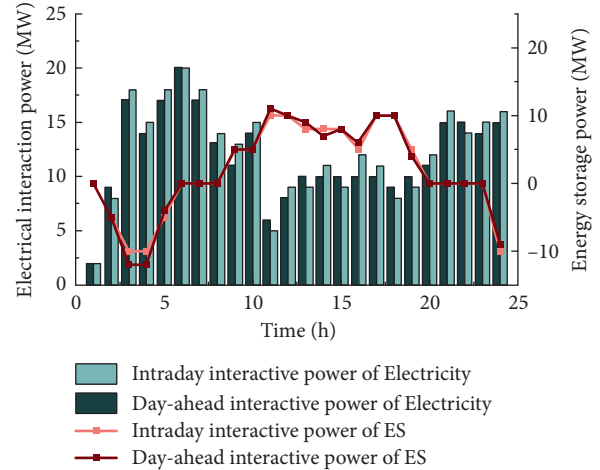


FIGURE 8: Intraday rolling dispatch adjustment effect of power grid.

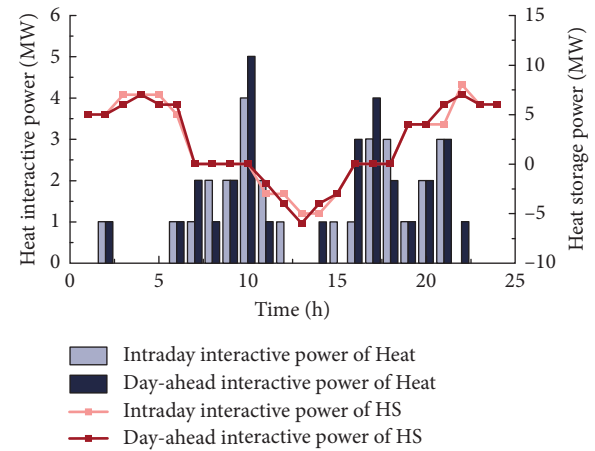


FIGURE 9: Intraday rolling scheduling adjustment effect of heat network.

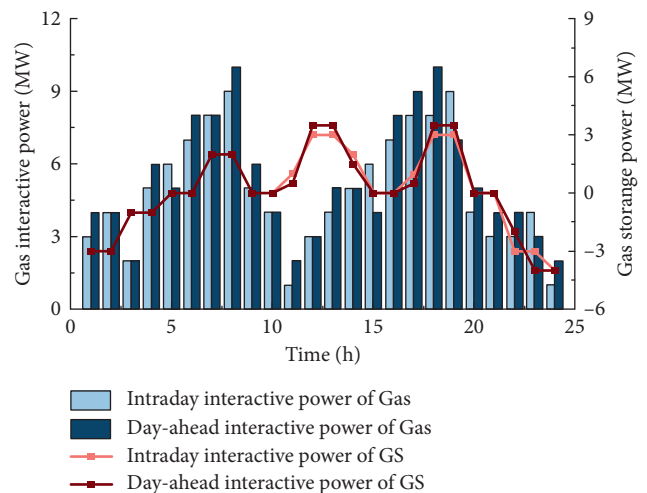


FIGURE 10: Intraday rolling scheduling adjustment effect of gas network.



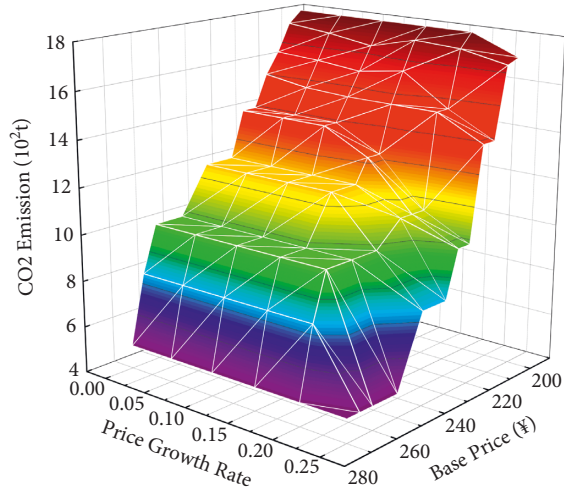


FIGURE 11: Carbon emission relationships for different base prices and price growth rates.

power of multiple loads. It ensures that the output adjustment is made on the basis of the effective scheduling plan before, and further eliminates the influence of the forecast error on the accuracy of the scheduling result.

According to the results of the daily rolling optimization, it can be seen that the energy purchased during the peak period of the load curve is reduced, and energy storage equipment is mainly used for adjustment. The rolling optimization scheduling results guide the energy storage device to perform more reasonable charging and discharging behaviors, so as to adjust the daily output in response to the source-load forecast error, and at the same time avoid the increase in loss costs caused by frequent charging and discharging, and ensure operational reliability.

The carbon emission relationship between different base prices and price growth rates is shown in Figure 11. It can be seen that with the increase in price growth rate, the correlation between carbon emissions and base price gradually increases. When the base price reaches 240, the relationship between carbon emissions and the price growth rate weakens, and when the base price reaches 270, the price growth rate has nothing to do with carbon emission allowances.

When the price growth rate is in the range of 0–0.25, with the increase in the price of carbon emission rights allowances, each production entity adjusts the output range of equipment to reduce carbon emissions. When the price growth rate is close to 0.25, the output of the equipment is stable and at the lower limit of the adjustable range, and there is no longer an adjustment margin. At this time, the difference between carbon emission and carbon emission right quota is at the boundary of carbon emission interval, and increasing the price growth rate cannot effectively restrain carbon emission. It can be seen from the above analysis that when the difference between carbon emission and carbon emission right quota exceeds the carbon emission range, the price growth rate can constrain carbon emission to a certain extent.

## 6. Conclusions

In this study, a multi-time-scale rolling optimization model with the lowest comprehensive operating cost of NZCP as the optimization goal is established based on the stepped carbon emission allowance trading mechanism. The optimization results under the three scenarios are compared and analyzed to provide a theoretical basis for the construction of NZCP.

- (1) A day-ahead-intraday rolling optimization model is established, the unit output plan is optimized in the day-ahead stage, and the output adjustment is formulated with local rolling optimization in the intraday stage. The fast response characteristics of energy storage equipment are fully utilized to participate in the intraday adjustment plan, which effectively reduces the cost of energy purchase and the operation and maintenance cost of energy storage devices, thereby reducing the operating cost of the system.
- (2) The stepped carbon allowance trading mechanism is proposed and the carbon allowance compensation coefficient is introduced, which verifies that its carbon emission restraint efficiency and economy are better than the unified carbon allowance trading mechanism. Combined with the low-carbon characteristics of the CCGPP-P2G system, it provides a good economy for the system while offsetting carbon emissions.
- (3) The carbon emission relationship between different base prices and price growth rates is analyzed. The difference between carbon emissions and carbon emission rights quotas should be within the length of the carbon emission range, and rationally setting price growth rates and base prices is conducive to constraining system carbon emissions within the total carbon allowances.

## Data Availability

The datasets generated for this study are available on request to the corresponding author.

## Conflicts of Interest

The authors declare that the research was conducted in the absence of any commercial or financial relationships that could be construed as potential conflicts of interest.

## Acknowledgments

This work was supported by Key R&D Program of Liaoning Province (2020JH2/10300101), Liaoning Revitalization Talents Program (XLYC1907138), and Key R&D Program of Shenyang (GG200252).

## References

- [1] H. Li, N. Zhang, C. Kang, G. H. Xie, and Q. H. Li, "Analytics of contribution degree for renewable energy accommodation

- factors," *Proceedings of the CSEE*, vol. 39, no. 4, pp. 1009–1018, 2019.
- [2] Y. Cheng, E. Du, X. Tian, N. Zhang, and C. Q. Kang, "Carbon capture power plants in power systems: review and latest research trends," *Journal of Global Energy Interconnection*, vol. 3, no. 4, pp. 339–350, 2020.
  - [3] Y. Li, H. Zhang, X. Liang, and B. Huang, "Event-triggered-based distributed cooperative energy management for multi-energy systems," *IEEE Transactions on Industrial Informatics*, vol. 15, no. 4, pp. 2008–2022, 2019.
  - [4] Y. Li, D. W. Gao, W. Gao, H. Zhang, and J. Zhou, "A distributed double-Newton descent algorithm for cooperative energy management of multiple energy bodies in energy internet," *IEEE Transactions on Industrial Informatics*, vol. 17, no. 9, pp. 5993–6003, 2021.
  - [5] National Development and Reform Commission, "National Energy Board. Notice on printing and distributing the "14th Five-Year Plan for Modern Energy System" [EB/OL]," 2022, [https://www.ndrc.gov.cn/xwdt/tzgg/202203/t20220322\\_1320017.html?code=&state=123](https://www.ndrc.gov.cn/xwdt/tzgg/202203/t20220322_1320017.html?code=&state=123).
  - [6] R. Wang, Q. Sun, P. Tu, J. Xiao, Y. Gui, and P. Wang, "Reduced-order aggregate model for large-scale converters with inhomogeneous initial conditions in DC microgrids," *IEEE Transactions on Energy Conversion*, vol. 36, no. 3, pp. 2473–2484, 2021.
  - [7] X. Li, R. Zhang, L. Bai, G. Li, T. Jiang, and H. Chen, "Stochastic low-carbon scheduling with carbon capture power plants and coupon-based demand response," *Applied Energy*, vol. 210, pp. 1219–1228, 2018.
  - [8] R. Wang, Q. Sun, W. Hu, Y. Li, D. Ma, and P. Wang, "SoC-based droop coefficients stability region analysis of the battery for stand-alone supply systems with constant power loads," *IEEE Transactions on Power Electronics*, vol. 36, no. 7, pp. 7866–7879, 2021.
  - [9] T. Ma, Z. Zhang, and B. Cui, "Impulsive consensus of nonlinear fuzzy multi-agent systems under DoS attack," *Nonlinear Analysis: Hybrid Systems*, vol. 44, Article ID 101155, 2022.
  - [10] T. Qin, H. Liu, J. Wang, Z. Feng, and W. Fang, "Carbon trading based low-carbon economic dispatch for integrated electricity-heat-gas energy system," *Automation of Electric Power Systems*, vol. 42, no. 14, pp. 8–13, 2018.
  - [11] Z. Chen, Z. Hu, C. Weng, and T. Li, "Multi-stage planning of park-level integrated energy system based on ladder-type carbon trading mechanism," *Electric Power Automation Equipment*, vol. 41, no. 9, pp. 148–155, 2021.
  - [12] N. Li, W. Wang, X. Ma, F. Li, F. Yang, and X. Li, "Distribution network expansion planning considering carbon trading cost and regional energy optimization," *Science Technology and Engineering*, vol. 22, no. 8, pp. 3101–3109, 2022.
  - [13] Z. Wang, Y. Teng, H. Hu, and Z. Chen, "Multi-energy system optimal model in consideration of coordinate disposal of power grid and gas network and waste," *High Voltage Engineering*, vol. 47, no. 1, pp. 63–72, 2021.
  - [14] Y. Teng, P. Sun, M. Zhang, Z. Chen, Robust optimization model of "Energy-environment-economy" based on the new rural industrial structure," *Proceedings of the CSEE*, vol. 42, no. 2, pp. 614–631, 2022.
  - [15] H. Yang, M. Xie, W. Huang, M. Zhang, B. Shi, Y. Hong, Z. Zhu, and W. Yu, Low-carbon economic operation of urban integrated energy system including waste treatment," *Power System Technology*, vol. 45, no. 9, pp. 3545–3552, 2021.
  - [16] C. Wang, C. Lv, P. Li, L. Shuquan and Z. Kunpeng, Multiple time-scale optimal scheduling of community integrated energy system based on model predictive control," *Proceedings of the CSEE*, vol. 39, no. 23, pp. 6791–6803+7093, 2019.
  - [17] X. Jin, Y. Mu, H. Jia, X. D. Yu, K. Xu, and J. Xu, "Model predictive control based multiple-time-scheduling method for microgrid system with smart buildings integrated," *Automation of Electric Power Systems*, vol. 43, no. 16, pp. 25–33, 2019.
  - [18] J. Tang, M. Ding, S. Lu, S. Li, J. Huang, and W. Gu, "Operational flexibility constrained intraday rolling dispatch strategy for CHP microgrid," *IEEE Access*, vol. 7, pp. 96639–96649, 2019.
  - [19] Z. Wang, S. Yan, Application of carbon capture technology in gas power plant," *Modern Chemical Industry*, vol. 38, no. 9, pp. 195–197, 2018.
  - [20] Q. Chen, C. Kang, and Q. Xia, "Operation mechanism and peak-load shaving effects of carbon-capture power plant," *Proceedings of the CSEE*, vol. 30, no. 7, pp. 22–28, 2010.
  - [21] Q. Chen, Z. Ji, C. Kang, and H. Ming, "Analysis on relation between power generation and carbon emission of carbon capture power plant in different operation modes," *Automation of Electric Power Systems*, vol. 36, no. 18, pp. 109–115, 2012.
  - [22] Y. Cui, P. Zeng, Z. Wang, M. Wang, J. Zhang, and Y. Zhao, "Low-carbon economic dispatch of electricity-gas-heat integrated energy system that takes into account the electricity price-type demand-side response to carbon-containing capture equipment," *Power System Technology*, vol. 45, no. 2, pp. 447–461, 2021.
  - [23] R. Wang, Q. Sun, D. Ma, and Z. Liu, "The small-signal stability analysis of the droop-controlled converter in electromagnetic timescale," *IEEE Transactions on Sustainable Energy*, vol. 10, no. 3, pp. 1459–1469, 2019.
  - [24] S. Clegg, and P. Mancarella, "Integrated modeling and assessment of the operational impact of power-to-gas (P2G) on electrical and gas transmission networks," *IEEE Transactions on Sustainable Energy*, vol. 6, no. 4, pp. 1234–1244, 2015.
  - [25] A. T. Sipra, N. Gao, and H. Sarwar, "Municipal solid waste (MSW) pyrolysis for bio-fuel production: a review of effects of MSW components and catalysts," *Fuel Processing Technology*, vol. 175, pp. 131–147, 2018.
  - [26] N. A. Qambrani, M. M. Rahman, S. Won, S. Shim, and C. Ra, "Biochar properties and eco-friendly applications for climate change mitigation, waste management, and wastewater treatment: a review," *Renewable and Sustainable Energy Reviews*, vol. 79, pp. 255–273, 2017.
  - [27] N. Scarlat, J. F. Dallemand, and F. Fahl, "Biogas: developments and perspectives in europe," *Renewable Energy*, vol. 129, pp. 457–472, 2018.

## Research Article

# An Assessment and Design of a Distributed Hybrid Energy System for Rural Electrification: The Case for Jamataka Village, Botswana

Ravi Samikannu <sup>1</sup>, Moses Tunde Oladiran <sup>2</sup>, Gladys Gamariel <sup>3</sup>, Patricia Makepe <sup>4</sup>,  
Ketshephaone Keisang <sup>2</sup> and Nyagong Santino David Ladu <sup>5</sup>

<sup>1</sup>Department of Electrical, Computer and Telecommunications Engineering,  
Botswana International University of Science and Technology, Palapye, Botswana

<sup>2</sup>Department of Mechanical, Energy and Industrial Engineering, Botswana International University of Science and Technology,  
Palapye, Botswana

<sup>3</sup>Department of Business, Management and Entrepreneurship, Botswana International University of Science and Technology,  
Palapye, Botswana

<sup>4</sup>Centre for Business Management, Entrepreneurship and General Education,  
Botswana International University of Science and Technology, Palapye, Botswana

<sup>5</sup>Department of Mathematics and Physics, Rumbek University of Science and Technology, Rumbek, South Sudan

Correspondence should be addressed to Ravi Samikannu; [ravis@biust.ac.bw](mailto:ravis@biust.ac.bw)

Received 20 June 2022; Revised 24 July 2022; Accepted 26 July 2022; Published 10 September 2022

Academic Editor: Qiuye Sun

Copyright © 2022 Ravi Samikannu et al. This is an open access article distributed under the Creative Commons Attribution License, which permits unrestricted use, distribution, and reproduction in any medium, provided the original work is properly cited.

This research focuses on an assessment and design of a hybrid Photo Voltaic (PV)-wind system for rural electrification in Jamataka village, Botswana. The assessment revealed the most pressing factors for the need for reliable energy and the issues that the village community had with existing electricity sources. Hybrid Optimization of Multiple Energy Resources (HOMER) software was used to perform all the hybrid system configurations, simulations, and selections. The assessment research was carried out using questionnaires and physical data collection on site. With a peak load of 27.31 kW, the annual average demand is 165.29 kWh/day. The results show that the PV/wind/battery system generates the most economic and technical benefits, as measured by the Net Present Cost (NPC). Due to the high initial expenditures on renewable energy systems, the Levelized Cost of Energy (LCOE) of the system is 65 percent higher than the present energy cost in Botswana for households and 57 percent higher for companies. The International Renewable Energy Agency's global report of renewable energy generation costs between 2010 and 2020 revealed a significant decrease, with utility-scale solar PV costs falling by 85% and onshore wind costs falling by 56 percent. As a result, the LCOE decreases as the cost of renewable energy decreases. Subsidies for renewable energy systems, on the other hand, can significantly reduce the LCOE.

## 1. Introduction

The electricity challenges faced by remote communities such as geographical constraints, economic, social, and cultural challenges are well known and documented [1–5]. Due to the high initial costs and intermittency of renewable energy sources like solar and wind, most renewable energy hybrid systems have design issues. Adding a diesel generator to the

renewable energy hybrid systems will be an efficient option to boost system reliability [6]. To minimize the high initial costs associated with renewable energy power systems, costs associated with manufacturing battery storage systems and renewable energy technologies should be minimized [7]. Globally, about billion people are estimated to be without electricity, with grid extension challenges being one of the key contributing factors [8]. Fossil fuels, which accounted



for nearly 80% of global energy in the last century, are fast depleting because of rising energy demand due to economic and population growth. As a result of this heavy reliance on fossil fuels, greenhouse gas emissions have increased, contributing to global warming and posing a serious threat to ecosystems and global health [9, 10]. However, the continued reduction in costs of renewable energy technologies such as solar, wind, and biomass technologies has also stimulated interest toward renewable energy sources [11–13]. Apart from cost benefits, renewable energy off-grid hybrid systems have other advantages, such as boosting local businesses, reducing pollution, and generating employment [5].

The challenges of energy provision in rural Botswana, as well as the impediments to the application of new technology in the energy industry, include uneven distribution of renewable energy resources, untapped solar potential, excessive heat affecting solar output production, human resource obstacles such as a low number of unskilled workers, and issues such as power theft arising from poverty [14].

Many studies have been undertaken on rural power systems, with most similar ones focusing on feasibility and techno-economic analysis. However, no similar study has been conducted in this rural location and the real-time data collection was captured. A feasibility study of a PV-wind hybrid power system for electrification of a rural village in Ethiopia, with fuel cells and rechargeable batteries as backups, produced different feasible alternative solutions with a small range of LCOE, much better than the previous generator set backup hybrid PV-wind system [15]. An economic evaluation study on solar hybrid energy systems for the Salalah region in Oman with approximated radiation ranging from 4.8 kWh/m<sup>2</sup>/day to 7.4 kWh/m<sup>2</sup>/day revealed that despite the huge quantity of pollution produced by the standalone generator, which is followed by the PV/generator set/wind/battery configuration, the PV/generator set/wind/battery design has the lowest energy cost when compared to the PV/wind/battery configuration and the stand-alone generator [16]. A techno-economic comparative analysis of renewable energy systems for a case study in Zimbabwe showed that a PV-wind hybrid system offers the most economic benefits, as measured by NPC and Pay Back Period (PBP) and the best operating efficiency [17]. Meanwhile, an optimization and techno-economic analysis of a photovoltaic/wind/battery/diesel system in northern Nigeria were carried out using the MATLAB environment for simulations and a genetic algorithm for optimization, with results indicating that the optimized system was more cost-effective and environmentally friendly than diesel generator and grid extension systems in the region [18]. The researchers also concluded that solar PV-based renewable hybrid systems play an important role in ensuring that rural communities in sub-Saharan Africa have access to reliable, sustainable, and modern electricity [18]. Ahmed, Albarawy, and Ibrahim [19] proposed a genetic algorithm to find the optimal sizing of PV/wind/battery/diesel generator with the goal of lowering levelized cost of energy and increasing reliability. They found that the LCOE decreases as design parameters increase and that average wind speed is inversely

proportional to the LCOE of the location under study. Canziani, Vargas, and Gastelo-Roque [20] investigated the technical features including installation, operation, and social implications of a hybrid PV/wind microgrid established in Laguna Grande, Peru. The microgrid plant was built based on community surveys about energy utilization, social-economic elements, and factors like predicted growth and available funding. The project was built in a collaborative manner, with the community being involved at various stages. Even though the hybrid energy system was effective in supplying electricity to the site, monitoring data revealed a 10% loss of load due to peak demand, technical issues, and occasional low solar and wind resources. A techno-economic study of stand-alone hybrid PV-wind turbine-diesel-battery energy system was undertaken using HOMER software simulation for various locations in Tamil Nadu, India, based on analysis of various system combinations [21]. The findings revealed that the PV-wind-diesel-battery configuration is the most cost-effective for all sites [21]. Jain and Sawle [22] studied the economic analysis of standalone and grid-connected hybrid renewable energy systems for a remote location in India. The authors found that PV/wind/microhydro/battery/converter/DG is the most reliable and cost-effective solution for off-grid scenarios. Solar PV, fuel cells, biogas, and microhydro hybrid energy systems are all sustainable and contribute to socio-economic growth [22]. Moghaddam, Bigdeli, and Moradlou [23] presented a design for a stand-alone PV/WT/battery system for Zanjan, Iran, with the main goal of minimizing the total cost of the hybrid system while considering reliability constraints such as generation and load uncertainties. Methods such as the improved crow search algorithm for optimal sizing were used. Simulation results were presented in deterministic and probabilistic formats, and load demand was calculated using Monte Carlo simulation. They concluded that a probabilistic approach of the hybrid system designing is necessary to know the accurate cost and reliability. An off-grid renewable energy hybrid system with different battery technologies including lead acid, lithium-ion, and nickel-iron for rural electrification in India was optimized using the MATLAB environment, and Salp Swarm algorithm was used to find an optimal configuration from configurations [24]. The results show that the nickel-iron battery-based renewable energy hybrid system offers the lowest levelized cost of energy when compared to other batteries for the configured system [24]. A study of hybrid energy systems for a rural location in Nigeria revealed that using a combination of locally available abundant energy resources reduces greenhouse gas emissions and improves power reliability [5]. A study of the techno-economic optimal configuration of a small PV-wind hybrid energy system with both battery and pumped hydro storage systems modeled for a remote island (Deokjeokdo Island, South Korea) [25]. HOMER Pro was employed for running simulation while considering actual electricity consumption data for a year and noting that energy storage accounts for a significant portion of cost in setting up renewable energy systems. The analysis showed that pumped hydro storage system is the most cost-effective storage system [25].

Hybrid energy system installation in rural areas is influenced by investment expenses, operation and maintenance costs, reliability, optimal configuration, and security [26, 27]. Combining renewable energy sources in hybrid systems optimally improves system reliability and efficiency while enhancing hybrid system economics and reduces greenhouse gas emissions [28]. Major power quality difficulties in hybrid energy systems, such as voltage and frequency fluctuation, and harmonics, can be addressed to a large extent with proper design, improved fast response control capabilities, and hybrid system optimization [29]. [30] Set up an event-triggered distributed hybrid control scheme to achieve secure and cost-effective operation of the integrated energy system. The outputs of the energy hubs are controlled using a containment and consensus algorithm, and according to the outputs, the power of the electricity and heat loads can be accurately shared without knowledge of the network parameters. Additionally, the results show a decrease in communication cost based on the event-triggered communication technique used to create the associated protocols. [31] presented a deep reinforcement learning-based data-driven optimal control strategy for a virtual synchronous generator to achieve control performance goals for frequency regulation and active power regulation. Simulation results confirm the viability and efficacy of the proposed method. The results of an optimal energy management and techno-economic analysis of a stand-alone hybrid PV/wind/DG/battery microgrid for a remote area in Tamil Nadu, India, using HOMER software, show that the PV/battery combination is the most cost-effective configuration and that in comparison with a traditional isolated distribution system with DG, it also results in a 68 percent reduction in emissions [32]. A reduced-order aggregate model based on balanced truncation approach has been developed as a preprocessing technique for the real-time modeling of large converters with inhomogeneous beginning conditions in DC microgrid. The results demonstrate a reduction in input-output mappings error, and the simulation outcomes demonstrate the precision of the suggested approach [33]. [34] Conducted research on a method for accurate current sharing and voltage regulation in hybrid wind/solar systems. The research used distributed adaptive dynamic programming to find the best control variable and achieve accurate current sharing/voltage regulation, and the results showed that the model met the predetermined goals.

The study's major goal is to assess energy demands, renewable technology acceptability, and obstacles faced by previous energy systems in a rural area, and then design an energy system to match those demands while also considering the system's economic and technical benefits. This work also explores the viability of electrifying the village with a highly renewable energy-based hybrid system and the relevance of doing so for minimizing locals' contribution to deforestation, enhancing system reliability, and lowering fuel costs.

In the assessment, a survey was conducted from September 07, 2020, to September 11, 2020. During the survey 98 household, 6 commercial enterprise, 2 community leaders, and 1 farmer were interviewed.

## 2. Location Description

Jamataka is a rural low-income village located in the central region of Botswana about 45 km west of the city of Francistown. Low standards of living characterize the village, a high unemployment rate with many people depending on government subsidies as a means of livelihood with an estimated income of a household of around 50 US Dollars (\$) per month. The village has a population of about 1320 people.

### 2.1. Energy Technologies in Use in Jamataka Village.

Figures 1 and 2 show the common energy technologies used by households and businesses in Jamataka. These energy technologies have drawbacks such as being unreliable and emitting CO<sub>2</sub>, for example, the generators. In addition, the available technologies are costly to maintain and operate. For instance, the generators need to be fueled and repaired when they break down.

Figure 1 shows an example of solar systems for lighting and charging purposes commonly used by Jamataka households. The solar lighting systems comprise a small-sized solar panel with a torch and radio. Alternatively, some systems use solar panels to charge old car batteries, which are then used to charge mobile phones. However, there seems to be a general lack of knowledge and capacity on the installation of solar home systems. The common practice observed from the community is that appliances are often directly connected to solar panels. In addition, there were reports of some appliances (phones and batteries) exploding and junction boxes of solar panels burnt due to lack of voltage regulators in the installations. Most Solar Home Systems (SHS) are small and used for charging radios, mobile phones, torches, and lights.

Typical small generators shown in Figure 2 are used only during special occasions like Christmas holidays and weddings. Most of the generators are owned by households with commercial activities like tailoring, tuck shops, and welding. Business enterprises also use Liquid Petroleum Gas (LPG) and direct current refrigerators.

### 2.2. Energy Consumption in the Village.

In terms of energy use, the majority of Jamataka households use petrol or diesel generators to power their activities (sewing and welding), while others use firewood and SHS. However, over half of the respondents interviewed indicated that the capacity of the current SHS does not meet their demand. The use of petrol or diesel fuel for running generators was reported as the most expensive energy source, with most businesses spending between \$17 and \$26 per month. Figure 3 shows the results of the interviews, which demonstrated a substantial level of dissatisfaction with generator capacity.

Figure 4 shows the willingness survey results on switching to electricity. Willingness and ability to switch to electricity survey indicated that over 83% of households interviewed were willing to switch to electricity if available. In Figure 4, 97.8% of the household interviewed indicated that they would switch to electricity for lighting purposes. It is clear that lighting energy has the highest need in the village. Mobile phone charging was another energy need why respondents

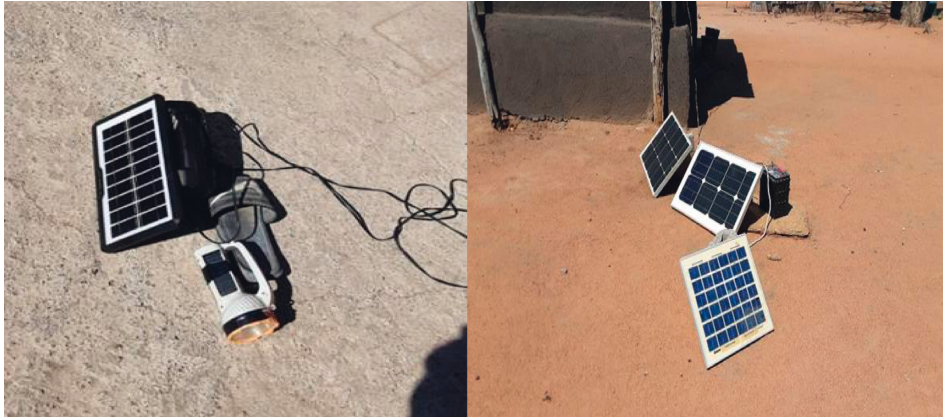


FIGURE 1: Solar systems in households in Jamataka.



FIGURE 2: Generators used by households in Jamataka.

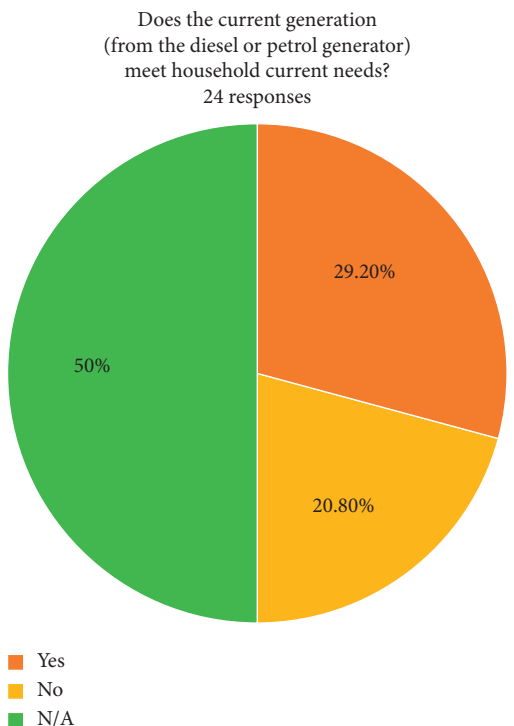


FIGURE 3: Diesel or petrol generators and households' current needs survey results.

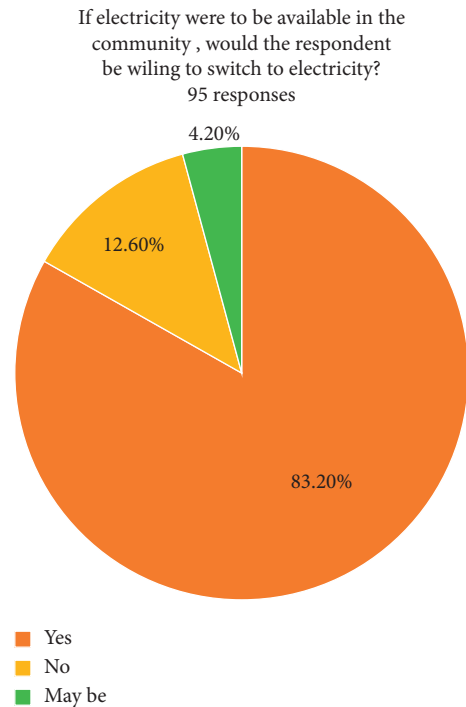


FIGURE 4: Willingness to switch to electricity.

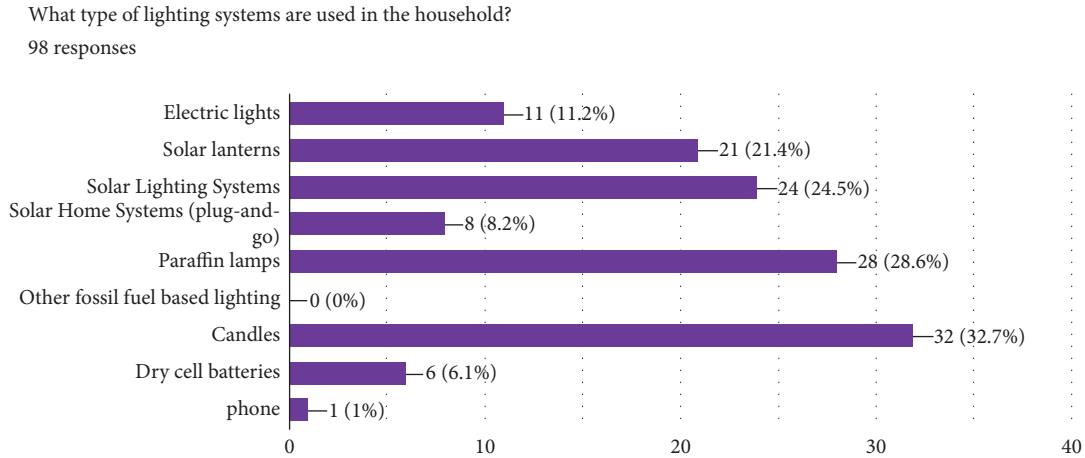


FIGURE 5: Lighting systems used in the village.

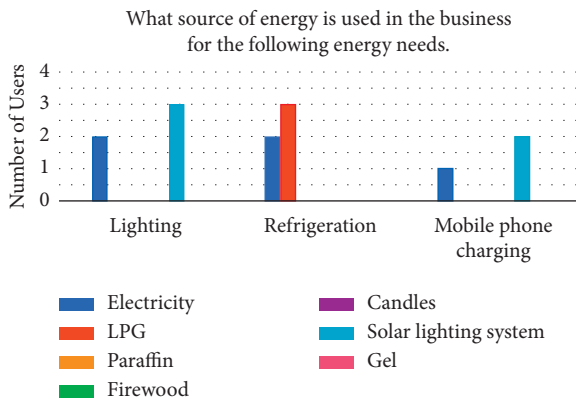


FIGURE 6: The village business energy sources.

wanted to switch to electricity, followed by entertainment, cooking, then refrigeration, in that order. Various reasons were cited for willingness to switch including convenience, security, and self-development achievement. Most respondents preferred a prepayment method for electricity consumption (75.3%), while 11.8% were indifferent to a post- or prepayment method.

Most households indicated that they preferred firewood for cooking because it was inexpensive and was easily available. This suggests that they are not likely to switch to an energy source for cooking where they will have to pay for it. The majority of households use open fire cooking, and stoves are very minimal.

Figure 5 shows that 32.7% of households use candles for lighting, followed by paraffin lamps with 29%. More than half of the respondents (i.e., 54%) preferred use of solar energy for lighting in one form or the other (solar lanterns, solar lighting systems, and solar plug and go), which is convenient, and they did not need to carry it around. The biggest challenge households had with solar systems was that they do not work when the weather is cloudy and most had to supplement with paraffin lamps or candles when their solar systems do not work. There were also cases of systems not lasting for the required number of hours.

There were six business enterprises identified in the village and these included minigroceries shops (termed tuckshops), tailoring, and one liquor shop. 50% of the enterprises own generators with an average of 2000 W shown in Figure 6.

### 3. Load Calculation

3.1. *Estimated Electrical Load for the Village.* The estimated electrical load is based on an assessment of the power consumption of households in the village.

Table 1 shows the electrical weekday load calculation for the year, with daily demand higher in the afternoon hours because of use of appliances like ceiling fans.

Figures 7 and 8 depict the village’s weekly load profile for the year and the monthly average load profile, respectively. The average electricity usage is roughly 165.29 kWh/day, and the scaled peak primary load demand is 27.31 kW. The total load is 1165.58 kWh/d.

3.2. *Location Resources.* The meteorological data obtained from NASA resource website via the HOMER software, such as solar resource, wind resource, and temperature, are used in the modeling section of this study.

Figure 9 depicts the village’s monthly average global solar radiation. The months of September to December and January to February have higher solar irradiance levels than other months. On a monthly basis, solar radiation is 5.8 kWh/m<sup>2</sup>/day. Data on solar radiation were collected over a 22-year period between 1983 and 2005.

Figure 10 shows that the monthly average wind speeds for the village are usually above 6 m/s in July to November and January to April, indicating that wind turbines could be used for various applications (e.g., water pumping, agro-processing, and power generation) during these months. The month with the highest wind speed of 7.47 m/s is October. The average wind speed is 6.43 meters per second. Even the lowest speeds are greater than 5 m/s, which is the minimum requirement for wind power applications. It is pertinent to mention that the village has a wind regime that is higher than the national average resource and would be a good location

TABLE 1: Load demand calculation for Jamataka.

S. no.	Category	Appliance	Power rating of appliances (W)	Number of appliances	Operating hours	AC load (kWh/d)
1	Households	Television	150	40	3	18
		Decoder	14	40	3	1.68
		Irons	1500	30	2	90
		Radios	100	70	3	21
		Washing machine	1300	10	2	26
		Hair dryers	1000	20	1	20
		Hair clippers	15	50	2	1.5
		Electric stoves	1200	30	6	216
		Electric kettles	1500	40	2	120
		Fridges	250	25	24	150
		Food blenders	250	70	5	87.5
		Electrical sewing machine	50	15	6	4.5
		Electrical welding machine	250	10	1	2.5
		Laptops	60	20	10	12
		Mobile phones	5	320	11	17.6
Light bulbs	20	600	5	60		
2	School	Printer	50	2	1	0.1
		Fan	90	10	3	2.7
		Fridge	250	1	5	1.25
		Desktop computer	100	3	8	2.4
		Lamps	20	40	12	9.6
4	Businesses	Fan	90	15	3	4.05
		Fridge	250	5	24	30
		Lamps	20	20	6	2.4
		Printer	50	3	9	1.35
		Speaker	2000	6	12	144
		TV	150	6	3	2.7
5	Churches	Fan	90	20	3	5.4
		Lamps	20	20	12	4.8
		Speaker	2000	5	3	30
6	Health post	TV	150	1	9	1.35
		Fan	90	10	4	3.6
		Fridge	250	1	24	6
		Desktop computer	100	2	16	3.2
		Lamps	20	20	12	4.8
		Printer	50	2	4	0.4
7	Police post	Microscope	100	2	6	1.2
		Desktop computer	100	2	8	1.6
		Lamps	20	15	12	3.6
		Fan	90	5	4	1.8
Total load (kWh/d)						<b>1116.58</b>

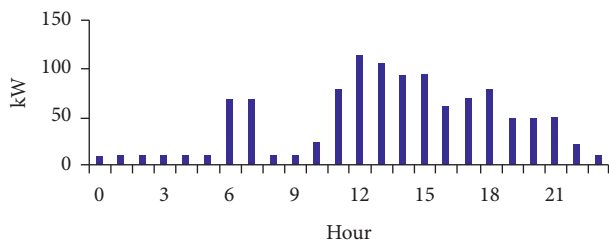


FIGURE 7: Weekday load profile of the village on an hourly basis during the year.

for different aero turbines applications. The wind data were gathered between 1984 and 2013.

Figure 11 shows that the average monthly temperatures vary from 15.35°C to 25.86°C. The yearly average temperature is 22.9°C, with the highest temperature recorded in November.

#### 4. Methodology

This section discusses components setups, mathematical modeling, costing, replacement, and operations and maintenance expenses. The components are a solar photovoltaic system, a wind turbine system, a diesel generator, a battery system, and a converter.

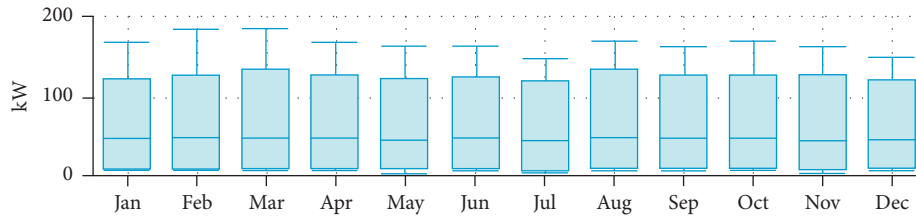


FIGURE 8: Monthly average load profile of the house.

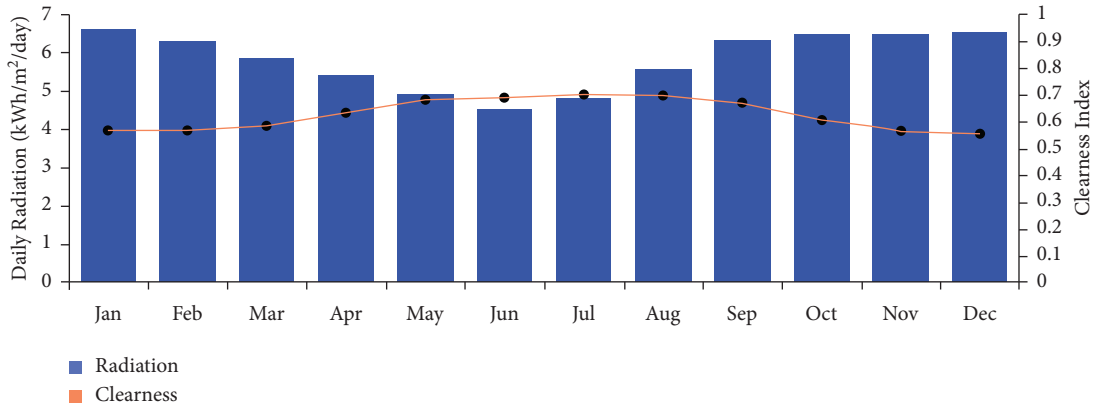


FIGURE 9: Monthly average global radiation at Jamataka.

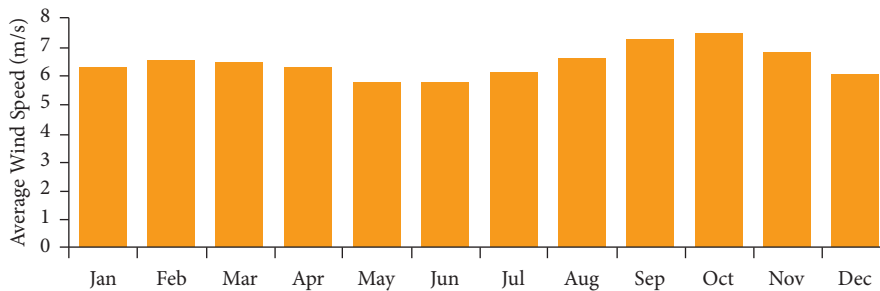


FIGURE 10: Average monthly wind speed of Jamataka.

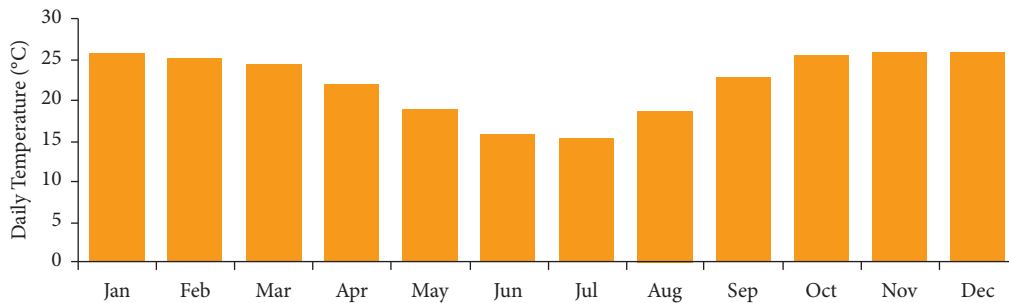


FIGURE 11: The monthly average temperature of Jamataka.

The system was optimized with the aid of the HOMER Pro software. HOMER Pro was created by the National Renewable Energy Laboratory in the United States and is largely used for the design of distributed generation systems via modeling, optimization, and sensitivity analysis techniques.

The system is designed so that its load may be met by a hybrid system that combines a PV and wind energy source, with a diesel generator added to the mix to address intermittent power supply problems. However, the results analysis will choose the configuration that offers the



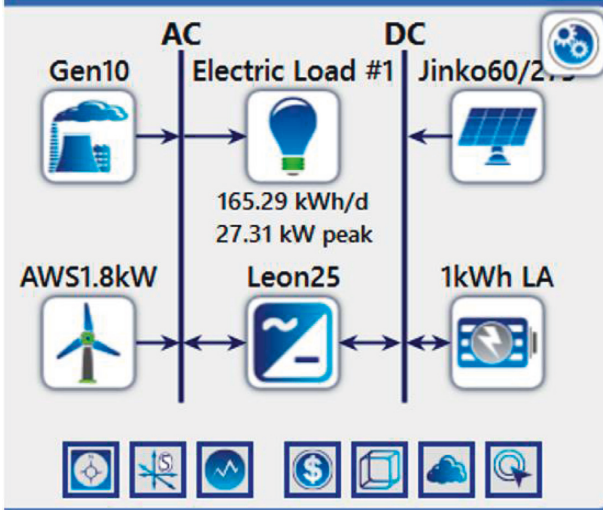


FIGURE 12: General optimized hybrid system architecture.

optimal balance of economic and technical benefits. The energy from solar PV and wind is stored in a battery bank through the bidirectional converter and charge controller. The output from the solar PV and wind is used to power the AC load considered in this study by converting the DC energy from the solar and battery to AC energy using an inverter.

Figure 12 depicts the proposed AC/DC hybrid system configuration.

**4.1. Photovoltaic System.** The PV module used in the simulation is a 60-polycrystalline cell module with an efficiency of 16.8% and a derating factor of 88 percent. Jinko Solar manufactured the module with a 275 Watts rated capacity and an operating temperature and temperature coefficient of 45°C and -0.4°C, respectively. The initial capital and replacement costs were set at \$472.73 per kW and \$436.36 per kW, respectively, and the annual operation and maintenance cost was assumed as 10% of the initial capital cost for this PV. The PV module has a 25-year life span.

The PV system's total power output is modeled as [35]

$$P_{pv}^t = N_{pv} \times P_{pv}(t), \quad (1)$$

where  $P_{pv}^t$  denotes total PV output power,  $N_{pv}$  represents the number of PV panels, and  $P_{pv}(t)$  stands for the hourly power produced from the PV system.

**4.2. Wind System.** Each wind turbine is rated at 1.8 kW, with a capital cost of \$6000 and a replacement cost of \$5600. The average cost of operating and maintaining a wind turbine is assumed as \$120 per year. This wind turbine has three blades and a hub height of 12 m, with a survival speed of 50 m/s. During the wind turbine modeling process, ambient temperature effects were considered.

The power produced by the wind depends on wind speed and the cross-sectional area it sweeps through [36]

$$P = \frac{1}{2} \rho A C_p V^3, \quad (2)$$

where  $P$  represents the wind power and it is measured in Watts,  $\rho$  symbolizes the air density measured in  $\text{kg/m}^3$ ,  $A$  stands for the cross-sectional area, which the wind sweeps through,  $V$  denotes the wind speed in m/s, and  $C_p$  defines the power coefficient of the wind generator.

**4.3. Diesel Generator.** In renewable energy hybrid systems, generators maintain consistent power for peak loads. For this investigation, a generic 10 kW fixed capacity generator was chosen. The capital cost is \$4,800 per generator, while the replacement cost is \$4,600 per generator. The cost of operation and maintenance is \$0.01 per hour. The price of fuel (diesel) in 2022 in Botswana is about \$1.08 per liter [37]. The lifetime of diesel generator (DG) is 15,000 operating hours with a minimum load factor of 25%.

The majority of the costs associated with running generators are due to fuel; hence, the fuel consumption rate is modeled as [38]

$$FC = \sum_{DG} (a + bP_{DG} + cP_{DG}^2), \quad (3)$$

where  $FC$  denotes the fuel consumption rate;  $a$ ,  $b$ , and  $c$  represent the diesel generator cost coefficient; and  $P_{DG}$  defines the generator power capacity.

**4.4. Battery System.** Batteries are utilized in renewable hybrid power systems to store extra energy that can be utilized when the system needs it. The battery's life is determined by how many times it is charged and discharged each day. The battery model used in this study is a generic 1 kWh lead-acid battery. An individual battery rating's nominal voltage, maximum capacity, and nominal capacity are 12 V, 83.4 h, and 1 kWh, respectively. Each battery's initial and replacement costs are set at \$550 and \$500, respectively.

The performance of a battery system is determined by its state of charge (SOC), which is expressed as [38]

$$SOC(t) = SOC(0) + \beta c \sum_i P_c^B(i, t) - \beta d \sum_j P_d^B(j, t), \quad (4)$$

where  $P_c^B$  and  $P_d^B$  represent power capacity for charging and discharging of the battery at time  $t$ , and  $\beta c$  and  $\beta d$  represent the charging and discharging efficiency of the battery, respectively.

The battery system must function within the permitted SOC limits established by each manufacturer as expressed by

$$SOC_{\min} \leq SOC(t) \leq SOC_{\max}. \quad (5)$$

The battery system performs at its optimum when depth of discharge (DOD) is taken into account.

$$SOC_{\min} = 1 - DOD. \quad (6)$$

**4.5. Converter.** Converting AC to DC and vice versa uses converters that consist of inverters and rectifiers. The

TABLE 2: Optimization results of the proposed system under different setups.

Item (units)	System setups			
	PV/WT/DG/battery	PV/WT/battery	WT/DG/battery	PV/DG/battery
<b>Economic performance</b>				
NPC (\$)	343181.3	339804.26	392603.98	404537.61
LCOE (\$)	0.2857	0.298	0.3404	0.3365
<b>Technical performance</b>				
Renewable fraction (%)	72.2	100	50	65.9
PV production (kWh/yr)	37083	65814	0	84667
WT production (kWh/yr)	41336	56838	51671	0
DG production (kWh/yr)	16771	0	28952	20592
Excess electricity (kWh/yr)	33655	62111	22204	41982
Unmet electric load (kWh/yr)	56.5	3124	2457	0.0539
Capacity shortage (kWh/yr)	332	6057	5608	11.4
Batteries nominal capacity (kWh)	31	50	7.01	56
Batteries lifetime throughput (kWh/yr)	23344	40000	5600	44800
Batteries expected life (yr)	10	4.43	3.4	7.74
Batteries autonomy (hr)	2.7	4.36	0.61	4.88
Maximum inverter output (kW)	10.4	14.9	1.67	18.5
Maximum rectifier output (kW)	6.71	11.2	1.33	1.27
<b>Emissions produced</b>				
Carbon dioxide (kg/yr)	16653	0	28249	19485
Carbon monoxide (kg/yr)	126	0	214	147
Unburned hydrocarbons (kg/yr)	4.59	0	7.79	5.37
Particulate matter (kg/yr)	7.64	0	13	8.94
Sulfur dioxide (kg/yr)	40.9	0	69.3	47.8
Nitrogen oxides (kg/yr)	143	0	243	168

converter utilized in this study has a 10-year life span and a 96 percent inverter and 94 percent rectifier efficiency. The initial capital cost is \$ 550 per kW, whereas the replacement cost is \$ 500 per kW. For each converter, an annual O&M cost of \$ 120 is considered.

Figure 12 depicts the general hybrid system that includes a DG, renewable energy sources, a converter, and a battery system.

## 5. Results and Discussion

This section contains the results and discussion of the hybrid system employed to supply the electrical power demand of Jamataka. The performance of the system in terms of technical, economic, and environmental factors was investigated using four distinct configurations. This study assumed a project's lifetime of 25 years. A benchmark interest rate of 3.75% was adopted from Trading Economics [39]. This value corresponds to Botswana's discount rate recorded from October 2021 to February 2022. Botswana's inflation rate for 2020 is 1.89 percent [40].

*5.1. Optimization Results.* HOMER tool optimizes hybrid system component sizes in the simulation to match the load demand of the case study site. As a result, all system combinations were evaluated in terms of NPC, COE, and technical performance indicators. The optimal solution was chosen based on the lowest value of NPC and environmental impact of each system from optimization results of every base case. Table 2

presents the four distinct setups that were considered for analysis.

The results indicate PV/WT/battery combination as the most viable option in terms of NPC and emissions. However, the LCOE of PV/wind WT/DG/battery combination has the lowest value followed by that of PV/wind WT/battery combination. The most viable hybrid system configuration consists of PV, WT, converter, and battery rated at 35.4 kW, 19.8 kW, 26.1 kW, and 50 units, respectively. This combination is the most sustainable energy system with a renewable fraction of 100%, 0% electricity supply from nonrenewable sources, and zero or low levels of emissions.

In general, all combinations have minor reliability issues of less than 6% because they have low unmet loads. The PV/WT/battery combination has the highest unmet load of about 3124 kWh/year, which is 5.8% of the total load. The PV/DG/battery combination, on the other hand, is the most reliable, with the lowest unmet load (0.0539 kWh/yr), which is 0.02% of the total load. The PV/DG/battery combination has the lowest reliability rank due to power intermittency since the energy sources that make up the combination include solar resource. Solar energy can only be harnessed during the day, but wind energy can mostly be harnessed at night. The diesel generator reduces the problem of intermittency in the other combinations.

The yearly battery throughputs and the battery lifespan have an inverse relationship. From the optimization exercise, the PV/WT/DG/battery combination has the lowest battery throughputs, estimated at 23344 kWh/year, resulting in the longest service lifespan, projected at 10 years. The WT/DG/battery combination, on the other hand, has the highest



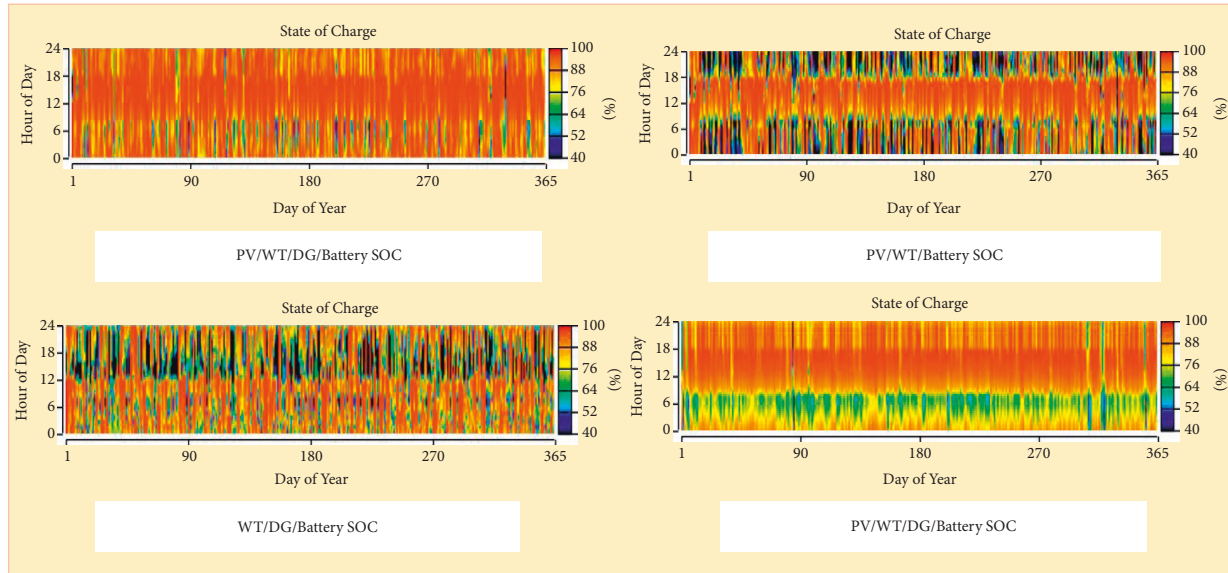


FIGURE 13: The battery system state of charge for the different combinations.

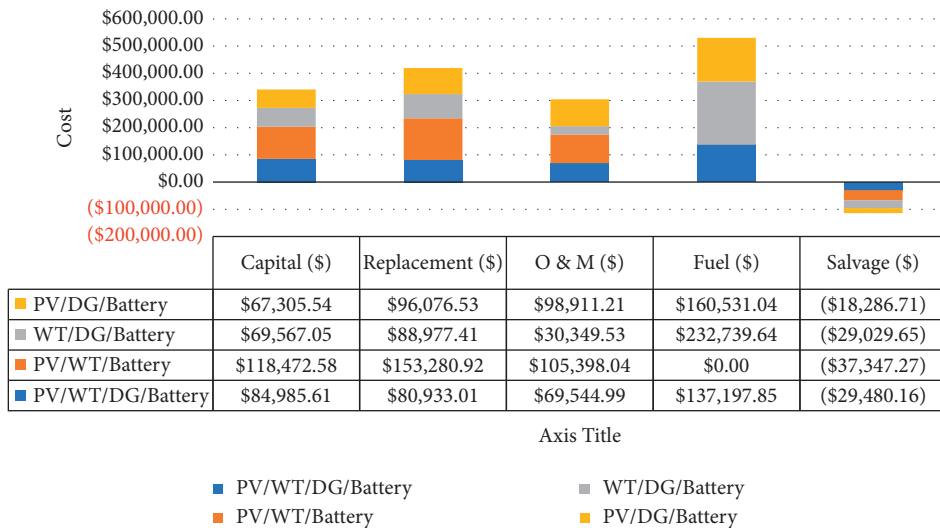


FIGURE 14: Cost summary of system setups.

throughputs, estimated at 5600 kWh each year, resulting in the lowest battery lifespan of 3.4 years.

PV/DG/battery combination has the highest average battery autonomy hours of 4.88 hours, followed by PV/WT/battery, PV/WT/DG/battery, and WT/battery combinations with 4.36 hours, 2.7 hours, and 0.61 hours, respectively.

Table 2 also shows that the PV/DG/battery combination has the largest inverter output of 18.5 kW, owing to the highest PV capacity, which charges the batteries, as opposed to the WT/DG/battery combination, which has the lowest output of 1.67 kW. In terms of rectifier output, the PV/WT/DG/battery combo has the maximum rectifier output of 6.71 kW.

The battery state of charge (SOC) is normally defined as the ratio of the available capacity and the maximum possible charge that can be stored in a battery. It can be measured as

an hour of the day, day of the year, or month of the year. In Figure 13, SOC is measured in hour of day with an initial value of 40%.

The cost summary for the five configurations is shown in Figure 14. The lowest capital cost, which is \$67305.54, is for the PV/DG/battery combination, which is 3.25%, 20.8%, and 43.19% less than the capital costs for PV/WT/battery, PV/WT/DG/battery, and PV/WT/battery setups, respectively.

Wind turbine, battery system, converter, and battery replacement costs account for main system replacement costs; however, PV has no replacement costs because the project duration is 25 years, corresponding to the PV lifespan.

Fuel costs are not necessary in the PV/WT/battery configuration, but they are \$ 232739.64 for the WT/DG/battery system, which is 31.03% and 41.05% more than PV/DG/battery and PV/WT/DG/battery, respectively.

The basic load suppliers in the optimum system are photovoltaic and wind turbines. When there is excess power left over after meeting the load demand, the solar panels and wind turbines also charge the battery bank. When there is insufficient or no power coming from the solar panels and wind turbines, the battery bank discharges to feed the load. This optimization considers load following, a hybrid energy dispatch technique in the HOMER Pro, because it frequently proves to be the best option in systems with a mix of renewable energy, especially when the renewable power output occasionally surpasses the load.

## 6. Conclusion

Hybrid energy system for a rural location in Botswana is designed, taking into account the site's renewable energy resources. HOMER Pro software is used for optimal sizing of components and to run simulations. Based on the results of the simulations, the following is determined:

- (i) The most optimal model (PV/wind/battery system) employs 100% renewable energy, resulting in zero carbon emissions. Solar generates 53.7% of production, while wind generates 46.3%. The system has a 25-year lifespan with a 7.6% return on investment and an 11.4% internal rate of return. Due to high initial investments in renewable energy and rural people's minimum earnings, government subsidies and favorable policies could help speed the development of renewable energy projects in Botswana's rural villages, lowering the LCOE.
- (ii) The site's adequate local renewable energy resources suit the adoption of renewable energy hybrid systems that are more reliable and effective.

By implementing this proposed system, the community will be able to lessen the deforestation caused by their reliance on firewood, as well as the health issues caused smoke because of using firewood. Furthermore, by augmenting current power sources in the village, the proposed system will contribute to the economic development of the community as households will have access to power for economic activities such as welding and hair salons, among others. Consequently, this will improve the standard of living for the people of Jamataka village. In the long run, educational attainment levels are likely to increase as pupils get access to learning technologies such as computers and Internet. In addition, learners are likely to have more time to study as they have access to lighting during the evening, thereby extending their study time.

The capacity of the battery system must be carefully considered when designing standalone renewable energy systems but must also take into account the costs associated with their operation and maintenance. As a result, optimizing the system is the best course of action.

Researchers, investors, and government energy departments can use this study as a guide as they choose hybrid energy systems for nearby villages and villages with wind and solar data that are very comparable to the one in this study.

## Data Availability

Data will be provided on request to the corresponding author.

## Conflicts of Interest

The authors declare that they have no conflicts of interest.

## Acknowledgments

This research work was undertaken under the SolaNetwork Project, which was funded through the "Innovate UK: Energy Catalyst Round 6: Transforming Energy Access Fund" (Grant reference number: 105280). The authors acknowledge Innovate UK and DPSun for funding and coordinating the SolaNetwork Project, respectively. Data collection and report preparation by research students, staff members, and Chandi Makuyana are duly acknowledged.

## References

- [1] M. Manhique, D. Barchiesi, and R. Kouta, "Rural electrification in Mozambique: challenges and opportunities," *E3S Web Conferences*, vol. 294, Article ID 02004, 2021.
- [2] N. Avila, J. Carvallo, B. Shaw, and D. M. Kammen, "The energy challenge in Sub-Saharan Africa: generating energy for sustainable and equitable development," 2017, <https://www.oxfamamerica.org/static/media/files/oxfam-RAEL-energySSA-pt1.pdf>.
- [3] N. S. D. Ladu, R. Samikannu, K. G. Gebreslassie et al., "Feasibility study of a standalone hybrid energy system to supply electricity to a rural community in South Sudan," *Scientific African*, vol. 16, Article ID e01157, 2022.
- [4] IRENA, *Renewables Readiness Assessment*, International Renewable Energy Agency, Switzerland, 2014.
- [5] O. G. Olasunkanmi, O. A. Roleola, P. O. Alao, O. Oyedeji, and F. Onaifo, "Hybridization energy systems for a rural area in Nigeria," *IOP Conference Series: Earth and Environmental Science*, vol. 331, no. 1, Article ID 012007, 2019.
- [6] F. Fodhil, A. Hamidat, and O. Nadjemi, "Potential, optimization and sensitivity analysis of photovoltaic-diesel-battery hybrid energy system for rural electrification in Algeria," *Energy*, vol. 169, pp. 613–624, 2019.
- [7] S. Negi and L. Mathew, "Hybrid renewable energy system: a review," *International Journal of Electronic and Electrical Engineering*, vol. 7, no. 5, pp. 535–542, 2014.
- [8] A. S. Duran and F. G. Sahinyazan, "An analysis of renewable mini-grid projects for rural electrification," *Socio-Economic Planning Sciences*, vol. 77, Article ID 100999, 2021.
- [9] A. Berrada and M. A. Laasmi, "Technical-economic and socio-political assessment of hydrogen production from solar energy," *Journal of Energy Storage*, vol. 44, no. PB, Article ID 103448, 2021.
- [10] L. Montoya-duque, S. Arango-aramburo, and J. Arias-gaviria, "Simulating the effect of the Pay-as-you-go scheme for solar energy diffusion in Colombian off-grid regions," *Energy*, vol. 244, Article ID 123197, 2022.
- [11] EUROPEAN COMMISSION, "Report\_on\_energy\_prices\_and\_costs\_in\_Europe\_Com\_2020\_951," 2020, [https://ec.europa.eu/energy/sites/ener/files/report\\_on\\_energy\\_prices\\_and\\_costs\\_in\\_europe\\_com\\_2020\\_951.pdf](https://ec.europa.eu/energy/sites/ener/files/report_on_energy_prices_and_costs_in_europe_com_2020_951.pdf).
- [12] IRENA, "Renewable power: Sharply falling generation costs," *International Renewable Energy Agency*, pp. 15–18, 2016.

- [13] N. S. D. Ladu, S. K. Subburaj, and R. Samikannu, "A review of renewable energy resources . Its potentials , benefits , and challenges in South Sudan," in *Proceedings of the 2021 International Conference on Advancements in Electrical, Electronics, Communication, Computing and Automation (ICAECA)*, Coimbatore, India, 2021.
- [14] J. Prasad and R. Samikannu, "Barriers to implementation of smart grids and virtual power plant in sub-saharan region—focus Botswana," *Energy Reports*, vol. 4, pp. 119–128, 2018.
- [15] M. Hailu Kebede and G. Bekele Beyene, "Feasibility study of PV-Wind-Fuel cell hybrid power system for electrification of a rural village in Ethiopia," *Journal of Electrical and Computer Engineering*, vol. 2018, Article ID 4015354, 9 pages, 2018.
- [16] P. C. Okonkwo, S. Murrigan, E. M. Barhoumi et al., "Economic evaluation of solar hybrid electric systems for rural electrification," *E3S Web Conferences*, vol. 152, 2020.
- [17] L. Al-g Hussain, R. Samu, and O. Taylan, *Techno-Economic Comparative Analysis of Inventions*, 2020.
- [18] N. Yimen, T. Tshotang, A. Kanmogne et al., "Optimal sizing and techno-economic analysis of hybrid renewable energy systems—a case study of a photovoltaic/wind/battery/diesel system in Fanisau, Northern Nigeria," *Processes*, vol. 8, no. 11, pp. 1–25, 2020.
- [19] E. Ahmed, M. Albarawy, and K. Ibrahim, "The most economical design of hybrid PV/Wind/Battery/Diesel generator energy system considering various number of design parameters based on genetic algorithm," *Fayoum University Journal of Engineering*, vol. 4, no. 1, pp. 191–206, 2021.
- [20] F. Canziani, R. Vargas, and J. A. Gastelo-Roque, "Hybrid photovoltaic-wind microgrid with battery storage for rural electrification: a case study in Perú," *Frontiers in Energy Research*, vol. 8, pp. 1–11, 2021.
- [21] M. Thirunavukkarasu and Y. Sawle, "A comparative study of the optimal sizing and management of off-grid solar/wind/diesel and battery energy systems for remote areas," *Frontiers in Energy Research*, vol. 9, no. November, pp. 1–21, 2021.
- [22] S. Jain and Y. Sawle, "Optimization and comparative economic analysis of standalone and grid-connected hybrid renewable energy system for remote location," *Frontiers in Energy Research*, vol. 9, no. October, pp. 1–17, 2021.
- [23] S. Moghaddam, M. Bigdeli, and M. Moradlou, "Optimal design of an off-grid hybrid renewable energy system considering generation and load uncertainty: the case of Zanjan city, Iran," *SN Applied Sciences*, vol. 3, no. 8, p. 732, 2021.
- [24] P. P. Kumar and R. P. Saini, "Optimization of an off-grid integrated hybrid renewable energy system with different battery technologies for rural electrification in India," *Journal of Energy Storage*, vol. 32, Article ID 101912, 2020.
- [25] S. Ali and C. M. Jang, "Optimum design of hybrid renewable energy system for sustainable energy supply to a remote Island," *Sustainability*, vol. 12, no. 3, p. 1280, 2020.
- [26] P. Pandiyan, R. Sitharthan, S. Saravanan et al., "A comprehensive review of the prospects for rural electrification using stand-alone and hybrid energy technologies," *Sustainable Energy Technologies and Assessments*, vol. 52, no. PB, Article ID 102155, 2022.
- [27] A. A. Khamisani, *Design Methodology of Off-Grid Pv Solar Powered System (A Case Study Of Solar Powered Bus Shelter)*, 2018.
- [28] D. Kumar and T. Tewary, "Techno-economic assessment and optimization of a standalone residential hybrid energy system for sustainable energy utilization," *International Journal of Energy Research*, vol. 46, no. 8, pp. 10020–10039, 2020.
- [29] R. A. Badwawi, M. Abusara, and T. Mallick, "A review of hybrid solar PV and wind energy system," *Smart Science*, vol. 3, no. 3, pp. 127–138, 2015.
- [30] N. Zhang, Q. Sun, L. Yang, Y. Li, L. Yang, and S. Member, "Event-triggered distributed hybrid control scheme for the integrated energy system," *IEEE Transactions on Industrial Informatics*, vol. 18, no. 2, pp. 835–846, 2022.
- [31] Y. Li, W. Gao, W. Yan et al., "Data-driven optimal control strategy for virtual synchronous generator via deep reinforcement learning approach," *Journal of Modern Power Systems and Clean Energy*, vol. 9, no. 4, pp. 919–929, 2021.
- [32] V. V V S N Murty and A. Kumar, "Optimal energy management and techno-economic analysis in microgrid with hybrid renewable energy sources," *Journal of Modern Power Systems and Clean Energy*, vol. 8, no. 5, pp. 929–940, 2020.
- [33] R. Wang, Q. Sun, P. Tu, J. Xiao, Y. Gui, and P. Wang, "Reduced-order aggregate model for large-scale converters with inhomogeneous initial conditions in DC microgrids," *IEEE Transactions on Energy Conversion*, vol. 36, no. 3, pp. 2473–2484, 2021.
- [34] R. Wang, D. Ma, M. J. Li, Q. Sun, H. Zhang, and P. Wang, "Accurate current sharing and voltage regulation in hybrid wind/solar systems: an adaptive dynamic programming approach," *IEEE Transactions on Consumer Electronics*, vol. 68, no. 3, pp. 261–272, 2022.
- [35] T. Adefarati and R. C. Bansal, "Reliability, economic and environmental analysis of a microgrid system in the presence of renewable energy resources," *Applied Energy*, vol. 236, pp. 1089–1114, 2019.
- [36] Z. Girma, "Hybrid renewable energy design for rural electrification in Ethiopia," *Journal of Energy Technologies and Policy*, vol. 3, no. 13, pp. 38–53, 2013.
- [37] "Botswana diesel prices," 2022, [https://www.globalpetrolprices.com/Botswana/diesel\\_prices/](https://www.globalpetrolprices.com/Botswana/diesel_prices/).
- [38] S. L. Gbadamosi and N. I. Nwulu, "Optimal configuration of hybrid energy system for rural electrification of community healthcare facilities," *Applied Sciences*, vol. 12, no. 9, p. 4262, 2022.
- [39] TRADING ECONOMICS, "Botswana interest rate - 2022 data - 2006-2021 historical - 2023 forecast - calendar," 2022, <https://tradingeconomics.com/botswana/interest-rate>.
- [40] A. O'Neill, "Botswana- inflation rate 2026 statista," 2022, <https://www.statista.com/statistics/407865/inflation-rate-in-botswana/>.

## Research Article

# A Consensus-Based Distributed Two-Layer Control Strategy with Predictive Compensation for Islanded Microgrid CPS against DoS Attack

Xinrui Liu <sup>1</sup>, Min Hou <sup>1</sup>, Jianjun Yang <sup>2</sup>, and Yufei Sun <sup>1</sup>

<sup>1</sup>College of Information Science and Engineering, Northeastern University, Shenyang, China

<sup>2</sup>State Grid Anhui Electric Power Company, Ma'anshan Power Supply Company, Ma'anshan, China

Correspondence should be addressed to Xinrui Liu; liuxinrui@ise.neu.edu.cn

Received 20 December 2021; Accepted 20 July 2022; Published 8 September 2022

Academic Editor: Akshay Kumar Saha

Copyright © 2022 Xinrui Liu et al. This is an open access article distributed under the Creative Commons Attribution License, which permits unrestricted use, distribution, and reproduction in any medium, provided the original work is properly cited.

**Summary.** Aiming at the problems of insufficient scalability and slow response speed of the traditional three-layer control structure based on the time scale, this study proposes a distributed two-layer control structure. The primary control uses traditional power-frequency droop control, and the second-level control adopts a consensus protocol to simultaneously achieve the goals of frequency synchronization, frequency non-difference, and power optimization in a distributed manner, which can effectively improve the performance of microgrid frequency adjustment and power optimization. The cyber layer of the AC microgrid cyber-physical system (CPS) is extremely vulnerable to denial-of-service (DoS) attacks, resulting in the inability to achieve control objectives. For this reason, this paper designs a consensus algorithm based on event-triggered and a predictive compensation control link that combines empirical mode decomposition (EMD) and extreme learning machine (ELM) on the basis of the two-layer control structure. Finally, a 4-node islanded microgrid simulation example is used to verify the effectiveness of the proposed strategy. The simulation results show that the two-layer control strategy can achieve microgrid frequency recovery and power optimization while effectively responding to different degrees of DoS attacks.

## 1. Introduction

The microgrid is one of the most important ways to connect distributed energy to the grid, and it usually works in two modes: islanded and grid-connected mode. In view of the complexity of the microgrid structure and the diversity of control objectives, hierarchical control is usually used to achieve stable and optimized operation of the microgrid. At present, the most widely used is the three-layer control structure based on time scale. [1, 2] Among them, the first level of control directly acts on distributed generators (DGs), its action time is at the level of seconds. The second layer is the secondary adjustment layer, which focuses on the dynamic operation control of the microgrid, its action time has risen from the second level to the minute level. The third layer is the optimization management layer, which has the longest role time and is mainly used to realize power flow

control and optimal scheduling. However, due to the long control time and slow response speed of the third layer, before the arrival of the third layer control command, the actual operation of the system may deviate from the expected optimal state due to the inevitable power disturbance in the microgrid, resulting in the reduction of the execution efficiency of power optimization and the deterioration of the economy of the microgrid. [3] Therefore, if the control structure is reduced to two layers, it will improve the operation efficiency of the microgrid.

The flexibility, reliability, and scalability of the distributed control mode are stronger than those of the centralized control mode. Therefore, the distributed control mode [4, 5] is generally used in microgrid. In particular, the multi-agent control method [6, 7] based on the consensus protocol is widely used to solve the problems of voltage regulation, frequency regulation, and optimization [8–11] in

hierarchical control due to its simple structure, flexible control, and only sparse communication. With the continuous development of the intelligent construction of the power grid, the microgrid gradually has the relevant characteristics of the cyber-physical system (CPS). [6, 12] The information layer in the microgrid CPS structure usually involves more control decisions and communication processes, and the use of communication data inevitably leads to communication problems such as delays, packet loss, and communication failures [13, 14]. The traditional three-layer control structure can no longer meet the security requirements of the equipment, and the network security of the microgrid CPS is worth further exploration.

In References [15, 16], a smart energy dispatching method based on distributed economic cooperative predictive control is proposed. In References [17–19], a pilot distributed follower decentralized control strategy for islanded microgrids is proposed, which realizes economic dispatch while ensuring voltage quality and frequency synchronization. However, the above literature are only based on the structure of the physical layer and do not consider the security of the information layer, which is extremely vulnerable to malicious attacks on the network. [20–22] References [6, 12] construct an information-physical collaborative hierarchical control structure and solves random communication problems by designing corresponding observers, controllers, and predictive compensators. In References [23, 24], aiming at the insufficient tolerance of MG to DoS attacks when edge routers in microgrid suffer from DoS attacks, a consensus-based secondary frequency controller with dynamic P-f droop control is proposed and its stability is analyzed. References [25, 26] study the realization of cyber-physical system security and stability control issues in complex networks under non-periodic DoS attacks. However, the above-mentioned literature only studies the network attack on the secondary control level, but does not propose an effective solution to the network attack for a microgrid with third control targets. A fully distributed microgrid frequency recovery and power optimization structure capable of responding to network attacks have not yet appeared. Therefore this paper proposes a distributed two-layer control structure that combines droop control and consensus algorithm in order to improve the performance of microgrid frequency adjustment and power optimization under the consideration of the network being attacked by DoS. The main contributions are as follows:

- (1) The distributed control structure designed in this study can overcome the shortcomings of centralized control and transfer the power optimization control to the second layer. While the frequency is restored to the nominal value, the incremental cost(IC) can be consistent, which can effectively improve the optimization operation efficiency of the microgrid.
- (2) Aiming at the DoS attacks that occur on the communication link of the cyber layer, the improved consensus algorithm based on event-triggered and predictive compensation that combines EMD and ELM can effectively respond to different degrees of DoS attacks.

## 2. Microgrid System Modeling

**2.1. Multi-Agents Distributed Model.** For a MG containing  $n$  DGs, DGs are regarded as nodes in the agent communication network, and the communication topology can be represented by an undirected graph  $G$ . In graph  $G$ , the adjacency matrix  $A = (a_{ij})_{n \times n}$  is usually used to describe the relationship between nodes, where  $a_{ij}$  represents the connection weight between node  $i$  and node  $j$ , and  $n$  is the number of nodes. If the  $j$ -th node has an edge pointing to the  $i$ -th node, then  $a_{ij} > 0$ ,  $i \neq j$ , otherwise  $a_{ij} = 0$ , the diagonal element  $a_{ii} = 0$ .

For a distributed multi-agents control system with  $n$  agents, due to the use of distributed control laws, the change of each agent's state depends on its own current state and the current state of its neighboring agents, which can be expressed for

$$u_i(t) = - \sum_{j \in N_i} a_{ij} (x_i(t) - x_j(t)). \quad (1)$$

Written in matrix form as

$$\begin{cases} \dot{\mathbf{X}} = \mathbf{U} \\ \mathbf{U} = -\mathbf{L}\mathbf{X}. \end{cases} \quad (2)$$

**Lemma 1.** Assuming that the multi-agents systems are undirected and connected, then its corresponding Laplacian matrix must be a real symmetric matrix, the aforementioned protocol can achieve the average consistency of the system, namely [23],

$$x_{1\infty} = x_{2\infty} = \dots = x_{n\infty} \approx \sum_{i=1}^n \frac{x_{i0}}{n}. \quad (3)$$

**2.2. Cost Function Model.** The operating cost of the  $i$ -th DGs can be described as follows:

$$C_i(P_i) = a_i P_i^2 + b_i P_i + c_i \quad i = 1, \dots, n. \quad (4)$$

The goal of economic dispatch of the islanded microgrid is to minimize the operating cost, namely,

$$C_{\text{total}} = \min \sum_{i=1}^n C_i(P_i). \quad (5)$$

The generated power of each distributed power source must meet the power balance constraint conditions:

$$\sum_{i=1}^n P_i = \sum_{j=1}^l P_{Dj} = P_D. \quad (6)$$

The DG generation power should also meet the following constraints:

$$P_{i,\min} \leq P_i \leq P_{i,\max} \quad i = 1, \dots, n. \quad (7)$$

Based on the Lagrangian multiplier method and the equal incremental rate theory, the target formula of



economic dispatch is transformed into an incremental factor synchronization control target, which includes

$$\begin{cases} \lambda_i(P_i) = \dot{C}_i(P_i) = 2a_i P_i + b_i = \lambda^*, & P_{i,\min} < P_i < P_{i,\max} \\ \lambda_i(P_i) = \dot{C}_i(P_i) = 2a_i P_{i,\min} + b_i, & P_i = P_{i,\min} \\ \lambda_i(P_i) = \dot{C}_i(P_i) = 2a_i P_{i,\max} + b_i, & P_i = P_{i,\max} \end{cases}. \quad (8)$$

Eq.(8) explains that if  $P_i$  is within the allowable output range, when the IC of all DG is equal to the optimal IC, the total power generation cost of the system is minimum. When  $P_i$  reaches the upper or lower limit of capacity, DGi should run on its bounded value, and the rest of the DGs should continue to run according to the above economic dispatch rules. The optimal IC can be calculated as:

$$\lambda^* = \frac{P_D + \sum_{i=1}^n (b_i/2a_i)}{\sum_{i=1}^n (1/2a_i)}. \quad (9)$$

### 3. Two-Level Distributed Control Strategy

**3.1. Control Structure and Control Objectives.** On the basis of P-f droop control, a consistent control strategy based on droop control is proposed to solve the problem of fully distributed data collection. Because there is no leader DG, dependence on the central controller under the centralized control structure is avoided. In this paper, a two-way communication network is adopted. Regarding each DG as an agent, the local controller of each agent exchanges IC information with the local controllers of its neighboring agents. Based on the transmission of IC information, the proposed consistency control strategy can simultaneously achieve frequency adjustment and optimal economic operation.

The hierarchical control structure constructed in this article is different from the traditional three-layer structure. This article only needs to establish a two-layer structure. At the second layer, both power optimization and frequency recovery are realized, aiming to greatly shorten the optimization operation time, and significantly improve the stability and optimization operation efficiency of the microgrid. Taking the  $i$ -th DG as an example, the hierarchical control architecture with CPS characteristics is shown in Figure 1.

The control objectives of this microgrid system can be summarized as follows:

Goal 1: Frequency synchronization.

$$\lim_{t \rightarrow \infty} (f_i - f_j) = 0, \quad \forall i, j \in \Omega. \quad (10)$$

Goal 2: Frequency error-free.

$$\lim_{t \rightarrow \infty} (f_i - f_{MG}^{\text{ref}}) = 0, \quad \forall i \in \Omega. \quad (11)$$

Goal 3: Consistent incremental cost.

$$\lim_{t \rightarrow \infty} (\lambda_i(P_i) - \lambda_j(P_j)) = 0, \quad \forall i, j \in \Omega. \quad (12)$$

In addition, the system also needs to meet the power balance constraints and the upper and lower limits of DG generation power, which have been explained in the previous section and will not be explained here.

**3.2. Primary Control Strategy.** The primary control considers the use of traditional droop control to achieve frequency stability, which is given as follows:

$$f_i = f_{MG}^{\text{ref}} - m_i (P_i - P_i^{\text{ref}}). \quad (13)$$

For a microgrid composed of multiple DGs in parallel, the frequency of each DG is equal, that is,  $f_i$  is equal. However, droop control is a differential control. Therefore, to make the frequency of each DG equal to the system frequency, a common method is to add frequency compensation to restore  $f_i$  to  $f_{MG}^{\text{ref}}$ .

**3.3. Secondary Frequency Modulation and Power Optimization Control Strategy.** The primary control only acts on the controllable DG unit of the physical layer, and the second layer control has been upgraded from the physical layer to the cyber layer, and requires sparse communication between DGs to achieve information exchange and coordinated control. Since the control scheme adopts a ring communication network to transmit the IC information of DGs, it can eliminate the requirement of Leader DG, reduce the information exchange between DGs, and improve efficiency. Since reactive power does not incur any costs, there is no need to discuss reactive power sharing schemes.

For the goal of frequency error-free control, it is realized by adding a PI controller, and the compensation amount is calculated according to the following formula:

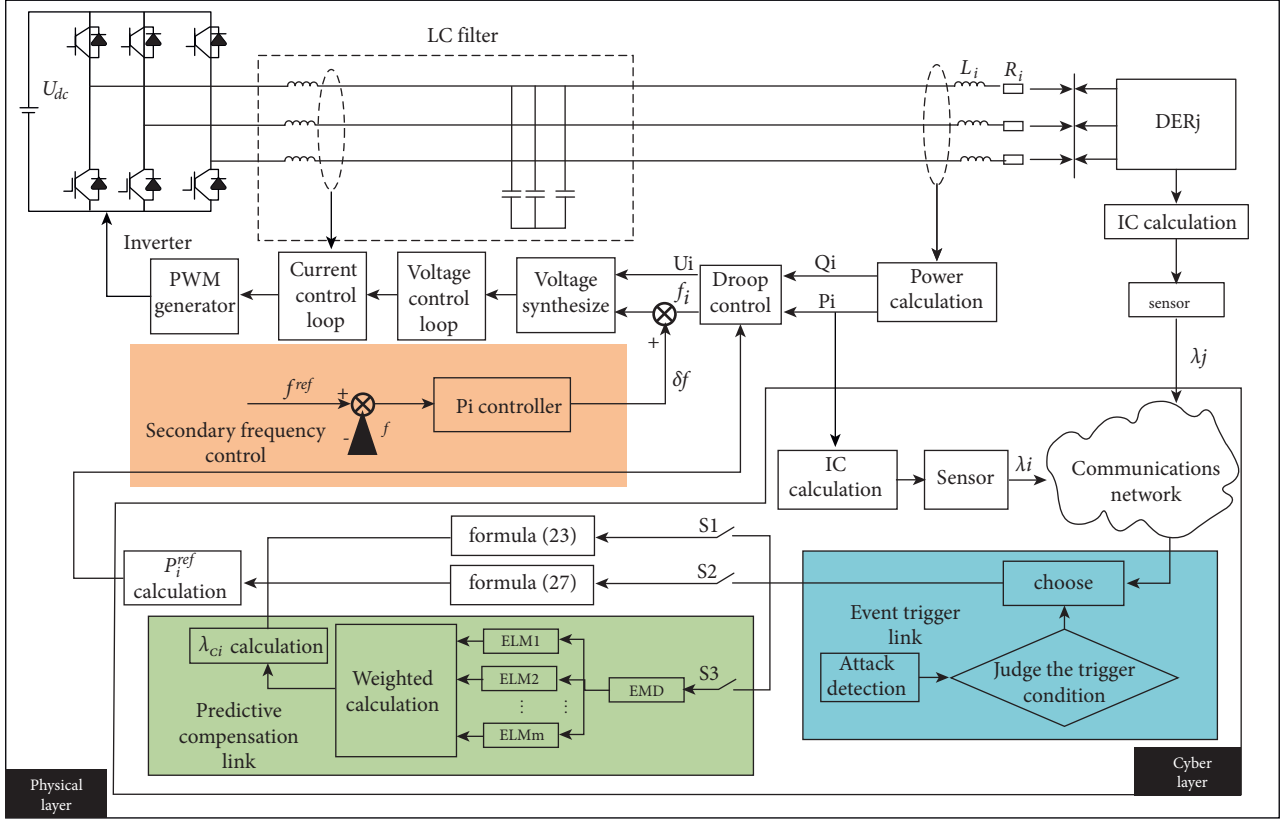
$$\delta f = k_{P,i} (f_{MG}^{\text{ref}} - f_i) + k_{I,i} \int (f_{MG}^{\text{ref}} - f_i) dt. \quad (14)$$

Aiming at the realization of the power optimization goal, without considering the DG capacity constraints, the control equation is designed as follows [21]:

$$P_i^{\text{ref}} = \frac{(\sum_{j=1}^n a_{ij} \lambda_j - \lambda_i - b_i)}{2a_i}, \quad (15)$$

$$f_i = f_{MG}^{\text{ref}} - m_i (P_i - P_i^{\text{ref}}) + k_{P,i} (f_{MG}^{\text{ref}} - f_i) + k_{I,i} \int (f_{MG}^{\text{ref}} - f_i) dt. \quad (16)$$

The IC information is selected as the consistency variable, and the local controller of DGi updates the reference power  $P_i^{\text{ref}}$  according to (15). In addition, the system frequency is stabilized based on (16). That is to say, the proposed method can update the output power reference value according to the neighboring IC information, and realize economic operation and frequency recovery, which is convenient to implement and simplifies the control loop.

FIGURE 1: The hierarchical control architecture diagram of the  $i$ -th DG.

The process of equations (15) and (16) to achieve frequency recovery and power optimization is as follows.

The matrix form of (15) and (16) is expressed as follows:

$$\mathbf{P}^{ref} = \frac{1}{2} \mathbf{a}^{-1} (\mathbf{A} \boldsymbol{\lambda} - \mathbf{b}), \quad (17)$$

$$\mathbf{f} = f_{MG}^{ref} - \mathbf{M}(\mathbf{P} - \mathbf{P}^{ref}) + \mathbf{K}_p (f_{MG}^{ref} - \mathbf{f}) + \mathbf{K}_I \Delta, \quad (18)$$

where  $\mathbf{P}^{ref} = [P_1^{ref}, P_2^{ref}, \dots, P_n^{ref}]^T$ ,  $\mathbf{a} = \text{diag}(a_1, a_2, a_3, \dots, a_n)$ ,  $\boldsymbol{\lambda} = [\lambda_1, \lambda_2, \dots, \lambda_n]^T$ ,  $\mathbf{b} = [b_1, b_2, \dots, b_n]^T$ ,  $\mathbf{K}_p = \text{diag}(k_{p,1}, k_{p,2}, \dots, k_{p,n})$ ,  $\mathbf{K}_I = \text{diag}(k_{I,1}, k_{I,2}, \dots, k_{I,n})$ ,  $\mathbf{f} = [f_1, f_2, \dots, f_n]^T$ ,  $\mathbf{f}_{MG}^{ref} = f_{MG}^{ref} \mathbf{1}^n$ ,  $\mathbf{P} = [P_1, P_2, \dots, P_n]^T$ ,  $\Delta = \int (\mathbf{f}_{MG}^{ref} - \mathbf{f}) dt$ .

The design of the adjacency matrix in this paper is as follows:

$$\mathbf{A} = \begin{bmatrix} 0 & 1 & \dots & 0 & 1 \\ 1 & 0 & 1 & \dots & 0 \\ 0 & 1 & 0 & \dots & 0 \\ \dots & \dots & \dots & \dots & 1 \\ 1 & 0 & \dots & 1 & \dots \end{bmatrix}_{n \times n}. \quad (19)$$

According to (17) and (18), (20) can be obtained as follows:

$$\mathbf{L} \boldsymbol{\lambda} = 2 \mathbf{a} \mathbf{M}^{-1} [(\mathbf{E} + \mathbf{K}_p) \Delta \mathbf{f} + \mathbf{K}_I \Delta], \quad (20)$$

where  $\Delta \mathbf{f} = \mathbf{f}_{MG}^{ref} - \mathbf{f}$ .

The Laplacian matrix of the communication graph has the following form:

$$\mathbf{L} = \begin{bmatrix} 2 & -1 & \dots & 0 & -1 \\ -1 & 2 & -1 & \dots & 0 \\ 0 & -1 & 2 & \dots & 0 \\ \dots & \dots & \dots & \dots & -1 \\ -1 & 0 & \dots & -1 & 2 \end{bmatrix}_{n \times n}. \quad (21)$$

According to (20), (22) can be obtained as follows:

$$-\sum_{j=1}^n a_{ij} (\lambda_i - \lambda_j) = \kappa_i \Delta f_i + \zeta_i \int \Delta f_i dt, \quad (22)$$

where  $\Delta f_i = f_{MG}^{ref} - f_i$ ,  $\kappa_i = (-2a_i/m_i)(1 + k_{p,i})$ , and  $\zeta_i = -2a_i k_{I,i}/m_i$ .

The left side of (22) denotes the consistency control, which can be defined as follows:

$$u_i(t) = -\sum_{j=1}^n a_{ij} (\lambda_i - \lambda_j). \quad (23)$$

Taking the IC as a consistency variable, the state of each variable will eventually be consistent under the control of the consistency algorithm, that is:  $\lambda_i = \lambda_j$ . Thus,

$$\kappa_i \Delta f_i + \zeta_i \int \Delta f_i dt = 0. \quad (24)$$

From the expressions of  $\kappa_i$  and  $\zeta_i$ , we can see that both  $\kappa_i$  and  $\zeta_i$  are negative constants. Therefore, if (24) holds,  $\Delta f_i = 0$ . So under the consensus algorithm and PI controller-based secondary frequency control, the frequency error will be eliminated. That is, when  $t \rightarrow \infty$ ,  $\Delta f_i \rightarrow 0$ . According to (22), it can be concluded that when the IC of each DG is equal, there is  $f_{MG}^{ref} - f_i = 0$ , that is, the frequency recovery of DGi is realized. It is concluded that the proposed control scheme can achieve power optimization and secondary frequency control on the same time scale. Compared with the three-layer control structure, it can effectively shorten the operating time of the system and improve the operating efficiency of the microgrid.

## 4. Control Strategies to against DOS Attacks

**4.1. DoS Attack Modeling.** The communication between DGs in MG is implemented based on the UDP protocol, which is a universal and easily affected protocol. In the process of communication, the data packets containing the IC information are transmitted through the channel, received by the data receiver of the DGs, written into the data buffer, and processed by the consistency controller in the DGs. Due to the openness of the communication network, the secondary control layer is easily attacked by attackers. The data path from the cyber layer DGi to DGj is shown in Figure 2.

The goal of DoS attack is to try to destroy the availability of data transmission and block the information transmission between DGs, thus making the secondary control strategy of microgrid invalid. Due to the attacker's limited energy, DoS attacks are distributed in sequence in time. Define the attack start time on the communication link.

$\{i, j\} \in \Omega$  as  $T_k^{ij}$ ,  $T_k^{ij} \geq 0$ . The duration of the attack is  $\tau_k^{ij}$ ,  $\tau_k^{ij} \geq 0$ ,  $k \in N^+$ , and satisfied  $T_{k+1}^{ij} > T_k^{ij} + \tau_k^{ij}$ . Then the k-th DoS attack can be expressed as  $\mathbf{U}_k^{ij} = [T_k^{ij}, T_k^{ij} + \tau_k^{ij}]$ .  $\mathbf{U}_{(t_0, t)}^{ij} = \bigcup \mathbf{U}_k^{ij} [t_0, t]$  represents the total DoS attack sequence set in the time interval  $[t_0, t]$ .

Assuming that data packets are transmitted through channels, routers provided by service providers, and other network equipment. Due to the openness and sharing of wireless media, sensor nodes are vulnerable to different network attacks. In this paper, it is assumed that the attacker launches DoS attacks on the router of the service provider, and the most direct impact of DoS attacks is the loss of data packets.

Define  $\alpha_i$  and  $\alpha_j$  as the packet loss rate of transmitted data after DGi and DGj are attacked respectively. The Equation is as follows:

$$u_i(t) = - \sum_{j=1}^n a_{ij} [(1 - \alpha_i)\lambda_i - (1 - \alpha_j)\lambda_j]. \quad (25)$$

When a DG in the microgrid suffers DoS attacks, the impact of the attack will gradually propagate throughout the network, which will seriously affect the authenticity of the data. Since DG can only judge the existence of attacks by  $\lambda_i$ ,  $\lambda_j$  and the tracking error. However, the tracking error will

also converge to 0 in the presence of DoS attacks. Therefore, the DG itself can not directly use the above information to judge whether there is an attack or not, nor can it eliminate the influence of attacks.

**4.2. DoS Attack Detection.** Intrusion detection, as an important means to ensure network security, can monitor network activities in real-time, judge the state of equipment, find the attacked equipment in time, and then take corresponding countermeasures. Traditional intrusion detection methods are to identify behaviors that are significantly different from normal traffic as abnormal behaviors. This method does not require prior knowledge of abnormal network behaviors and can achieve better detection accuracy.

Under the CPS architecture, it is known that the attack will cause the data packets sent by the router to be abnormal, so the change of the data packets can be used as the basis for detection.

Define the detection function for DoS attacks on communication link  $\{i, j\} \in \Omega$  as  $\theta_{ij}(t)$ ,  $\theta_{ij}(t) \in \{0, 1\}$ . When DoS attacks occur on the communication link  $\{i, j\} \in \Omega$ , the detection function  $\theta_{ij}(t)$  can detect that the attack has occurred, and its value is set to 1 and kept, denoted as  $\theta_{ij}(t) : \rightarrow 1$ . When there are no DoS attacks, the value of  $\theta_{ij}(t)$  is set to 0 and kept, which is recorded as  $\theta_{ij}(t) : \rightarrow 0$ . All  $\theta_{ij}(t)$  are independent. The mathematical probability formula combined with the previous DoS attack model can be expressed as follows:

$$\begin{cases} \text{Prob}\{\theta_{ij}(t) = 1\} = E\{\theta_{ij}(t)\} = \gamma_{ij} \\ \text{Prob}\{\theta_{ij}(t) = 0\} = 1 - E\{\theta_{ij}(t)\} = 1 - \gamma_{ij} \end{cases}, \quad (26)$$

where  $\gamma_{ij} \in [0, 1]$  is a known constant and is related to  $\alpha_i$  and  $\alpha_j$ .

**4.3. Event-Triggered Control.** Taking into account the limited communication bandwidth between the agents in the microgrid, this paper uses event-triggered control to reduce the amount of communication between the agents. Due to the different degrees of DoS attacks, the defined packet loss rate  $\alpha$  is a constant between  $[0, 1]$ . When the packet loss rate is within the controllable range, an improved consistency formula based on event-triggered is proposed, and the influence of DoS attacks on the consistency control process is overcome by setting the gain coefficient  $k_{\lambda_i}$  and the correction amount  $\zeta$ . However, when the packet loss rate is too high, that is, the extreme case of DoS attacks, the above methods can no longer meet the control requirements of the system. Therefore, it is considered to replace the real data with the data obtained by prediction compensation to complete the IC consistency control process.

The improved consistency formula based on event-triggered is as follows:

$$u_i(t) = -k_{\lambda_i} \sum_{j=1}^n a_{ij} [(1 - \alpha_i)\lambda_i - (1 - \alpha_j)\lambda_j] + \zeta. \quad (27)$$



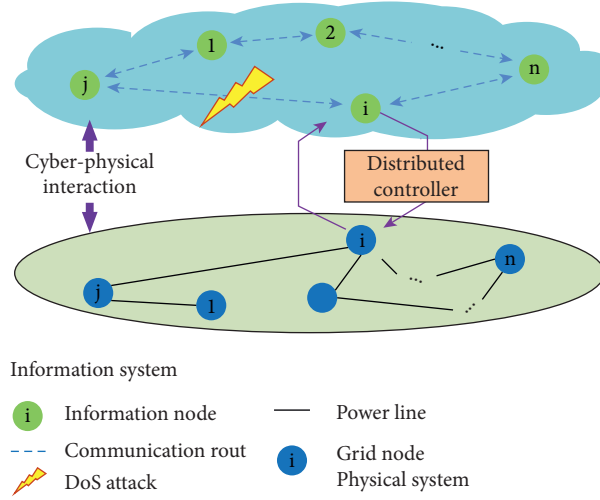


FIGURE 2: Data path from DGi to DGj.

This paper takes DG1 and DG2 as examples to give a brief proof process to illustrate the conditions that (27) must meet to complete the consistency control process. It is known that the incremental costs  $\lambda_1$  and  $\lambda_2$  satisfy the first-order equation.

$$\begin{cases} \dot{\lambda}_1 = u_1 \\ \dot{\lambda}_2 = u_2, \end{cases} \quad (28)$$

where

$$u_1(t) = -k_{\lambda 1} \sum_{j=1}^n a_{1j} [(1 - \alpha_1)\lambda_1 - (1 - \alpha_j)\lambda_j] + \zeta$$

$$u_2(t) = -k_{\lambda 2} \sum_{j=1}^n a_{2j} [(1 - \alpha_1)\lambda_1 - (1 - \alpha_j)\lambda_j] + \zeta$$

Laplace transformation on the above formulas can be obtained:

$$\lambda_1(s) = \frac{k_{\lambda 1} \sum_{j=1}^n a_{1j} (1 - \alpha_j) \lambda_j(s) + \lambda_1(t)|_{t=0} + \zeta/s}{s + k_{\lambda 1} \sum_{j=1}^n a_{1j} (1 - \alpha_1)}, \quad (29)$$

$$\lambda_2(s) = \frac{k_{\lambda 2} \sum_{j=1}^n a_{2j} (1 - \alpha_j) \lambda_j(s) + \lambda_2(t)|_{t=0} + \zeta/s}{s + k_{\lambda 2} \sum_{j=1}^n a_{2j} (1 - \alpha_2)}. \quad (30)$$

In the formulas,  $\lambda_1(s)$  and  $\lambda_2(s)$  are the state quantities of the IC after Laplace transformation, and  $\lambda_1(t)|_{t=0}$  and  $\lambda_2(t)|_{t=0}$  are the initial values of the IC of DG1 and DG2, respectively. Define the IC state deviation obtained by DG1 and DG2 as follows:

$$e(t) = \lambda_1(t) - \lambda_2(t), \quad (31)$$

$$\begin{aligned} \lim_{t \rightarrow \infty} e(t) &= \lim_{s \rightarrow 0} s e(s) = \lim_{s \rightarrow 0} s (\lambda_1(s) - \lambda_2(s)) \\ &= \frac{\zeta [k_{\lambda 2} \sum_{j=1}^n a_{2j} (1 - \alpha_2) + k_{\lambda 1} \sum_{j=1}^n a_{1j} (1 - \alpha_1)]}{k_{\lambda 1} \sum_{j=1}^n a_{1j} (1 - \alpha_1) \cdot k_{\lambda 2} \sum_{j=1}^n a_{2j} (1 - \alpha_2)}. \end{aligned} \quad (32)$$

At this time, when  $k_{\lambda i}$  and  $\zeta$  meet the following condition, the system can meet the consistency requirements.

$$\frac{\zeta [k_{\lambda 2} \sum_{j=1}^n a_{2j} (1 - \alpha_2) + k_{\lambda 1} \sum_{j=1}^n a_{1j} (1 - \alpha_1)]}{k_{\lambda 1} \sum_{j=1}^n a_{1j} (1 - \alpha_1) \cdot k_{\lambda 2} \sum_{j=1}^n a_{2j} (1 - \alpha_2)} = 0. \quad (33)$$

Set the triggered functions to  $S_1(t)$ ,  $S_2(t)$  and  $S_3(t)$ , which are defined as follows according to the previous description:

$$\begin{cases} S_1(t) = \{(i, j) \in \Omega: \theta_{ij}(t) = 0\} \\ S_2(t) = \{(i, j) \in \Omega: \theta_{ij}(t) = 1 \text{ and } \alpha_i \cup \alpha_j \in (0, 1)\} \\ S_3(t) = \{(i, j) \in \Omega: \theta_{ij}(t) = 1 \text{ and } \alpha_i \cap \alpha_j = 1\} \end{cases} \quad (34)$$

When the triggered condition of (34) is met, DGi will send a request to the DGj to obtain its state information and update the control parameters. Among them, triggered condition  $S_1(t)$  means that when the detection function  $\theta_{ij}(t) = 0$  on the communication link  $\{i, j\} \in \Omega$ , that is, when the link is not subjected to DoS attacks, the control process is directly completed by (23).  $S_2(t)$  means that when  $\theta_{ij}(t) = 1$  on the communication link  $\{i, j\} \in \Omega$ , that is, when the link is under DoS attacks and the packet loss rate is within the controllable range, the control process is completed by (27).  $S_3(t)$  means that when  $\theta_{ij}(t) = 1$  on the communication link  $\{i, j\} \in \Omega$ , that is, when the link is under DoS attacks and the packet loss rate is 1, the control process is completed by the predictive compensation control.

**4.4. Predictive Compensation Control.** The inability of agent  $i$  to receive the data of agent  $j$  will result in the inability to achieve the IC consistency, and thus fail to complete the restoration of the system frequency on the same time scale. In order to avoid the coupling problem between agents caused by directly predicting the data of agents, this paper uses the historical power data of agents at a moment in time, and calculates the IC through the predicted power, so as to obtain the corresponding control parameters.

In order to better analyze the consistent dynamic characteristics, Equation (23) is discretized. Let the sampling

period be  $T_s$ ,  $t = t_0 + kT_s$ , abbreviated as  $t = k$ .  $\lambda(k)$  is sent every sampling period, and the corresponding discrete consistency algorithm can be written as follows:

$$\lambda_i(k+1) = \sum_{j=1}^n w_{ij}(k)\lambda_j(k) = \lambda_i(k) + \sum_{j \neq i} w_{ij}(k)(\lambda_j(k) - \lambda_i(k)),$$

$$i = 1, 2, \dots, n. \quad (35)$$

The corresponding matrix form is

$$\lambda(k+1) = \mathbf{W}(k)\lambda(k). \quad (36)$$

In order to ensure the consistency of the system and still converge to the average value,  $\mathbf{W}(k)$  is constructed according to the Metropolis method.

According to whether the agent is attacked by DoS, set the control parameter  $\lambda_{Ai}$  to indicate the latest update signal obtained by the agent  $i$  based on the event-triggered. When the triggered condition  $S_3(t)$  is met,  $\lambda_{Ai}$  can be expressed as

$$\lambda_{Ai} = \theta_{ij}(k)\lambda_{ci} + (1 - \theta_{ij}(k))\lambda_i. \quad (37)$$

Predictive compensation control is designed according to the following steps:

- (1) EMD is used to preprocess the historical data, and multiple intrinsic mode functions (IMFs) are obtained from the historical data. The IMF component must meet the following two conditions:
  - (i) During the entire period, the number of extreme points and zero crossing points are equal, or the difference does not exceed 1
  - (ii) At any moment, the average value of the upper envelope and the lower envelope is zero
- (2) For this series of IMFs, a sliding window is used to intercept historical time series to obtain data samples. Intercept the data sample of length  $D$  as an input sample, then the data at the next moment is the expected value output by the ELM model. [12].

EMD is carried out in accordance with the flow chart given in Figure 3. The structure of the entire ELM network is shown in Figure 4.

Suppose that the input layer of the network has  $n$  neurons, the output layer has  $m$  neurons, and the hidden layer has  $L$  neurons. The activation function is  $G(\cdot)$ . Input sample  $\mathbf{X} = [IMF_1, IMF_2, \dots, IMF_n]^T$ , output sample  $\mathbf{Y} = [p_{ELM1}, p_{ELM2}, \dots, p_{ELMm}]^T$ . The output function of the ELM model can be expressed as

$$f_L(\mathbf{X}) = \sum_{j=1}^L \beta_j G(w_j \cdot IMF_i + h_j), \quad i = 1, 2, \dots, n. \quad (38)$$

Where:  $w_j = [w_{j1}, w_{j2}, \dots, w_{jn}]^T$ ,  $\beta_j = [\beta_{j1}, \beta_{j2}, \dots, \beta_{jm}]^T$  are the input and output connection weight of the  $j$ -th hidden layer neuron.

- (3) In order to make the model with the smallest prediction error have a larger weight, the outputs of  $m$  ELMs are weighted as follows. The weighted result is

$$P_{ELM} = \sum_{i=1}^m \eta_i P_{ELMi}. \quad (39)$$

Where:  $\eta_i = (\sum_{i=1}^m |e_i| - |e_i|) / (m-1) \sum_{i=1}^m |e_i|$ .  $e_i = P_i - P_{ELMi}$ .

Then when the agent is attacked, the IC obtained after the predictive compensation control is as follows:

$$\lambda_{ci} = 2a_i P_{ELM} + b_i. \quad (40)$$

## 5. Calculation Examples and Simulation

**5.1. Simulation Model.** In this section, the simulation topology is a four-node microgrid system, as shown in Figure 5.

The MATLAB/SIMULINK to verify the two-layer control strategy proposed above. The microgrid system consists of 4 DGs, the impedance of the power supply is taken as  $Z_i = 0.0679 + j4.11 \times 10^{-4} \Omega$ . The line impedances meet  $Z_{11} = Z_{13}$  and  $Z_{12} = Z_{14}$ . Taking as  $0.175 + j4.04 \times 10^{-4} \Omega$  and  $0.12 + j4.04 \times 10^{-4} \Omega$ . The simulation parameters and cost coefficients of each DG are shown in Table 1.

### 5.2. Performance Test and Comparison under Two-Layer Control Structure

**5.2.1. Comparison with Traditional Three-Layer Control.** In order to verify the advanced nature of the proposed control strategy, the two-layer control method in this study is compared with the distributed three-layer control method designed in Reference [27]. Set the simulation environment as:  $0 \sim 1s$ , only droop control is used, and at  $t = 1s$ , the upper control is activated. The simulation results under the two control strategies are shown in Figure 6.

Figures 6(a)–6(c) are the simulation results of the traditional three-layer control method, and Figures 6(d)–6(f) are the simulation results of the two-layer control method proposed in this paper. It can be seen that after the upper-layer control is activated, both methods can achieve the goals of frequency regulation and power optimization, but compared with the three-layer control method corresponding to Figures 6(a)–6(c), the method proposed in this paper has a faster power optimization speed. The traditional three-layer control needs 0.5 s to achieve incremental factor synchronization, while the control proposed in this paper only needs 0.2 s, which shows that the performance of the two-layer control strategy is better than the traditional three-layer control.

**5.2.2. System Performance during Load Fluctuations.** This part tests the frequency recovery and power optimization effects when the load fluctuates. The system is connected to the control strategy proposed in this study for power

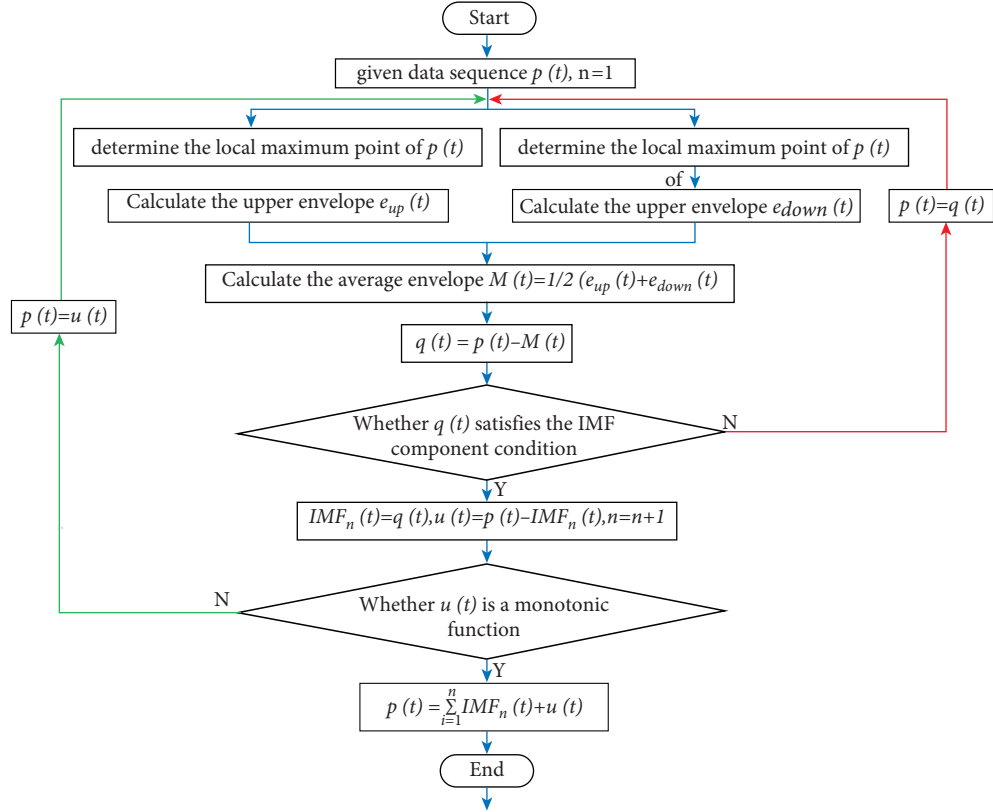


FIGURE 3: Flow chart of EMD algorithm.

optimization and frequency recovery at  $t = 1s$ , and disconnected at  $t = 6s$ . Set the simulation environment as: (1) At  $t = 2s$ , Load 1 increases to 70 kw. (2) At  $t = 3s$ , Load 2 increases to 100 kw. (3) At  $t = 4s$ , Load 3 is reduced to 70 kw. (4) At  $t = 5s$ , Load 4 is reduced to 60 kw. The simulation results are shown in Figure 7.

Figures 7(a)–7(c) show the changes in the output active power, incremental cost, and frequency of these four DGs, respectively. As can be seen from Figure 7(b), the initial values of ICs are 0.30750.24840.2865, 0.2306. After starting the control strategy at  $t = 1s$ , the IC of each DG tends to be consistent and finally stabilizes at 0.2651. After the load demand changes, the IC can still be consistent. It can be concluded that no matter how the load is changed, the IC of each DG can be driven to the same level under the control strategy designed in this study, so the control objectives are well met. As can be seen from Figure 7(c), the frequency of the microgrid can be stabilized at the nominal value of 50 Hz, and the frequency changes little. Therefore, the proposed control scheme can effectively realize the economic operation and frequency adjustment of the islanded microgrid without considering the DG capacity constraints.

**5.2.3. System Plug and Play Performance.** The distributed control method requires the system to be able to meet the change of topology, so in order to verify the plug-and-play performance of the method in this paper, the simulation

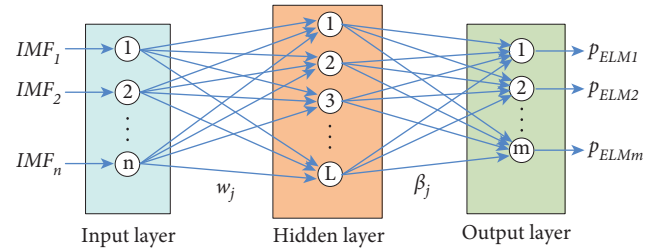


FIGURE 4: Topology diagram of ELM structure.

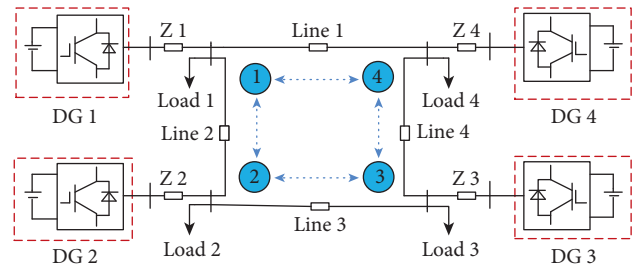


FIGURE 5: Islanded microgrid structure.

process is as follows: The islanded microgrid runs under the condition of total constant load demand of 280 kW, the specific load requirements are shown in Table 2. The system accesses the second-layer control strategy for power optimization and frequency recovery at  $t = 1s$ , and disconnects

TABLE 1: Simulation parameters and cost coefficients of each DG.

DGi	$P_i^{ref}$	$m_i$	Load1~Load4	$a_i$	$b_i$	$c_i$
DG1	$80 \times 10^3$	$1 \times 10^{-5}$	$60kw + 10jkVar$	$1.594 \times 10^{-3}$	$2.0252 \times 10^{-2}$	0.8466
DG2	$70 \times 10^3$	$1 \times 10^{-5}$	$90kw + 10jkVar$	$1.195 \times 10^{-3}$	$5.6606 \times 10^{-2}$	0.5146
DG3	$60 \times 10^3$	$1 \times 10^{-5}$	$80kw + 0jkVar$	$1.743 \times 10^{-3}$	$4.1998 \times 10^{-2}$	1.2948
DG4	$50 \times 10^3$	$1 \times 10^{-5}$	$70kw + 10jkVar$	$1.361 \times 10^{-3}$	$6.6732 \times 10^{-2}$	0.6972

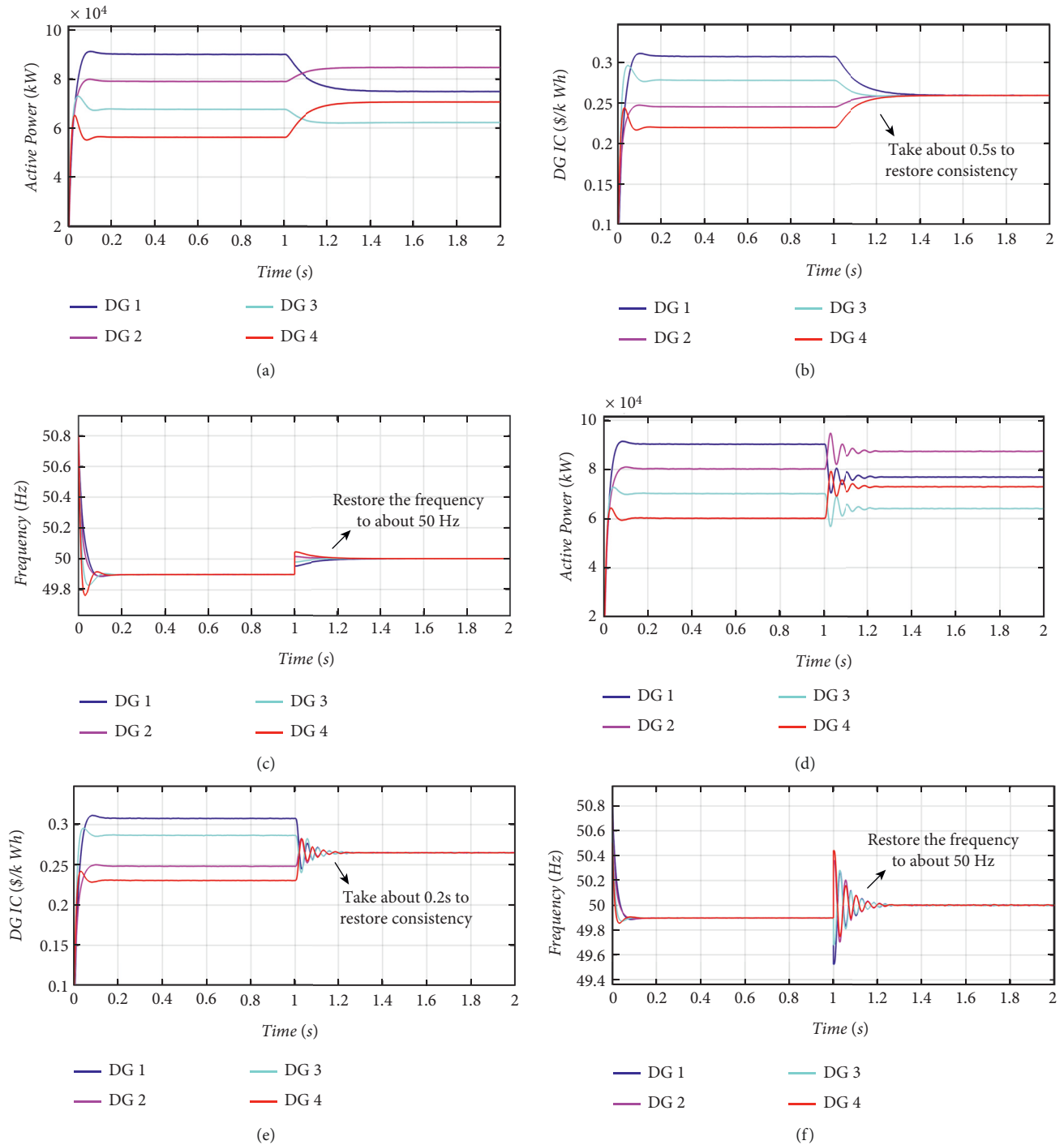


FIGURE 6: Comparison of control effects of two hierarchical structures.

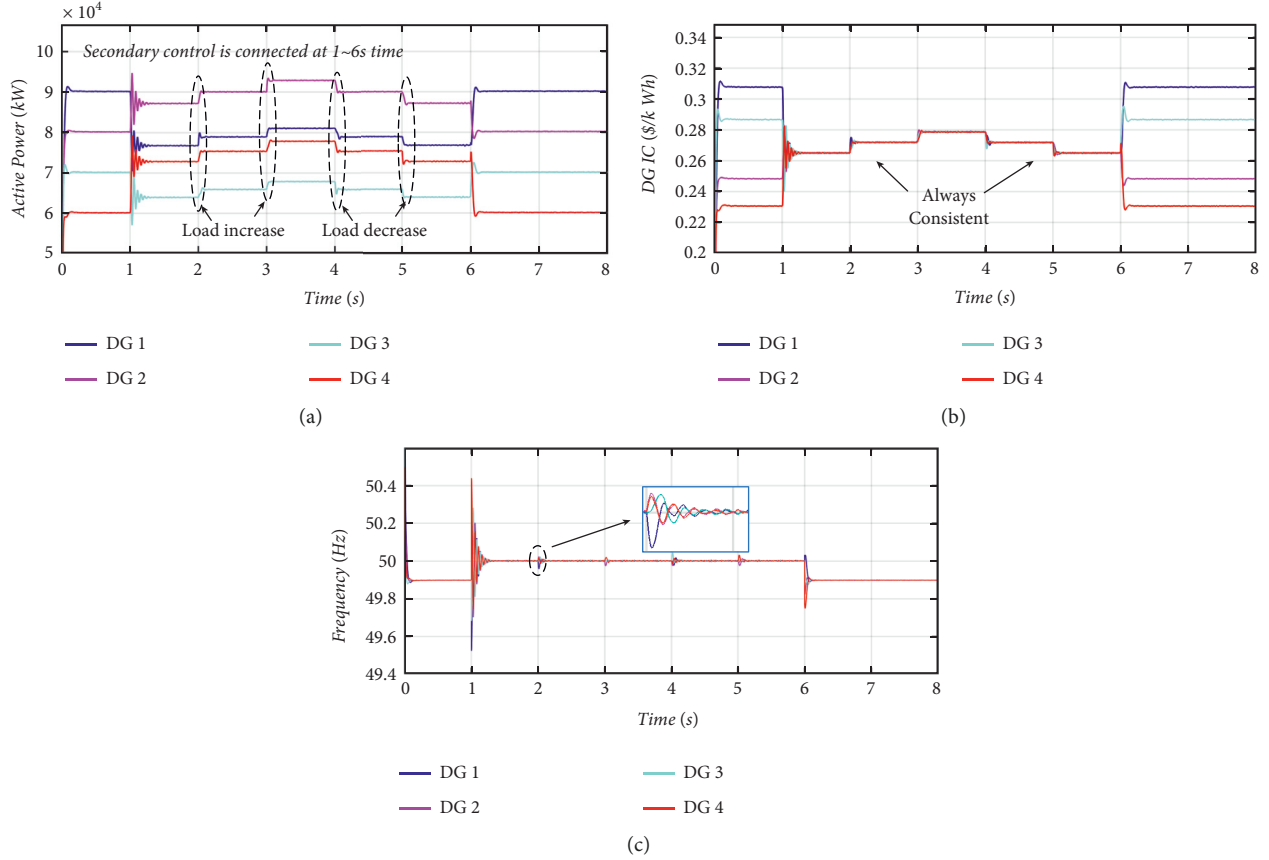


FIGURE 7: Frequency recovery and power optimization results when load fluctuates.

TABLE 2: Load demand of each DG.

Load <sub>i</sub>	Load1	Load2	Load3	Load4
Value,kW	0	100	90	90

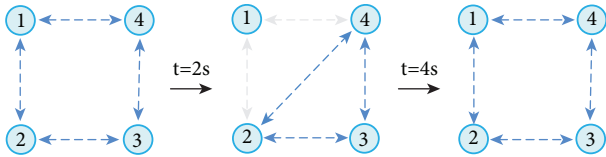


FIGURE 8: Schematic diagram of communication topology changes.

at  $t = 6s$ . Set the simulation environment as: (1) At  $t = 2s$ , DG1 is cut off from system. (2) When  $t = 4s$ , DG1 is put into the system, and the connection with the system is restored. Figure 8 shows the change in communication topology. The other control parameters and cost coefficients of DG are the same as above and remain unchanged. The simulation results are shown in Figure 9.

As can be seen from Figures 9(a)–9(c), the system can operate stably during the DG input and removal process. Figure 9(a) shows that due to DG1 exiting operation at  $t = 2s$ , the output power of DG1 is reduced to zero, and DG2, DG3, and DG4 share the total load of the system. At

$t = 4s$ , DG1 reconnects to the microgrid, and its output power increases from 0 to 7.237 kW. Figure 9(b) shows that in the whole process, although the DGs have changed, the ICs of DGs participating in the power supply are always consistent, so the control requirements can be well met. In addition, Figure 9(c) shows that when the DGs change, the frequency fluctuation can be restored to the nominal value in a short time. Therefore, the proposed control method can well meet the plug-and-play requirement of the microgrid system.

**5.2.4. DoS Attack Impact Analysis.** As mentioned earlier, the impact of DoS attacks is modeled as data loss that occurs on the communication link  $\{i, j\} \in \Omega$ , the size of the packet loss rate directly affects the speed and the effect of the consistency convergence process. In order to analyze the impact of different packet loss rates on system control objectives, the simulation process is set as follows: The studied islanded microgrid runs under the simulation parameters of Table 1, and accesses the second-layer control strategy at  $t = 4s$ , and disconnects at  $t = 6s$ . In the communication system, the data transmitted by DG1 to other DGs during the period  $t_1 = 2s$  to  $t_2 = 4s$  is under attack, and the packet loss rate is  $\alpha_1$ . The results of the system frequency and the IC of each DG in the period  $t_1 \sim t_2$  under different packet loss rates are shown in Figure 10.

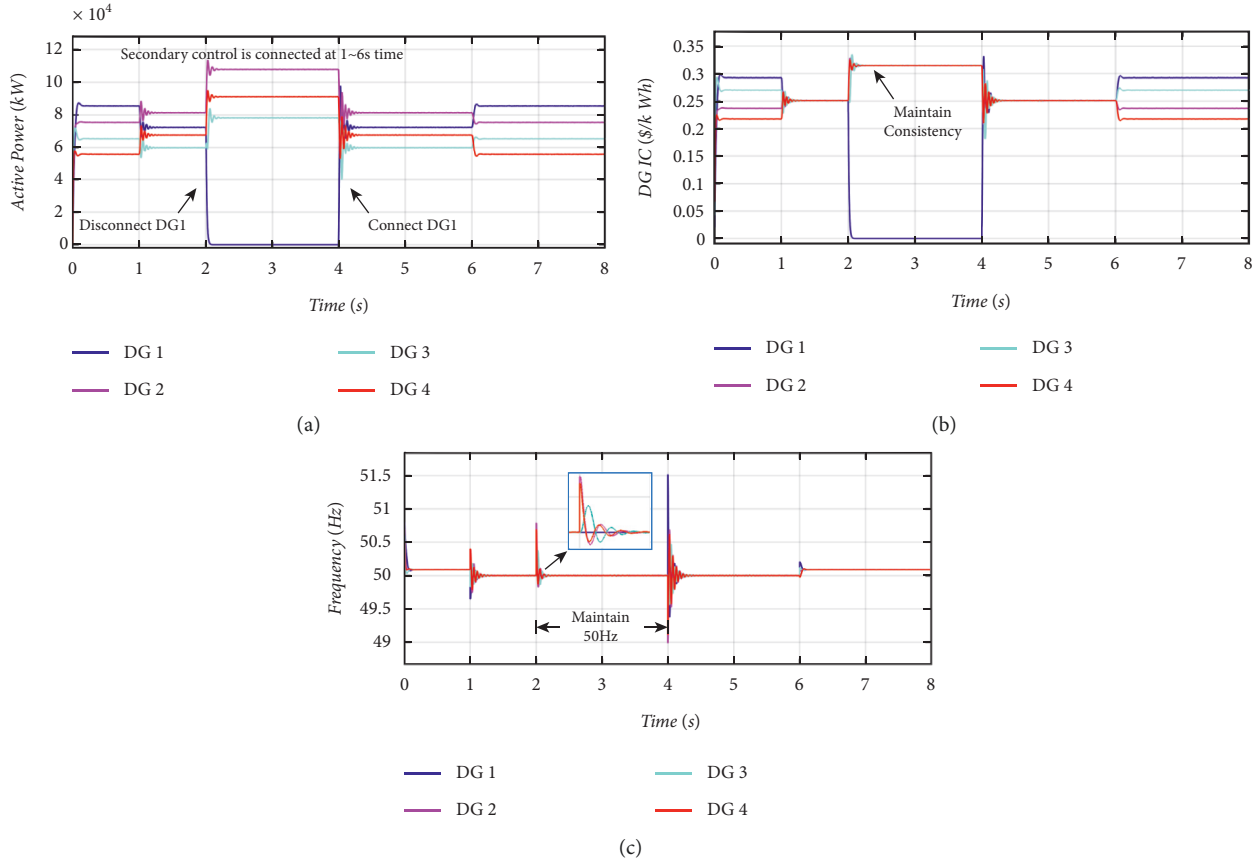


FIGURE 9: System plug-and-play simulation results.

As can be seen from Figures 10(a) and 10(b), when the packet loss rate is small, the impact of the attack on DG1 is mainly causes the IC curve of DG1 to produce a large overshoot during this period, which deviates from the consistent value reached by the system except for DG1. The system frequency fluctuates during the attack period and deviates from the nominal frequency of 50 Hz. As can be seen from Figures 10(c) and 10(d), when the packet loss rate is large, the consistency control of the IC in the period  $t_1 \sim t_2$  fails, and the change of DG1 is the largest. The system frequency has a great overshoot at the moment of the attack and greatly deviates from the nominal frequency. Therefore it can be concluded that the main impact is the consistency control process of the IC, and the secondary control method is still effective in the rest of the time.

**5.3. Verify the Effect of Improving Consistency Strategy.** In order to verify the effectiveness of the improved consistency strategy based on event-triggered in the case of weaker DoS attacks for frequency restoration and power optimization of the microgrid, use the same simulation process. Select the time period  $t_1 \sim t_2$  during which DoS attacks occur, and the simulation time is 2s. Assuming that at  $t_1 = 1$ s, the system detects DoS attacks, and then

initiates the improved consistency strategy based on event-triggered. The results of changes in the IC and frequency are shown in Figure 11.

As can be seen from Figures 11(a) and 11(b), starting the improved consistency strategy can restore the destroyed IC consistency. The recovery time is about 0.05s. The system frequency can achieve stability after fluctuations. When the packet loss rate is large, as can be seen from Figures 11(c) and 11(d), the improved consistency strategy is still effective, but the consistency recovery time of the IC is prolonged, about 0.35s. The system frequency has a large overshoot during the recovery process, but it can still be stabilized at 50 Hz. It can be concluded that in the case of weaker DoS attacks, the improved consistency strategy based on event-triggered can achieve our control goals, which proves the effectiveness of the proposed strategy.

**5.4. Verify the Effect of Predictive Compensation Control.** As mentioned above, when an extreme situation occurs in DoS attacks, consider using the data obtained by predictive compensation control instead of the real data to complete the IC consistency control process. Select time period  $t_1 \sim t_2$  when the DoS attack occurs. The changes in IC and system frequency are shown in Figure 12. When a DG suffers DoS



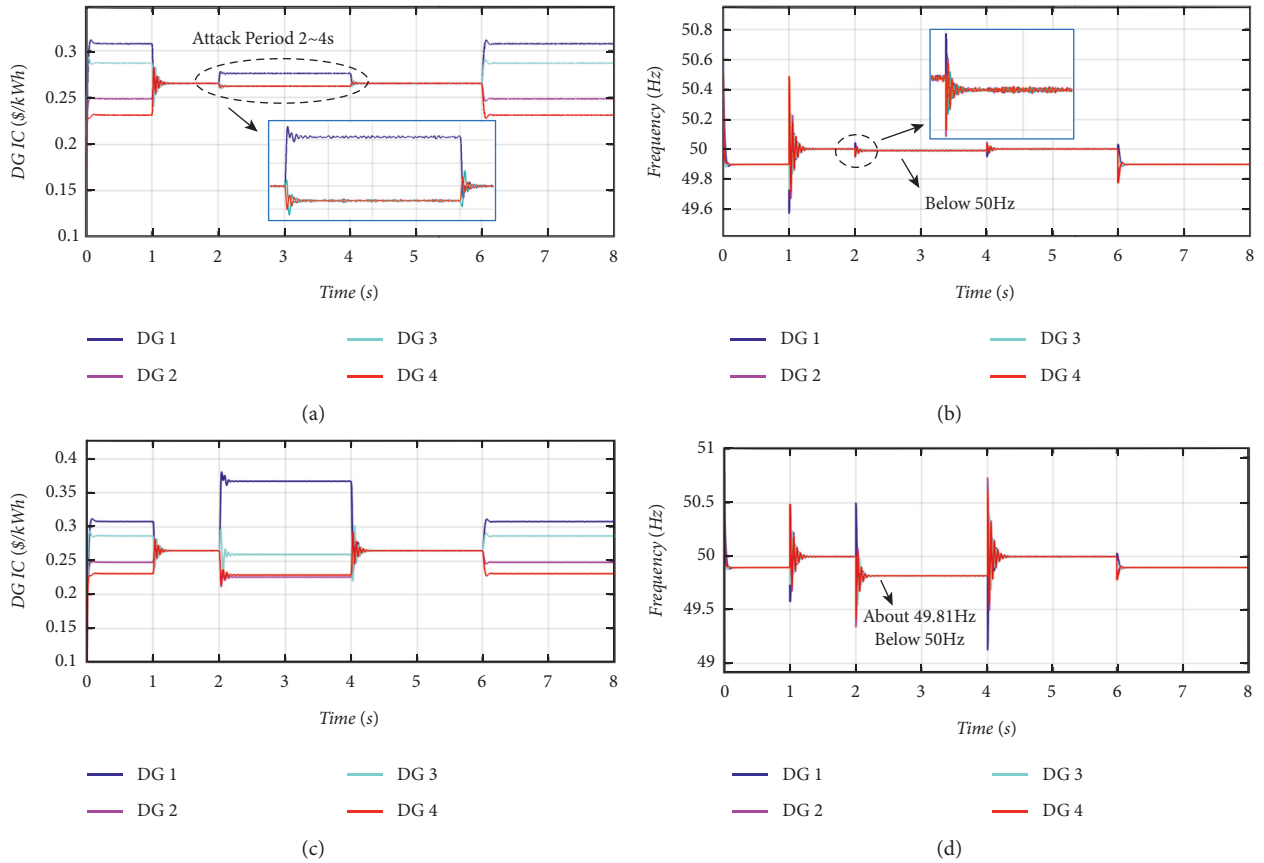


FIGURE 10: Comparison of the impact of DoS attacks.

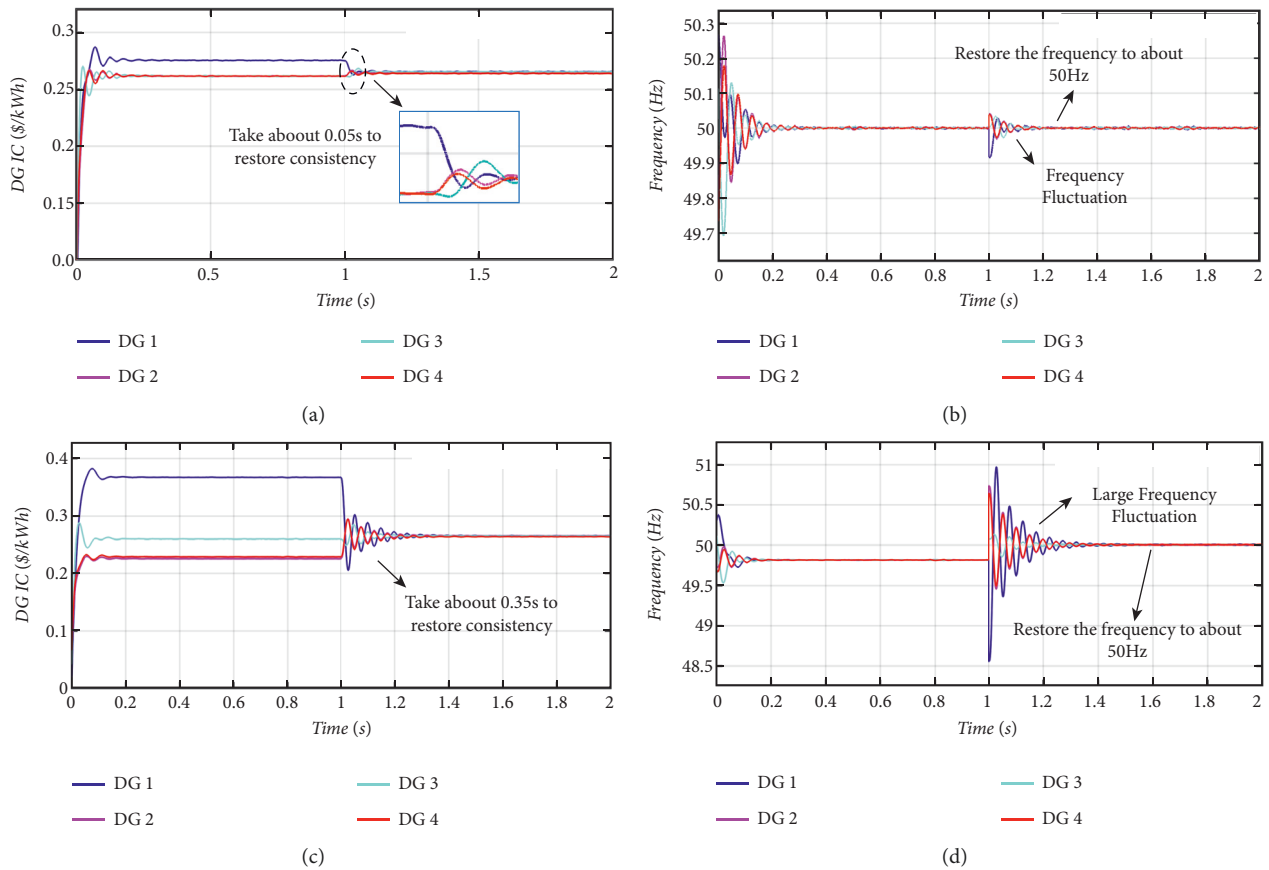


FIGURE 11: Comparison of control effects of improved consistency strategy.

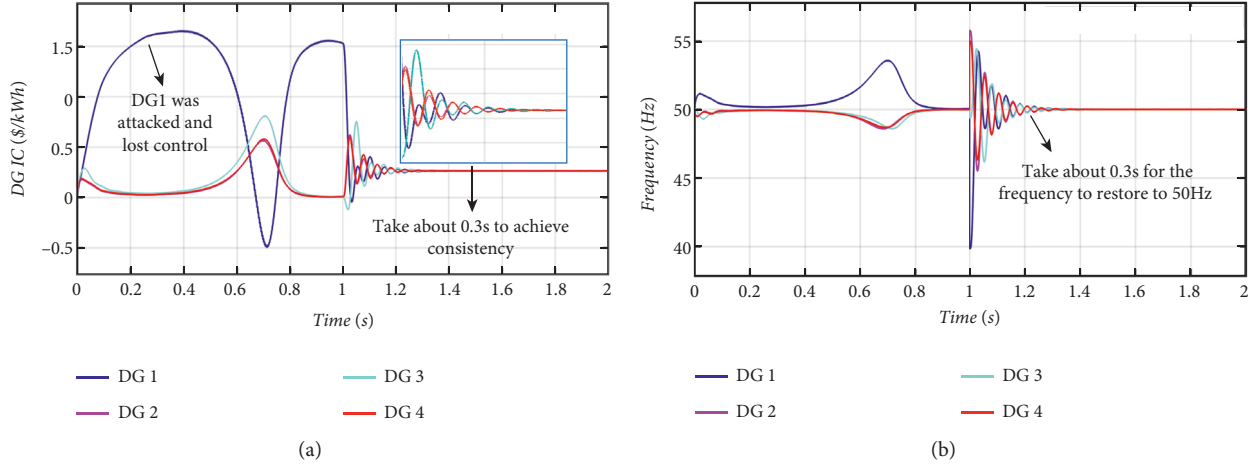


FIGURE 12: Predictive compensation strategy control effect diagram.

attacks to completely drop its packets, the attacks will gradually spread throughout the network, which will seriously affect the fidelity of the information. After  $t_1 = 1s$ , because the event-triggered mechanism calculates the impact of packet loss on the secondary control, the predicted data obtained from the output of the predictive compensation is used to replace the real data to complete the subsequent consistency control process.

As can be seen from Figures 12(a) and 12(b), the IC and frequency of each DG can be restored to be consistent at about 0.3 s. According to the above analysis, for extreme DoS attacks, the secondary control strategy based on event-triggered can well use the predictive compensation data to suppress the overshoot and complete the IC consistency control process, while stabilizing the system frequency at the nominal value.

## 6. Conclusion

This paper proposes a distributed two-layer control structure for the islanded microgrid system with CPS characteristics. The control structure can realize the distributed frequency adjustment and power optimization of the microgrid at the same time, effectively shortening the operating time of the system, and significantly improving the power optimization distribution capability of the microgrid. Aiming at the possible network attacks at the cyber layer, in order to reduce the impact of different degrees of DoS attacks on the system, this paper designs an improved consensus algorithm based on event-triggered and predictive compensation control that combines EMD and ELM. Finally, the 4-node MG system is simulated and analyzed, and the experimental results show that this method can effectively eliminate the influence of DoS attacks on consistency control, keep the system frequency at 50 Hz, and keep the IC consistency of all DGs. The results show that this method can meet the control requirements of frequency synchronization, frequency error-free, and optimal operation cost.

## Abbreviations

CPS:	Cyber-physical system
DoS:	Denial-of-service
EMD:	Empirical mode decomposition
ELM:	Extreme learning machine
DGs:	Distributed generators
MG:	Microgrid
IC:	Incremental cost
IMFs:	Intrinsic mode functions
DG <sub>i</sub> :	The $i$ -th DGs
$x_i$ :	The state variable
$u_i$ :	The control variable
$x_{i\infty}$ :	The final state variable of the $i$ -th agent
$x_{i0}$ :	The initial state variable of the $i$ -th agent $n$ , the total number of DGs
$a_i b_i, c_i$ :	The cost coefficients of DG <sub>i</sub>
$l$ :	The total number of loads
$N_i$ :	Neighbor set of agent $i$
$A$ :	Adjacency matrix of the communication graph
$L$ :	Laplacian matrix of the network
$E$ :	The identity matrix
$W(k) \in \mathbf{R}^{n \times n}$ :	The state transition matrix of the system
$C_i$ :	The cost function of DG <sub>i</sub>
$C_{\text{total}}$ :	The total cost
$P_i$ :	The generated active power of DG <sub>i</sub>
$P_{Dj}$ :	The power of the $j$ -th load
$P_D$ :	The power demand of the total load
$P_{i,\min}$ :	The minimum power generation of DG <sub>i</sub>
$P_{i,\max}$ :	The maximum power generation of DG <sub>i</sub>
$\lambda_i(P_i)$ :	The IC of DG <sub>i</sub>
$f_i$ :	The frequency emitted by DG <sub>i</sub>
$\Omega$ :	The set of all DGs
$f_{MG}^{\text{ref}}$ :	The rated output frequency of the system
$P_i^{\text{ref}}$ :	The rated active power of DG <sub>i</sub>
$m_i$ :	The droop coefficient
$k_{p,i}, k_{I,i}$ :	The proportional coefficient and integral coefficient of DG <sub>i</sub>

$\alpha_i$ : The packet loss rate of DGI  
 $\lambda_{ci}$ : The IC calculated by the predictive compensation control.

## Data Availability

Data sharing not applicable to this article as no datasets were generated or analyzed during the current study.

## Conflicts of Interest

Submission of this study does not involve any conflict of interest.

## Acknowledgments

This work was supported by the National Key R&D Program of China under grant (2018YFA0702200), Liaoning Natural Science Foundation (2021-MS-086), the National Natural Science Foundation of China (62173074), the Key Project of National Natural Science Foundation of China (U20A2019).

## References

- [1] V. Nikam and V. Kalkhambkar, "A review on control strategies for microgrids with distributed energy resources, energy storage systems, and electric vehicles," *International Transactions on Electrical Energy Systems*, vol. 31, no. 1, Article ID e12607, 2021.
- [2] G. Shahgholian, "A brief review on microgrids: operation, applications, modeling, and control," *International Transactions on Electrical Energy Systems*, vol. 31, no. 6, Article ID e12607, 2021.
- [3] B. Sahoo, S. K. Routray, and P. K. Rout, "AC, DC, and hybrid control strategies for smart microgrid application: a review," *International Transactions on Electrical Energy Systems*, vol. 31, no. 1, Article ID e12683, 2021.
- [4] J. W. Simpson-Porco, Q. Shafiee, F. Dörfler, J. C. Vasquez, J. M. Guerrero, and F. Bullo, "Secondary frequency and voltage control of islanded microgrids via distributed averaging," *IEEE Transactions on Industrial Electronics*, vol. 62, no. 11, pp. 7025–7038, 2015.
- [5] M. M. Mobashsher, R. Keypour, and M. Savaghebi, "Distributed optimal voltage control in islanded microgrids," *International Transactions on Electrical Energy Systems*, vol. 31, no. 11, Article ID e13045, 2021.
- [6] A. Constanza and C. Boberto, "Secondary control strategies for frequency restoration in islanded microgrids with consideration of communication delays," *IEEE Transactions on Smart Grid*, vol. 7, 2016.
- [7] A. Selakov, D. Bekut, and A. T. Sarić, "A novel agent-based microgrid optimal control for grid-connected, planned island and emergency island operations," *International Transactions on Electrical Energy Systems*, vol. 26, no. 9, pp. 1999–2022, 2016.
- [8] F. L. Li, C. X. Dou, X. L. Hu, Z. Q. Zhang, and T. F. Zhang, "Finite-time consensus for frequency and voltage restoration in microgrid under communication interruptions," *International Transactions on Electrical Energy Systems*, vol. 31, no. 4, Article ID e12830, 2021.
- [9] J. B. Almada, R. P. Leão, R. G. Almeida, and R. F. Sampaio, "Microgrid distributed secondary control and energy management using multi-agent system," *International Transactions on Electrical Energy Systems*, vol. 31, no. 10, Article ID e12886, 2021.
- [10] A. H. Tayebi, R. Sharifi, A. H. Salemi, and F. Faghihi, "Presentation of an  $H_\infty$  based frequency control for islanding provisional microgrid consisting of hybrid AC/DC microgrid," *International Transactions on Electrical Energy Systems*, vol. 31, no. 10, Article ID e12715, 2021.
- [11] M. M. Hossain and C. Peng, "Predictive event-triggered  $H_\infty$  load frequency control for hybrid power systems under denial-of-service attacks," *IET Generation, Transmission & Distribution*, vol. 14, no. 26, pp. 6457–6467, 2020.
- [12] B. Zhang, C. X. Dou, D. Yue, Z. Zhang, and T. Zhang, "A cyber-physical cooperative hierarchical control strategy for islanded microgrid facing with random communication failure," *IEEE Systems Journal*, vol. 14, no. 2, pp. 2849–2860, 2020.
- [13] C. X. Huang, J. Wang, S. Deng, and D. Yue, "Real-time distributed economic dispatch scheme of grid-connected microgrid considering cyber attacks," *IET Renewable Power Generation*, vol. 14, no. 14, pp. 2750–2758, 2020.
- [14] Y. J. Zhang, T. Yang, and Z. H. Tang, "Active fault-tolerant control for load frequency control in multi-area power systems with physical faults and cyberattacks," *International Transactions on Electrical Energy Systems*, vol. 31, no. 7, Article ID e12906, 2021.
- [15] I. Brahmia, J. Wang, L. Oliveira, and H. Xu, "Hierarchical smart energy management strategy based on cooperative distributed economic model predictive control for multi-microgrids systems," *International Transactions on Electrical Energy Systems*, vol. 31, no. 2, Article ID e12732, 2021.
- [16] Y. Y. Zou, Y. Dong, S. Y. Li, and Y. G. Niu, "Multi-time hierarchical stochastic predictive control for energy management of an island microgrid with plug-in electric vehicles," *IET Generation, Transmission & Distribution*, vol. 13, no. 10, pp. 1794–1801, 2019.
- [17] H. Han, Q. P. Xia, Y. Sun, X. C. Hou, and M. Su, "Leader-distributed follower-decentralized control strategy for economic dispatch in cascaded-parallel microgrids," *International Transactions on Electrical Energy Systems*, vol. 31, no. 9, e12964, 2021.
- [18] E. Shafiee Roudbari, M. T. H. Beheshti, and S. M. Rakhtala, "Voltage and frequency regulation in an islanded microgrid with PEM fuel cell based on a fuzzy logic voltage control and adaptive droop control," *IET Power Electronics*, vol. 13, no. 1, pp. 78–85, 2020.
- [19] F. Dehghani, M. Tourandaz Kenari, and M. A. Shafiyi, "A novel hybrid droop control strategy for DC microgrid with simultaneous consideration of operating costs and flexibility," *International Transactions on Electrical Energy Systems*, vol. 31, no. 6, Article ID e12896, 2021.
- [20] S. Rath, D. Pal, P. S. Sharma, and B. K. Panigrahi, "A cyber-secure distributed control architecture for autonomous AC microgrid," *IEEE Systems Journal*, vol. 15, no. 3, pp. 3324–3335, 2021.
- [21] S. W. Zheng, K. Liao, J. W. Yang, and Z. He, "Droop-based consensus control scheme for economic dispatch in islanded microgrids," *IET Generation, Transmission & Distribution*, vol. 14, no. 20, pp. 4529–4538, 2020.
- [22] H. H. Yuan, Y. Q. Xia, H. J. Yang, and Y. Yuan, "Resilient control for wireless networked control systems under DoS attack via a hierarchical game," *International Journal of Robust and Nonlinear Control*, vol. 28, no. 15, pp. 4604–4623, 2018.

- [23] B. Y. Wang, Q. Y. Sun, R. K. Han, and D. Ma, "Consensus-based secondary frequency control under denial-of-service attacks of distributed generations for microgrids," *Journal of the Franklin Institute*, vol. 358, no. 1, pp. 114–130, 2021.
- [24] B. J. Karaki and M. S. Mahmoud, "Scaled consensus design for multiagent systems under DoS attacks and communication-delays," *Journal of the Franklin Institute*, vol. 358, no. 7, pp. 3901–3918, 2021.
- [25] Y. Li, F. Y. Song, J. L. Liu, X. Xie, and E. Tian, "Decentralized event-triggered synchronization control for complex networks with nonperiodic DoS attacks," *International Journal of Robust and Nonlinear Control*, vol. 32, no. 3, pp. 1–21, 2021.
- [26] Y. C. Sun and G. H. Yang, "Robust event-triggered model predictive control for cyber-physical systems under denial-of-service attacks," *International Journal of Robust and Nonlinear Control*, vol. 29, no. 14, pp. 4797–4811, 2019.
- [27] W. Wenjun, T. Binfeng, H. Julong, and G. Fengyang, "Hierarchical optimization strategy for microgrid based on finite-time consensus algorithm," *Proceedings of the CSU-EPSA*, vol. 32, no. 6, pp. 7–13, 2020.

## Research Article

# Techno-Economic Feasibility Analysis of a Solar Photovoltaic Hybrid System for Rural Electrification in Sierra Leone for Zero Carbon Emission

Martin Sankoh <sup>1</sup>, Bakary Diarra <sup>2</sup>, Ravi Samikannu <sup>3</sup>,  
and Nyagong Santino David Ladu <sup>4</sup>

<sup>1</sup>Department of Mechanical and Maintenance Engineering, Fourah Bay College, University of Sierra Leone, Freetown, Sierra Leone

<sup>2</sup>Department of Electrical Engineering, University of Sciences, Techniques and Technologies of Bamako, Mali, West Africa

<sup>3</sup>Department of Electrical Computer and Telecommunications Engineering, Botswana International University of Science and Technology, Botswana

<sup>4</sup>Department of Mathematics and Physics, Rumbek University of Science and Technology, Rumbek, South Sudan

Correspondence should be addressed to Martin Sankoh; [sankohmartinsidi@gmail.com](mailto:sankohmartinsidi@gmail.com)

Received 6 March 2022; Revised 3 May 2022; Accepted 16 May 2022; Published 31 August 2022

Academic Editor: Qiuye Sun

Copyright © 2022 Martin Sankoh et al. This is an open access article distributed under the Creative Commons Attribution License, which permits unrestricted use, distribution, and reproduction in any medium, provided the original work is properly cited.

Remote area electrification is a crucial need in sub-Saharan Africa's drive to attain universal electrification. In Sierra Leone, with a rural population of over 5 million, the electrification rate accounts for less than 10% of the total inhabitants. This paper presents a comparative techno-economic analysis carried out to determine the most feasible of four individual options for off-grid mini-grid power generation system utilizing sources that include: Solar Photo Voltaic (SPV), Diesel Generator (DG), and Battery Storage (BS) system, to provide electricity for a rural and remote village located in the northwestern part of Sierra Leone (longitude 9.1°W and latitude 12.6°N), with an average daily solar irradiance between 4.6 and 6 kWh/m<sup>2</sup>/day. An assessment of the total electrical load estimated an expected daily consumption of 178 kWh. Simulation, optimization, and sensitivity analyses of each one of the individual power generation systems were carried out using HOMER software. Economic parameters such as Cost of Capital (CC), Net Present Cost (NPC), Levelized Cost of Electricity (LCOE), technical parameters (energy production characteristics), and greenhouse gases emissions were compared and analyzed. Key findings from the simulation result indicate that systems consisting of DG only (\$29,750) and SPV/BS (\$110,131) obtained the least and highest CC, respectively. Similarly, in a respective manner, the highest and least NPC were obtained for systems with DG only (\$496,336) and PV/DG/BS (\$152,491) over a 25-year project lifetime. Furthermore, the least LCOE was obtained for the system comprising PV/DG/BS (\$0.336/kWh). With an expected annual generation of (75,121 kWh), PV/DG/BS was obtained to be the most optimal solution. The sensitivity analysis observed that a reduction in the discount rate consequently reduces the LCOE of such a system. Furthermore, the model accounts for a 90% renewable energy fraction, with a significant reduction in the amount of annual GHG emissions, when compared with a generation system using diesel generator only.

## 1. Introduction

The sustainable energy development aims to create access to reliable and sustainable electricity supply for all by 2030. The continent of Africa is reported with an approximate population of 1.2 billion people, with 60% of this total population residing in rural area, whereas rural electrification

accounts for approximately 45% of this total (The Alliance for Rural Electrification (ARE), 2020). Extending electricity access to many rural and remote communities of Africa is still a major challenge. A few literatures [1–3] have cited some of the associated technical and economic challenges that serve as a major hindrance to electricity grid extension to rural and remote locations.

Sierra Leone has a total national population of 8 million people, with 65% of this total residing in rural communities. The country however is faced with a challenge of creating access to sustainable electricity supply to meet the needs of about 80% of its population who presently live without access to on-grid electricity supply. In 2021, national electricity access rate was reported by [4] as 23%; meanwhile, rural electrification accounted for less than 10% of the inhabitants.

Electricity in rural areas is accessed mainly through the use of stand-alone diesel or gasoline generation units, rooftop solar-home systems, or solar pico-lanterns. Other sources of domestic energy supply include the use of kerosene lamps and nonrechargeable alkaline battery torchlights for lighting, as well as biomass wood for cooking and heating—which often results in health threats to mostly women and children who usually carry out domestic or commercial cooking activities.

Sierra Leone possesses exploitable potentials of renewable energy resources, namely, biomass, hydro, and solar energy resources. Solar energy potential is predominant, with an annual average direct normal irradiation ranging between 4.6 and 6 kWh/m<sup>2</sup>/day. To date, there has been no comprehensive survey on the use of solar energy technologies in Sierra Leone. However, SPV systems in the form of mini-grids, stand-alone systems, and solar pico-lanterns are known to be widely used in generating and supplying power for use in households, hospitals, schools, and other important social facilities including communal water supply and farm irrigation systems.

Rural electrification remains a major challenge in Sierra Leone, where these communities mostly account for low-income inhabitants. Furthermore, the relatively high cost of extending the centralized national electricity grids has made the use of stand-alone off-grid power generation systems, mainly in the form of hybrid mini- and microgrids, as well as stand-alone systems, utilizing solar PV units, a preferred model of electricity generation and supply in the few communities, which have been electrified these communities. Solar photovoltaics systems have been widely noted to provide a suitable option to meet electricity needs for off-grid locations. However, academic studies on off-grid hybrid solar minigrids are few and far between. This work seeks to contribute to this regard by providing a methodology carrying out the technical and an economic analysis on four options of power generation systems for application in a typical rural and remote location in Sierra Leone.

The power generation models considered for analysis include source(s) employing:

- (1) DG only
- (2) A combination of SPV and DG
- (3) A combining SPV and BS
- (4) A combination of SPV, DG, and BS

This study aimed at carrying out a comparative technical and an economic analysis for supplying reliable electricity to a remote village. The objectives of this study carried out the following: energy resources and electrical load demand

assessment and simulation of energy models (also called scenarios) using homer software.

The comparative analysis is carried out based on results obtained from the simulation software—Hybrid Optimization for Multiple Electric Renewables (HOMER) software. Using HOMER software, simulations were carried out for each one of the four power systems considered. Specific economic characteristics including CC, the NPC, the LCOE, the technical characteristics of the system (including the sizes of each of the component included in a power system), as well as the electricity production characteristic (including the quantity of electricity produced and the overall and individual production characteristics) were analyzed in this study.

This paper presents methods and findings obtained from the simulation and analysis carried out. The remaining part of this manuscript is presented in the following format:

- (i) Section 1 reviews existing literature on case studies of related projects that have been carried out on the subject across the sub-Saharan Africa continent and beyond
- (ii) Section 2 defines the relevant study approach used to conduct the research, as well as the application of HOMER software
- (iii) Section 3 provides a comparative analysis of the four scenarios based on the results obtained and further discusses key findings obtained from the simulation results for the various scenarios considered
- (iv) Section 4 outlines the conclusions and recommendations drawn from the study

*1.1. Literature Review.* Due to the intermittency in power production from the use of SPV systems as a single source of power generation in their applications, hybrid power systems, combining SPV system with at least a generation source and or a storage device, have been widely researched and proposed as a suitable option to provide reliable power supply for off-grid applications worldwide [5]. Power generation using such systems can be from both renewable and nonrenewable energy resources including SPV systems, wind turbines, hydro power plants, diesel generator, steam turbines, or other nonconventional power generation sources.

Across Africa and beyond, a body of literature exists on techno-economic feasibility studies of SPV hybrid system, to assess their potential in terms of providing reliable electricity supply for off-grid communities across SSA. Many of these studies sought to assess the associated technical requirements and economic cost, carrying out a comparative analysis in order to determine the feasibility of different possible options of hybrid systems for the particular locations considered. For the existing studies cited in this work, assessments were carried out with the use of HOMER software—a specialized software designed to carry out feasibility study for hybrid mini- and microgrids. Existing



literature on techno-economic studies across sub-Saharan Africa are cited as follows.

A work by authors [6] assessed the techno-economic feasibility of hybrid electricity systems including SPV, DG, and BS system for electricity generation for selected off-grid rural locations in Jos community, located in northern Nigeria. A similar study [7] considered as case study a remote village, Fouay, located in Benin. The authors of [8] carried out a comparative techno-economic assessment amongst three options of HES: hybrid SPV, stand-alone SPV, and stand-alone DG in northern Cameroon. Other similar case studies outside of Africa include works outside of Africa can be cited from [9–11]. Literature from the cited works have indicated the viability of hybrid SPV systems as a means creating electricity access to rural and isolated communities.

In Sierra Leone, academic literature on the techno-economic feasibility of solar PV systems are few. However, closely related research works include a study on grid-connected renewable system in Freetown [12] and a comparative study on hybrid renewable power generation [13].

## 2. Methodology and Materials

A breakdown of the study methodology is summarized in the following steps:

- (i) Resources assessment and electrical load data collection
- (ii) Daily electrical load data estimation
- (iii) Simulation of the four power model scenarios

In the resources assessment phase, renewable energy generation resources were assessed in order to identify their potentials for power generation for the case study site. For this reason, both solar and wind energy resources were assessed. Data for the assessment were obtained from NASA online data set containing information on energy and climate resources for the location.

Homer software is used to carry out simulation, optimization, and sensitivity analyses for the four scenario of power systems considered. Sensitivity analysis is carried out on the most economical system to determine as well as carrying out a sensitivity analysis on the best-case system. The methodologies mentioned are discussed in subsequent sections.

**2.1. Profile of the Study Area.** Masunthu village is in Kambia district, northwestern part of Sierra Leone (longitude  $9.1^{\circ}\text{W}$  and latitude  $12.6^{\circ}\text{N}$ ). The community has a land size of approximately  $110,000\text{ m}^2$  (Google Earth, 2021), with the community located at approximately 27 kilometres from the district's administrative headquarter town (Google maps data).

The community hosts 1,004 inhabitants, where 54% represents female inhabitants (Local village statistics, October 2021). The primary source of economic livelihood is subsistence farming, where value addition activities such as local garri production and soapmaking are carried out. The

basic social facilities present include church, cinema, clinic, playing field, mosques, schools, shops, and water supply system.

The community is in an equatorial climatic zone with two distinctive seasonal weather patterns: rainy season (lasting from May to November) and dry season (lasting from December to April). The former is characterized by long periods of sunshine with average sunshine hours of between 4.5 and 6 hours a day, while the latter is characterized by higher levels of rainfall (between 2,000 and 3,000 mm) and frequency of cloudy days (Meteorological statistics, 2012). The vegetation type is tropical savannah grassland. Figure 1 shows ariel view of the Masunthu village.

**2.2. Electricity Situation.** The community is located off-grid and approximately 80.4 km (50 miles) from the closest national transmission grid (Google Earth, 2021), the Bumbuna hydro power transmission line. Primary energy use in the village meets the needs for domestic cooking, lighting, and powering of electronic devices (radio and phone charging). According to the United Nations multi-tier framework for energy access, electricity access for the village is categorized under the “Tier-1” framework [14], where pico-solar lanterns and torchlights with small photovoltaic cells and batteries are used to provide nighttime lighting for households. Charging of phones is accessed through a local telecentre for 0.1 USD per charge cycle per phone. Electricity generated from a 250 Wp solar module supplies power to an existing underground water pumping system used for community water supply purposes.

**2.2.1. Solar Energy Resources Assessment.** Table 1 summarize data on solar and wind energy potential of the case study area. The information from the data indicates solar energy as a source with viable potential for electricity generation. Wind power generation is infeasible due to low average wind speeds.

**2.2.2. Electrical Load Assessment.** Load assessments were completed in order obtain information necessary for estimating the expected daily electrical energy demand for the village. The assessment used a survey questionnaire developed in principle with the standard GIZ procedure minigrad sizing. A total of 50 questionnaires were issued and interviews were conducted with representatives from households, small businesses, and other social facilities that include schools and religious houses. Part A of the questionnaire asked general questions on the villagers' present means of meeting their needs for lighting, cooking, phone charging, and other uses of electricity. The load consumers were categorized into three categories, including household, commercial, and community loads. Table 2 shows the summary of village electrical loads.

Based on predictable factors such as villagers' daily routine and their expected consumption patterns, a few

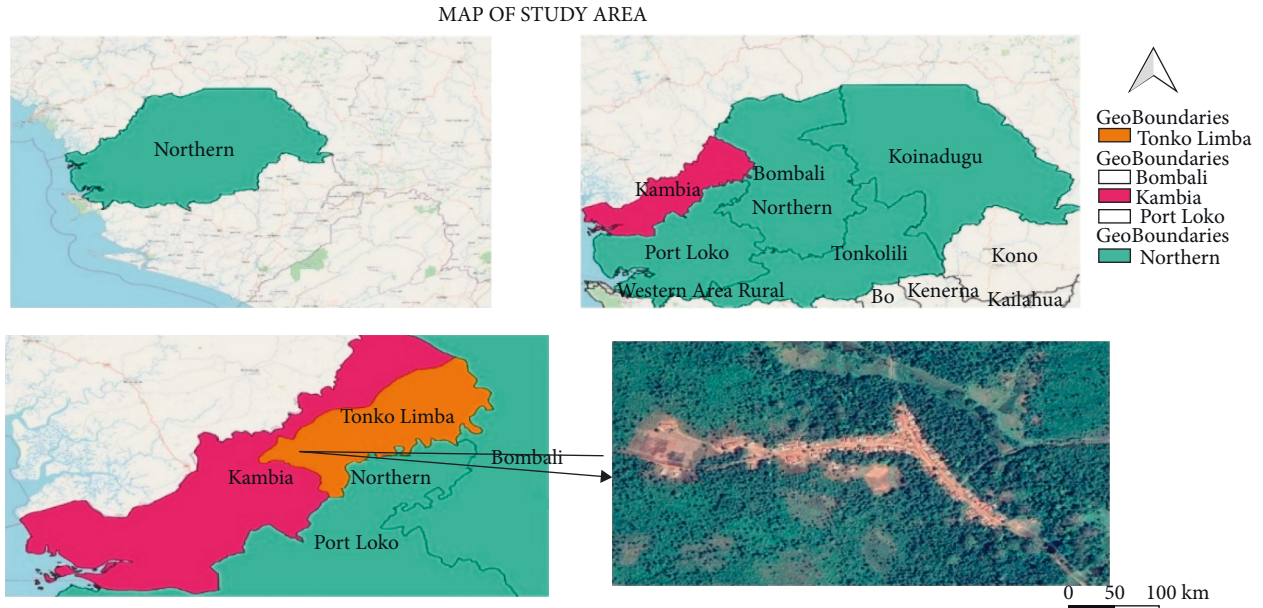


FIGURE 1: Aerial view of the Masunthu village. Source: Google maps.

TABLE 1: Solar and wind energy characteristics of Masunthu.

Month	Air temperature (°C)	Earth temperature (°C)	Atmospheric pressure (kPa)	Relative Humidity (%)	Wind speed (m/s)	Daily solar radiation: horizontal (kWh/m <sup>2</sup> /d)	Equivalent number of no-sun days
January	26.000	25.9	99.4	73.3	3.600	5.600	4.31
February	28.170	26.8	99.4	77.0	3.640	6.130	2.22
March	29.510	27.0	99.3	80.3	3.880	6.440	2.13
April	29.420	26.9	99.3	83.0	3.950	6.300	1.57
May	27.980	26.4	99.5	85.9	3.540	5.480	2.92
June	26.190	25.4	99.6	87.7	3.760	4.740	6.48
July	24.880	24.3	99.7	87.5	4.710	4.340	5.08
August	24.530	23.9	99.7	88.0	5.150	4.060	4.57
September	25.020	24.5	99.6	88.0	4.140	4.560	4.35
October	25.630	25.1	99.5	87.5	2.990	4.760	4.31
November	25.640	25.4	99.4	85.5	2.570	4.890	4.27
December	24.940	25.1	99.4	80.1	3.340	5.280	3.5
Annual	<b>24.6</b>	<b>25.5</b>	<b>99.5</b>	<b>83.7</b>	<b>3.77</b>	<b>5.22</b>	<b>45.71</b>

Source: International Energy Agency, 2021.

TABLE 2: Summary of village electrical loads.

Type	Number
Church	1
Mosque	1
Health clinic	1
School	2
Cinema	1
Shop	3
Street lighting	15
Tailoring centre	1
Household	91

assumptions were made in the estimation of the total electrical load.

The assumptions include the following:

- (i) Power ratings of equipment are assumed to be of standard average sizes, to cater for the probability of the use of nonenergy saving electrical devices: computer (120 W), fan (65 W), fridge (120 W), light (10 W), and phone (5W).
- (ii) Only low power consuming Alternating Current (AC) loads were considered in the sizing process.

- (iii) Load types were categorized into two seasonal loads: (1) summer loads and (2) winter loads (representing load consumption in the dry and rainy seasons, respectively).

- (iv) The hourly load consumption was calculated using the following formula:

$$\text{Hourly Load consumption (kWh)} = \text{Electrical Load (kW)} * \text{Time of use (hour)}. \quad (1)$$

Table 3 shows the load demand category.

### 2.3. Homer Software Simulation

**2.3.1. Simulation Scenarios.** Simulation scenarios is found in Table 4. Economic specifications for solar panel is given in Table 5.

**2.3.2. Description of HOMER Software.** HOMER software is an optimization tool developed in 1993 by the National Renewable Energy Laboratory (NREL), widely used to carry out techno-economic feasibility studies for both off-grid and grid-connected applications worldwide [15]. HOMER software carries out three key functions: simulation, optimization, and sensitivity analysis [16]. Figure 2 shows the Homer software and user interface. Specific technical and economic parameters as inputs that include:

- (i) Load and energy resources input. The daily electrical load consumption is used as an input to generate the daily electrical load profile (load consumption).
- (ii) Power system component input. These include the details of aggregate components that make up a power generation or a storage system, including their technical and cost specifications where necessary.
- (iii) Specific economic inputs. Project lifetime, inflation rate, interest rate, and diesel fuel price

HOMER runs multiple *simulations* on a selected power generation model, in the process, optimizing the technical and economic performance of the system over an entire calendar year of 365 days.

Technical output calculated by HOMER include the following: the total size of the system, specifications and performance of the individual components, power produced, economic outputs calculated that include the LCOE, and the annualized and total NPC and CC. GHG emissions calculations are also made. The key economic parameters are defined as follows.

The NPC of a generation system gives the sum of all associated income and outlay costs over the lifetime of the project.

The Levelized Cost of Energy (LCOE) is the minimum cost of energy beyond which an investment made is infeasible. LCOE compares investment alternatives

amongst two or multiple projects. In HOMER, LCOE is defined as the average cost per kWh of useful energy.

### 2.4. Simulation Input Parameters

#### 2.4.1. Components

**Solar PV panel.** Solar module converts irradiance into electricity using the photoelectric effect. HOMER calculates the size required and the power output of the SPV array. Table 5 shows the economic specifications for solar panel.

**Power converter.** A power converter converts between alternating current (AC) and direct current (DC) voltage. The input characteristics of the selected power converter are summarized in Table 6. The required size of the converter is calculated by using HOMER.

**Diesel generator.** Diesel generator when used in hybrid system can serve as a source of secondary or backup power supply. The economic input characteristics of the diesel generator are given in Table 7.

**Battery bank.** The battery bank stores and supply energy when needed. Technical and economic inputs for the battery unit are as specified in Table 8.

#### 2.4.2. Specific Economic Inputs and Sensitivity Inputs.

The specific project economic inputs used in the simulation are summarized as given in Table 9 which shows the economic input for diesel generator.

The price of diesel fuel, discount rate, as well as the inflation rates were obtained from national figures as of October 2021 [17]. In order to carry out the sensitivity analyses, values higher and lower than the original ones were selected. Observable project economic output variables include LCOE, NPC, and CC.

Diesel fuel prices in Sierra Leone are susceptible to unstable surges in market prices. As of October 2021, the pump-price of a litre of diesel fuel is 0.75 USD.

The nominal discount rate of 24% was used, as this represents the interest rate charged on financial lending provided by the Central Bank of Sierra Leone. The real discount rate used is calculated in homer as given in equation (2):

$$R = \frac{(r - f)}{(1 + f)}, \quad (2)$$

TABLE 3: Load demand category.

Category	Load type	Summer (kWh/day)	Winter (kWh/day)
1. Community load	Church	1.21	1.21
	Health centre	20.43	20.43
	Mosque	1.18	1.18
	School (2)	13.42	7.81
	Street lighting (15)	6.6	6.6
	Total (kWh/day)	42.84	34.19
2. Commercial load	Cinema	4.18	4.18
	Shop (3)	5.31	4.24
	Training centre	2.83	1.79
	Total (kWh/day)	12.32	10.21
3. Household load	DVD	6.75	6.75
	Fan	18.66	0
	Fridge	6.50	6.50
	Light	33.67	33.67
	Phone	8.41	8.41
	Radio	26.70	26.70
	TV	22.50	22.50
	Total (kWh/day)	123.21	104.53
Daily load (kWh/day)		178.37	148.93

TABLE 4: Simulation scenarios.

Scenario	Configuration
Scenario a (SA)	DG only
Scenario B (SB)	PV + DG
Scenario C (SC)	PV + BS
Scenario D (SD)	PV + DG + battery

TABLE 5: Economic specifications for solar panel.

Capita cost (\$/kW)	800
Replacement cost	N/A
O&M (\$)	10
Lifetime (years)	25



FIGURE 2: HOMER software user interface.

TABLE 6: Economic specifications for power converter.

Capital (\$/kW)	350
Replacement cost (\$/kW)	350
O&M (\$)	—
Lifetime (years)	15

TABLE 7: Economic input characteristics for diesel generator.

Generator fuel	Diesel
Capital (\$/kW)	850
Replacement cost (\$/kW)	850
O&M (\$/hr)	0.02
Lifetime (hrs)	20,000

TABLE 8: Techno-economic input for battery storage.

Name	EnergySafe SX
Capacity (Ah)	411
Voltage (V)	12
Throughput (kWh)	2,589
Depth of discharge (%)	70
Number of parallel strings	4
Capital (\$)	250
Replacement cost	250
O&M	—
Lifetime (years)	6
Efficiency (%)	97

TABLE 9: Economic input for diesel generator.

Table of sensitivity input variables		
Variable	Value	Sensitivity input values
Interest rate/discount rate (%)	24	30, 15, 4
Inflation rate (%)	10.2	13, 6, 3
Diesel fuel price (\$)	1	0.95, 1.25
Project lifetime (years)	25	

TABLE 10: Characteristics of controller.

Type	HOMER cycle charging/load following
Capacity (kW)	—
Capital (\$)	3000
Replacement cost	3000
O&M (\$)	—
Lifetime (years)	15

where  $R$  is real discounted rate,  $r$  is nominal discounted rate, and  $f$  is the expected inflation rate (18).

**2.4.3. Operational and Control Strategies.** Both the cycle charging and the load following dispatch strategies were selected in different simulation processes [18]. In the simulation, the load following strategy was used for SB, whereas cycle charging was used for cases of SC and SD. Table 10 shows the characteristics of controller.

### 3. Results and Discussion

**3.1. Daily Electrical Load Profile.** Figure 3 gives the daily electrical load profile for Masunthu village. A total daily consumption of 178 kWh was estimated. Community, commercial, and household loads account for 24, 7, and 67%, respectively, of the total consumption.

Electrical energy demand is lowest between periods of 00:00 and 08:00, as Villagers register their typical sleeping time during this period. There is also an expected rise in demand between 05:00 am and 06:00 am, mainly due to the muslim villagers rising to attend their daily religious prayers.

During energy demand for household is expected to be low as villagers attend to their daily occupations; meanwhile, electricity demand from commercial and community loads is expected to increase.

Peak energy demand is expected to occur in the evening hours between 7:00 pm and 10:00 pm due to an increase in the expected household demand. Consumption is estimated to vary on a seasonal basis, with electricity demand in summer estimated to be higher than that in the winter due to an increasing use of electrical power consuming appliances.

Simulation was done for each one of the four individual scenarios. The schematics of scenario for different configurations obtained from the simulation are, shown as given in

TABLE 11: Architectures of the four simulation scenarios.

System architecture for the different simulation scenarios					
	DG (kW)	SPV (kW)	BS (units)	Converter (kW)	Controller
Scenario A	35	—	—	—	—
Scenario B	30	56.2	—	17.7	Load following
Scenario C	—	77	108	30.2	Cycle charging
Scenario D	30	45	68	31	Cycle charging

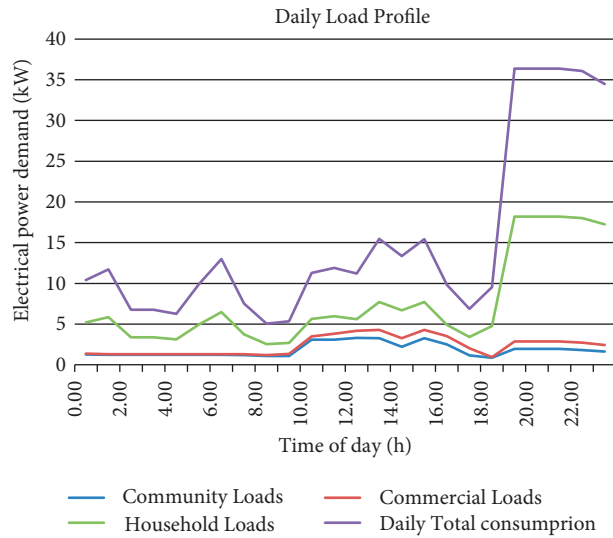


FIGURE 3: Daily electrical load profile of the village.

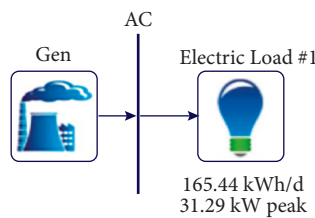


FIGURE 4: Schematic of scenario A.

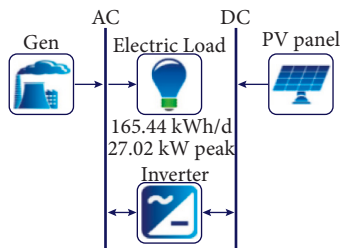


FIGURE 5: Schematic of scenario B.

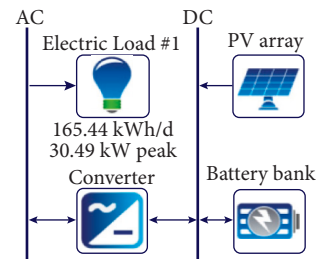


FIGURE 6: Schematic of scenario C.

Figures 4–7. Table 11 shows the architectures of the four simulation scenarios. Table 12 shows the technical and economic characteristics of the four scenarios.

A breakdown of the NPC over a 25-year period obtained for each of the scenarios are given as shown in Figures 8–11.

SA (\$496,336) gives the highest NPC amongst the four scenarios simulated, due to its high associated cost of fuel

and maintenance cost. SD (\$152,491) gives the lowest NPC, slightly lower as compared to the NPC obtained for SC (\$153,349). The NPC obtained for SB (\$309,541) doubles those obtained for SC and SD.

The high cost of battery storage component required makes SC (\$110,131) the system with the highest initial



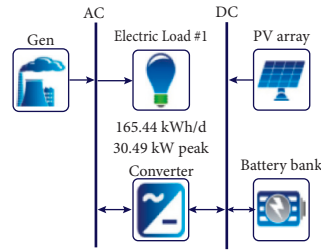


FIGURE 7: Schematic of scenario D.

TABLE 12: Technical and economic characteristics of the four scenarios.

Architecture	Scenario type			
	Scenario A (SA) Diesel only	Scenario B (SB) PV + diesel	Scenario C (SC) PV + battery	Scenario D (SD) PV + diesel + battery
NPC (\$)	496,336	309,541	153,350	152,491
CC (\$)	29,750	78,147	110,131	97,482
LCOE (\$/kWh)	0.955	0.677	0.337	0.336
O&M (\$)	23,201	24,141	937	1,266
Total electricity production (kWh/yr.)	91,869	137,090	112,728	75,121
Excess electricity produced (kWh/yr.)	31,483	75,877	47,952	10,165
Renewable fraction	0	0.10	1	0.87
Fuel consumption (L)	38,816	21,730	0	2,302
Greenhouse gas emission (kg/yr.)	103,103	57,733	0	6,117

TABLE 13: Summary of technical specifications of the most optimal system.

Components	Specification
PV array	45.5 kW
Battery	68 units
Diesel generator	31 kW
Converter	28 kW

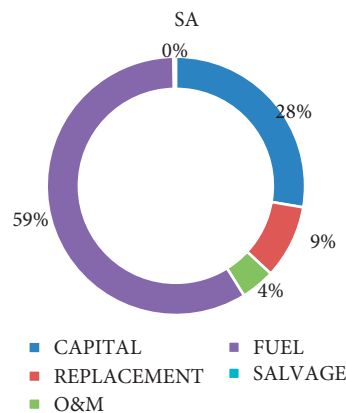


FIGURE 8: NPC breakdown for SA.

capital cost. Initial capital cost is relatively lowest with SA (\$29,750).

SD (\$/kWh 0.336) gives then lowest LCOE, almost equal to the LCOE of SC (\$/kWh 0.337). The highest LCOE is

associated with SA (\$0.995/kWh), which generates power using DG only, followed by SB (\$/kWh 0.677).

SC possesses the least lifetime O&M cost (\$937) due to the use of a completely renewable energy system. SB

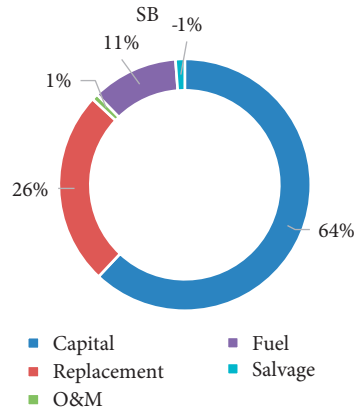


FIGURE 9: NPC breakdown for SB.

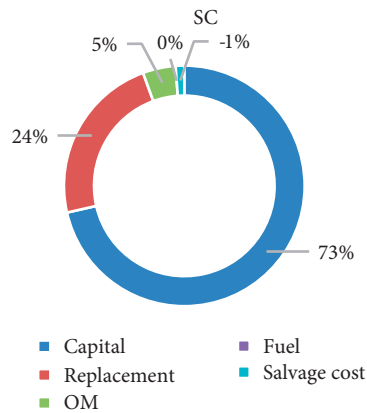


FIGURE 10: NPC breakdown for SC.

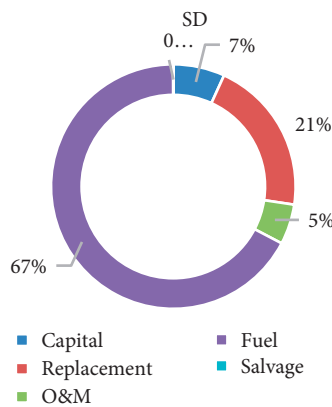


FIGURE 11: NPC breakdown for SD.

(\$24,141) that combines SPV and DG gives the highest O&M cost, closely followed by SC (\$23,201).

The highest total annual energy generated is obtained with SC (112,728 kWh/yr.), which accounts also for the highest excess electricity produced (75,877 kWh/yr.). SD (75,121 kWh/yr) generates the least amount of electricity and produces relatively minimum excess energy.

3.2. *The most optimal system.* Table 13 shows the summary of technical specifications of the most optimal system. Among the four different scenarios considered in this study, SD comprising SPV/DG/BS system is taken to be the most optimal system with the following characteristics based on a relative comparison:

system with the lowest NPC and LCOE

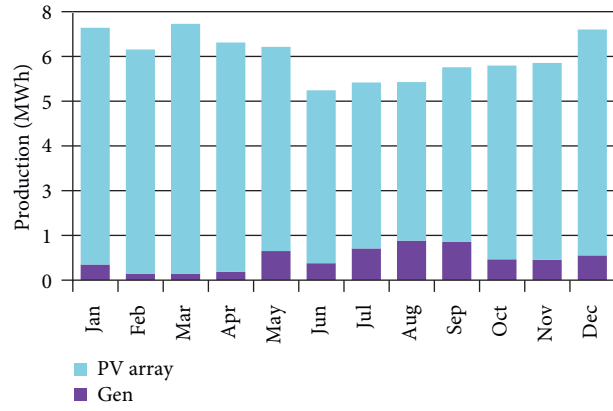


FIGURE 12: Annual electricity production.

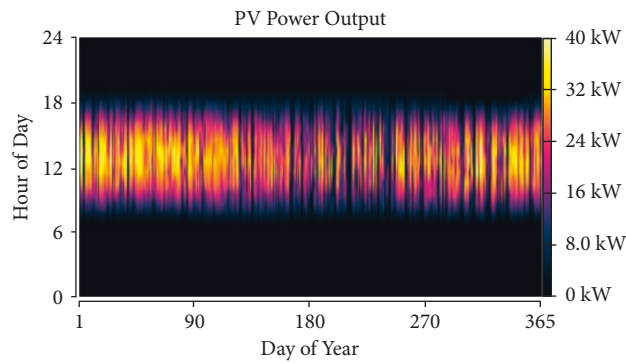


FIGURE 13: Power output from PV array.

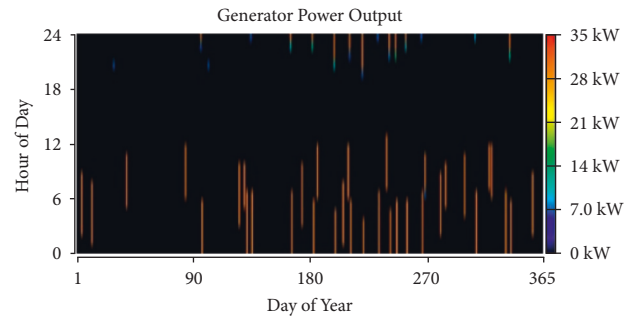


FIGURE 14: Power output from DG.

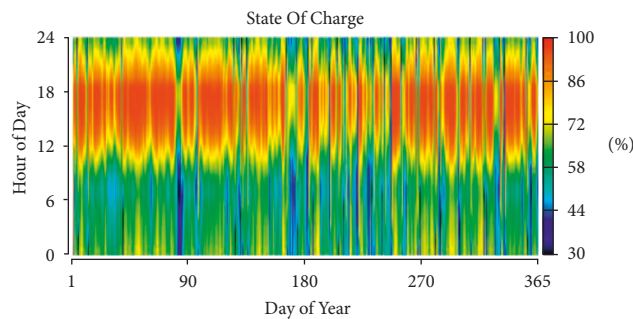


FIGURE 15: Battery state of charge.

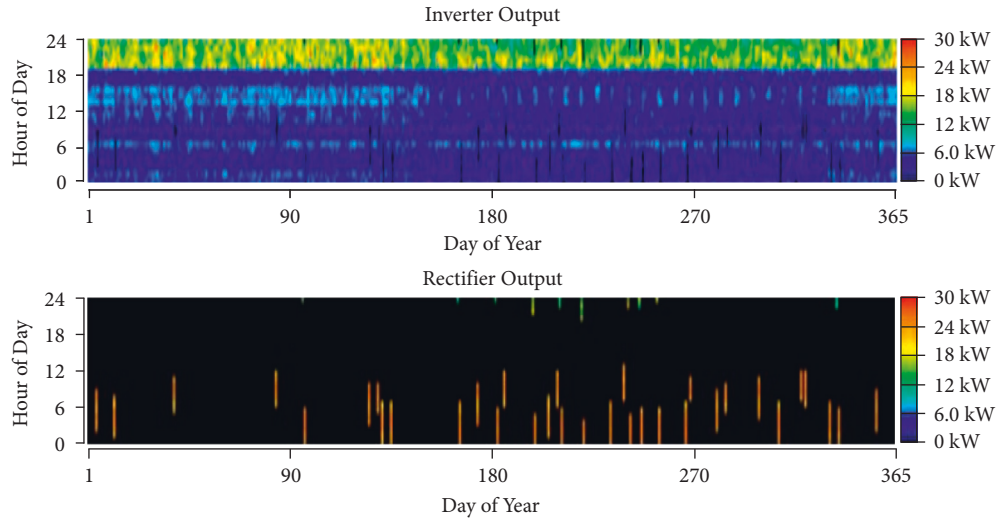


FIGURE 16: Converter power output.

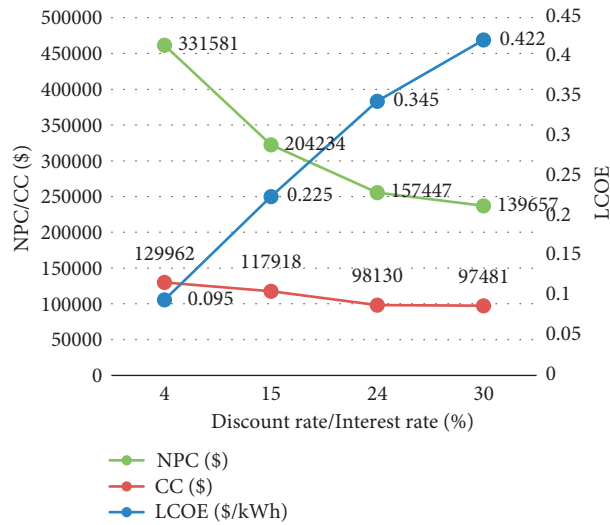


FIGURE 17: Sensitivity output for discount rate.

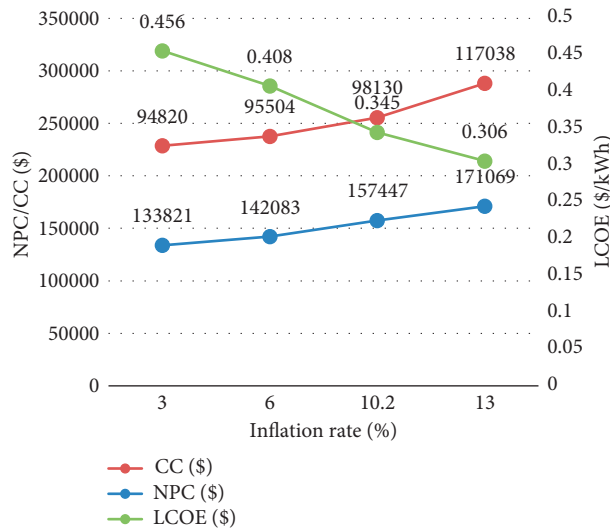


FIGURE 18: Sensitivity output for inflation rate.

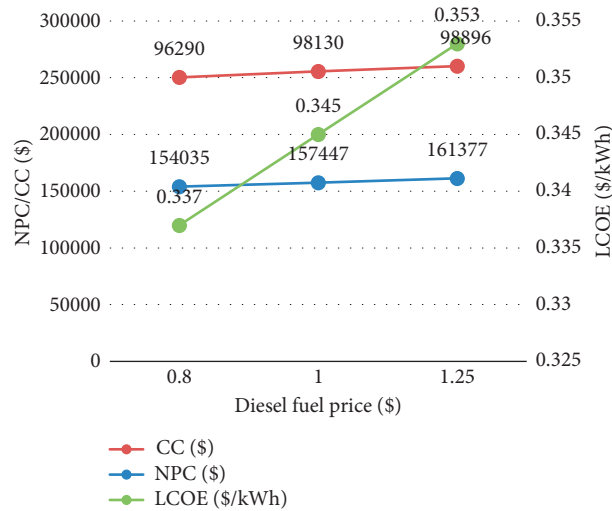


FIGURE 19: Sensitivity output for diesel fuel price.

Technically maximizes the use of renewable energy

Emits minimum amount of GHG relative to SA and SB

The proposed hybrid PV system for village electricity is expected to supply a daily load of 165 kWh, with a peak load of 30 kW. Electrical power from the system is generated using SPV and DG. The system has a renewable energy fraction of 88% and significantly minimizes GHG emissions relative to SA and SB that employ a DG only.

The proposed system has an expected annual power output of 75,295 kWh. The power produced from the SPV array in this model 68,002 kWh/yr. while the DG produces 7,257 kWh/yr. The months of March and June have the lowest and highest expected PV power output, respectively. Output from the DG is expected to be low during the dry season due to limited use and increases during the rainy season as the generator runtime increases. Figures 12, –16 show the performance curves for the system.

**3.3. Results from Sensitivity Analysis.** Figures 17–19 show the results obtained for the sensitivity analyses for model SD [19–22].

## 4. Conclusions

This study carried out a comparative technical and economic feasibility analysis among four different options (configurations) of power generation systems using generation options of SPV, DG, and BS systems using Homer software. Homer software was used to carry out simulation, optimization, and sensitivity analyses on each of the selected power system configuration. The scenario considered power generation by diesel generator only, a hybrid system consisting of DG and BS, hybrid system comprising SPV and BS, and a three-way hybrid power system comprising SPV/DG/BS.

With a national rate of inflation of 10.2%, a discount rate of 24%, and a price of \$1 per litre of diesel fuel, simulations

results obtained hybrid system, model SD, as the most optimal system representing the least NPC and LCOE. The proposed system comprises 45.5 kW PV array, 31 kW DG, and 68 lead-acid batteries. Economically, the model accounts for the cheapest energy generation, with a total NPC of \$152,491 and LCOE of \$0.336/kWh. Technically, the model is expected to generate an annual electrical energy of 75,121 kWh. This model also considerably reduces the annual amount of GHG emissions (6,117 kg) when compared to power generation using DG only (21,730 kg) or the hybrid system combining PV and DG (57,733 kg).

Hybrid SPV systems play an important role in rural and remote area power generation and supply; as such, this study recommends there is need for further scientific and academic studies to be carried on assessing the feasibility of such power systems for similar application across other locations of rural Sierra Leone.

Based on the sensitivity analysis, this study recommends fiscal and economic policies and incentives such as reducing the discount rate charged should be considered on financial lending provided towards SPV projects for rural villages that can significantly lower the capital cost of such projects, thus lowering the cost of energy produced. This has the tendency of increasing adoption rate of community households, which are mostly low-income earners.

## Nomenclature

AfDB:	African Development Bank
BS:	Battery storage
CC:	Capital cost
DG:	Diesel generator
GDP:	Gross domestic product
GHG:	Greenhouse gas
HES:	Hybrid electricity system
HOMER:	Hybrid optimization for multiple electric renewables

HRES:	Hybrid renewable energy system
IEA:	International energy agency
IRENA:	International renewable energy agency
LCOE:	Levelized cost of energy
NPV:	Net present value
PV:	Photovoltaic,
RE:	Renewable energy
SA:	Scenario A
SB:	Scenario B
SC:	Scenario C
SD:	Scenario D
SDG:	Sustainable development goals
SE4ALL:	Sustainable energy for all
SL:	Sierra Leone
SPV:	Solar photovoltaic
SSA:	Sub-Saharan Africa
UN:	United Nations
UNDP:	United Nations Development Program
WB:	World Bank.

### Data Availability

The data are available from the corresponding author upon request.

### Conflicts of Interest

The authors declare that they have no conflicts of interest.

### References

- [1] D. F. Barnes, *The Challenge of Rural Electrification*, Resources for the Future, Washington, D.C., U.S, 2007.
- [2] J. Peters, M. Sievert, and M. A. Toman, "Rural electrification through mini-grids: challenges ahead," *Energy Policy*, vol. 132, no. May, pp. 27–31, 2019.
- [3] A. Zomers, "The challenge of rural electrification," *Energy for Sustainable Development*, vol. 7, no. 1, pp. 69–76, 2003.
- [4] S. A. Hirmer, H. George-Williams, J. Rhys, D. McNicholl, and M. McCulloch, "Stakeholder decision-making: understanding Sierra Leone's energy sector," *Renewable and Sustainable Energy Reviews*, vol. 145, Article ID 111093, 2021.
- [5] J. F. Manwell, "Hybrid energy systems," *Encyclopedia of Energy*, 2004.
- [6] M. S. Adaramola, S. S. Paul, and O. M. Oyewola, "Assessment of decentralized hybrid PV solar-diesel power system for applications in Northern part of Nigeria," *Energy for Sustainable Development*, vol. 19, no. 1, pp. 72–82, 2014.
- [7] O. D. T. Odou, R. Bhandari, and R. Adamou, "Hybrid off-grid renewable power system for sustainable rural electrification in Benin," *Renewable Energy*, vol. 145, pp. 1266–1279, 2020.
- [8] N. E. Mbaka, N. J. Mucho, and K. Godpromesse, "Economic evaluation of small-scale photovoltaic hybrid systems for mini-grid applications in far north Cameroon," *Renewable Energy*, vol. 35, no. 10, pp. 2391–2398, 2010.
- [9] C. L. Azimoh, P. Klintonberg, F. Wallin, B. Karlsson, and C. Mbohwa, "Electricity for development: mini-grid solution for rural electrification in South Africa," *Energy Conversion and Management*, vol. 110, pp. 268–277, 2016.
- [10] M. H. Jahangir and R. Cheraghi, "Economic and environmental assessment of solar-wind-biomass hybrid renewable energy system supplying rural settlement load," *Sustainable Energy Technologies and Assessments*, vol. 42, Article ID 100895, 2020.
- [11] C. Li and W. Yu, "Techno-economic comparative analysis of off-grid hybrid photovoltaic/diesel/battery and photovoltaic/battery power systems for a household in Urumqi, China," *Journal of Cleaner Production*, vol. 124, pp. 258–265, 2016.
- [12] D. A. Konneh, M. E. Lotfy, R. Shigenobu, and T. Senjyu, "Optimal sizing of grid-connected renewable energy system in Freetown Sierra Leone," *IFAC-PapersOnLine*, vol. 51, no. 28, pp. 191–196, 2018.
- [13] D. Konneh, H. Howlader, R. Shigenobu, T. Senjyu, S. Chakraborty, and N. Krishna, "A multi-criteria decision maker for grid-connected hybrid renewable energy systems selection using multi-objective particle swarm optimization," *Sustainability*, vol. 11, no. 4, p. 1188, 2019.
- [14] T. World Bank, "Turning the Lights on Across Africa," 2013, <https://openknowledge.worldbank.org/handle/10986/16623>.
- [15] A. Kassam, "HOMER software: training guide for renewable energy base station design | mobile for development," *Homer Manual*, vol. 21, 2010.
- [16] Homer Energy, "Homer pro," *Manual Homer Energy*, pp. 1–241, 2019.
- [17] A. B. Johnny, *Consumer Price Index*, 2021.
- [18] S. A. Shezan, K. N. Hasan, A. Rahman, M. Datta, and U. Datta, *Selection Of Appropriate Dispatch Strategies For Effective Planning And Operation Of a Microgrid*, 1–9, Sierra Leone. (n.d.), 2021.
- [19] A. Henry, *Electricity Sector Reform Roadmap*, 2017, <https://rise.esmap.org/data/files/library/sierra-leone/Energy%20Access/EA%2014.1B.pdf>.
- [20] Homer's, "Calculations," 2021, [https://www.homerenergy.com/products/pro/docs/latest/homers\\_calculations.html](https://www.homerenergy.com/products/pro/docs/latest/homers_calculations.html).
- [21] E. Muh, *A Comparative Assessment of Hybrid Renewable Energy Systems for Sustainable Rural Electrification in Cameroon*, Pan African University Institute of Water and Energy Sciences, Algeria, North Africa, 2017.
- [22] *Rural Electrification | the Alliance for Rural Electrification*, 2022, <https://www.ruralelec.org/rural-electrification>.



## Research Article

# Distributed Energy Management for Zero-Carbon Port Microgrid

Jing Song <sup>1</sup>, Qihe Shan <sup>1</sup>, Tao Zou <sup>2</sup>, Jingwei Hu <sup>3</sup>, and Fei Teng <sup>4</sup>

<sup>1</sup>Navigation College, Dalian Maritime University, Dalian 116026, China

<sup>2</sup>Research Institute of Intelligent Networks, Zhejiang Lab, Hangzhou 311121, China

<sup>3</sup>State Grid Liaoning Electric Power Company Limited Economic Research Institute, Shenyang 110170, China

<sup>4</sup>College of Marine Electrical Engineering, Dalian Maritime University, Dalian 116026, China

Correspondence should be addressed to Qihe Shan; shanqihe@dmlu.edu.cn and Tao Zou; zout@zhejianglab.com

Received 15 December 2021; Revised 1 July 2022; Accepted 6 July 2022; Published 2 August 2022

Academic Editor: Faroque Azam

Copyright © 2022 Jing Song et al. This is an open access article distributed under the Creative Commons Attribution License, which permits unrestricted use, distribution, and reproduction in any medium, provided the original work is properly cited.

A zero-carbon port microgrid that integrates carbon capture power plants is proposed to build the green port and promote the achievement of the dual-carbon goal. To achieve the optimal economic operation of the port microgrid and reduce carbon emissions, an energy management model considering carbon trading mechanisms is established. Furthermore, a distributed energy management method is proposed for the zero-carbon port based on the alternating direction method of multipliers (ADMMs). The simulation results prove the effectiveness and accuracy of the proposed method, which can effectively improve the economy of the port microgrid and reduce the carbon emission of the port.

## 1. Introduction

With the continuous acceleration of the global economic integration process, shipping has been developing rapidly. As the key nodes to realize the interconnection of maritime trade and transportation, the annual carbon emissions of ports have risen to almost 100 million tons, together with the increasing emission of the harmful gases year by year [1]. Moreover, long-distance transportation will gradually shift from highway transportation to waterway transportation, which will bring greater energy demand [2] and carbon emissions in the future [3]. Therefore, it is extremely essential, for the realization of the dual-carbon goal, to establish a green port and study its energy management issues so as to construct a zero-carbon port microgrid.

The energy management of port microgrid is an optimization problem that needs to consider multiple constraints [4]. At present, many scholars have studied the energy management methods of ports. Kanellos et al. [5] proposed an energy management method based on multi-agent systems to realize the optimal economic port, considering a large number of flexible loads. Parise et al. [6] proposed the port energy master plan on the basis of

considering the electrical infrastructures of port facilities. Kermani et al. [7] proposed a comprehensive energy management method based on blockchain technology to reduce the peak power consumption generated by the terminal. With the rapid growth of energy consumption and people's increasing attention to environmental protection, various measures have been taken to reduce carbon emissions from power systems, which are mainly divided into two categories, one is to use the renewable energy and change the low-carbon system framework and the other is to use the market regulation mechanisms, including carbon trading and carbon tax. Both types of carbon reduction measures have been extensively studied by related scholars. Wu et al. [8] proposed a novel carbon-oriented extended planning model for an integrated electricity and gas system with electric vehicle fast-charging stations and demonstrated the validity of the model. Conlon et al. [9] proposed a modeling framework with a trade-off between increased low-carbon generation and decarbonization of heating and vehicle electrification and demonstrated that the framework plus can achieve equivalent emission reductions at lower costs. Fu et al. [10] considered a stepped carbon tax, established a computable equilibrium model, and proved the

effectiveness of carbon tax on carbon reduction. With the rapid development of waterway transportation in the future, the energy demand for port microgrids will accordingly increase, followed by the significant growth of carbon emission [11], so how to implement carbon emission reduction for ports has received a lot of attention from scholars. Bo et al. [12] studied the port logistic carbon emission management system through a specific model in the concept of the Internet of things. Li et al. [13] utilized game theory to calculate the cost of government subsidies for using shore power to reduce port carbon emissions. De et al. [14] studied an environmental issue related to fuel consumption and carbon emissions while considering the issue of sustainable container transportation of the port. Kanellos [15] proposed a multi-objective operation scheduling method for large ports, which regulates port power demand to limit port carbon emissions. However, at present, most scholars only reduce port carbon emissions to a certain extent, and few can truly achieve zero-carbon emissions. Therefore, it is indispensable to consider a port microgrid and establish an energy management model for the port microgrid to achieve the lowest or even zero carbon.

The energy management problems can be solved by centralized algorithms and distributed algorithms [16], and the former generally rely on a powerful centralized controller. Wu et al. [17] proposed a cost-effective energy dispatch method for residential smart grid with centralized renewable energy. Olivares [18] proposed a centralized energy management method for island microgrids based on the model predictive control algorithm. Sahoo et al. [19] proposed a novel centralized energy management approach to improve power quality for the hybrid microgrid with solar cells. Long et al. [20] proposed a low-carbon economic dispatch model for multi-energy microgrids to minimize daily operating costs by considering multistep carbon trading, and the simulation results showed that the proposed model can effectively reduce carbon emissions. On account of the large-scale renewable energy on the port microgrid, which presents distributed characteristics, the centralized energy management algorithm with a centralized controller is no longer suitable for solving the energy management problem of the port microgrid [21–23]. Accordingly, distributed energy management algorithms have been widely studied in recent years. Li et al. [24] proposed a distributed algorithm based on event triggering to realize day-ahead and real-time collaborative energy management for multi-energy systems. Gennitsaris and Kanellos [25] proposed a multi-agent real-time distributed demand response system to reduce operating costs and ensure the real-time limitation of ship emissions. Li et al. [26] proposed a consensus-based distributed power system control scheme together with a robust control method to maintain the optimal power dispatch state when the communication fails. Energy management problem for microgrids has also been solved by many scholars using the distributed method. Du et al. [27] proposed a distributed algorithm based on consensus theory and gradient estimation techniques to solve the optimal energy management problem of microgrids faster. Shi et al. [28] defined the energy management problem as an optimal

power flow problem and proposed a distributed energy management strategy for the microgrid. Liu et al. [29] proposed a distributed ADMM-based energy management method for multi-microgrid and proved its effectiveness. Although the existing centralized and distributed methods can solve the energy management problem, the distributed characteristics of the power supply device, and the carbon reduction mission of the port microgrid, how to solve the energy management problem of the zero-carbon port microgrid by using the distributed algorithm still needs to be studied.

Overall, a zero-carbon port microgrid with a carbon capture power plant is proposed, of which the optimal economical energy management considering the carbon trading is studied in this study. The innovations of this study can be summarized as follows: constructing the zero-carbon port microgrid, establishing an energy management model, and getting a distributed optimal solution. The specific innovations are as follows:

- (1) A zero-carbon port microgrid that integrates a carbon capture power plant is proposed. The carbon capture power plant can capture the carbon dioxide emitted from the combustion of traditional fossil energy, which can greatly realize a green port microgrid. Under the target of low carbon, the port microgrid with the carbon capture power plant can also ensure the reliable and stable operation.
- (2) An energy management model considering carbon trading is established. The introduced carbon trading is to deal with the carbon dioxide emitted to the air that has not been captured by the carbon capture power plant, which ensures the realization of the zero-carbon goal of the port. In addition, with the carbon trading, the economic efficiency of the port microgrid can be improved by selling surplus carbon quotas.
- (3) An ADMM-based distributed energy management method is proposed to solve the energy management problem of zero-carbon port microgrid and obtain the optimal zero-carbon energy management solution, and the optimality of the proposed method is also illustrated.

The remainder of the study is organized as follows. Section 2 establishes the structure of zero-carbon port microgrid and explains its characteristics. Section 3 builds the energy management model for zero-carbon port microgrid. Section 4 introduces the basic graph theory, and the ADMM-based distributed energy management method is presented. In Section 5, several case studies are presented to show the effectiveness of the proposed algorithm. Section 6 concludes the study.

## 2. The Structure and Characteristics of Zero-Carbon Port Microgrid

The proposed zero-carbon port microgrid (see Figure 1) contains power devices (i.e., carbon capture power plant,

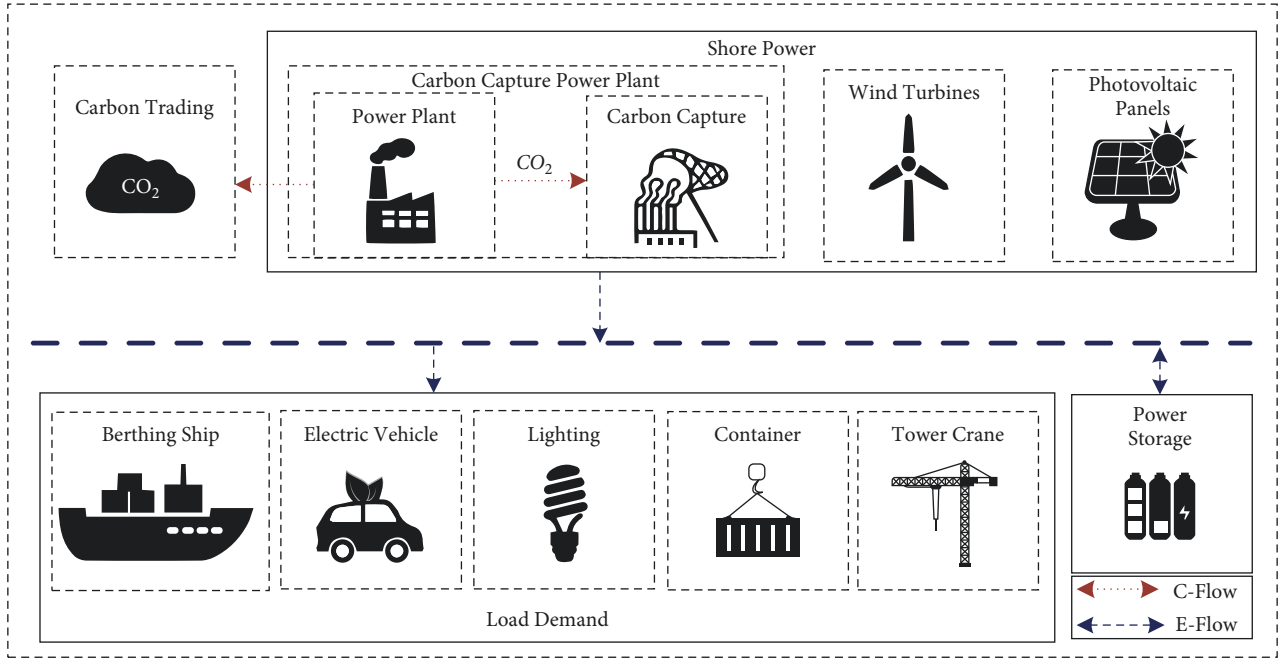


FIGURE 1: Structure of the zero-carbon port microgrid.

photovoltaic panels, and wind turbines), the loads (i.e., lighting systems, electric vehicles, tower cranes, shore cranes, and berthing ship), and power storage device. The port power plant with the carbon capture device can effectively reduce carbon dioxide emissions. Most of the carbon dioxide produced by fossil energy combustion will be captured by the carbon capture device. Furthermore, a small amount of carbon dioxide emitted into the air will be processed through carbon trading. Therefore, through the comprehensive consideration of carbon capture and carbon trading, a zero-carbon port microgrid can be realized.

Further, the carbon emission treatment process of the port microgrid is presented in detail in Figure 2. Most of the carbon dioxide emitted from fossil fuel combustion can be captured by carbon capture device and stored by carbon storage device. A fraction of the carbon dioxide released into the air that is not captured is processed by carbon trading. The mass of the carbon dioxide captured by carbon capture power plant is directly proportional to the mass of the produced carbon dioxide, which is related to fuel types and fuel emission factors. Among them, the emission factor refers to the mass of the carbon dioxide emitted after burning unit mass fuel. The masses of the carbon dioxide captured and produced are calculated as follows:

$$\begin{aligned} Q_{ccs} &= \eta Q_{dis}, \\ Q_{dis} &= \gamma P_{fu}, \end{aligned} \quad (1)$$

where  $Q_{ccs}$  is the mass of the carbon dioxide to be treated by carbon capture device;  $\eta$  is the efficiency coefficient of carbon dioxide capture;  $Q_{dis}$  is the mass of carbon dioxide emitted after fossil fuel combustion;  $\gamma$  is the mass of carbon dioxide emission per unit power; and  $P_{fu}$  is the power provided by fossil fuel combustion.

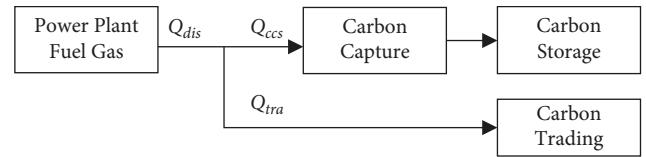


FIGURE 2: Carbon emission treatment process.

In the process of carbon treatment, carbon capture equipment is actually an electrical device. Since carbon capture is also an electrical load, it consumes part of the power generated by burning fossil fuels. The total power consumption of carbon capture device is divided into two parts. One part is the fixed energy consumption to maintain the normal operation of the carbon capture function, which is independent of the mass of the carbon dioxide captured. The other part is the operation energy consumption of carbon capture device, which is related to the mass of the carbon dioxide to be treated. Hence, the output power of the carbon capture power plant can be expressed as follows [30, 31]:

$$P_{co} = P_{fu} - P_{ccs}, \quad (2)$$

$$P_{ccs} = P_m + P_{ccso}, \quad (3)$$

$$P_{ccso} = \tau(Q_{ccs})^2, \quad (4)$$

where  $P_{co}$  is the output power of the carbon capture power plant for the microgrid;  $P_{ccs}$  is the total power consumed by carbon capture;  $P_{ccso}$  is the operating power consumed by carbon capture; and  $\tau$  is the coefficient of power consumed by carbon treating.

The carbon dioxide captured by the carbon capture power plant will be stored, and the cost of storing carbon dioxide is as follows:

$$F_{\text{sto}} = C_{\text{sto}} Q_{\text{ccs}}, \quad (5)$$

where  $F_{\text{sto}}$  is the carbon storage cost of the storage device;  $C_{\text{sto}}$  is the cost coefficient of sealing carbon per unit mass.

As shown above, the carbon beyond the capacity of the carbon capture device should be processed through carbon trading mechanism to realize zero-carbon port microgrid. The carbon trading mechanism is to take carbon emission rights as a commodity. For a fixed port microgrid, the government imposes carbon emission quotas based on its power generating capacity [32]. If the amount of carbon emitted is less than the allotted amount, the surplus carbon quotas can be sold for a profit. If the amount is more than the allotted amount, it needs to spend money to buy the insufficient part. The relevant formulas can be expressed as follows:

$$F_{\text{tra}} = C_{\text{tra}}((Q_{\text{dis}} - Q_{\text{ccs}}) - Q_q), \quad (6)$$

$$Q_q = \varphi P_{\text{fu}}, \quad (7)$$

where  $F_{\text{tra}}$  is the carbon trading cost;  $C_{\text{tra}}$  is the cost coefficient of carbon trading price;  $Q_q$  is the carbon emission quota; and  $\varphi$  is the coefficient of carbon emission quota.

### 3. Energy Management Model for Zero-Carbon Port Microgrid

Considering the structure of the zero-carbon port microgrid proposed in Section 2, the optimization objective is to minimize the operating cost while reducing the carbon emissions of ports. As stated beforehand, port power plants with the carbon capture device can absorb large amounts of carbon dioxide emitted by fossil fuel combustion, while the unabsorbed carbon dioxide is processed according to carbon trading mechanisms. Therefore, different from the objective function of normal energy management problems, the cost function associated with carbon is additionally considered in the objective function of this study. For the reliable and stable operation of the port microgrid in this process, a variety of constraints still need to be considered, such as supply and demand balance constraints, power supply devices, and output power constraints. It is worth noting that the power consumed to achieve carbon capture is considered as part of the load of the port microgrid in the supply-demand balance constraint.

In this section, the model of zero-carbon port microgrid is constructed, where the objective function consists of three parts: the power generation cost, the power storage cost, and the carbon cost, and each part of the objective function is described specifically. The constraints of the zero-carbon port microgrid model are also described, including the equality constraint of supply-demand balance and the conventional inequality constraints.

**3.1. Objective Function.** The objective of this study was to reduce the carbon emissions while ensuring the economy of the port microgrid. The power supply device of the port microgrid includes power generation device and energy storage device, so the cost of power generation and the cost of power storage are included in the objective function. At the same time, the carbon cost is added to the objective function. To realize carbon emission reduction, the carbon capture power plant is used to process the generated carbon dioxide, and the carbon trading market mechanism is also used to process the emitted carbon dioxide, generating costs or earning profits. Therefore, the objective function of the energy management problem is divided into three parts: power generation cost, power storage cost, and carbon cost, which is expressed as follows:

$$F = \min\{F_1 + F_2 + F_3\}, \quad (8)$$

where  $F_1$ ,  $F_2$ , and  $F_3$  are the port power generation cost, the power storage cost, and the carbon cost, respectively.

**3.1.1. Power Generation Cost.** The power generation cost of the port microgrid includes the cost of carbon capture power plant, photovoltaic panels, and wind turbines, which can be expressed as follows:

$$\begin{aligned} F_1 &= F_{\text{ccs}} + F_{\text{pv}} + F_w, \\ F_{\text{ccs}} &= \sum_{h_1 \in N_1} a_{h_1} (P_{\text{fu}, h_1})^2 + b_{h_1} P_{\text{fu}, h_1} + c_{h_1}, \\ F_{\text{pv}} &= \sum_{h_2 \in N_2} a_{h_2} (P_{\text{pv}, h_2})^2 + c_{h_2}, \\ F_w &= \sum_{h_3 \in N_3} a_{h_3} (P_{w, h_3})^2 + c_{h_3}, \end{aligned} \quad (9)$$

where  $F_{\text{ccs}}$ ,  $F_{\text{pv}}$ , and  $F_w$  are the power generation costs of carbon capture power plant, photovoltaic panels, and wind turbines, respectively;  $a_h$ ,  $b_h$ , and  $c_h$  ( $h = 1, 2, 3$ ) are the coefficients of the power generation cost;  $P_{\text{fu}, h}$  and  $P_{w, h}$  ( $h = 2, 3$ ) are the output power of photovoltaic panels and wind turbines; and  $N_1$ ,  $N_2$ , and  $N_3$  are the node sets of carbon capture power plant, photovoltaic panels, and wind turbines, respectively.

**3.1.2. Power Storage Cost.** The power storage cost of the port microgrid can be expressed as follows [33]:

$$F_2 = \sum_{h_4 \in N_4} a_{h_4} (P_{s, h_4} + b_{h_4})^2, \quad (10)$$

where  $P_{s, h_4}$  is the output power of the power storage device;  $F_2 = a_{h_4} (P_{s, h_4} + b_{h_4})^2$ , and  $b_{h_4}$  is the cost coefficient of the power storage device.

**3.1.3. Carbon Cost.** To achieve the goal of zero-carbon port, carbon cost must be taken into consideration seriously. Carbon cost includes carbon trading cost and carbon storage cost, which can be expressed as follows:

$$F_3 = F_{\text{tra}} + F_{\text{sto}}. \quad (11)$$

Substituting (3)–(7) into (11), it can be calculated as follows:

$$F_3 = C_{\text{tra}} \left( ((1 - \eta)\gamma - \varphi) \sum_{h_1 \in N_1} P_{\text{fu},h_1} \right) + C_{\text{sto}} \eta \gamma \sum_{h_1 \in N_1} P_{\text{fu},h_1}. \quad (12)$$

It can be seen that carbon cost is only related to the variable  $P_{\text{fu},h_1}$ .

**3.2. Constraints.** To ensure the secure and stable operation of the zero-carbon port microgrid, the following constraints need to be considered.

**3.2.1. Power Balance Constraint.** Considering the lighting system and other electrical devices of the port microgrid, combined with the total output of power generation devices, the following constraint can be obtained:

$$\begin{aligned} & \sum_{h_1 \in N_1} P_{\text{fu},h_1} + \sum_{h_2 \in N_2} P_{w,h_2} + \sum_{h_3 \in N_3} P_{\text{pv},h_3} \\ & + \sum_{h_4 \in N_4} P_{s,h_4} = P_{\text{ccs}} + \sum_{h \in W} L_{p,h}, \end{aligned} \quad (13)$$

where  $W$  is the total node set of loads ( $W = N_1 \cup N_2 \cup N_3 \cup N_4$ );  $L_{p,h}$  is the total power load of the port microgrid.

**3.2.2. Power Output Constraint.** Considering that the power output of the power generation device is within a certain range, there exist upper and lower bounds to guarantee the safety of the port microgrid. So, the power outputs of the power generation device need to satisfy the following constraints [33]:

$$\begin{aligned} P_{\text{fu}}^{\min} \leq P_{\text{fu},h_1} \leq P_{\text{fu}}^{\max}, P_w^{\min} \leq P_{w,h_2} \leq P_w^{\max} \\ P_{\text{pv}}^{\min} \leq P_{\text{pv},h_3} \leq P_{\text{pv}}^{\max}, P_s^{\min} \leq P_s \leq P_s^{\max}, \end{aligned} \quad (14)$$

where  $P_{\text{fu}}^{\min}$ ,  $P_w^{\min}$ ,  $P_{\text{pv}}^{\min}$ , and  $P_s^{\min}$  are the minimum output power of each carbon capture power plant, photovoltaic panel, wind turbine, and power storage device, respectively;  $P_{\text{fu}}^{\max}$ ,  $P_w^{\max}$ ,  $P_{\text{pv}}^{\max}$ , and  $P_s^{\max}$  are the maximum output power of each carbon capture power plant, photovoltaic panel, wind turbine, and power storage device, respectively.

**3.2.3. Power Storage Constraint.** Too much or too little charged and discharged power will damage the power storage device, so the following constraint can be obtained:

$$\text{SoC}_{\min} \leq 1 - \frac{P_s}{P_e} \leq \text{SoC}_{\max}, \quad (15)$$

where  $P_e$  is the power storage capacity;  $\text{SoC}_{\min}$  and  $\text{SoC}_{\max}$  are the minimum state of charge and the maximum state of charge of the power storage device. (15) can be changed to a box inequality as (14).

## 4. Distributed Energy Management Method for Zero-Carbon Port Microgrid

Due to the various distributed power generation devices in the considered zero-carbon port microgrid, an ADMM-based distributed energy management method is proposed to solve the above energy management problem and the optimal zero-carbon energy management solution can be obtained.

**4.1. Graph Theory.** The port microgrid is abstracted into a collection of  $N$  node sets, and the interaction relationship between the node sets can be expressed by a weighted directed graph  $G = \{V, E, A\}$  [34], where  $V = \{v_i, i = 1, \dots, N\}$  is a node set containing  $N$  elements in total; the total number of  $W$  elements is  $N$ ;  $E \subseteq V \times V$  is the edge set; and  $A = [a_{ij}] \in R^{N \times N}$  is the adjacency matrix of the graph. If  $a_{ij} > 0$ , it represents  $(v_j, v_i) \in E$ ; that is, node  $j$  can transmit information to node  $i$ ; if  $a_{ij} = 0$ , it represents  $(v_j, v_i) \notin E$ ; that is, node  $j$  cannot transmit information to node  $i$ .

**4.2. Optimal Condition Analysis.** In this section, the optimal conditions of the energy management problem will be analyzed.

(12) is a linear term related to  $P_{\text{fu},h_1}$  only, and (9) is a polynomial in which there is a linear term related to  $P_{\text{fu},h_1}$ . Therefore, (12) can be combined with the first term in (9) to calculate, and obviously, (9)–(12) can be rewritten as follows:

$$F_i(P_i) = \frac{(P_i - \alpha_i)^2}{2\beta_i} + \phi, \quad i \in 1, 2, \dots, N, \quad (16)$$

where  $F_i(P_i)$  is the cost of the  $i$ th device;  $\alpha_i$ ,  $\beta_i$ , and  $\phi$  are equivalent transformation coefficients of the cost functions.

Then, the energy management problem of the zero-carbon port microgrid can be rewritten as follows:

$$\begin{aligned} \min \quad & \sum_{i=1}^N F_i(P_i) = \frac{(P_i - \alpha_i)^2}{2\beta_i} \\ \text{s.t.} \quad & \sum_{i=1}^N P_i = \sum_{i=1}^N L_i + P_{\text{ccso}}, \end{aligned} \quad (17)$$

$$P_i^{\min} \leq P_i \leq P_i^{\max}$$

where  $P_i^{\max}$  and  $P_i^{\min}$  are the upper and lower power bounds of each device, respectively;  $P_{\text{ccso}} = S_i P_i^2$  is the consumed power of the carbon capture power plant, which is related to the power generation of the carbon capture power plant; and  $S_i$  is the consumed power coefficient.

The above optimization problem can be solved using the Lagrange multiplier method [35], and the Lagrange function is as follows:

$$L(P_i, \lambda, \bar{\nu}, \underline{\nu}) = \sum_{i=1}^N (F_i(P_i)) + \lambda \left( \sum_{i=1}^N L_i + P_{\text{ccso}} - \sum_{i=1}^N P_{i,t} \right) + \bar{\nu}(P_i - P_i^{\max}) + \underline{\nu}(P_i^{\min} - P_i), \quad (18)$$

where  $\lambda$ ,  $\bar{\nu}$ , and  $\underline{\nu}$  are Lagrangian multipliers of equality constraints and inequality constraints, respectively. Without considering the inequality constraints of the problem, derivation of the Lagrangian function can be obtained as follows:

$$\frac{\partial L}{\partial P_i} = \frac{P_i - \alpha_i}{\beta_i} + \lambda(2S_i P_i - 1) = 0. \quad (19)$$

Then, the local optimal solution can be presented as follows:

$$P_i^* = \frac{\alpha_i + \lambda\beta_i}{1 + 2S_i P_i \lambda}, \quad (20)$$

where  $P_i^*$  is the local optimal solution without considering the inequality constraints. When considering the inequality constraints, the global optimal solution is described as follows:

$$P_i^* = \begin{cases} \frac{\alpha_i + \lambda\beta_i}{1 + 2S_i P_i \lambda}, & P_i^{\min} \leq \frac{\alpha_i + \lambda\beta_i}{1 + 2S_i P_i \lambda} \leq P_i^{\max}, \\ P_i^{\max}, & \frac{\alpha_i + \lambda\beta_i}{1 + 2S_i P_i \lambda} > P_i^{\max}, \\ P_i^{\min}, & \frac{\alpha_i + \lambda\beta_i}{1 + 2S_i P_i \lambda} < P_i^{\min}. \end{cases} \quad (21)$$

**4.3. Distributed Energy Management.** As the optimal solution of the energy management problem exists based on the above analysis, the algorithm including three iterations (22)–(24) is given as follows:

$$\lambda_i(k+1) = \lambda_i(k) + \xi_i \left[ \sum_{j=1}^N a_{ij} (\lambda_j(k) - \lambda_i(k)) \right] + \psi(k) \Delta \hat{P}_i(k). \quad (22)$$

$$P_i(k) = \Gamma(\lambda_i(k)) = \begin{cases} \frac{\alpha_i + \lambda_i(k)\beta_i}{1 + 2S_i P_i \lambda_i(k)} & P_i^{\min} \leq \frac{\alpha_i + \lambda_i(k)\beta_i}{1 + 2S_i P_i \lambda_i(k)} \leq P_i^{\max}, \\ P_i^{\max} & \frac{\alpha_i + \lambda_i(k)\beta_i}{1 + 2S_i P_i \lambda_i(k)} > P_i^{\max}, \\ P_i^{\min} & \frac{\alpha_i + \lambda_i(k)\beta_i}{1 + 2S_i P_i \lambda_i(k)} < P_i^{\min}. \end{cases} \quad (23)$$

$$\Delta \hat{P}_i(k+1) = \Delta \hat{P}_i(k) + \zeta \left[ \sum_{j=1}^N a_{ij} (\Delta \hat{P}_j(k) - \Delta \hat{P}_i(k)) \right] + \Delta P_i(k+1) - \Delta P_i(k), \quad (24)$$

where  $\xi_i > 0$  is the step size of the algorithm;  $\psi(k) > 0$  is the feedback gain;  $\Delta \hat{P}_i(k)$  is the  $k$ th iteration of mismatched power; and  $P_i(k)$  is the output power of the  $i$ th device in  $k$ th iteration, which is calculated by  $\lambda_i$ .

For the above algorithm, the following conditions need to be met [35].

Condition 1: the algorithm step size  $\xi_i \in (0, 1/\sum_{j=0}^N a_{ij})$

Condition 2: the algorithm step size  $\zeta \in (0, 1/\max_{i=1,2,\dots,N} \sum_{j=1}^N a_{ij})$

Condition 3: the feedback gain  $\psi(k) > 0$ ,  $\lim_{k \rightarrow \infty} \psi(k) = 0$ , and  $\sum_{k=0}^{\infty} \psi(k) = \infty$

As in literature [35],  $\lim_{k \rightarrow \infty} 1_N^T \Delta \hat{P}(k) = 0$  can be definitely proved with the contradiction method according to conditions 1–3. The convergence can be obtained as follows:

$$\lim_{k \rightarrow \infty} 1_N^T \Delta \hat{P}(k) = 0 \rightarrow \sum_{i=1}^N P_i(k) + \sum_{i=1}^N \Delta \hat{P}_i(k) = \sum_{i=1}^N L_i. \quad (25)$$

With the above analysis (specific proof can be found in literature [35]), it can be concluded that the supply-demand balance of the port microgrid can be realized asymptotically. Therefore, the energy management problem of the zero-carbon port microgrid proposed in this study can be effectively solved by the algorithm. The algorithm flow chart is shown in Figure 3, and the algorithm steps are shown in Table 1. According to the convergence of the algorithm, the optimal solution can be obtained.

## 5. Case Analysis

Four cases are given and analyzed for a zero-carbon port microgrid in this section. The communication topology diagram of the zero-carbon port microgrid is shown in Figure 4, including a carbon capture power plant, two photovoltaic panels, two wind turbines, and a power storage device. The parameters of each device are shown in Table 2.

The effectiveness of the energy management method based on the zero-carbon port microgrid is verified in this section. Case 1 utilizes a centralized method to solve the optimization problem. Case 2 studies distributed energy management without the carbon capture power plant. Case 3 studies distributed energy management with the carbon capture power plant and a changing carbon trading price. In Case 4, to further verify the stability of the port microgrid, the change in load demand and plug-and-play power supply devices is considered during the operation of the port



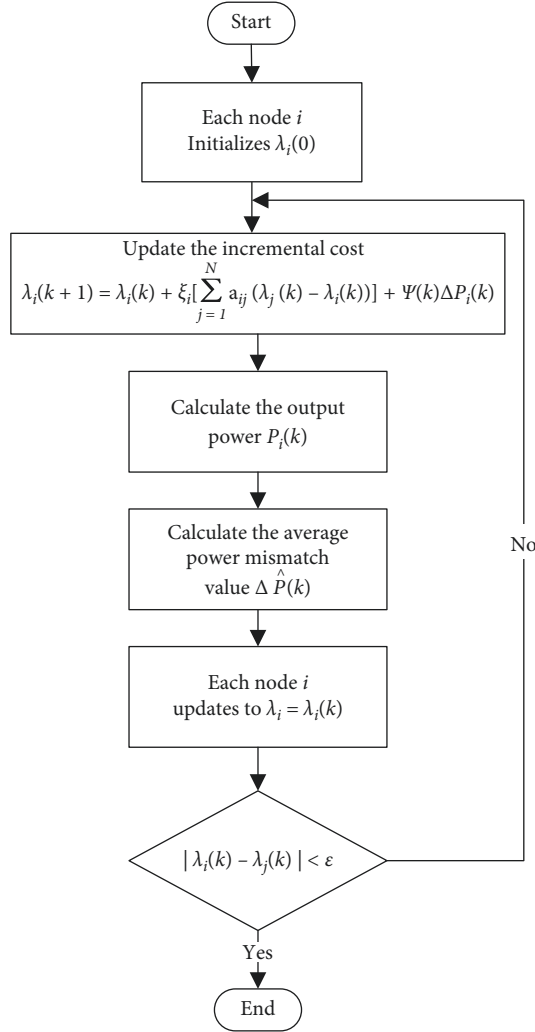


FIGURE 3: Flow chart of the algorithm.

microgrid. Afterwards, the impact on the total cost of the port microgrid operation and carbon emissions is analyzed.

**5.1. Case 1: Centralized Energy Management with Carbon Capture Power Plant.** In this case, a centralized method is utilized to solve the energy management problem of the zero-carbon port microgrid. The purpose is to verify the accuracy of the distributed method utilized in this study. The total load of the port microgrid is 1200 MW, and the output power of each device is shown in Figure 5.

The output power of each device can meet the load required by zero-carbon port microgrid, with a total cost of 10,454 \$ and a total carbon emission of 31.79 t. However, owing to the large number of renewable energy power generation devices with distributed physical characteristics, the centralized method is no longer applicable for the energy management problem of zero-carbon port.

**5.2. Case 2: Distributed Energy Management without Carbon Capture Power Plant.** To verify whether the zero-carbon port microgrid with the carbon-containing power plant

proposed in this study can truly achieve carbon emission reduction, the port microgrid in this case utilizes the power plant without carbon capture device, but still considers carbon trading. The simulation results are as follows.

In this case, the total operation cost is 11,386 \$, and the total carbon emission is 144.0 t. The output power of each power generation device is shown in Figure 6(a). It can be seen that the output power of the port power plant is relatively low, because the carbon trading mechanism preferentially selects the power generation device with low-carbon emissions for power generation, but the port microgrid without carbon capture power plant still has high carbon emissions. The carbon emission of port microgrid without carbon capture power plant is shown in Figure 6(b). Although the distributed energy management method utilized in this case is suitable for solving this problem, the port microgrid without the carbon capture power plant has high carbon emissions and serious environmental pollution.

**5.3. Case 3: Distributed Energy Management with Carbon Capture Power Plant.** In this case, the distributed energy management method is utilized for the zero-carbon port microgrid with the same data as the above cases. Simulation results are shown in Figure 6.

The total operation cost is 11,260 \$, and the total carbon emission is 29.72 t. The power mismatch of each device is shown in Figure 7(c). It is clear, according to the figure, that all the mismatch converges to 0, which proves that the output power of each device can meet the power load demand of the port microgrid. The output power of each device is shown in Figure 8. It can be clearly seen that the value fluctuates slightly at the beginning and then reaches a plateau. The mass of port carbon emission is shown in Figure 7(d), which manifests that the carbon emissions of the port microgrid containing the carbon capture power plant are significantly reduced compared with Figure 7(b).  $\lambda(k)$  that refers to Lagrangian iterator is shown in Figure 7(a). The physical characteristics of  $\lambda(k)$  refer to the incremental cost of each power generation device in the port microgrid. The iterative operator tends to be stable, which testifies that the distributed method can converge to an optimal solution, which is approximately equal to the result in Case 1.

Since the carbon trading price is changed with the market supply and demand, the influence of the changing carbon trading price on the carbon capture power plant in the zero-carbon port microgrid needs to be studied, as shown in Figures 7(b) and 7(d). Among them, CCP stands for the port microgrid with the carbon capture power plant, and GPP stands for the port microgrid without the carbon capture power plant.

As seen in Figure 8, compared with GPP, the carbon emission of CCP is significantly less. With the carbon trading price increasing, the carbon emissions of GPP have been significantly reduced. Owing to the relatively small carbon emissions of CCP, the change in carbon trading price has little effect on its carbon emissions. Hence, it can be concluded that the integrated carbon capture power plant can greatly reduce carbon emissions of the port microgrid,

TABLE 1: Distributed energy management algorithm.

---

 Algorithm: distributed energy management algorithm
 

---

Initialization:

Each node  $i$  initializes  $\lambda_i(0)$ .

Iteration:

(1): Each node iterates according to local information and exchanges information through neighbors. the power generation device updates its own incremental cost at the next iteration through (22).

(2): Each node calculates the output power of the  $k$  th iteration, as shown in (23).(3): For the output power of each device, the average power mismatch value of all nodes of the port microgrid at  $k + 1$  th iteration is calculated by the average consistent algorithm, as shown in (24).Each node  $i$  updates to  $\lambda_i = \lambda_i(k)$ .Let  $k = k + 1$ , until  $|\lambda_i(k) - \lambda_j(k)| < \varepsilon, i = 1, 2, \dots, N; j = 1, 2, \dots, N. (\varepsilon$  is a small positive constant).End.
 

---

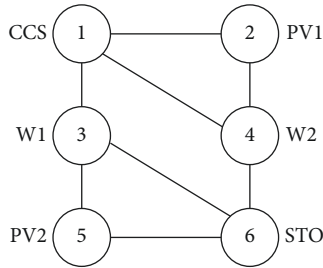


FIGURE 4: Zero-carbon port microgrid communication topology.

TABLE 2: Parameters of the device.

Device	$a_i$	$b_i$	$c_i$	$P_i^{\min}$	$P_i^{\max}$
CCS	0.25	2	2	30	300
PV1	0.3	0.029	0	0	300
W1	0.29	0.019	0	0	280
W2	0.21	0.01	0	0	290
PV2	0.21	0.01	0	0	400
STO	0.2	1.6	3.2	-280	280

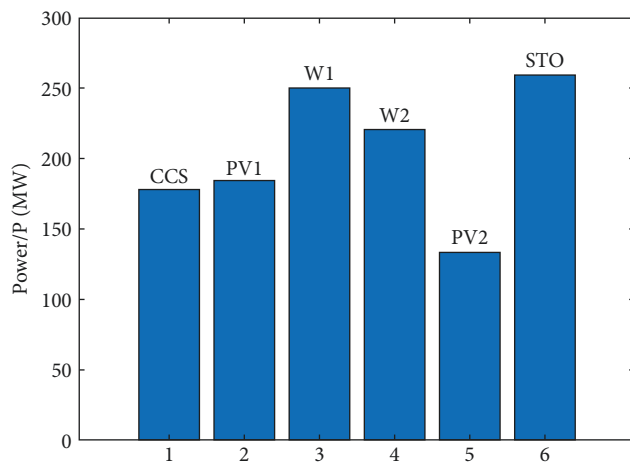


FIGURE 5: Output power of each device.

which is an effective way to achieve zero-carbon port microgrid.

It can be concluded from Figure 9 that with the carbon trading price increasing, the total cost of CCP becomes lower, while the total cost of GPP becomes higher. The

reason is that the carbon capture device can capture most of the carbon emissions from CCP, and CCP can also profit from the carbon trading with surplus quotas. Hence, it is liable to figure out that installing carbon capture device would not only reduce carbon emissions but also reduce the operation cost of zero-carbon port microgrid. The higher the carbon trading price is, the higher the profit, and the lower the total operation cost of the port microgrid will be.

The port microgrids in Case 1 and Case 3 both contain a carbon capture device, and the amount of carbon emissions is 31.9 t and 29.7 t, respectively. The difference is not large, which can illustrate the effectiveness of the distributed energy management method proposed in this study. However, in Case 2, the carbon emission of the port microgrid without carbon capture power plants is 144.0 t, and there is a huge difference in the quantity of the carbon emission. This means that the use of the carbon capture power plant in port microgrid can reduce carbon emission by 79.4%. In conclusion, the zero-port microgrid with carbon capture power plants proposed in this study can effectively reduce carbon emissions.

Case 3 is compared with the previous cases, which shows that the port microgrid including carbon capture power plants proposed in this study can greatly reduce carbon emissions and at the same time verifies the effectiveness of the distributed energy management method. In addition, Case 3 analyzes the impact of the carbon trading unit price on the port microgrid. The higher the carbon trading unit price, the higher the economy of the port microgrid with carbon capture power plants.

*5.4. Case 4: Distributed Energy Management considering the Change in Load Demand and Plug-and-Play Power Supply Devices.* In this section, the change in load demand and plug-and-play power supply devices are considered during the operation of the port microgrid, and the power supply of each power supply device is analyzed to further explore the stability of the port microgrid. The simulation results of changing the load demand are shown in Figure 10, and the simulation results of considering plug-and-play power supply devices are shown in Figure 11.

Load demand changes occur frequently while the port microgrid is in operation. To study the operation of port microgrid under sudden load demand change, in this case,

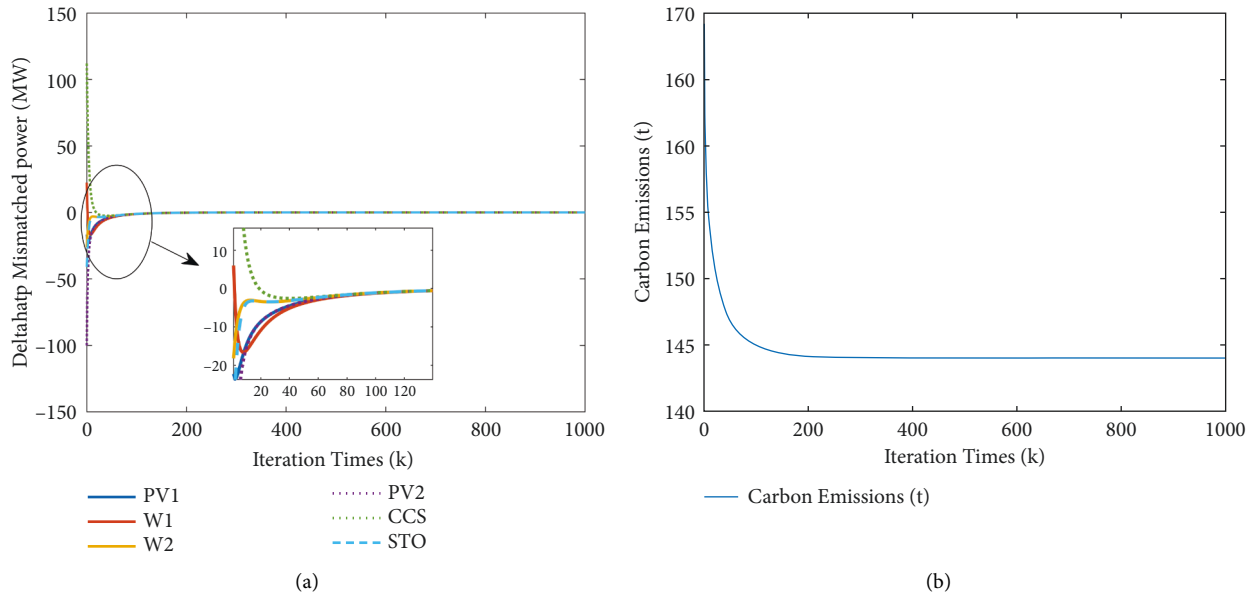


FIGURE 6: Simulation results. (a) Dynamic curve of output power of each device. (b) Dynamic curve of carbon emissions.

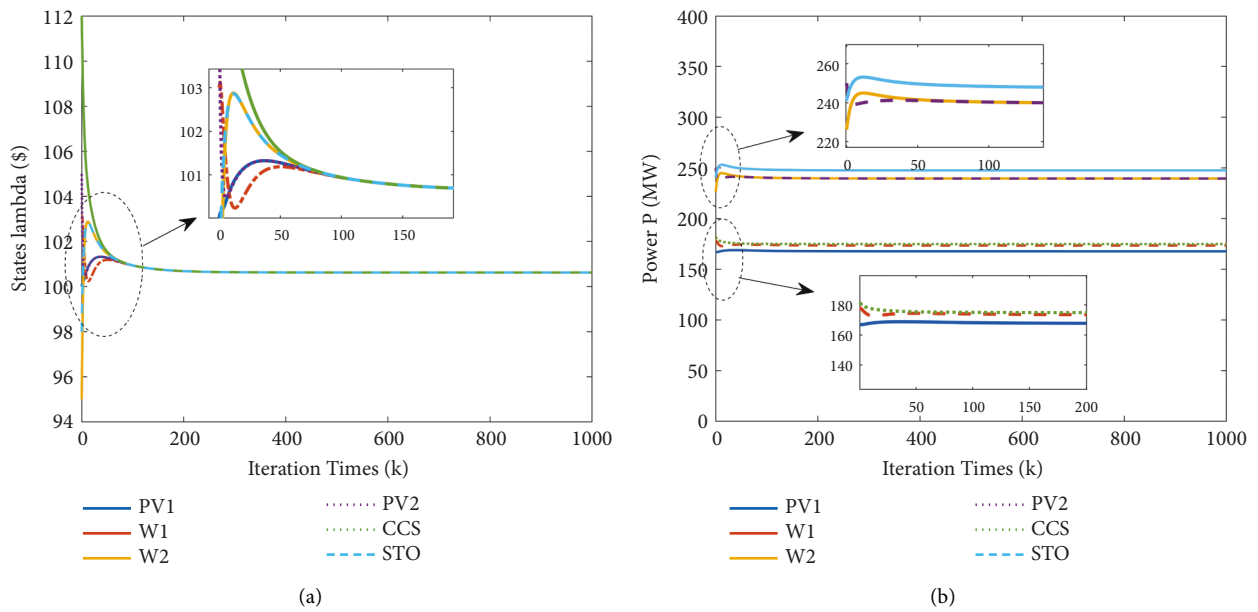


FIGURE 7: Continued.

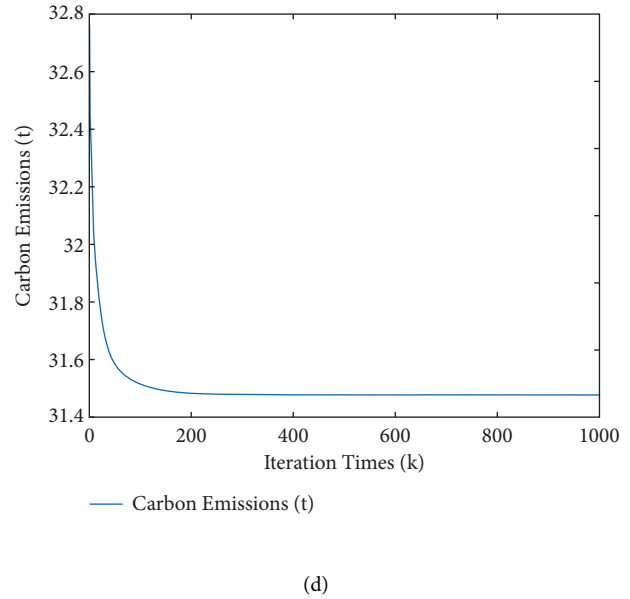
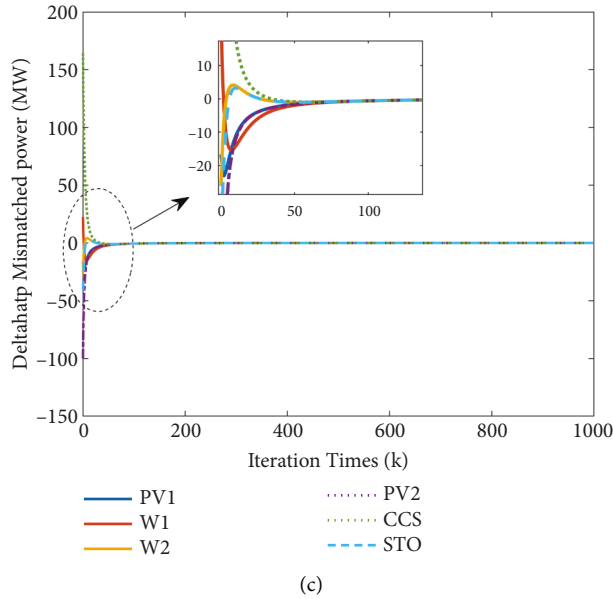


FIGURE 7: Simulation results. (a) Dynamic curve of iterative operator  $\lambda$ . (b) Dynamic curve of output power of each device. (c) Dynamic curve of power mismatch. (d) Dynamic curve of carbon emissions.

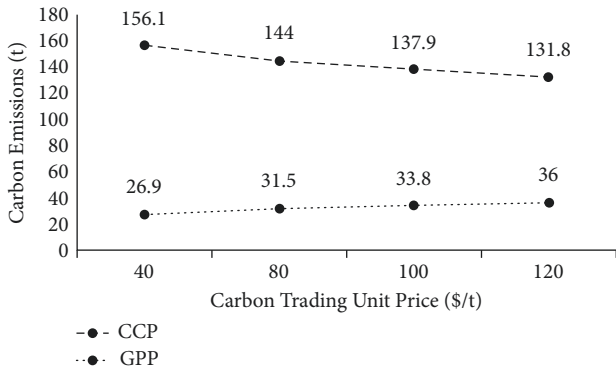


FIGURE 8: Impact of carbon trading price on carbon emissions.

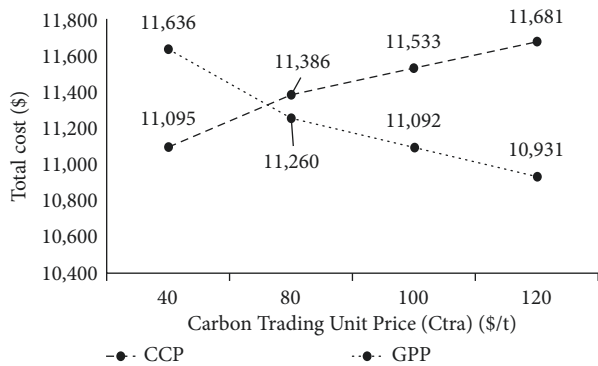


FIGURE 9: Impact of carbon trading price on total cost.

the port load demand changes from 1200 MW to 1260 MW at the 1000th iteration of the port microgrid. The simulation results are shown in Figure 10, and it can be seen that the cost and carbon emission increase slightly with the increase in the load demand. The optimal operation cost is 11,610 \$,

and the carbon emission is 31.66 t. As port's load demand increases by 60 MW, its cost increases by 350 \$, and the increased cost is 3.1% of the total cost. At the same time, the carbon emissions increases by 1.97 t, and the increased carbon emissions are 6.1% of the total carbon emissions. It can be seen that the change in the load demand of the port microgrid has a greater impact on its cost compared with the carbon emission.

As seen in Figure 10(a), the iterative operator has a small fluctuation after the increase in load demand, but soon reaches stability, and there is a small increase compared with the pre-stabilization, which is less than 2% of the original value. It can be seen from Figure 10 that the power supply of each device fluctuates to meet the balance of supply and demand due to the sudden increase in load demand. The power supply for each device increased somewhat in comparison with that before the load demand adjustment, but the fluctuation is extremely tiny and will soon be able to reach stability. As shown in Figure 10(c), although there is a significant rapid change in the mismatched power, stability is still reached after 50 iterations. As load demand increases, carbon emissions increase because carbon capture power plants need to burn more fossil energy to meet the balance between supply and demand. When the load demand suddenly changes while the port microgrid is operating steadily, the port microgrid can still immediately recover stability, demonstrating the stability of the algorithm proposed in this study and further ensuring the reliability of the port microgrid.

To ensure the reliable and stable operation of the port microgrid when the plug-and-play power supply device is interrupted, in this energy management case, at the 1000th iteration, PV1 is interrupted and only five devices remain to handle the port microgrid's power supply. The optimal operation cost is 13358 \$, and the carbon emission is 32.0 t.

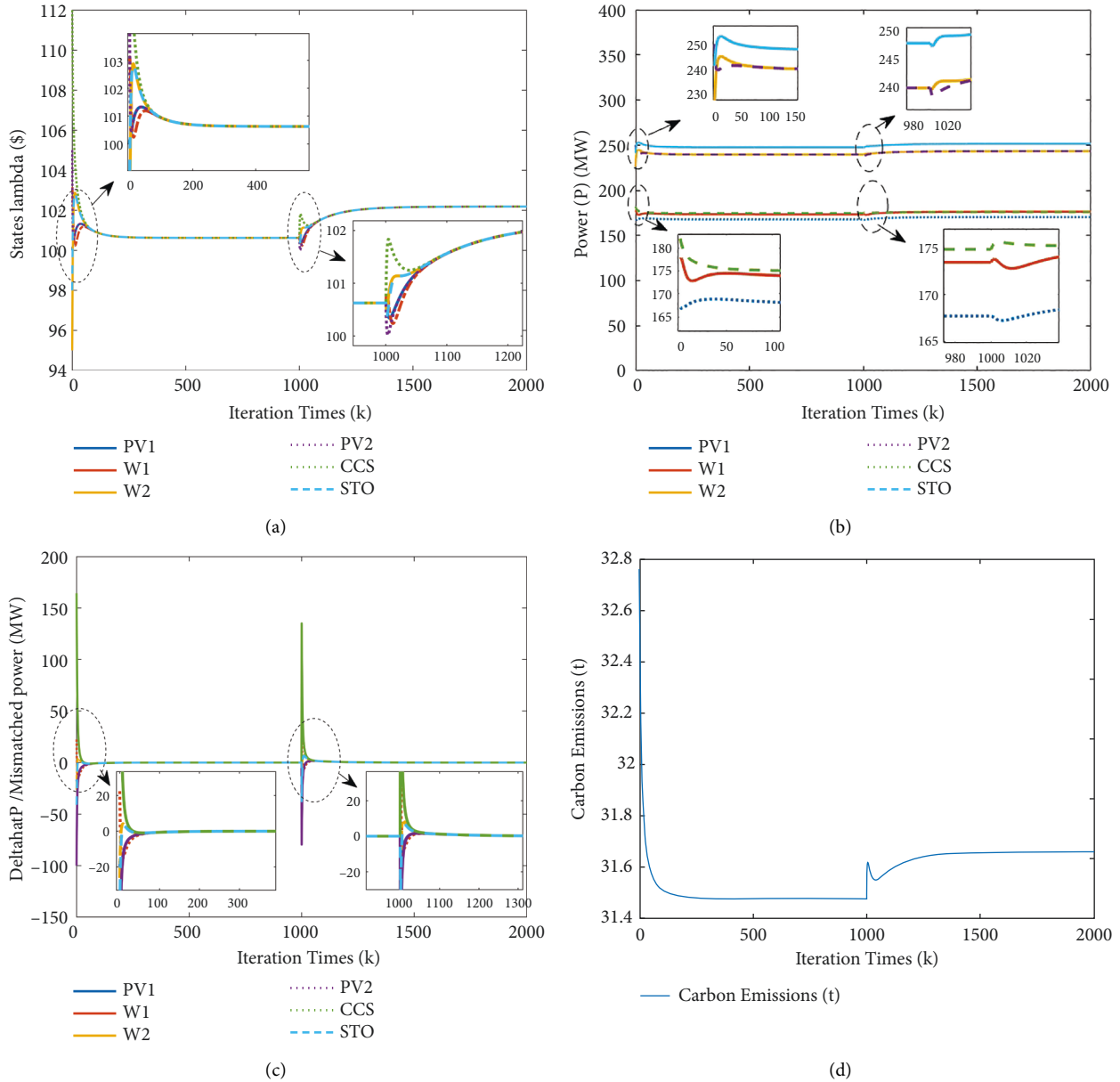


FIGURE 10: Simulation results. (a) Dynamic curve of iterative operator  $\lambda$ . (b) Dynamic curve of output power of each device. (c) Dynamic curve of power mismatch. (d) Dynamic curve of carbon emissions.

Compared with the normal operation of the port microgrid, the optimal operation cost increases by 15.7%, and the carbon emission increases by 7.7%. Although the load demand does not increase, the impact of the interruption of the energy supply device on the optimal operating cost is significant.

As can be seen from Figure 11(a), when PV1 is interrupted, it has a great influence on the iteration operator, and the value rises from 100.7 to 113.8, increasing by 13.1. When PV1 is interrupted, the output power of PV1 suddenly drops to 0, the curve of the power supply of each device fluctuates, and the remaining power supply devices are rapidly adjusted and the power supply is increased to ensure that the port microgrid can continue to operate stably. The curve of  $\lambda(k)$  has small curve fluctuation and fast convergence. The curve

of mismatched power fluctuates greatly, because at the moment of device interrupt, the power supply gap of 200 MW needs to be made up. Since PV1 is a new energy source and does not release carbon dioxide while in operation, more fossil fuels will need to be burnt to maintain the port microgrid's operation after it has been interrupted, which will increase carbon emissions. Even though the port microgrid fluctuates after interrupting, it can be promptly changed to return to stability, proving the stability of the proposed model and algorithm and further guaranteeing the reliability of the port microgrid.

To sum up, Case 1 uses a centralized algorithm to solve the energy management problem of the port microgrid; Case 2 uses a distributed algorithm to solve the energy management problem of the port microgrid without the carbon

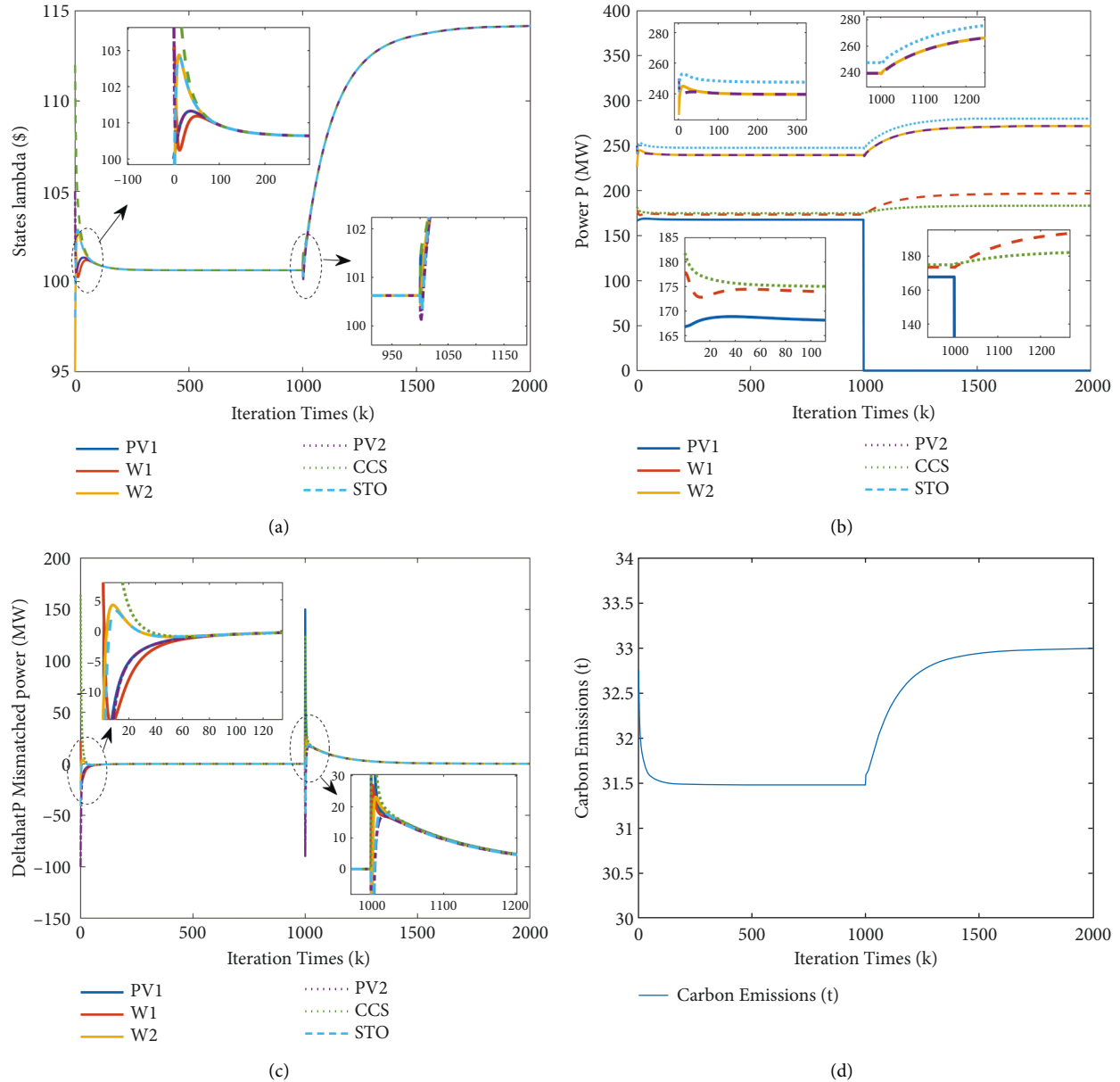


FIGURE 11: Simulation results. (a) Dynamic curve of iterative operator  $\lambda$ . (b) Dynamic curve of output power of each device. (c) Dynamic curve of power mismatch. (d) Dynamic curve of carbon emissions.

capture device; Case 3 uses a distributed algorithm to solve the energy management problem of port microgrid with carbon capture device and studies the impact of carbon trading price on the zero-carbon port microgrid; and in Case 4, the change in load demand and plug-and-play power supply devices are considered.

The error between the results obtained in Case 1 and Case 3 is less than 8%, which can further verify the accuracy and effectiveness of the algorithm mentioned in this study. However, due to the distributed characteristics of the port microgrid, the centralized algorithm is not suitable for solving the energy management problem of the port microgrid.

In Case 4, when the load demand and plug-and-play power supply devices are changed, the port microgrid is still

able to operate reliably and stably after a brief fluctuation, proving the effectiveness of the proposed algorithm.

In conclusion, the port microgrid with carbon capture power plants proposed in this study can effectively reduce carbon emissions, and the distributed energy management method in this study can accurately and quickly solve the energy management problems of zero-carbon port microgrid to ensure the economic, reliable, and stable operation of the port.

## 6. Conclusions

An energy management problem for a zero-carbon port microgrid, integrating carbon capture power plants, has been studied in this study. With carbon trading mechanisms,



an energy management model has been proposed to achieve the optimal economic operation and minimal carbon emissions of the considered port microgrid. Then, due to the distribution characteristics of the port microgrids containing a large amount of renewable energy, a distributed energy management method based on the ADMM has been raised to solve the proposed optimization problem. The simulation results have illustrated that the carbon capture plant can reduce 79.4% of carbon emissions from the port microgrid. The considered energy management problem has also been solved using a centralized algorithm with a difference of 7% with distributed optimal solutions, which has proved the accuracy and effectiveness of the proposed algorithm.

In the future, carbon dioxide captured by carbon capture could be processed and sold to improve the port economics. In addition, to further build the green port, the port will be constructed without fossil fuels for power supply, but to use renewable energy and connect with the main power grid to ensure its operation reliability.

## Nomenclature

$Q_{ccs}$ :	Mass of carbon dioxide captured
$\eta$ :	Efficiency coefficient of carbon dioxide capture
$Q_{dis}$ :	Mass of carbon dioxide emitted after fossil fuel combustion
$\gamma$ :	Mass of carbon dioxide emission per unit power
$P_{fu}$ :	Power provided by fossil fuel combustion
$P_{co}$ :	Output power of the carbon capture power plant
$P_{ccs}$ :	Total power consumed by carbon capture
$P_{ccso}$ :	Operating power consumed by carbon capture
$\tau$ :	Coefficient of power consumed by carbon treating
$F_{sto}$ :	Cost of the carbon storage device
$C_{sto}$ :	Cost coefficient of sealing carbon per unit mass
$F_{tra}$ :	Cost of carbon trading
$C_{tra}$ :	Cost coefficient of carbon trading price
$Q_q$ :	Carbon emission quota
$\phi$ :	Coefficient of carbon emission quota
$F_1, F_2, \text{ and } F_3$ :	Power generation cost, the storage cost, and the carbon cost
$F_{ccs}, F_{pv}, \text{ and } F_w$ :	Power generation cost of carbon capture power plant, photovoltaic panels, and wind turbines
$a_h, b_h, \text{ and } c_h$ :	Coefficients of the power generation cost
$P_{fu,h} \text{ and } P_{w,h}$ :	Output power of photovoltaic panels and wind turbines
$N_1, N_2, \text{ and } N_3$ :	Node sets of carbon capture power plants, photovoltaic panels, and wind turbines
$P_{s,h_4}$ :	Output power of the power storage device
$W$ :	Total node set of loads
$p^{\min}$ :	Minimum output power of each device
$p^{\max}$ :	Maximum output power of each device
$P_e$ :	Power storage capacity

$SoC_{\min}$ and $SoC_{\max}$ :	Minimum state of charge and the maximum state of charge
$L_{p,h}$ :	Total power load of the port microgrid
$F_i(P_i)$ :	Cost of the $i$ th device
$\alpha_i, \beta_i, \text{ and } \phi$ :	Equivalent transformation coefficients of the cost functions
$P_i^*$ :	Local optimal solution
$\xi_i$ :	Step size of the algorithm
$\psi(k)$ :	Feedback gain
$\Delta \hat{P}_i(k)$ :	$k$ th iteration of mismatched power
$P_i(k)$ :	Output power of the $i$ th device in $k$ th iteration.

## Data Availability

The data of this study can be obtained by contacting the corresponding author.

## Conflicts of Interest

The authors declare that they have no conflicts of interest.

## Acknowledgments

This research was supported by the Key Research Project of Zhejiang Lab (2021LE0AC02); High Level Talents Innovation Support Plan of Dalian (Young Science and Technology Star Project) (under grant no. 2021RQ058); National Natural Science Foundation of China (under grant nos. 51939001, 61976033, 61751202, 61903092, and U1813203); the Science and Technology Innovation Funds of Dalian (under grant no. 2018J11CY022); and the Liaoning Revitalization Talents Program (under grant nos. XLYC1908018 and XLYC1807046).

## References

- [1] X. Wang, W. Huang, W. Wei, N. Tai, R. Li, and Y. Huang, "Day-ahead optimal economic dispatching of integrated port energy systems considering hydrogen," *IEEE Transactions on Industry Applications*, vol. 58, no. 2, pp. 2619–2629, 2022.
- [2] A. K. Barik, S. Jaiswal, and D. C. Das, "Recent trends and development in hybrid microgrid: a review on energy resource planning and control," *International Journal of Sustainable Energy*, vol. 41, no. 4, pp. 308–322, 2021.
- [3] Y. Wu and J. Dong, "Local stabilization of continuous-time T-S fuzzy systems with partly measurable premise variables and time-varying delay," *IEEE Transactions on Systems, Man, and Cybernetics: Systems*, vol. 51, no. 1, pp. 326–338, 2021.
- [4] A. De, A. Choudhary, and M. K. Tiwari, "Multiobjective approach for sustainable ship routing and scheduling with draft restrictions," *IEEE Transactions on Engineering Management*, vol. 66, no. 1, pp. 35–51, 2019.
- [5] F. D. Kanellos, E. S. M. Volanis, and N. D. Hatziaargyriou, "Power management method for large ports with multi-agent systems," *IEEE Transactions on Smart Grid*, vol. 10, no. 2, pp. 1259–1268, 2019.
- [6] G. Parise, L. Parise, L. Martirano, P. Ben Chavdarian, S. Chun-Lien, and A. Ferrante, "Wise port and business energy management: port facilities, electrical power distribution,"

- IEEE Transactions on Industry Applications*, vol. 52, no. 1, pp. 18–24, 2016.
- [7] M. Kermani, G. Parise, E. Shirdare, and L. Martirano, “Transactive energy solution in a port’s microgrid based on blockchain technology,” in *Proceedings of the 2020 IEEE International Conference on Environment and Electrical Engineering and 2020 IEEE Industrial and Commercial Power Systems Europe*, Madrid, Spain, June 2020.
  - [8] T. Wu, X. Wei, X. Zhang, G. Wang, J. Qiu, and S. Xia, “Carbon-oriented expansion planning of integrated electricity-natural gas systems with EV fast-charging stations,” *IEEE Transactions on Transportation Electrification*, vol. 8, no. 2, pp. 2797–2809, 2022.
  - [9] T. Conlon, M. Waite, Y. Wu, and V. Modi, “Assessing trade-offs among electrification and grid decarbonization in a clean energy transition: application to New York State,” *Energy*, vol. 249, Article ID 123787, 2022.
  - [10] Y. Fu, G. Huang, L. Liu, and M. Zhai, “A factorial CGE model for analyzing the impacts of stepped carbon tax on Chinese economy and carbon emission,” *Science of the Total Environment*, vol. 759, Article ID 143512, 2021.
  - [11] Y. Zheng, Y. Song, D. J. Hill, and Y. Zhang, “Multiagent system based microgrid energy management via asynchronous consensus ADMM,” *IEEE Transactions on Energy Conversion*, vol. 33, no. 2, pp. 886–888, 2018.
  - [12] D. Bo, D. Kangcheng, C. Guang, C. Huiyun, and Y. Hongying, “Carbon emission management system of port logistics based on internet of things technology,” *Agro Food Industry Hi-Tech*, vol. 28, no. 1, pp. 1094–1098, 2017.
  - [13] X. Li, H. Kuang, and Y. Hu, “Using system dynamics and game model to estimate optimal subsidy in shore power technology,” *IEEE Access*, vol. 8, pp. 116310–116320, 2020.
  - [14] A. De, J. Wang, and M. K. Tiwari, “Fuel bunker management strategies within sustainable container shipping operation considering disruption and recovery policies,” *IEEE Transactions on Engineering Management*, vol. 68, no. 4, pp. 1089–1111, 2021.
  - [15] F. D. Kanellos, “Multiagent-system-based operation scheduling of large ports’ power systems with emissions limitation,” *IEEE Systems Journal*, vol. 13, no. 2, pp. 1831–1840, 2019.
  - [16] Y. Li, W. Gao, W. Yan et al., “Data-driven optimal control strategy for virtual synchronous generator via deep reinforcement learning approach,” *Journal of Modern Power Systems and Clean Energy*, vol. 9, no. 4, pp. 919–929, 2021.
  - [17] Y. Wu, V. K. N. Lau, D. H. K. Tsang, L. P. Qian, and L. Meng, “Optimal energy scheduling for residential smart grid with centralized renewable energy source,” *IEEE Systems Journal*, vol. 8, no. 2, pp. 562–576, 2014.
  - [18] D. Olivares, C. Cañizares, and M. Kazerani, “A centralized optimal energy management system for microgrids,” in *Proceedings of the 2011 IEEE Power and Energy Society General Meeting*, Detroit, MI, USA, July 2011.
  - [19] B. Sahoo, S. K. Routray, and P. K. Rout, “A novel centralized energy management approach for power quality improvement,” *International Transactions on Electrical Energy Systems*, vol. 31, no. 10, Article ID 12582, 2021.
  - [20] Y. Long, Y. Li, Y. Wang et al., “Low-carbon economic dispatch considering integrated demand response and multistep carbon trading for multi-energy microgrid,” *Scientific Reports*, vol. 12, no. 1, 2022.
  - [21] Y. Li, H. Zhang, X. Liang, and B. Huang, “Event-triggered based distributed cooperative energy management for multienergy systems,” *IEEE Transactions on Industrial Informatics*, vol. 15, no. 4, pp. 2008–2022, 2019.
  - [22] W. Rui, S. Qiuye, M. Dazhong, and H. Xuguang, “Line impedance cooperative stability region identification method for grid-tied inverters under weak grids,” *IEEE Transactions on Smart Grid*, vol. 11, no. 4, pp. 2856–2866, 2020.
  - [23] Y. Li, D. W. Gao, W. Gao, H. Zhang, and J. Zhou, “A distributed double-Newton descent algorithm for cooperative energy management of multiple energy bodies in energy internet,” *IEEE Transactions on Industrial Informatics*, vol. 17, no. 9, pp. 5993–6003, 2021.
  - [24] Y. Li, D. W. Gao, W. Gao, H. Zhang, and J. Zhou, “Double-mode energy management for multi-energy system via distributed dynamic event-triggered Newton-Raphson algorithm,” *IEEE Transactions on Smart Grid*, vol. 11, no. 6, pp. 5339–5356, 2020.
  - [25] S. G. Gennitsaris and F. D. Kanellos, “Emission-aware and cost-effective distributed demand response system for extensively electrified large ports,” *IEEE Transactions on Power Systems*, vol. 34, no. 6, pp. 4341–4351, 2019.
  - [26] Q. Li, D. W. Gao, H. Zhang, Z. Wu, and F. Y. Wang, “Consensus-based distributed economic dispatch control method in power systems,” *IEEE Transactions on Smart Grid*, vol. 10, no. 1, pp. 941–954, 2019.
  - [27] W. Du, L. Yao, D. Wu, L. Xinrong, L. Guodong, and Y. Tao, “Accelerated distributed energy management for microgrids,” in *Proceedings of the 2018 IEEE Power & Energy Society General Meeting (PESGM)*, Portland, OR, USA, August 2018.
  - [28] W. Shi, X. Xie, C. C. Chu, and R. Gadh, “Distributed optimal energy management in microgrids,” *IEEE Transactions on Smart Grid*, vol. 6, no. 3, pp. 1137–1146, 2015.
  - [29] Y. Liu, H. Beng Gooi, and H. Xin, “Distributed energy management for the multi-microgrid system based on ADMM,” in *Proceedings of the 2017 IEEE Power & Energy Society General Meeting*, Chicago, IL, USA, July 2017.
  - [30] Q. Chen, C. Kang, and Q. Xia, “Operation mechanism and peak-load shaving effects of carbon-capture power plant,” in *Proceedings of the Chinese Society for Electrical Engineering*, March 2010.
  - [31] Y. Cui, P. Zeng, Z. Wang, M. Wang, J. Zhang, and Y. Zhao, “Multiple time scales scheduling strategy of wind power accommodation considering energy transfer characteristics of carbon capture power plant,” in *Proceedings of the Chinese Society for Electrical Engineering*, vol. 41, no. 3, pp. 946–960, 2021.
  - [32] F. Tian, Y. Jia, H. Ren, Y. Bai, and T. Huang, “Source-load” low-carbon economic dispatch of integrated energy system considering carbon capture system,” *Power System Technology*, vol. 44, no. 9, pp. 3346–3354, 2020.
  - [33] F. Teng, Q. Shan, and T. Li, “Intelligent ship integrated energy system and its distributed optimal scheduling algorithm,” *Acta Automatica Sinica*, vol. 46, no. 9, pp. 1809–1817, 2020.
  - [34] H. Zhang, Y. Li, D. W. Gao, and J. Zhou, “Distributed optimal energy management for energy internet,” *IEEE Transactions on Industrial Informatics*, vol. 13, no. 6, pp. 3081–3097, 2017.
  - [35] W. Chen and T. Li, “Distributed economic dispatch for energy internet based on multi agent consensus control,” *IEEE Transactions on Automatic Control*, vol. 66, no. 1, pp. 137–152, 2021.

## Research Article

# A Novel Short-Term Power Load Forecasting Method Based on TSNE-EEMD-LSTM

Mingkun Jiang,<sup>1,2</sup> He Jiang ,<sup>1,2</sup> Yan Zhao ,<sup>1,2</sup> Chenjia Hu,<sup>1,2</sup> and Jian Xu<sup>1,2</sup>

<sup>1</sup>School of Renewable Energy, Shenyang Institute of Engineering, Shenyang 110136, China

<sup>2</sup>Key Laboratory of Regional Multi-energy System Integration and Control of Liaoning Province, Shenyang 110136, China

Correspondence should be addressed to He Jiang; [jianghescholar@163.com](mailto:jianghescholar@163.com)

Received 29 March 2022; Revised 18 May 2022; Accepted 24 May 2022; Published 6 July 2022

Academic Editor: Qiuye Sun

Copyright © 2022 Mingkun Jiang et al. This is an open access article distributed under the Creative Commons Attribution License, which permits unrestricted use, distribution, and reproduction in any medium, provided the original work is properly cited.

In this paper, a novel power load forecasting model is proposed to fully extract the periodic characteristics of short-term load at various time scales and explore the potential correlations between influencing factors and characteristics of load components. Firstly, the t-distributed stochastic neighbor embedding algorithm is used to map sample points of high-dimensional load influencing factors to low-dimensional space, and the ensemble empirical mode decomposition algorithm is employed to split the historical load curve into multiple signal components with different frequencies. Then, several long short-term memory networks including nonlinear mapping and time series models are established to mine the relationship between low-dimensional comprehensive influencing factors and each intrinsic mode function component by utilizing different inputs. Finally, the effectiveness of the hybrid model is verified via using the short-term load dataset of 3-hour data granularity in a certain region, and the influence of key parameters of the model on the forecasting effect is discussed.

## 1. Introduction

Load forecasting in short term is one of the important daily tasks in the contemporary power system. The unit output plan and economic dispatch strategy based on good forecasting results can improve the operation stability and economy of the system to a certain extent. Because the short-term load is influenced by succession uncertain factors, the model can be expressed as the sum of nonlinear mapping relationships between short-term load and related influencing factors and a series of uncertain random loads.

Up to now, there have been some state-of-the-art works to explore the ways to enhance the accuracy of load forecasting from the aspect of uncertain random loads. Reference [1] used user behavior to reflect the fluctuation of some uncertain loads, used smart meters to extract user-level data, analyzed the similarity of user behavior, and introduced them into the forecasting model. Reference [2] proposed a multistep forecasting model containing three channels (load, time, and user behavior). The user behavior type was identified by combining convolution automatic encoder and

k-means, and it was used as a feature to combine with the feature information obtained by the other two channels for the comprehensive forecasting of short-term power load. Most of the existing user behavior feature extraction starts from the similarity of user energy consumption curve, classifies and forecasts users. However, the user's energy consumption law itself has strong randomness, and the error generated by the classification will be transmitted to the final forecasting results through the forecasting model, resulting in the instability of the model in practical application.

At present, mainstream load forecasting research still focuses on how to better and more comprehensively excavate the nonlinear mapping relationship between load and its influencing factors. This kind of research mainly adopts machine learning modeling methods [3–5]. Reference [6] used the Bat algorithm and Kalman filtering method to optimize the support vector machine (SVM) and combined the fuzzy combination weight and empirical mode decomposition to forecast the load in short term. Reference [7] established a combination forecasting model including SVM and generalized regression model and used the weight

determination theory to determine the final forecasting results. In Reference [8], the daily load curve was clustered, and a step-wise compound forecasting model was constructed based on a convolutional neural network (CNN) and long short-term memory (LSTM) neural network [8]. Reference [9] utilized a CNN to construct a deep learning model and carried out load forecasting for users with similar energy consumption. Under the comprehensive influence of many influencing factors, short-term power load still has certain periodic characteristics, and the aforementioned research methods to extract the periodic characteristics of load by influencing factors inevitably lead to incomplete feature extraction.

To solve this problem, empirical mode decomposition (EMD) [10–12] was introduced into load forecasting models. EMD can decompose the complex load curve into multiple intrinsic mode functions (IMFs) [10] with various frequencies and amplitudes and sole residual signal. In such studies, each sub-signal was often used for multiple modeling via the same forecasting model, such as the state-dependent autoregressive model [10] and CNN-LSTM model [11], ignoring the characteristics of each sub-signal. Appropriate and different ways of load modeling according to the characteristics of different IMFs can undoubtedly better and more comprehensively extract the load characteristics.

In this paper, a novel hybrid model for load forecasting in short term is proposed on the basis of previous studies. First, with the help of the time series memory capacity, the LSTM [13] model is divided into two categories by different model inputs, and different IMFs are modeled in an appropriate way to excavate the potential information of various IMFs. Second, the ensemble empirical mode decomposition (EEMD) [14] is applied to split the load signal, so as to overcome the mode mixing phenomenon that is easy to occur in the EMD and avoid its adverse impact on the forecasting effect. The nondestructive dimension reduction of power load influencing factors is carried out by t-distributed stochastic neighbor embedding (TSNE) [15], which reduces the amount of model calculation and the redundant features extracted from the model. Third, several LSTM models in two types that have different inputs are established by using the data obtained by TSNE and EEMD. This study introduces the algorithms used in the proposed hybrid model, and gradually elaborates the structure and construction process of the model. Finally, two key parameters of the model are discussed through examples and experiments, and the forecasting performance of the model is verified. As a result, the main contributions and highlights can be summarized as follows:

- (1) The EEMD algorithm is employed to decompose the power load curve into load components with different time-scale characteristics, and the appropriate modeling is carried out according to the characteristics of different components, which provides a new application form for the time series decomposition of load.
- (2) The nondestructive dimension reduction of power load influencing factors is realized through TSNE,

which solves the problems of long training time of hybrid model composed of multiple sub-models.

- (3) This paper provides a new short-term load forecasting scheme, which can also be applied to the forecasting fields of new energy generation and integrated loads.

## 2. Data Processing and Basic Forecasting Model

*2.1. Decomposition of Load Curve Based on EEMD.* EMD and EEMD belong to nonlinear signal decomposition algorithms, which decompose a nonstationary time series signal into several groups of IMFs with frequency from high to low and a group of residual signals representing the overall trend of the original signal. For the power load signal, the IMFs components of different frequencies contain the periodic characteristics of power load at different time scales. With the decrease of IMFs component frequency, the low-frequency component represented by the residual signal contains the load trend of power load for a time.

Due to this phenomenon of missing data and abnormal data in the acquisition process of power load data, this phenomenon may lead to the discontinuity of the original load signal or the existence of signal step-change on the time scale, which makes such data prone to modal aliasing when using EMD for signal decomposition. Modal aliasing refers to the characteristic signal that an IMF component contains different time scales at the same time [14], which affects the signal decomposition effect and load modeling. As an improved method of EMD, based on EMD, EEMD adds the process of adding white noise to the signal many times and calculating the mean value of each sub-signal, which can avoid the occurrence of modal aliasing.

The steps of EEMD signal splitting are as follows:

- (1) Set the number of adding white noise:  $M$ .
- (2) Add normal distribution white noise to the historical load curve to constitute the signal  $f_{i,j}$ ,  $i \in [1, M]$  and  $j \in [1, N]$ ,  $N$  denotes the number of sub-signals obtained by decomposition after step (5).
- (3) Find out all the local maximum and minimum values contained in the signal, and fit the envelope curves with the maximum and minimum points, respectively.
- (4) The mean curve  $g_{i,j}$  constructed by two envelope curves is obtained, and the difference  $h_{i,j}$  between the signal  $f_{i,j}$  and the curve  $g_{i,j}$  is obtained. The mean curve  $g_{i,j}$  will participate in the next iteration, and  $f_{i,j+1} = g_{i,j}$ .
- (5) Repeat steps (3) and (4) until the difference between signal  $f_{i,j}$  and curve  $g_{i,j}$  is small enough, that is, the signal  $f_{i,j}$  cannot be decomposed again. At this time, the quantity of  $h_{i,j}$  obtained by decomposition is  $N$ .
- (6) Repeat steps (2) to (5) until the original signal is processed  $M$  times by white noise and decomposed. At this time, the mean of all  $h_{i,j}$  is obtained by calculating the  $M$  times signal decomposition,

namely, the signal components obtained by EEMD. The calculation formula is given by

$$I_j = \frac{1}{M} \sum_{i=1}^M h_{i,j}, \quad (1)$$

where  $I_j$  is each component of the original load signal obtained by EEMD, and each component satisfies

$$f = \sum_{j=1}^N I_j, \quad (2)$$

where  $f$  is the original power load signal,  $I_1, I_2, \dots, I_{N-1}$  are the IMF components, and  $I_N$  is the residual.

**2.2. Dimension Reduction of Influencing Factors Based on TSNE.** TSNE algorithm is improved from stochastic neighbor embedding (SNE). SNE deems that the distance between corresponding points in original dimension and converted dimension is also similar, and conditional probability is used to represent the similarity of this distance relationship [15].

In SNE algorithm, for the data points  $X_\alpha$  and  $X_\beta$  of the influencing factors of power load in any high-dimensional space, the probability of  $X_\beta$  as the proximity point of  $X_\alpha$  is set to be  $P_{\beta|\alpha}$ . After mapping to the low-dimensional space, the probability of low-dimensional mapping point  $x_\beta$  as the proximity point of  $x_\alpha$  is set to be  $Q_{\beta|\alpha}$ , and the calculation formulas of  $P_{\beta|\alpha}$  and  $Q_{\beta|\alpha}$  are expressed as

$$P_{\beta|\alpha} = \frac{\exp\left[-(2\delta_\alpha^2)^{-1}\|X_\alpha - X_\beta\|^2\right]}{\sum_{k \neq \alpha} \exp\left[-(2\delta_\alpha^2)^{-1}\|X_\alpha - X_k\|^2\right]}, \quad (3)$$

$$Q_{\beta|\alpha} = \frac{\exp\left[-\|x_\alpha - x_\beta\|^2\right]}{\sum_{k \neq \alpha} \exp\left[-\|x_\alpha - x_k\|^2\right]}, \quad (4)$$

where  $\delta_\alpha$  is the standard deviation of Gaussian distribution with  $X_\alpha$  as the center point,  $X_k$  and  $x_k$  are the arbitrary initial data points in original dimension and mapping points in converted dimension, respectively.

The cost function  $C$  is constructed and defined as

$$C = \sum_{\alpha} \sum_{\beta} P_{\beta|\alpha} \log \frac{P_{\beta|\alpha}}{Q_{\beta|\alpha}}. \quad (5)$$

At this time, the data dimension reduction problem is transformed into an optimal problem. Through iterative calculation, when the cost function  $C$  takes the minimum value, the optimal solution of the mapping point of original dimension samples in converted dimension can be obtained. The iterative process is given by

$$x^r = x^{r-1} + \eta \frac{\partial C}{\partial x} + \varepsilon(r)(x^{r-1} - x^{r-2}), \quad (6)$$

where  $x^r$  represents the sample points in lower dimension obtained in iteration  $r$ ,  $r$  denotes the number of iterations,  $\eta$  is the learning rate,  $\varepsilon(r)$  is the learning momentum in iteration  $r$ ,  $\partial C/\partial x$  is the gradient vector, and the gradient  $\partial C/\partial x_\alpha$  at point  $x_\alpha$  is written as

$$\frac{\partial C}{\partial x_\alpha} = 2 \sum_{\beta} (P_{\beta|\alpha} - Q_{\beta|\alpha} + P_{\alpha|\beta} - Q_{\alpha|\beta})(x_\alpha - x_\beta). \quad (7)$$

In the SNE algorithm, the samples in both the original dimension and converted dimension use Gaussian distribution to represent the similarity between data, which will lead to the inconvenience of data congestion in the converted dimension, which is laborious to distinguish [16], and increase the difficulty of model feature extraction. In addition, the probability of data points calculated by the SNE algorithm in original dimension and converted dimension is asymmetric and the calculation of gradient is complex.

Given these limitations of the aforementioned SNE algorithm, the TSNE algorithm has made the following improvements based on SNE:

- (1) In the TSNE algorithm, the symmetric SNE method is applied to calculate the probability of samples in original dimension and simplify the calculation of gradient formula. The probability of samples  $P_{\beta|\alpha}$  and the joint probability density of data points  $P_{\alpha\beta}$  in original dimension can be expressed as

$$P_{\beta|\alpha} = \frac{\exp\left[-(2\delta_\alpha^2)^{-1}\|X_\alpha - X_\beta\|^2\right]}{\sum_{k \neq \alpha} \exp\left[-(2\delta_\alpha^2)^{-1}\|X_\alpha - X_k\|^2\right]}, \quad (8)$$

$$P_{\alpha\beta} = \frac{P_{\alpha|\beta} + P_{\beta|\alpha}}{2n}, \quad (9)$$

where  $n$  is the number of data points of high-dimensional space load influencing factors.

- (2) In SNE, Gaussian distribution is used to represent the similarity between sample points in space with different dimensions, while TSNE improves the Gaussian distribution in converted dimension to t-distribution, which reduces the inconvenience of data crowded and difficulty in distinguishing after dimension reduction. So far, the joint probability density of low-dimensional space samples  $Q_{\alpha\beta}$  can be defined as

$$Q_{\alpha\beta} = \frac{\left(1 + \|x_\alpha - x_\beta\|^2\right)^{-1}}{\sum_{k \neq l} \left(1 + \|x_k - x_l\|^2\right)^{-1}}, \quad (10)$$

where  $x_k$  and  $x_l$  are the mapping points of any low-dimensional space samples, respectively.



TSNE algorithm uses joint probability density to replace conditional probability in the SNE algorithm. For any joint probability density between samples, there are  $P_{\alpha\beta} = P_{\beta\alpha}$  and  $Q_{\alpha\beta} = Q_{\beta\alpha}$ . The improved cost function  $C$  and gradient  $\partial C/\partial x_\alpha$  can be written as

$$C = \sum_{\alpha} \sum_{\beta} P_{\alpha\beta} \log \frac{P_{\alpha\beta}}{Q_{\alpha\beta}}, \quad (11)$$

$$\frac{\partial C}{\partial x_\alpha} = 4 \sum_{\beta} (P_{\alpha\beta} - Q_{\alpha\beta}) (x_\alpha - x_\beta) \left(1 + \|x_\alpha - x_\beta\|^2\right)^{-1}. \quad (12)$$

Finally, the TSNE algorithm uses (6) to continuously iteratively obtain the optimal solution of mapping points in low-dimensional space.

**2.3. LSTM Neurons.** LSTM is an improved recurrent neural network (RNN) published by Hochreiter and Schmidhuber [13], which overcomes the difficulty of training RNN in practical applications. LSTM neural network has a strong storage capacity of time series features and has strong adaptability in feature extraction of data with such properties. LSTM unit can be divided into input subunit, output subunit, forgetting subunit, and alternative cell state, and their respective states are expressed as

$$D^t = \tanh(W_D X_{\text{lstm}}^t + U_D H_{\text{lstm}}^{t-1} + b_D), \quad (13)$$

$$I^t = \sigma(W_I X_{\text{lstm}}^t + U_I H_{\text{lstm}}^{t-1} + b_I), \quad (14)$$

$$O^t = \sigma(W_O X_{\text{lstm}}^t + U_O H_{\text{lstm}}^{t-1} + b_O), \quad (15)$$

$$F^t = \sigma(W_F X_{\text{lstm}}^t + U_F H_{\text{lstm}}^{t-1} + b_F) \quad (16)$$

where  $D^t$  is the alternative cell state at  $t$  moments,  $\tanh$  is the hyperbolic tangent activation function,  $W_D$  and  $U_D$  are the weights assigned to  $X_{\text{lstm}}^t$  and  $H_{\text{lstm}}^{t-1}$  in the calculation of the alternative cell state,  $X_{\text{lstm}}^t$  is the input of this unit at  $t$  moments,  $H_{\text{lstm}}^{t-1}$  is the output of this unit at  $t-1$  moments,  $t$  represents time,  $b_D$  is a bias term for alternative cell state,  $I^t$ ,  $O^t$  and  $F^t$  are the gating coefficients of the input subunit, output subunit, and forgetting subunit,  $\sigma$  is the Sigmoid function,  $W_I$ ,  $W_O$  and  $W_F$  are the weights assigned to  $X_{\text{lstm}}^t$  in the three subunits.  $U_I$ ,  $U_O$  and  $U_F$  are the weights assigned to  $H_{\text{lstm}}^{t-1}$  in the three subunits, and  $b_I$ ,  $b_O$  and  $b_F$  are the bias terms of the three subunits.

Thus, the weight value and bias value of each door control the size of the corresponding gating coefficient. The gating coefficient of the input subunit is applied to control how much information in the alternative cell state can be written in the updated cell state, and the gating coefficient of the forgetting subunit is utilized to restrict how much information from the previous cell state can be inherited to updated cell state. The state of the cell of this LSTM unit at  $t$  moments can be written as

$$C^t = I^t D^t + F^t C^{t-1}, \quad (17)$$

where  $C^t$  and  $C^{t-1}$  are the states of this cell at  $t$  moments and  $t-1$  moments, respectively.

Similarly, the function of the LSTM unit output gating coefficient is to control how many cells state information activated by activation function can be output from this unit, so the output of a single LSTM unit is given by

$$H_{\text{lstm}}^t = O^t \times \tanh(C^t), \quad (18)$$

where  $H_{\text{lstm}}^t$  is the output data of this unit at  $t$  moments.

LSTM network is composed of multiple memory units and even multi-layer LSTM unit layers. In the training, the weight value and bias value of all LSTM units are determined by iteration with the minimum loss function as the goal. At this time, the input-output mapping relationship of the whole network can represent the nonlinear connection between influencing ingredients and power load or the time series tendency from the historical load.

### 3. Hybrid Model Based on TSNE-EEMD-LSTM

According to the aforementioned introduction, the TSNE-EEMD-LSTM model proposed in this paper includes power load decomposition, influence factor dimension reduction, and load forecasting combination modeling. The proposed model structure is shown in Figure 1.

In step 1 of Figure 1, the influence factors dimension reduction based on TSNE algorithm and load signal decomposition based on EEMD algorithm are described, respectively.

There are six types of power load influencing factors in the original dataset, including time, temperature, pressure, humidity, wind speed, and precipitation. These influencing factors together constitute a high-dimensional sample space, and these points in the original dimension are reduced to a lower dimension by TSNE algorithm. It is assumed that the number of the target dimension is  $S$ , and the projection of sample points in  $S$ -dimensional space on each coordinate system is the value of each comprehensive influencing factor.

When the value of  $S$  is 2 or 3, the data after dimension reduction can be visually represented, which is convenient for intuitive analysis of the distribution relationship of points in lower dimension. The visualization effect is shown in Figure 2 and Figure 3. The mapping points in the low-dimensional space still maintain good dispersion after the dimension reduction of the power load influencing factor data by the TSNE algorithm.

According to relevant conclusions in reference [14], some essential parameters in EEMD are set as follows:

- (1) The standard deviation of white noises amplitude added to the original data is 0.2 times that of them.
- (2) The number of adding white noise  $M$  is set to 200.

The results of signal decomposition of power load application EEMD are shown in Figure 4.

Each IMF component has different frequencies and characteristics. The IMF1 component has the largest



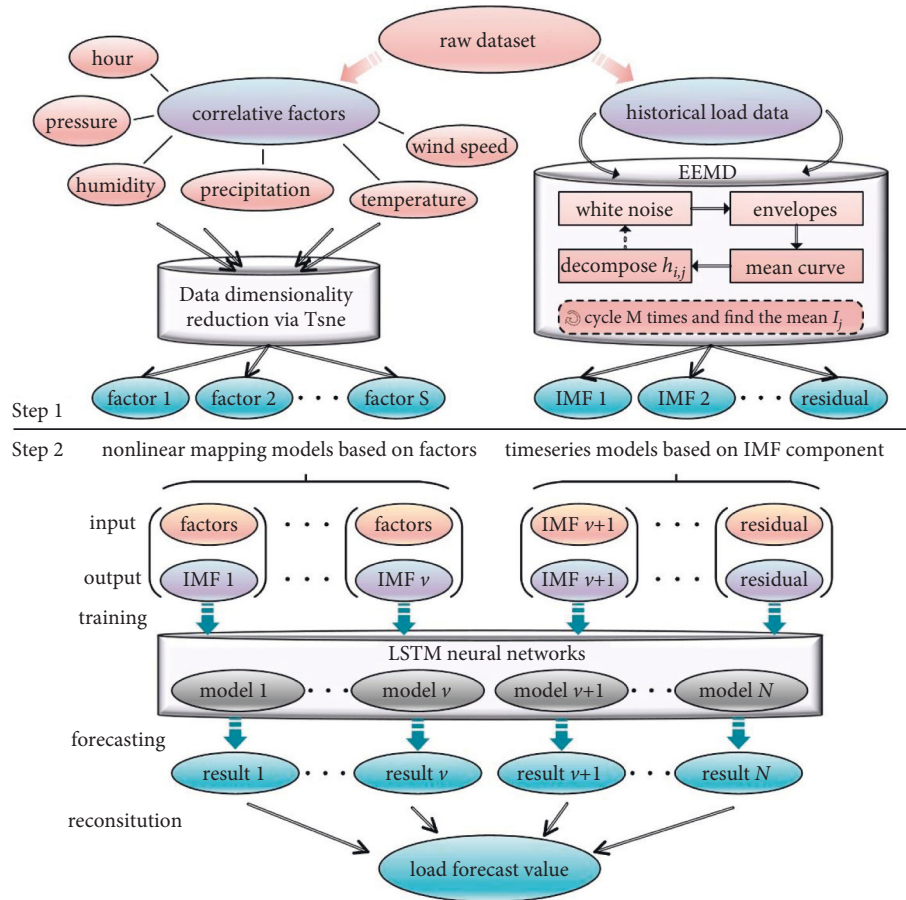


FIGURE 1: TSNE-EEMD-LSTM model.

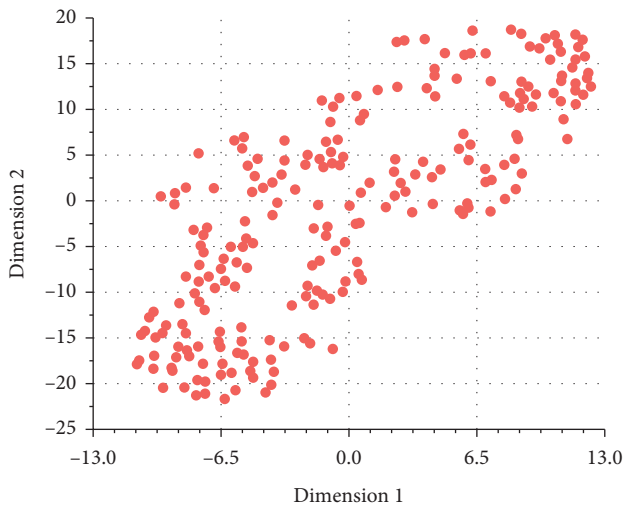


FIGURE 2: 2D spatial mapping points.

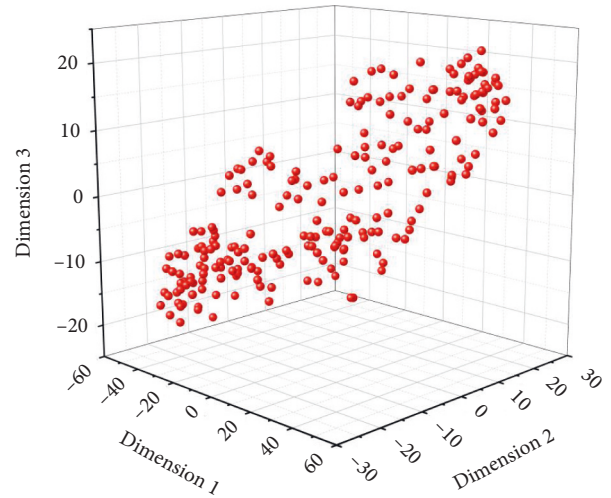


FIGURE 3: 3D spatial mapping points.

variation frequency and changes dramatically with the change of each sample number in the original data, which contains the load characteristics of the minimum particle size. The period of the IMF2 component is almost the same as the original signal, and the change of each extreme point has a similar trend with the peak and valley value of the original signal, which indicates that the IMF2 component

may contain characteristic information related to the peak and valley value of daily load. The frequency of the IMF3 component to the IMF6 component decreases gradually; these signals may contain several days, a week, or longer load periodic characteristics.

In step 2 of Figure 1,  $N$  forecasting models based on LSTM are established. Figure 4 shows that the original load

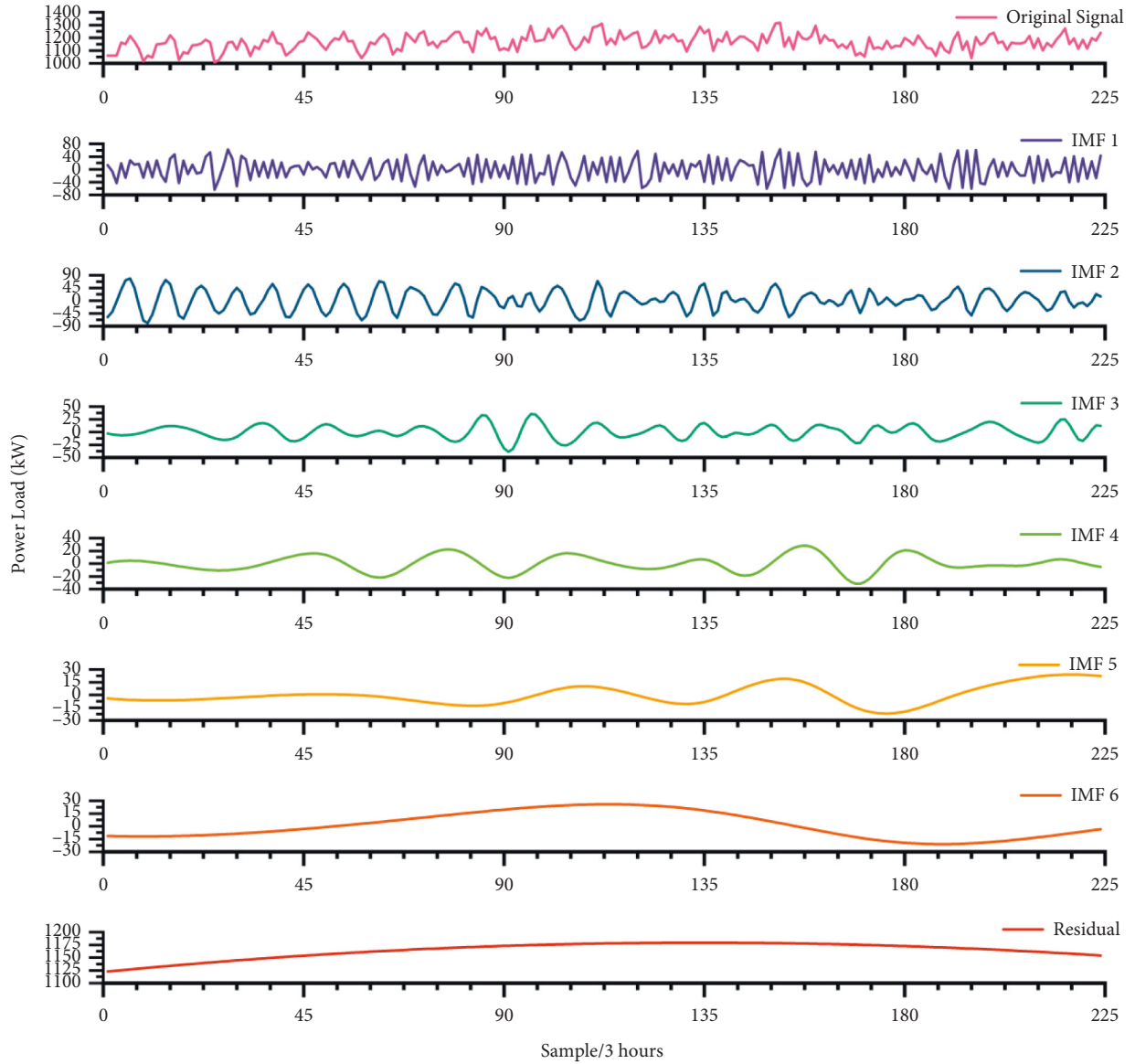


FIGURE 4: Original load signal and each IMF component.

signal is decomposed into six IMF components and one residual signal, so  $N = 7$ . The established seven models can be divided into two categories. One is the nonlinear mapping model based on the influencing factors, which is applied to explore the nonlinear connection between the influencing ingredients and corresponding load component data. The other is the time series model to explore the time series trend of certain load component curves on the basis of itself.

The nonlinear mapping model takes the comprehensive influencing factors of power load in low-dimensional space as the input of the model, and each IMF component or residual signal as the output of the model. Assuming that the target dimension of the TSNE algorithm is  $S$ , the data of comprehensive influencing factors in low-dimensional space is  $[A_1, A_2, \dots, A_S]$ , and then the output data of LSTM network participating in model supervised learning at  $\tau$

moments is  $y^\tau$ , the corresponding input data of LSTM network is  $[A_1^\tau, A_2^\tau, \dots, A_S^\tau]^T$ .

Time series model, the input or output of the model is the same IMF component or residual signal sequence. If the output data of a LSTM network participating in model supervised learning at  $\tau$  moments is  $y^\tau$ , the corresponding input data of the LSTM network is  $[y^{\tau-8}, y^{\tau-7}, \dots, y^{\tau-1}]^T$ .

When applying to forecast, the execution process is shown in Figure 5. Trained models include  $\nu$  nonlinear mapping models and  $N - \nu$  time series models. Firstly, TSNE is used to reduce the data dimension of the power load influencing factors needed in the forecasting day, and the data points of the influencing factors in original dimension are mapped to the lower dimension. Then, influencing mapping factors in converted dimension are input into trained  $\nu$  nonlinear mapping models, and the historical data

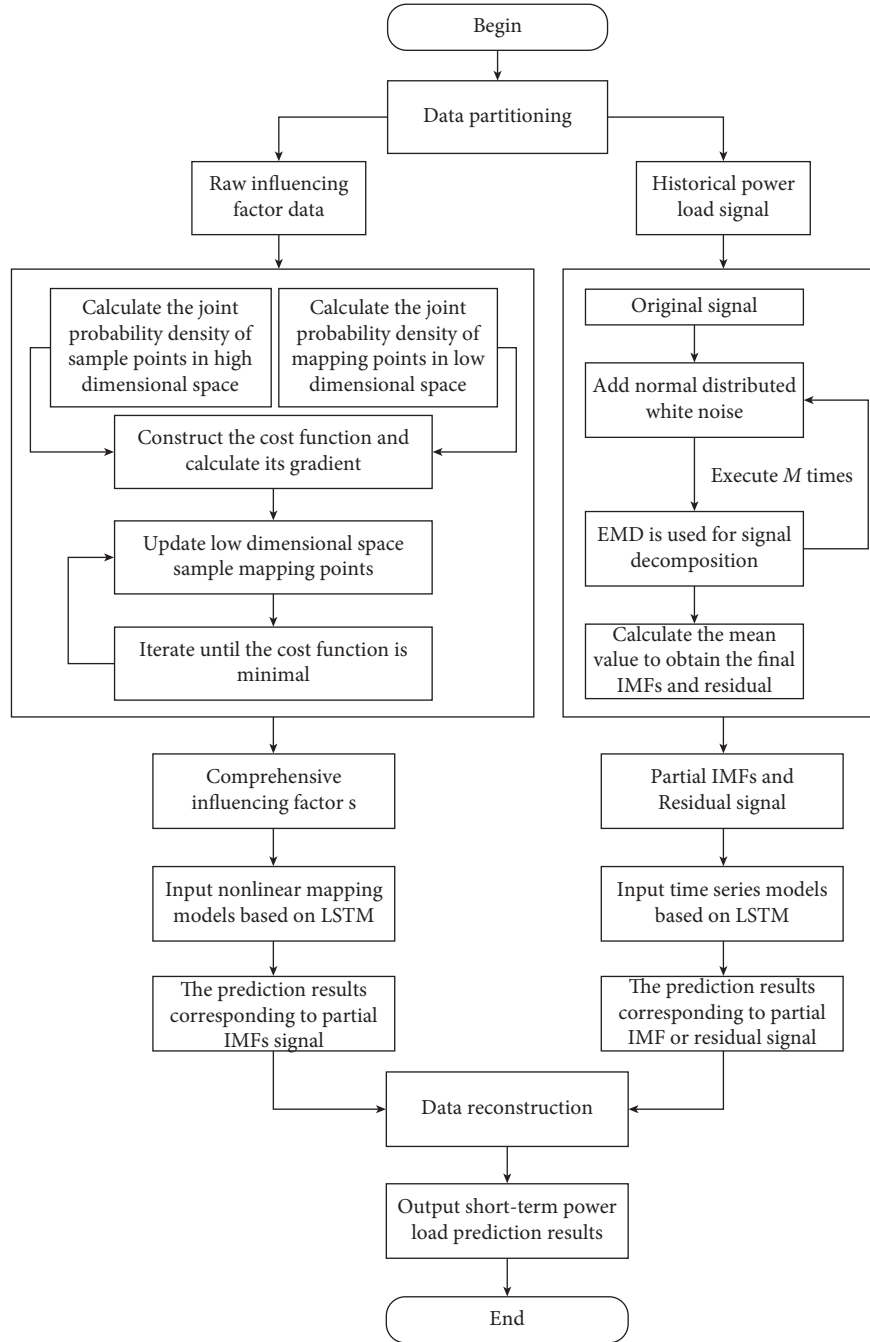


FIGURE 5: Forecasting process of the hybrid model.

of IMF components or residual signals corresponding to the models are input to  $N - \nu$  time series models. Finally, a total of  $N$  model outputs are obtained, and the  $N$  model outputs are reconstructed according to Equation (2) to get the final forecasting results.

#### 4. Experimental Verification and Discussion

In this section, the essential parameters of the model are discussed and the forecasting performance of the combined model is testified by using datasets including the 31-day 3-hour granular load data of a city and the corresponding time

temperature, pressure, and other six kinds of power load influencing factors data.

*4.1. Discussion on Key Parameters of Model.* Selecting appropriate parameters is advantageous to enhance the forecasting effect of the proposed model. This part will discuss the influence of low EEMD parameter  $S$  and the number  $\nu$  of nonlinear mapping models based on LSTM on the forecasting efficiency of the model.

Different  $S$  will affect the calculation and forecasting speed of the nonlinear mapping model. To verify this

hypothesis, six IMFs and one residual signal gained via EEMD are used as the output of supervised learning models to establish seven nonlinear mapping models, and then the average total time required to complete the training and forecasting of these seven models is counted when  $S$  takes different values. In Figure 6, there is a tendency that when the input dimension of the model decreases, the total time required to complete the model training and forecasting is shorter. That is, the forecasting speed of the model increases with the decrease of  $S$ .

The forecasting speed of the model can be improved by mapping the influencing factors of power load to the low-dimensional space for model building. However, the data gained via TSNE have similar distribution relations in different dimensions. When the target dimension is too low, the projection process of raw data in lower dimension will become difficult, and even the phenomenon of feature loss occurs. This kind of phenomenon is explained as that when the low-dimensional space dimension is too low, the data mapping points cannot carry sufficient feature information.

Therefore, we compare the forecasting accuracy of the combined model with different  $S$  and  $v$ . Among them, each group of composite models is composed of seven models, namely, nonlinear mapping models or time series models. At this time, the number of nonlinear mapping models is  $v$ , and the number of time series models is  $7 - v$ . Except for different model structures, the parameters of the two models are all the same. In terms of model structure, the nonlinear mapping model consists of a layer of LSTM, which has 60 LSTM units, and the time series model consists of three LSTM layers, each of which has 60 LSTM units. The reason for this distinction is that the input of the time series model is the load information at the historical time, and the data itself has the characteristics of time series. Therefore, it is necessary to extract the relevant characteristics from more layers of the LSTM layer. The input of the nonlinear mapping model is the comprehensive influencing factor data in low-dimensional space, and it does not have a time-series relationship. Therefore, only one layer of the LSTM layer is set to simplify the calculation of the model.

The experimental results are shown in Figure 7. When  $S = 4$  and  $v = 6$ , the combined model has the highest average forecasting accuracy.

Laterally, the combination model with the same  $S$  will have the best forecasting performance at  $v = 6$ , that is, the combination model using all IMF components to build nonlinear mapping model and using residual signal to build time series model has the best effect, indicating that the relatively flat residual signal is more suitable for time series forecasting method. When  $v = 0$ , the combined model consists of seven time series models, that is, all IMF components and residual signals are modeled by time series models. At this time, the average forecasting accuracy of the combined model is the lowest, indicating that each IMF component is not suitable for time series forecasting.

Vertically, the models with higher accuracy are concentrated in the middle part of Figure 7, indicating that too large or too small  $S$  will influence the efficiency of the proposed model. Part of the reason is that there is a certain

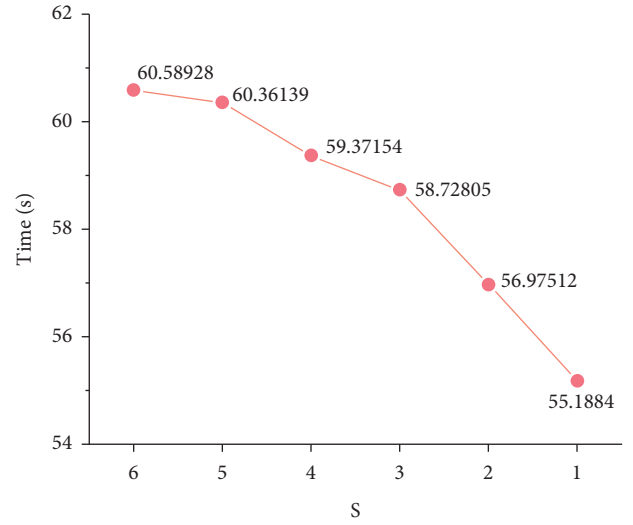


FIGURE 6: Total time to complete all model training and forecasting at different  $S$ .

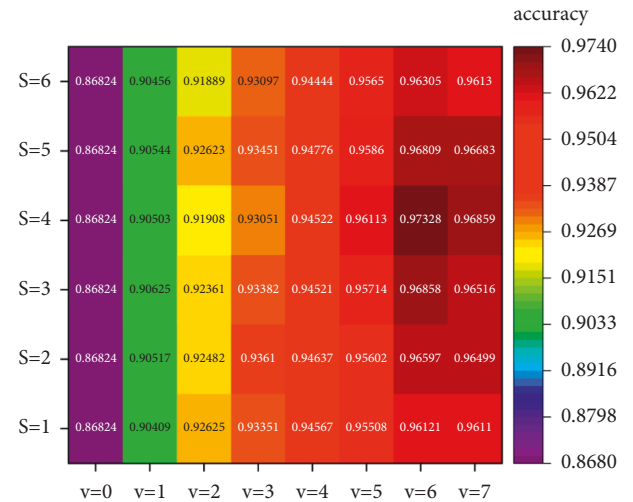


FIGURE 7: Average forecasting accuracy of combined models with different  $S$  and  $v$ .

potential connection between the influencing factors of high-dimensional space. If all the input forecasting models are not reduced by data dimension, it will make the model extract some redundant features, increase the calculation amount of the model, and even bring negative improvement to the forecasting accuracy of the combined model. On the contrary, if the dimension of influencing factors is reduced to 2 or lower, the data in low-dimensional space cannot carry all features of the raw data, thus reducing the generalization ability of the model.

**4.2. Model Comparison.** To test the performance of the proposed model in short-term load forecasting, this paper establishes multiple models for simulation and comparison, including the time series model based on LSTM (TLSTM), the nonlinear mapping model based on LSTM (MLSTM),

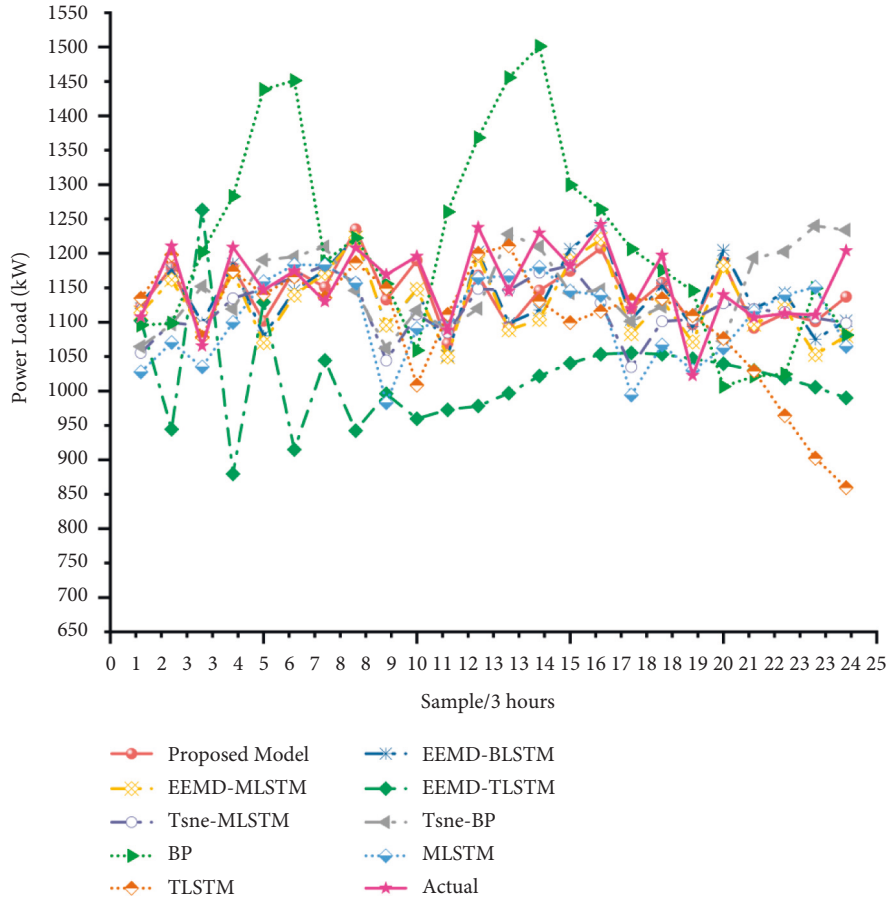


FIGURE 8: The performance of forecasting of each model.

the back propagation neural network (BP), the model combining TSNE and MLSTM (TSNE-MLSTM), the model combining TSNE and BP (TSNE-BP), the model combining EEMD and MLSTM (EEMD-MLSTM), the model combining EEMD and TLSTM (EEMD-TLSTM), and the model combining EEMD, MLSTM, and TLSTM (EEMD-BLSTM). Among them, BP uses three hidden layers, each hidden layer contains 60 neurons, and LSTM model parameters are set as above.

The forecasting results of each model are shown in Figure 8, and the detailed comparison information is demonstrated in Table 1, including the mean absolute percentage error (MAPE), the root mean square error (RMSE), and the mean absolute error (MAE).

In Figure 8, the load forecasting value of each sample point of the EEMD-TLSTM model deviates from the actual load value greatly, and the IMF component with high-frequency characteristics has a large error when using the time series model to forecast. The accuracy of TLSTM model is superior to that of EEMD-TLSTM, but its forecasting accuracy is still not remarkable in the comparison of all models, mainly due to the strong fluctuation of the original load signal, the effect of load forecasting directly using the time series model is not good. On the contrary, if the original load signal is decomposed by EEMD, the decomposed IMF component is used to build the MLSTM model, and the

TABLE 1: Error of forecasting results of each model.

Forecasting model	MAPE (%)	RMSE (kW)	MAE (kW)
Proposed model	2.6716	39.3329	31.0916
EEMD-BLSTM	3.6951	50.3015	42.7011
EEMD-MLSTM	3.8699	54.7858	45.1035
TSNE-MLSTM	4.4523	67.2027	52.2686
TSNE-BP	6.0121	77.4130	69.4224
MLSTM	5.7885	84.5392	68.0465
TLSTM	6.3646	108.5245	73.9725
BP	10.2852	147.7220	118.6361
EEMD-TLSTM	13.1761	177.7819	155.0436

residual signal is used to build the TLSTM model. Then, the appropriate models are used to forecast, respectively, such as EEMD-BLSTM and proposed model, and the forecasting efficiency will be significantly improved.

Ultimately, due to the fact that TSNE reduces the dimension of the influencing factors of power load in high-dimensional space, the potential redundant features in the comprehensive influencing factors in low-dimensional space are less, so that the forecasting effects of TSNE-MLSTM and TSNE-BP compared with MLSTM and BP models are improved by 1.9186% and 4.2731%, respectively. The proposed model also improves the accuracy of 1.0235% for the EEMD-BLSTM model with the EEMD algorithm. The forecasting



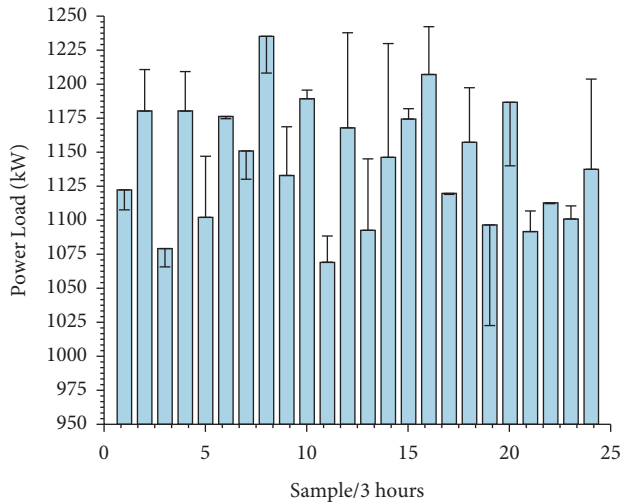


FIGURE 9: Forecasting results and errors of each sample point. The error bars represent absolute error between the forecasting value and actual value.

values of each sample point in proposed model are shown in Figure 9. The size of the error bars in Figure 9 indicates the absolute error. The position of the bar end is the actual load data of each sample point. The RMSE of the proposed model is 39.3329 kW, and the MAE is 31.0916 kW. The forecasting results are close to the actual load value.

## 5. Conclusions

This paper establishes a short-term power load forecasting model based on TSNE-EEMD-LSTM. TSNE is used to map the data of power load influencing factors in original dimension to the lower dimension, which reduces the calculation of redundant features. EEMD is used to split the power load curve into multiple IMF components with different frequencies and a flat residual signal. Based on the characteristics of IMF components and residual signals, appropriate models based on LSTM are established, including the nonlinear mapping model with low-dimensional space comprehensive influencing factors as model input and the time series model with historical data of signal components as model input. Finally, the important parameters of the combined model are determined by comparative experiments, and the feasibility of the proposed hybrid model in short-term load forecasting is verified. Several following conclusions are drawn:

- (1) There are redundant features between the original power load influencing factors. The multiple extractions of redundant features by the forecasting model will increase the calculation amount of the model, decrease the forecasting speed of the model, and even lead to poor generalization ability of the model. TSNE algorithm can greatly retain data structure and reduce redundant feature extraction. When the original influencing factors are time, temperature, pressure, humidity, wind speed and

rainfall, it is best to map the influencing factors to the four-dimensional space.

- (2) The IMFs signal and residual signal decomposed by EEMD have different characteristics. Using these characteristics to build several targeted sub-models can improve the accuracy of prediction. In this paper, the LSTM model is divided into nonlinear mapping model and time sequence model by changing the model input. All IMFs signals are suitable for modeling by nonlinear mapping model, and the residual signal is suitable for modeling by time series model.
- (3) The TSNE-EEMD-LSTM model proposed in this paper can avoid extracting redundant features as much as possible and fully tap the potential characteristics of influencing factors, which has an excellent performance in the comparison of multi-model forecasting performance.

The shortcomings of this study and follow-up work:

The models used in this paper are based on LSTM, and work types are divided by changing the input of the model. In the subsequent research, more advanced and more appropriate forecasting models will be taken into account to improve the performance of each sub-model in the hybrid model. In the future, it is expected that our proposed scheme can be applied to the forecasting fields of new energy generation [17,18] and integrated loads [19–21].

## Data Availability

The data that support the findings of this study are available from the corresponding author upon reasonable request.

## Conflicts of Interest

The authors declare that they have no conflicts of interest.

## Acknowledgments

This work was supported by 2022 Innovation and Entrepreneurship Training Program for College Students of Shenyang Institute of Engineering, Scientific Research Project of Education Department of Liaoning Province (LJKQZ2021079), Doctoral Scientific Research Foundation of Liaoning Province (2020-BS-181) and Liaoning Revitalization Talents Program (XLYC1907138).

## References

- [1] F. L. Quilumba, W.-J. Lee, H. Huang, D. Y. Wang, and R. L. Szabados, "Using smart meter data to improve the accuracy of intraday load forecasting considering customer behavior similarities," *IEEE Transactions on Smart Grid*, vol. 6, no. 2, pp. 911–918, 2015.
- [2] X. Shao and C. S. Kim, "Multi-step short-term power consumption forecasting using multi-channel LSTM with time location considering customer behavior," *IEEE Access*, vol. 8, pp. 125263–125273, 2020.



- [3] T. H. Ouyang, Y. S. He, H. J. Li, Z. Y. Sun, and S. Baek, "Modeling and forecasting short-term power load with copula model and deep belief network," *IEEE Transactions on Emerging Topics in Computational Intelligence*, vol. 3, no. 2, pp. 127–136, 2019.
- [4] R. Wang, Q. Sun, P. Tu, J. Xiao, Y. Gui, and P. Wang, "Reduced-order aggregate model for large-scale converters with inhomogeneous initial conditions in DC microgrids," *IEEE Transactions on Energy Conversion*, vol. 36, no. 3, pp. 2473–2484, 2021.
- [5] W. C. Kong, Z. Y. Dong, Y. W. Jia, D. J. Hill, Y. Xu, and Y. Zhang, "Short-term residential load forecasting based on LSTM recurrent neural network," *IEEE Transactions on Smart Grid*, vol. 10, no. 1, pp. 841–851, 2019.
- [6] Q. Liu, Y. Shen, L. Wu, J. Li, L. Zhuang, and S. Wang, "A hybrid FCW-EMD and KF-BA-SVM based model for short-term load forecasting," *CSEE Journal of Power and Energy Systems*, vol. 4, no. 2, pp. 226–237, 2018.
- [7] H. Bo, Y. Nie, and J. Wang, "Electric load forecasting use a novelty hybrid model on the basic of data preprocessing technique and multi-objective optimization algorithm," *IEEE Access*, vol. 8, pp. 13858–13874, 2020.
- [8] C. Shang, J. Gao, H. Liu, and F. Liu, "Short-term load forecasting based on PSO-KFCM daily load curve clustering and CNN-LSTM model," *IEEE Access*, vol. 9, pp. 50344–50357, 2021.
- [9] K. Aurangzeb, M. Alhussein, K. Javaid, and S. I. Haider, "A pyramid-CNN based deep learning model for power load forecasting of similar-profile energy customers based on clustering," *IEEE Access*, vol. 9, pp. 14992–15003, 2021.
- [10] W. Xu, H. Hu, and W. Yang, "Energy time series forecasting based on empirical mode decomposition and FRBF-AR model," *IEEE Access*, vol. 7, pp. 36540–36548, 2019.
- [11] Z. Kong, C. Zhang, H. Lv, F. Xiong, and Z. Fu, "Multimodal feature extraction and fusion deep neural networks for short-term load forecasting," *IEEE Access*, vol. 8, pp. 185373–185383, 2020.
- [12] S. Das, B. R. Prusty, and K. Bingi, "Review of adaptive decomposition-based data preprocessing for renewable generation rich power system Applications," *Journal of Renewable and Sustainable Energy*, vol. 13, no. 6, Article ID 062703, 2021.
- [13] S. Hochreiter and J. Schmidhuber, "Long short-term memory," *Neural Computation*, vol. 9, no. 8, pp. 1735–1780, 1997.
- [14] Z. Wu and N. E. Huang, "Ensemble empirical mode decomposition: a noise-assisted data analysis method," *Advances in Adaptive Data Analysis*, vol. 01, no. 01, pp. 1–41, 2009.
- [15] J. Liu, Q. Li, H. Yang, Y. Han, S. Jiang, and W. Chen, "Sequence fault diagnosis for PEMFC water management subsystem using deep learning with t-SNE," *IEEE Access*, vol. 7, pp. 92009–92019, 2019.
- [16] M. A. Da Silva Lopes, A. D. Dória Neto, and A. De Medeiros Martins, "Parallel t-SNE applied to data visualization in smart cities," *IEEE Access*, vol. 8, pp. 11482–11490, 2020.
- [17] W. Liu, C. Ren, and Y. Xu, "PV generation forecasting with missing input data: a super-resolution perception approach," *IEEE Transactions on Sustainable Energy*, vol. 12, no. 2, pp. 1493–1496, 2021.
- [18] M. Li, M. Yang, Y. Yu, and W.-J. Lee, "A wind speed correction method based on modified hidden markov model for enhancing wind power forecast," *IEEE Transactions on Industry Applications*, vol. 58, no. 1, pp. 656–666, 2022.
- [19] W. Y. Liu, "Cooling, heating and electric load forecasting for integrated energy systems based on CNN-LSTM," in *Proceedings of the 2021 6th International Conference On Power And Renewable Energy (ICPRE)*, Shanghai, China, 2021.
- [20] R. Wang, Q. Sun, W. Hu, Y. Li, D. Ma, and P. Wang, "SoC-based droop coefficients stability region analysis of the battery for stand-alone supply systems with constant power loads," *IEEE Transactions on Power Electronics*, vol. 36, no. 7, pp. 7866–7879, 2021.
- [21] E. Liu, Y. Wang, and Y. Huang, "Short-term forecast of multi-load of electrical heating and cooling in regional integrated energy system based on deep LSTM RNN," in *Proceedings of the 2020 IEEE 4th Conference on Energy Internet and Energy System Integration (EI2)*, Wuhan, China, 2020.

## Research Article

# Annular Directed Distributed Algorithm for Energy Internet

Jiaming Tan <sup>1</sup> and Hongyou Li <sup>2</sup>

<sup>1</sup>Faculty of Electrical and Control Engineering, Liaoning Technical University, Huludao, China

<sup>2</sup>Professorate Senior Engineer, China Energy Engineering Group Co., Ltd, Huludao, China

Correspondence should be addressed to Jiaming Tan; [m15124403461@163.com](mailto:m15124403461@163.com)

Received 25 February 2022; Revised 13 April 2022; Accepted 13 May 2022; Published 5 July 2022

Academic Editor: Yonghao Gui

Copyright © 2022 Jiaming Tan and Hongyou Li. This is an open access article distributed under the Creative Commons Attribution License, which permits unrestricted use, distribution, and reproduction in any medium, provided the original work is properly cited.

This article investigates an annular directed distributed double optimal algorithm to manage many we-energy frameworks in energy management of energy Internet (EI). The we-energy (WE) is an integrated energy hub containing varied energy devices of different functions including multi-energy production, consumption, and conversion. On this basis, all WE models cooperate to search for a minimum value of an objective function. Energy management in EI has two main goals. On the one hand, it needs to attain the optimality of economy with influence about the fluctuation of distributed renewable energy and randomness of terminal users. On the other hand, the EI should protect the privacy of terminal users well. Besides, discovering optimality value in the oscillation near convergence point, EI also needs a decrease in communication frequency and refraining of Zeno behavior. Zeno behavior means some operation is triggered infinite times in finite times of iteration. For realizing these proposes, this literature establishes an EI system that transfers cyber information in an annular directed path. The algorithm in this EI system adopts a novel annular distributed double-control price guiding strategy. In addition, this algorithm employs other two methods including the alternating direction method of multipliers method and the Newton-downhill method to optimize economy and reach convergence, respectively. Meanwhile, that algorithm adopts a small positive constant  $w$  to avoid Zeno behavior. The performance of that algorithm is demonstrated through simulation results. Moreover, the optimality, convergence analysis, and avoiding Zeno behaviors are strictly proved by convex optimization and the monotone-bounded convergence theorem.

## 1. Introduction

Due to increasing concern about cosmopolitan environmental problems, the strategy of carbon emission reduction, and the utilization of environmentally friendly energy resources, the concept of energy internet (EI) [1] is developing at a marvelous speed in recent years. EI is a multi-energy system with a large number of advanced technology containing the theory of multiagent systems; the cyber communication and the physical energy transmission method [2]; the intelligent strategy of energy management; game and synergy theory about the multi-energy resource in a certain region; demand response between every energy units; optimal operation with various energy devices with different functions, among others. EI, a new pattern of energy system, devotes itself to satisfying terminal users' various kinds of energy demand and enhancing the renewable energy's

utilization efficiency [3]. However, due to the fluctuation of renewable energy resources [4–6], the randomness of terminal users, and complex but strong coupling in various of energy, the optimal dispatch in EI is exceedingly difficult and the method about that is exceedingly unadvanced for complex multi-energy distributed systems and eagerly needed to be reinforced nowadays.

We can divide the recent research concerning optimal dispatch of EI into two categories approximately: one is the traditionally centralized optimal strategy, and the other is the newly developing distributed optimal strategy. There are several documents about the centralized optimal strategy. The work in [7] solved the energy management with a non-convex object, and [8] introduced a two-stage multi-objective optimal scheduling in EI. The centralized optimal strategy has high quality in many fields including optimal performance, speed of convergence, and conquering

disturbance caused by energy generators and terminal users. So traditional single energy systems including traditional power systems generated by terminal users always adopt the centralized optimal strategy. However, the centralized optimal strategy needs a large-scale energy generator that naturally disperses renewable energy resources that could not build. Centralized EI also brings too much compute and control pressure to its central processing unit. What's more, the communication frequency in centralized EI is too high, and local malfunctions in the centralized optimal strategy influence global systems strikingly. Besides, it is impossible for the centralized optimal strategy to protect users' privacy because of its concentrated physical framework. Therefore, the centralized optimal strategy will be replaced by the distributed optimal strategy sooner or later [9]. The literature [10, 11] proposed non-iterative algorithms for the distributed solution of multiagent optimal dispatch problems. The distributed optimal strategy can greatly decrease the frequency of communication and reduce the impact of local malfunction on global systems. The distributed optimal strategy is plug and play, so that it is very easy for distributed EI to expand its scale. And the distributed optimal strategy can protect users' privacy to a certain extent in the present researches. Most important of all, it is impossible for natural disperse renewable energy resources to build large-scale centralized energy generators, so the only way to utilize renewable energy is the distributed optimal strategy. All advantages above are greatly significant to EI and can only be satisfied by the distributed optimal strategy and not by the centralized optimal strategy. For the foregoing reasons, it is no wonder that concern in the study of EI transfers from the centralized optimal strategy to the distributed optimal strategy in recent years.

However, the difficulty of energy management in the distributed optimal strategy is much higher than that in the centralized optimal strategy on account of renewable energy resources' fluctuation and terminal users' randomness. Due to the long distance between energy producers and terminal users in the centralized optimal strategy, although it will strongly increase the cost of energy transmission, the fluctuation of renewable energy resources and the randomness of terminal users scarcely affect the EI system. But in the distributed optimal strategy, the distance between generators and terminal users may be very short, so if the fluctuation of renewable energy resources and the randomness of terminal users couple together, it will impact the stability of EI strongly. For solving the problem, various literatures use various strategies. The literature [6] revealed the disturbance caused by renewable energy resources' fluctuation in power systems. The literature [12] presented an unsupervised algorithm to extract the EV charging loads non-intrusively from the smart meter data. The literature [13] optimized power trading by Stackelberg game. But methods below aimed at power systems, and the type of energy was only power. These methods cannot solve energy management of EI with strong coupling between different types of energy.

Generally, we resolve a big complex system to some small and single systems and study small systems

respectively to study the big system which is hard to study directly. So, we used agents to study multiagents [12], and we used microgrids to study power systems [14]. But what can we use to study EI? Different people had different ideas. Swiss scholars proposed the energy hub [15], which resolves EI into some small unit for the first time, and interpreted that energy can transform into another kind of energy in EI firstly. Subsequently, Li.L proposed prosumer in [16] to move forward a new step about establishing a small unit, which explained basic energy unit in EI is not only an energy producer and an energy consumer. The prosumer makes much progress not only in coupling between generators and terminal users but also in cooperating among different energies [17]. Sun et al. summed up all models above and referenced the theory of multiagents [18] and proposed we-energy (WE) [19]. We-energy is a full-duplex, hole distributed without a center, intelligent and peer-to-peer energy unit in EI. Compared with other models, WE is most suitable for the current EI for the several reasons below. Firstly, the WE is a full-duplex model, while other models including energy hubs are half-duplex models. Secondly, the WE is equal to the hole network. In other words, the WE is completely a selfish and rational model. So, the decision of the WE is very hard to be influenced by other we-energies, which is very suitable for the distributed algorithms. Thirdly, the WE is a point-to-point model, but other models are point-to-plane models. The WE communicates to other Wes, while others communicate to the hole network. So, the WE is more suitable for the algorithm in this article. Because of these reasons, this study adopts the WE as a basic energy unit.

Since the distributed framework and the large-scale system of EI, the suitable method of energy management between WE is the distributed algorithm realized by multiagent. The literature [20] used the distributed algorithm to optimize residential WE and designed an operation method that maps the infeasible solutions into the feasible region. The literature [21] mixed the alternating direction method of multipliers into the distributed algorithm for the first time. The literature [22] converted synchronous communication into out of synchronous communication by event-triggered in the distributed algorithm. But the distributed algorithm in [21, 23] considered energy conversions as must-run energy load and flexible energy load, which made energy conversion could only supply all load in one type of energy demand. For terminal users, the energy that the producer generated and conversion devices transformed made no difference, so EI by no means differentiated load into must-run load and flexible load. In addition, the literature [21, 23] ignored Zeno behavior in the algorithm, which could increase iteration times closed to infinity value under some initial values.

Although the distributed optimal strategy and the distributed algorithm reduce communication frequency and protect users' privacy in EI to a certain degree, the communication frequency's reduction and privacy's protection still need to be reinforced. Nowadays, the energy that terminal users need, generators produce, and energy transformers convert is becoming more and more random, varied, and unstable. Furthermore, time delay [22],

controllability deficiency [24], and Zeno behavior that always consists in the Newton–Raphson algorithm [23] do serious harm to EI. What is most terrible is Zeno behavior, because it will increase times of iteration to a large value, even to a measureless value. Moreover, traditional researches about privacy protecting only protected privacy from unneighborly agents, but they did nothing about neighbor agents [25–27]. That method had disadvantages. On the one hand, network sparse caused by only-neighbor communication destroyed the controllability of EI due to the theory in [24]. On the other hand, some users were not willing to trust their neighbor agents. To solve these problems, this literature based on the alternating direction method of multipliers in EI [28], Newton–Raphson algorithm [23], and auction-based algorithm [29] proposes an annular directed distributed algorithm, which leads WEs to communicate in an annular route. Compared with traditional distributed optimization methods, the annular directed distributed algorithm can not only observably reduce communicating intensity but also protect all users' data that cannot be acquired by other agents including neighbor agents. However, in conventional distributed optimization methods, some ratios, power output, or estimated prices have to be shared among neighbored agents so they cannot protect all data. In addition, this study establishes a small number to avoid Zeno behaviors about Newton-downhill factors which traditional researches do not consider. The contributions of this study are summarized as follows:

- (1) Reinforce the protection of users' privacy. In the annular directed distributed algorithm, devices' data can only be extracted by themselves. By the annular directed distributed algorithm, all we-energies only transfer a power-heat-gas energy flow to another we-energy. Besides, all devices inside the we-energy only transfer that power-heat-gas flow, too. The energy flow is the summation of previous energy manufacture, energy conversion, and encryption factors. Firstly, each energy device does not know where the energy flow begins (the start place is randomness and that of each time of iteration is different), so the energy device does not know the operating condition of each device. Secondly, the privacy of the started device is protected by encryption factors. When the energy flow starts, it will add several values to each type of energy. With this method, the second device cannot know the operating condition of the first device. However, traditional research cannot protect several types of data among neighbor agents [25–27]. In traditional researches, some ratios, power output, or estimated prices have to be shared among neighbored agents so they cannot protect all data.
- (2) Reduce the intensity of communication and change the information in communication from last time data to updated data. Firstly, the communication in the annular directed distributed algorithm is single-directed communicating and the communication in traditional researches [27] is non-directed. The non-directed communication means the EI needs to communicate in both ways. So, the intensity of single-directed communication is half of the non-directed communication. Secondly, communication in traditional research is one-to-many communication, while the communication in this article is one-to-one communication. There are several contributions to one-to-one communication. Firstly, the encryption of energy flow described hereinbefore needs that. Secondly, the data one-to-many communication transfers are the data in last time all above, but the data one-to-one communication transfers are the data that have already been updated by the new energy price in this time of iteration, so the information in one-to-one communication is newer than that in one-to-many communication.
- (3) Avoid abnormal energy conversion successfully. It is worth noting that the price guiding the alternating direction method of multipliers is unsuitable for the energy conversion because the price guiding always leads to the overshoot in energy conversion. Firstly, the cost functions of energy conversion devices are always linear but the cost functions of energy manufacture devices are always convex so too much energy will increase the energy-producing price but will not change the energy conversion price. Secondly, because the energy sold price need to be changed in the control center of the hole EI, a distributed we-energy cannot change the energy price even though too much energy changes to another type of energy. For the reasons, above one type of cheap energy will change all of themselves to another expensive energy even though the energy conversion may consume all this type of energy and produce too many other energies. For avoiding that, this study enlightened by the idea of mistest in reinforcement learning. The literature [30] proposed a mistesting method to solve the problem of energy conversion and use downhill factors to ensure the astringency of the algorithm.
- (4) Avoid Zeno behavior in the Newton-downhill method successfully. Zeno behavior means some operation is triggered infinite times in finite times of iteration. In this literature, Zero behavior means Newton-downhill factors are adjusted too many times in one time of iteration. Theoretically speaking, the Newton-downhill method will go converge sooner or later, so the Zeno behavior will never appear. However, in the realistic project, if the downhill factor changes too many times in one time of iteration, we will regard it as Zeno behavior. This article solved that issue.
- (5) Prove that the annular directed distributed algorithm holds asymptotic convergence when the Zeno coefficient reaches maximum value by the monotone-bounded convergence theorem. Meanwhile, optimal performance of the equilibrium point is certified by difference theorem and convex optimization. And by the theory of finite and infinite, avoiding Zeno behavior in certain accuracy is proved, too.



The rest of this study is organized as follows: Section 2 presents the WE model, energy device models, constraints of main features, and requirements about energy devices. Section 3 introduces some basic knowledge about graph theory; presents the annular directed distributed algorithm for the first time; and proves astringency, optimality, and avoiding Zeno behaviors of it. In Section 4, several simulation results are presented to prove the effectiveness of that. Section 5 concludes the study.

## 2. The We and Device Models in EI

**2.1. System Modeling and Test Systems.** The distributed energy producer includes distributed renewable generators, distributed renewable heat devices, distributed coal or oil combined heat and power devices, and equivalent distributed gas producers. There are two things worth noting: one is that there are no distributed fuel generators and distributed fuel heat devices because they are both more inefficiently than distributed combined heat and power devices. The other is that there are two kinds of combined heat and power devices in EI: one is the distributed coal or oil combined heat and power devices belonging to the distributed energy producer, which produces power and heat by coal or oil, and the other is the distributed gas combined heat and power devices belonging to the distributed energy conversion devices, which produces power and heat by gas. The distributed energy conversion devices include distributed power to gas devices, distributed electric boilers, and distributed gas combined heat and power devices. The distributed energy storage devices include distributed power storage devices, distributed heat storage devices, and distributed gas storage devices. The distributed terminal users and the distributed energy transform devices cannot be divided into smaller devices.

The distributed energy producer satisfies the constraints below:

$$\begin{cases} P_i^{\text{DP}} = P_i^{\text{DRG}} + P_i^{\text{DCOC}}, \\ H_i^{\text{DP}} = H_i^{\text{DRHD}} + H_i^{\text{DCOC}}, \\ G_i^{\text{DP}} = G_i^{\text{DGP}}, \end{cases} \quad (1)$$

where  $i$  is the serial number of WE. If there are  $n$  WEs in EI,  $i$  belongs to 1 to  $n$ .  $P_i^{\text{DP}}$ ,  $H_i^{\text{DP}}$ , and  $G_i^{\text{DP}}$  are the total power, heat rate, and gas rate produced by the distributed energy producer devices in  $i$ th WE, respectively.  $P_i^{\text{DRG}}$  and  $P_i^{\text{DCOC}}$  are the power rate of the distributed renewable generators and the distributed coal or oil combined heat and power devices in  $i$ th WE, respectively.  $H_i^{\text{DRHD}}$  and  $H_i^{\text{DCOC}}$  are the heat rate of DRHD and the distributed coal or oil combined heat and power devices in  $i$ th WE.  $G_i^{\text{DGP}}$  is the gas rate of the distributed gas producers in  $i$ th WE.

The distributed energy conversion devices satisfy the constraints below:

$$\begin{cases} P_i^{\text{DCD}} = P_i^{\text{DCD}} - P_i^{\text{DP2G}} - P_i^{\text{DEB}}, \\ H_i^{\text{DCD}} = H_i^{\text{DEB}} + H_i^{\text{DGC}}, \\ G_i^{\text{DCD}} = G_i^{\text{DP2G}} - G_i^{\text{DGC}}, \end{cases} \quad (2)$$

where  $P_i^{\text{DCD}}$ ,  $H_i^{\text{DCD}}$ , and  $G_i^{\text{DCD}}$  are the total power, heat rate, and gas rate exchanged by the distributed energy conversion devices in  $i$ th WE, respectively—plus or minus of them represents the output or input.  $P_i^{\text{DGC}}$ ,  $P_i^{\text{DP2G}}$ , and  $P_i^{\text{DEB}}$  are the exchanging power rate in the distributed gas combined heat and power devices, the distributed power to gas devices, and the distributed electric boiler in  $i$ th WE, respectively.  $H_i^{\text{DEB}}$  and  $H_i^{\text{DGC}}$  are the exchanging heat rate in the distributed electric boiler and the distributed gas combined heat and power devices in  $i$  WE, respectively.  $G_i^{\text{DCD}}$ ,  $G_i^{\text{DP2G}}$ , and  $G_i^{\text{DGC}}$  are the exchanging gas rate in the distributed energy conversion devices, the distributed power to gas devices, and the distributed gas combined heat and power devices in  $i$ th WE, respectively.

**2.2. WE Model.** WE is a basic energy unit that can have devices all above. The model of WE in power-gas-heat EI is as follows:

$$\begin{bmatrix} P_i \\ H_i \\ G_i \end{bmatrix} = \begin{bmatrix} \lambda_{i,P,P} & \lambda_{i,P,H} & \lambda_{i,P,G} \\ \lambda_{i,H,P} & \lambda_{i,H,H} & \lambda_{i,H,G} \\ \lambda_{i,G,P} & \lambda_{i,G,H} & \lambda_{i,G,G} \end{bmatrix} \begin{bmatrix} P'_i \\ H'_i \\ G'_i \end{bmatrix}, \quad (3)$$

where  $P$ ,  $H$ , and  $G$  are power, heat, and gas, respectively. Vector  $[P_i \ H_i \ G_i]^T$  and  $[P'_i \ H'_i \ G'_i]^T$  are energy flow in terminal side and network side—plus or minus and an absolute value of the element in vector represent the direction and rate of energy flow, respectively. Besides, the following constraints are limited to micro-power-system in WE:

$$\begin{cases} P'_i = P_i^{\text{DP}} + P_i^{\text{DTD}}, \\ P_i - P'_i = P_i^{\text{DSD}}, \end{cases} \quad (4)$$

where  $P_i^{\text{DTD}}$  is the power flow between  $i$ th WE and others—plus or minus and the absolute value of it are the direction and rate of power flow, respectively. The following constraints in micro-heat-system and micro-gas-system in WE are similar to constraints above. All  $P$  are changed into  $H$  or  $G$  correspondingly. Matrix  $\lambda$  represents energy flow's proportion of allocation and efficiency of energy conversion. How to design matrix  $\lambda$ ? Different research has different points of view in it. Ref. [8] models matrix  $\lambda$  as the dot product of Hadamard matrices and efficiency matrices. But Ref. [8] prohibits circumflex in WE. The circumflex is harmful to smart grid, but may not be harmful to the distributed energy conversion devices in EI because the distributed energy conversion devices could never shorten out. Although circumflex will waste certain energy due to loss in energy conversion, because of a lot of start-stop constraints and ramping rate limits in the distributed energy conversion devices, circumflex is needed in energy management. So, this study models matrix  $\lambda$  as follows:

$$\lambda = K \times A + K' \times A', \quad (5)$$

where  $A'$  and  $A$  are Hadamard matrices. An element in  $A$  is 1 or 0 represent that there is or is not corresponding energy flowing from network side to terminal side. Oppositely, that

in  $A'$  is 1 or 0 represents that there is or is not corresponding energy flowing from terminal side to network side. Elements in  $K$  and  $K'$  are corresponding energy flow's proportion of allocation and efficiency of corresponding energy conversion. For example, if an element in  $K$  is  $\kappa_{a,b}$ ,

$$\kappa_{a,b} = v_{a,b}\eta_{a,b}. \quad (6)$$

There will be  $v_{a,b}$  proportion of energy  $a$  from network side converting into energy  $b$  in terminal side, and conversion efficiency is  $\eta_{a,b}$ . So,  $\kappa_{a,b}$  is a positive number smaller than 1. Oppositely, if an element in  $K'$  is  $\kappa'_{a,b}$ ,

$$\kappa'_{a,b} = \frac{1}{v_{a,b}'\eta_{a,b}'}. \quad (7)$$

There will be  $v'_{a,b}$  proportion of energy  $a$  from terminal side converting into energy  $b$  in network side, and conversion efficiency is  $\eta'_{a,b}$ . So,  $\kappa'_{a,b}$  is a number larger than 1. It is worth nothing that, if  $v'_{a,b}$  equals to zero,  $\kappa'_{a,b}$  will be meaningless. On this occasion, we stipulate  $v'_{a,b}\eta'_{a,b}$  as a small positive number  $\zeta$  in order to run the distributed algorithm. Constraints in  $A'$  ensure that  $\zeta$  could not influence precision of results. So, in power-gas-heat EI, the WE matrix is as follows:

$$\begin{bmatrix} P \\ H \\ G \end{bmatrix} = \begin{bmatrix} A' \circ \begin{bmatrix} 1 & 1 & 1 \\ \frac{v_{PP}^{SST} \eta_{PP}^{SST}}{v_{PH}^{DEB} \eta_{PH}^{DEB}} & \frac{v_{PH}^{DEB} \eta_{PH}^{DEB}}{v_{PG}^{DP2G} \eta_{PG}^{DP2G}} & \frac{v_{PG}^{DP2G} \eta_{PG}^{DP2G}}{v_{PG}^{EWC} \eta_{PG}^{EWC}} \\ \frac{1}{\zeta} & 1 & \frac{1}{\zeta} \\ 1 & 1 & 1 \\ \frac{v_{GP}^{DGC} \eta_{GP}^{DGC}}{v_{GH}^{DGC} \eta_{GH}^{DGC}} & \frac{v_{GH}^{DGC} \eta_{GH}^{DGC}}{v_{GG}^{EWC} \eta_{GG}^{EWC}} & \frac{v_{GG}^{EWC} \eta_{GG}^{EWC}}{v_{GG}^{EWC} \eta_{GG}^{EWC}} \end{bmatrix} + \begin{bmatrix} P' \\ H' \\ G' \end{bmatrix}, \\ A \circ \begin{bmatrix} v_{PP}^{SST} \eta_{PP}^{SST} & 0 & v_{GP}^{DGC} \eta_{GP}^{DGC} \\ v_{PH}^{DEB} \eta_{PH}^{DEB} & 1 & v_{GH}^{DGC} \eta_{GH}^{DGC} \\ v_{PG}^{DP2G} \eta_{PG}^{DP2G} & 0 & v_{GG}^{EWC} \eta_{GG}^{EWC} \end{bmatrix} \end{bmatrix} \quad (8)$$

where SST is a solid-state transformer and EWC is corresponding energy without conversion. Energy flow in the network side satisfies the constraints below:

$$\left\{ \sum_{i=1}^n P'_i = 0, \sum_{i=1}^n H'_i = 0, \sum_{i=1}^n G'_i = 0, \right. \quad (9)$$

where  $n$  is the total of WEs.

### 2.3. The Distributed Energy Producer Device Models and Cost Functions

**2.3.1. The Distributed Renewable Generators and the Distributed Renewable Heat Device Models.** The distributed renewable generators include wind-driven generators and solar-driven generators. But DRHD only includes solar-

driven heat devices. Wind and solar are free, and the operating cost of taking the advantage of renewable energy resources is such little that it can be ignored. Models and cost functions of the distributed renewable generators and DRHD are as follows:

$$\begin{aligned} P_{i,t}^{DRG} &= P_{i,t}^{wind} + P_{i,t}^{solar}, \\ H_{i,t}^{DRHD} &= H_{i,t}^{solar}, \\ C_{i,t}^{DRG} &= 0, \\ C_{i,t}^{DRHD} &= 0, \end{aligned} \quad (10)$$

where wind and solar are kinds of renewable energy resources.  $C$  is the operating cost function of corresponding device.  $t$  is hours from 0 to 24.  $P$  and  $H$  are the rate of power and heat. It is worth noting that energy management in this study is hourly dispatch, so all-time in this study is in hour units.

Constraints of the distributed renewable generators and DRHD are as below:

$$\begin{aligned} P_i^{wind-min} &\leq P_{i,t}^{wind} \leq P_i^{wind-max}, \\ P_i^{solar-min} &\leq P_{i,t}^{solar} \leq P_i^{solar-max}, \\ H_i^{solar-min} &\leq H_{i,t}^{solar} \leq H_i^{solar-max}, \end{aligned} \quad (11)$$

where min and max are corresponding minimum rate and corresponding maximum rate of corresponding energy in corresponding WE.

**2.3.2. The Distributed Coal or Oil Combined Heat and Power Device Models.** The distributed coal or oil combined heat and power devices adopt coal fuel to produce power and heat. Models and cost functions of the distributed renewable generators and DRHD are as follows:

$$\begin{aligned} P_{i,t}^{DCOC} &= \eta_i^{DCOC} F_{i,t}^{DCOC} \frac{1}{\varphi_{i,t}^{DCOC} + 1}, \\ H_{i,t}^{DCOC} &= \eta_i^{DCOC} F_{i,t}^{DCOC} \frac{\varphi_{i,t}^{DCOC}}{\varphi_{i,t}^{DCOC} + 1}, \end{aligned} \quad (12)$$

where  $P_{i,t}^{DCOC}$  and  $H_{i,t}^{DCOC}$  are power and heat rate of the distributed coal or oil combined heat and power devices generating, respectively, and  $F_{i,t}^{DCOC}$  is the thermal rate of coal the distributed coal or oil combined heat and power devices consuming.  $\eta_i^{DCOC}$  is the energy conversion of the distributed coal or oil combined heat and power devices.  $\varphi_{i,t}^{DCOC}$  is the ratio of heat and power. It is worth noting that, coal does not belong to power-heat-gas network of EI. So, energy management cannot influence coal's price and the production of coal. People cannot produce coal or oil, after all.

$$\varphi_{i,t}^{DCOC} = \frac{Prh}{Prp}, \quad (13)$$



where  $Prh$  and  $Prp$  are the price of heat and power obviously. The operating cost function of the distributed coal or oil combined heat and power devices is

$$C_{i,t}^{\text{DCOC}} = a_i^{\text{DCOC}} P_i^{\text{DCOC}2} + b_i^{\text{DCOC}} P_i^{\text{DCOC}} + \alpha_i^{\text{DCOC}} H_i^{\text{DCOC}2} + \beta_i^{\text{DCOC}} H_i^{\text{DCOC}} + c_i^{\text{DCOC}} P_i^{\text{DCOC}} H_i^{\text{DCOC}} + \chi_i^{\text{DCOC}}, \quad (14)$$

where  $a_i^{\text{DCOC}}$ ,  $b_i^{\text{DCOC}}$ ,  $\alpha_i^{\text{DCOC}}$ ,  $\beta_i^{\text{DCOC}}$ ,  $c_i^{\text{DCOC}}$ , and  $\chi_i^{\text{DCOC}}$  are constants, and  $a_i^{\text{DCOC}}$ ,  $\alpha_i^{\text{DCOC}}$ , and  $\chi_i^{\text{DCOC}}$  are positive constants. The distributed coal or oil combined heat and power devices satisfy the constraints below:

$$\begin{aligned} -P_i^{\text{DCOC-ramp}} &\leq P_{i,t}^{\text{DCOC}} - P_{i,t-1}^{\text{DCOC}} \leq P_i^{\text{DCOC-ramp}}, \\ a_i^{\text{DCOC}} P_{i,t}^{\text{DCOC}} + e_i^{\text{DCOC}} H_{i,t}^{\text{DCOC}} + f_i^{\text{DCOC}} &\geq 0, \\ a_i^{\text{DCOC}} P_{i,t}^{\text{DCOC}} + e_i^{\text{DCOC}} H_{i,t}^{\text{DCOC}} &\leq g_i^{\text{DCOC}}, \\ h_i^{\text{DCOC}} &\leq \phi_{i,t}^{\text{DCOC}} \leq j_i^{\text{DCOC}}, \end{aligned} \quad (15)$$

where  $P_i^{\text{DCOC-ramp}}$  is the power ramping constrain of the distributed coal or oil combined heat and power devices.  $a_i^{\text{DCOC}}$ ,  $e_i^{\text{DCOC}}$ ,  $f_i^{\text{DCOC}}$ ,  $g_i^{\text{DCOC}}$ ,  $h_i^{\text{DCOC}}$ , and  $j_i^{\text{DCOC}}$  are constants.

**2.3.3. The Distributed Gas Producer Models.** The operating cost function of the distributed gas producers is

$$C_{i,t}^{\text{DGP}} = a_{i,t}^{\text{DGP}} G_{i,t}^{\text{DGP}2} + b_{i,t}^{\text{DGP}} G_{i,t}^{\text{DGP}} + c_{i,t}^{\text{DGP}}, \quad (16)$$

where  $b_{i,t}^{\text{DGP}}$ , and  $c_{i,t}^{\text{DGP}}$  are constants and  $a_{i,t}^{\text{DGP}}$  is a positive constant.  $G$  represents the rate of gas. The limit of the distributed gas producers is

$$0 \leq G_{i,t}^{\text{DGP-min}} \leq G_{i,t}^{\text{DGP}} \leq G_{i,t}^{\text{DGP-max}}, \quad (17)$$

where  $G_{i,t}^{\text{DGP-min}}$  and  $G_{i,t}^{\text{DGP-max}}$  are lower and higher limits of the distributed gas producers, respectively.

## 2.4. The Distributed Energy Conversion Device Models and Cost Functions

**2.4.1. The Distributed Power to Gas Devices and the Distributed Electric Boiler Models.** The models and cost functions of the distributed power to gas devices are as follows:

$$\begin{aligned} G_{i,t}^{\text{DP2G}} &= \eta_{i,t}^{\text{DP2G}} P_{i,t}^{\text{DP2G}}, \\ C_{i,t}^{\text{DP2G}} &= \theta_{i,t}^{\text{DP2G}} P_{i,t}^{\text{DP2G}}, \end{aligned} \quad (18)$$

where  $\eta_{i,t}^{\text{DP2G}}$  is the energy conversion efficiency of the distributed power to gas devices.  $\theta_{i,t}^{\text{DP2G}}$  is a positive constant. The limit of the distributed power to gas devices is

$$P_{i,t}^{\text{DP2G-min}} \leq P_{i,t}^{\text{DP2G}} \leq \frac{1}{n} \times P^{\text{network}}, \quad (19)$$

where  $P_{i,t}^{\text{DP2G-min}}$  is the start-stop constraint of the distributed power to gas devices,  $P^{\text{network}}$  is the surplus power rate in the network of EL. The models, operating cost functions, and limits of the distributed electric boiler are similar to that

of the distributed power to gas devices. We only need to replace gas with heat.

**2.4.2. The Distributed Gas Combined Heat and Power Device Models.** The model and operating cost functions of the distributed gas combined heat and power devices are as follows:

$$\begin{aligned} P_{i,t}^{\text{DGC}} &= \eta_i^{\text{DGC}} G_{i,t}^{\text{DGC}} \frac{1}{\phi_{i,t}^{\text{DGC}} + 1}, \\ H_{i,t}^{\text{DGC}} &= \eta_i^{\text{DGC}} G_{i,t}^{\text{DGC}} \frac{\phi_{i,t}^{\text{DGC}}}{\phi_{i,t}^{\text{DGC}} + 1}, \\ \phi_{i,t}^{\text{DGC}} &= \frac{Prh}{Prp}, \\ C_{i,t}^{\text{DGC}} &= \theta_{i,t}^{\text{DGC}} G_{i,t}^{\text{DGC}}, \end{aligned} \quad (20)$$

where  $P_{i,t}^{\text{DGC}}$  and  $H_{i,t}^{\text{DGC}}$  are the power and heat rates of the distributed gas combined heat and power devices generation,  $G_{i,t}^{\text{DGC}}$  is the gas rate of coal of the distributed gas combined heat and power devices consumption,  $\eta_i^{\text{DGC}}$  is the energy conversion of the distributed gas combined heat and power devices, and  $\phi_{i,t}^{\text{DGC}}$  is the ratio of heat and power. The constraints of the distributed gas combined heat and power devices is:  $G_{i,t}^{\text{DGC-min}} \leq G_{i,t}^{\text{DGC}} \leq (1/n) \times G^{\text{network}}$ , which is similar to that in the distributed power to gas devices. The constraints of  $\phi_{i,t}^{\text{DGC}}$  is similar to that in the distributed coal or oil combined heat and power devices.

## 2.5. The Distributed Energy Storage Devices Models and Cost Functions

**2.5.1. The Distributed Energy, the Distributed Power Store Device, the Distributed Heat Storage Devices, and the Distributed Gas Storage Device Models.** The distributed power storage devices have an optimal condition about reserve of stored power. If the stored power is less than optimal condition too much, it will harm batteries and other devices. If stored power is more than optimal condition too much, the stored power will loss too much. So, the optimal performance of the distributed power store device is

$$O_{i,t}^{\text{DPSD}} = a_i^{\text{DPSD}} P_{i,t}^{\text{S-DPSD}} (P_{i,t}^{\text{S-DPSD}} - 2\mu_i^{\text{DPSD}}) + b_i^{\text{DPSD}}, \quad (21)$$

where  $O$  is the optimal function of the reserved power in the distributed power store device,  $P_{i,t}^{\text{S-DPSD}}$  is the stored power in time  $t$ ,  $\mu_i^{\text{DPSD}}$  is the optimal reserve power in the distributed power store device,  $a_i^{\text{DPSD}}$  and  $b_i^{\text{DPSD}}$  are constants, and  $a_i^{\text{DPSD}}$  is a negative constant. The cost function of the distributed power store device is

$$C_{i,t}^{\text{DPSD}} = O_{i,t}^{\text{DPSD}} - O_{i,t-1}^{\text{DPSD}} + \theta_{i,t}^{\text{DPSD}} \|P_{i,t}^{\text{DPSD}}\|_2, \quad (22)$$

where  $\theta_{i,t}^{\text{DPSD}}$  is a positive constant and  $P_{i,t}^{\text{DPSD}}$  is the power rate of the distributed power store device. If  $P_{i,t}^{\text{DPSD}}$  is positive, it expresses power output, vice versa. So, we can know

$$P_{i,t}^{\text{DPSD}} = P_{i,t-1}^{\text{S-DPSD}} - P_{i,t}^{\text{S-DPSD}}. \quad (23)$$

The distributed power store device needs to satisfy the limits below:

$$\begin{aligned} -P_i^{\text{in-DPSD}} &\leq P_{i,t}^{\text{DPSD}} \leq P_i^{\text{out-DPSD}}, \\ P_i^{\text{min-S-DPSD}} &\leq P_{i,t}^{\text{S-DPSD}} \leq P_i^{\text{max-S-DPSD}}, \end{aligned} \quad (24)$$

where  $P_i^{\text{in-DPSD}}$  and  $P_i^{\text{out-DPSD}}$  are the maximum limits of power input and output rate of the distributed power store device, and  $P_i^{\text{min-S-DPSD}}$  and  $P_i^{\text{max-S-DPSD}}$  are capacity minimum and maximum values, respectively.

The models, operating cost functions, and limits of the distributed heat storage devices and the distributed gas storage devices are similar to that of the distributed power store device. We only need to replace power with heat or gas.

The energy loss in the distributed energy transform devices is very loss, for convenience, so we ignored that.

**2.6. Energy Load Models.** The must-run load and controllable load which traditional research including Ref. [20, 21] adopts may be unsuitable for EI because of several reasons that I proposed in the preceding part of this study. So, we only adopt  $P_{i,t}^{\text{EL}}$ ,  $H_{i,t}^{\text{EL}}$ , and  $G_{i,t}^{\text{EL}}$  to represent power heat and gas

loads. If EI supplies less energy to WEs than which they need, the terminal users' energy demand will not be satisfied. But if EI supplies more energy to WEs than which they need, it will waste a lot of energy. So, the operating cost of EL depends on the unbalance between energy supply and demand. The cost function of power EL is as follows:

$$\begin{aligned} C_t^{\text{P-EL}} &= \theta_{i,t}^{\text{P-EL}} \left\| P_{i,t}^{\text{supply}} - P_{i,t}^{\text{EL}} \right\|_2^2, \\ \theta_{i,t}^{\text{P-EL}} &= \begin{cases} \theta_{1,t}^{\text{P-EL}}, P_{i,t}^{\text{supply}} \leq P_{i,t}^{\text{EL}}, \\ \theta_{2,t}^{\text{P-EL}}, P_{i,t}^{\text{supply}} \geq P_{i,t}^{\text{EL}}, \end{cases} \end{aligned} \quad (25)$$

where  $\theta_{1,t}^{\text{P-EL}}$  and  $\theta_{2,t}^{\text{P-EL}}$  are two positive constants. The reason for dividing  $\theta_{i,t}^{\text{P-EL}}$  into  $\theta_{1,t}^{\text{P-EL}}$  and  $\theta_{2,t}^{\text{P-EL}}$  is that the harm of surplus and lack of power is different. The cost functions of heat and gas are similar to that of power. The only difference is the type of energy.

**2.7. Object Functions.** This study focuses on the economical optimization by energy management in WEs and EI. So, the object function is used to co-planning all WEs to realize the maximize of the economy in (22):

$$\max F = \sum_{i=1}^n (W_{i,t}), \quad (26)$$

$$W_{i,t} = \sum_{j=1}^m (\text{Pr}p \times \Delta P_i^j + \text{Pr}h \times \Delta H_i^j + \text{Pr}g \times \Delta G_i^j - \text{Pr}f \times F_i^j - C_i^j), \quad (27)$$

where  $W_{i,t}$  is the economy function of each WE;  $j$  is the serial number of each devices in WE;  $\text{Pr}g$  and  $\text{Pr}f$  are price of gas and coal;  $\Delta P_i^j$ ,  $\Delta H_i^j$ , and  $\Delta G_i^j$  are energy flow rate of power, heat, and gas, respectively. If they are positive, it means that the devices output the corresponding energy, vice versa. Of course, they can be zero.  $F_i^j$  is consumption of coal, which is non-negative.  $C_i^j$  is the operating cost function of devices.

### 3. The Annular Directed Distributed Algorithm and Its Certifications

**3.1. Basic Knowledge of Graph Theory.** The graph theory adopts  $\text{Graph} = (V, E, B)$  to represent a graph.  $V = \{v_i | i = 1, 2, \dots, n\}$  is a finite nonempty set of nodes in the graph. And the  $E \subseteq V \times V$  is the set of sides. The side  $(v_i, v_j)$  means that there is a side between  $v_i$  and  $v_j$ .  $B = [b_{i,j}] \in R^{m \times n}$  is the weighting neighbor matrix of the graph. The weighting neighbor matrix  $B$  is used to express the relationship between nodes and sides. The diagonal elements in that are all zero constantly. If the non-diagonal element  $b_{i,j} > 0$ ,  $(v_i, v_j) \in E$ . But if  $b_{i,j} = 0$ ,  $(v_i, v_j) \notin E$ . In the undirected graph, sides between nodes are not directed, so  $(v_i, v_j) \in E$  equals to  $(v_j, v_i) \in E$ . The paths between  $v_i$  and  $v_j$

consist of a lot of sides like  $(v_i, v_{i1}), (v_{i1}, v_{i2}) \dots (v_{ik}, v_j)$ . If there is a path between  $v_i$  and  $v_j$ , we define that  $v_i$  and  $v_j$  are connected. If entire pairs of nodes are connected, we define that the graph is connected. If all elements in  $B$  except diagonal elements are positive, the graph is complete.

**3.2. The Relationship between Graph Theory and EI.** Traditional researches [19, 20] use an undirected connected graph to model EI, use nodes to model WE or other agents about energy microgrid, and use sides to model channels which can transfer information and energy because they think the undirected connected graph can not only control all WEs in EI due to the path between entire pairs of nodes but also protect users' privacy data which could only be acquired by neighbor nodes. They may be right to some extent. Agents in the unconnected graph cannot communicate among all nodes and that in the complete graph cannot protect users' privacy. But that model has some serious disadvantages. Firstly, agents' privacy data can be acquired by neighbor agents, which cannot protect users' privacy entirely. Secondly, only-neighbor communicating causes a lot of trouble for the distributed algorithm in comparison with that in the complete graph. As for solving

this problem, some researches pursue the consensus of tiny growth rate about voltage, air pressure in gas pipeline, and flow of hot water [29]. Although the consensus makes the distributed algorithms easily, it may not be the most optimal method for energy management. Thirdly, if an agent is strict with privacy and unwilling to communicate with other agents, the only way is to segment it from the whole system of EI. That agent will be operated in island mode and other agents will be operated in grid-connected mode, which is very bad for unifying dispatch of EI. Fourthly, only-neighbor energy transformation leads to a lot of energy loss and operating costs. Information has privacy, but energy flow does not have, after all! Last but not least, the connected but most complete graph is not well distributed in compactness, which is very bad for controllability of EI in accordance with the theory [24] proposed.

For solving these problems, this study proposed a new algorithm named the annular directed distributed algorithm. In the annular directed distributed algorithm, the path of information and energy is separate. The information path is a directed annular path, which is shown in Figure 1 and the hole energy path constitutes an undirected complete graph. After ensuring all devices' operating conditions, how to transmit corresponding energy from the supply side to the demand side will be an elementary math problem that does not need algorithms. So, the most significant problem of energy management in the annular directed distributed algorithm is how to ensure devices' optimal operating condition in the information side.

**3.3. Main Algorithm.** The proposed management in the annular directed distributed algorithm is to ensure devices' optimal operating condition in the information side. The main algorithm is shown in Table 1. The method in step 12 is:

If we want to change the type  $a$  of energy to the type  $b$  of energy, the energy input will be updated by the method that:

$$I_{a,i,t}^{k+1} = I_{a,i,t}^k \left[ dh \left( \frac{\eta_a^b \times Prb}{Pra + \theta_a^b} - 1 \right) + 1 \right], \quad (28)$$

where  $I$  is the input of energy  $a$  (the starting value of  $I$  is initialized by step 3),  $k$  is the number of iteration times,  $\eta_a^b$  is the efficiency of energy conversion, and  $Pra$  and  $Prb$  are the energy prices of energy  $a$  and  $b$ . What is noteworthy is that if a device can change one type of energy to two or more types of energies, the price of output energies is the weighted average of all output energies, and weighted factors are the rate ratio of that energy to hole output energies.  $\theta_a^b$  is the energy conversion price from energy  $a$  to energy  $b$ ,  $dh$  is a downhill factor whose effect is to adjust devices' operating condition in case of divergence of the annular directed distributed algorithm.  $dh$  does not change between different types of the distributed energy conversion devices, the starting value in each iteration of  $dh$  is 1, and the updating conditions and methods of that will be introduced below.

The method in step 14 is as follows:

$$\begin{cases} P_{i,t}^{\text{supply}} = P_{i,t}^r \times P_{x,t}, \\ H_{i,t}^{\text{supply}} = H_{i,t}^r \times H_{x,t}, \\ G_{i,t}^{\text{supply}} = G_{i,t}^r \times G_{x,t}. \end{cases} \quad (29)$$

where  $P_{i,t}^{\text{supply}}$ ,  $H_{i,t}^{\text{supply}}$ , and  $G_{i,t}^{\text{supply}}$  are the power, heat, and gas which the energy management supplied to energy load in  $i$ th WE, respectively. But they may not be equal to  $P_{i,t}^{\text{EL}}$ ,  $H_{i,t}^{\text{EL}}$ , and  $G_{i,t}^{\text{EL}}$ . So, we should adjust energy prices. We use cost functions of ELs as subgradient functions to adjust the energy price. We adjust power price like Figure 2.  $w$  in Figure 2 is a small positive constant, which may be different with different types of energy. By the way, the precision of  $Psd$  and  $Psm$  is no possibility infinite in practical engineering, so if they are very less theoretically, we regard them as zero.  $r$  is another Newton-downhill factor about avoiding overshoot, if one type of energy supply-demand mismatch changes symbol,  $r = 0.5 \times r$ .

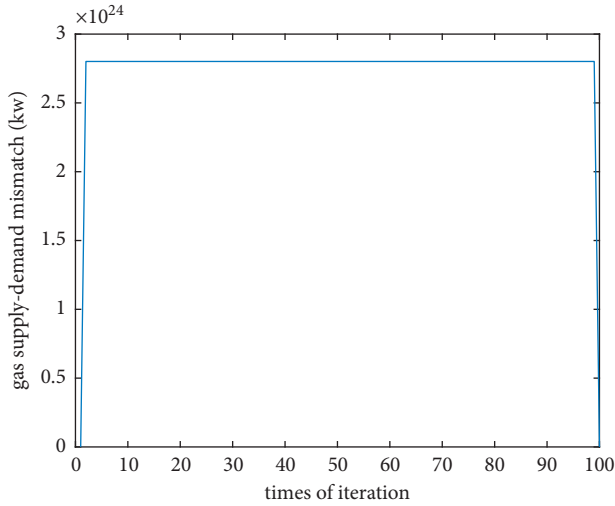
The method to adjust the price of gas and heat is similar to that of power, so we only need to change the energy type. After price adjustment, we should inspect the astringency of the algorithm. Whichever supply-demand mismatching in all types of energy absolute value in  $k + 1$  times of iteration is more than that in  $k$  times of iteration, or supply-demand mismatching in all types of energy value changes symbol, the result in step 14 must be invalid. The algorithm will return step 12 or step 3, respectively, and energy management will amend downhill factor  $dh$  or  $r$  to half of quondam value and repeat processes above until all energy supply-demand mismatching absolute value in  $k + 1$  times of iteration is no more than that in  $k$  times of iteration. Besides, the value of  $dh$  or  $r$  in  $k$  times of iteration should not be retained into  $k + 1$  times of iteration. It will initialize into 1 again in that. What is always ignored by traditional research but is very significant to energy management is there is a problem of Zeno behavior. Zeno behaviors mean some operation is triggered infinite times in finite times of iteration. In the annular directed distributed algorithm, Zeno behaviors are that the frequency of that  $r$  or  $dh$  change is too high in one time of iteration.

It is worth noting that, because accuracy in down-to-earth engineering is limited, if the energy supply-demand mismatch is very less, we can regard energy supply-demand balance as achieved and stop algorithm. Besides, if we do not stop the algorithm in that circumstance, the algorithm result may be choppy near the exact value due to the energy mismatch is less than that the small positive constant  $w$  adjusted.

Four things need to be added. Firstly, after one time of iteration, the sequence of WEs should be changed. The  $i$ th WE will be the  $(i + 1)$ th WE, and the first WE will be the last WE. We should transmit all information from the old first WE to the new first WE before iteration. The reason for that is too much control and computing load is at the last WE. Changing the sequence can relieve the load of the last WE. Besides, it can also increase the precision and universality of algorithm results. Secondly, all initialized energy flow and energy load flow is needed to be initialized over and over

TABLE 1: Annular distributed algorithm.

- 
- Initialize and iterate: ( $k = 1, i = 1, r = 1, dh = 1$ );
- (1) Set initial value of  $Prp, Prh, Prg, w$ .
  - (2) Input all reserves of stored energy of each of the distributed energy store devices in time  $t - 1$ .
  - (3) Set initial value of energy input of all the distributed energy conversion devices in a small value in all WEs, including  $P_{i,t}^{DP2G}, P_{i,t}^{DEB}$ , and  $G_{i,t}^{DGC}$ .
  - (4) Initialize power-gas-heat energy flow  $P_{x,t}, H_{x,t}$ , and  $G_{x,t}$  and power-gas-heat energy load flow  $P_{L,t}^{all}, H_{L,t}^{all}$ , and  $G_{L,t}^{all}$ . Input them into control center of terminal load in first WE. Turn to first WE.
  - (5) Store  $P_{x,t}, H_{x,t}, G_{x,t}, P_{L,t}^{all}, H_{L,t}^{all}$ , and  $G_{L,t}^{all}$  by the designations of  $P_{x,t}^s, H_{x,t}^s, G_{x,t}^s, P_{L,t}^{S-all}, H_{L,t}^{S-all}$ , and  $G_{L,t}^{S-all}$  in control center of terminal load in first WE.
  - (6)  $P_{L,t}^{all}, H_{L,t}^{all}$ , and  $G_{L,t}^{all}$  equals to the sum of corresponding type of energy loads of  $i$ th WE and corresponding  $P_{L,t}^{all}, H_{L,t}^{all}$ , and  $G_{L,t}^{all}$ .
  - (7) If  $i < n, i = i + 1$ , transmit  $P_{L,t}^{all}, H_{L,t}^{all}$ , and  $G_{L,t}^{all}$  to  $i$ th WE, and return step 6, else, continue.
  - (8) If  $i = 1$ , transmit  $P_{L,t}^{all}, H_{L,t}^{all}$ , and  $G_{L,t}^{all}$  to control center of terminal load in first WE.  $P_{L,t}^{all}, H_{L,t}^{all}$ , and  $G_{L,t}^{all}$  is equal to themselves subtracting corresponding  $P_{L,t}^{S-all}, H_{L,t}^{S-all}$ , and  $G_{L,t}^{S-all}$  which are stored in first WE.
  - (9) Compute and store ratios of load to  $P_{L,t}^{all}, H_{L,t}^{all}$ , and  $G_{L,t}^{all}$  by the designations of  $P_{i,t}^r, H_{i,t}^r$ , and  $G_{i,t}^r$  in control center of terminal load in  $i$ th WE.
  - (10) If  $i < 5, i = i + 1$ , transmit  $P_{L,t}^{all}, H_{L,t}^{all}$ , and  $G_{L,t}^{all}$  to  $i$ th WE, and return step 9, else,  $i = 1$ , continue.
  - (11) Update entire operating conditions containing energy input or output volumes of all the distributed energy producer and the distributed energy store devices in  $i$ th WE to the value that (26) and (27) can get peak value. Because all parts of (27) are linear or non-convex, the work is very easy and does not need complex algorithm.
  - (12) Update entire operating conditions containing energy input or output volumes of all the distributed energy conversion devices in  $i$ th WE by method described below.
  - (13) Add all energy input and output volumes in all the distributed energy producer, the distributed energy conversion devices, and the distributed energy store devices in  $i$ th WE to  $P_{x,t}, H_{x,t}$ , and  $G_{x,t}$ . If  $i < n, i = i + 1$ , transmit the volumes of  $P_{x,t}, H_{x,t}$ , and  $G_{x,t}$  to  $i$ th WE and return to the step 11, else  $i = 1$ , transmit the volumes of  $P_{x,t}, H_{x,t}$ , and  $G_{x,t}$  to  $i$ th WE, continue.
  - (14) If all types of energy supply-demand balance are reached, energy management finishes, else, if one type of energy supply-demand mismatch absolute value is higher than that in last time of iteration,  $dh = 0.5 \times dh$ , return step 11, else, if one type of energy supply-demand mismatch changes symbol,  $r = 0.5 \times r$ , return step 3, else,  $r = 1, dh = 1, k = k + 1$ , return step 11.
- 

FIGURE 1: Gas supply-demand mismatch (kw) in 100 times of  $w$ .

again in each iteration. The annular directed distributed algorithm has a great advantage in which it can protect each user's privacy much better than traditional EI or traditional multiagent systems [25–27].

Although preceding researchers can protect users' privacy which cannot be searched by all agents, neighbor agents still can access their private data. But in the annular directed distributed algorithm, all agents can only access total before themselves. However, the privacy of the first agent cannot be protected by this method, hence we use fictitious initial

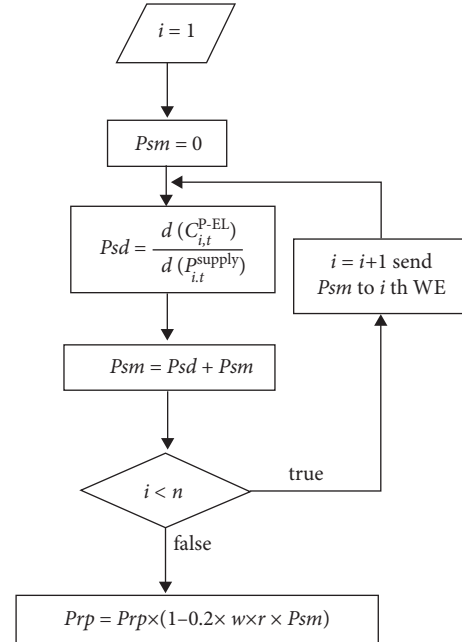


FIGURE 2: Power price adjusting.

energy flows to protect it. For reinforcing the confidentiality of privacy data, initial energy flows should be changed each iteration. Thirdly, privacy protecting is needed not only among different WEs, but also inside WEs. The information inside WEs transmitted in one directed line whose direction is identical to the direction of the information path between



WEs. Fourthly, although the annular information path has numerous advantages, it is exceeding sensitive to malfunctions. For handling this issue, if a device in one WE is broken down, the energy load in that WE will operate by island mode and other WEs will operate by a mode combined to the grid as normal. Finally, in the annular directed distributed algorithm, the information path is different from the energy transmission path. The energy transmission path is independent of privacy protecting, so all devices can transmit energy to others. After realizing a balance between energy supply and energy demand, how to transmit energy in the shortest way is an easy problem which does not need complex algorithms, so this study does not discuss energy transmission path. It is worth noting that the optimization in this article is distributed. The principle is to adjust energy price to change the energy mismatch. If the adjust of energy price is overshoot to the optimization valve, the algorithm will be oscillation or divergency and the energy supply-demand balance will never be reached. So, we should adopt the Newton-downhill method to avoid the overshoot of energy price.

We list the data exchange and privacy protection that is required by the proposed distributed algorithm and conventional distributed methods in Tables 2 and 3 (✓ for entirely exchanging, ✗ for not exchanging, ● for cryptographically exchanging) (✓ for protecting, ✗ for not protecting).

From that two tables you can know that the proposed algorithm can protect the data of power-heat-gas output or input conditions of each device better. It is worth noting that, all manufactures of one type of energy are commercial competitors, so are all we-energies. So, it is unreasonable for conventional distributed methods to regard some energy manufactures and some we-energies as neighbor agents and exchange data among them. The data cryptographically exchanging method in this article is a better method.

#### 4. Testification of Convergence Analysis, Optimality, and Avoiding Zeno Behaviors

The convergence of the algorithm and the balance between energy supply and energy demand are proved below.

Firstly, we establish an assumption that the operating condition of the distributed energy conversion devices in  $k + 1$  times of the iteration is equal to those in  $k$  times of the iteration. Under that circumstance, all energy supply-demand is decided by formula (27). We discuss power supply-demand as an example. We can calculate power input or output in each of the distributed energy producer and the distributed energy store devices by solving the partial differential equation below.

$$\frac{\partial(W_{i,t})}{\partial(\Delta P_i^j)} = 0. \quad (30)$$

And we can disassemble  $W_{i,t}$  by:

$$Q = \sum_{j=1}^m (\text{Pr}h \times \Delta H_i^j + \text{Pr}g \times \Delta G_i^j - \text{Pr}f \times F_i^j - C_i^j), \quad (31)$$

$$W_{i,t} = \sum_{j=1}^m (\text{Pr}p \times \Delta P_i^j + Q).$$

So, we can transform (28) into

$$\frac{\partial(Q)}{\partial(\Delta P_i^j)} = -\text{Pr}p. \quad (32)$$

Due to the non-convex of  $Q$ ,  $\partial(Q)/\partial(\Delta P_i^j)$  is a decreasing function. If power is excess in EI, the price of that will decrease. So, the solution of (32) will be less, vice versa. Moreover, because of the downhill factor  $r$ , if overshoot will never appear,  $r$  will reduce until overshoot vanishes. And the change of  $r$  only alters the adjusting extent of power price but does nothing about adjusting the direction of that. So  $r$  does not affect the monotonicity of power price. It is worth noting that the monotonicity of power price aims at power price when adjusting of  $r$  finishes. The power price of the overshoot systems needs to be abandoned so it is meaningless to energy management. Above all, we can draw a conclusion in line with mathematical induction that under the assumption that the operating condition of the distributed energy conversion devices in  $k + 1$  times of the iteration is equal to that in  $k$  times of the iteration, the power price, which is one of the results of the algorithm, is monotone. However, without the assumption, is the power price monotone? The answer is right. A contradiction method is used to prove it.

First of all, we set up an assumption that the power price is not monotone. So, step 12 to step 14 will be an endless loop and  $dh$  will be halved over and over again. Hence,

$$dh = \lim_{m \rightarrow +\infty} \left(\frac{1}{2}\right)^m = 0. \quad (33)$$

So, the operating condition of the distributed energy conversion devices in  $k + 1$  times of the iteration is equal to that in  $k$  times of the iteration. On the basis of the conclusions mentioned above, the algorithm is monotone, which is in contradiction with the assumption at the beginning of the contradiction method. So, we can prove that the power price is monotone. It is worth noting that the proof process does not contain the circumstance that when the power supply-demand mismatch tends to a very small value. If that mismatch is very small, we will deem that the power supply-demand is balanced and we will regard it and  $Psm$  as zero in practical engineering. Due to the finite precision of measurement and operation in practice, it is useless to discuss the small power supply-demand mismatch.

Because  $w$  is small, power supply-demand mismatch cannot change direction without going through a small value. And due to the reason above, if that is small, we will regard  $Psm$  as 0 so the power price will not update. So, the power price is unilateral bounded and the bound is the value when that mismatch is exceedingly small.

TABLE 2: Privacy protecting between we-energies.

Type of data exchange among neighbor we-energies	The proposed distributed algorithm	Conventional distributed methods	Privacy protection for that data in proposed distributed algorithm	Privacy protection for that data in conventional distributed methods
Power output or input ratio	●	✓	✓	✗
Heat output or input ratio	●	✓	✓	✗
Gas output or input ratio	●	✓	✓	✗
Power price	✓	✓	✗	✗
Heat price	✓	✓	✗	✗
Gas price	✓	✓	✗	✗

TABLE 3: Privacy protecting inside we-energies.

Type of data exchange inside each we-energy	The proposed distributed algorithm	Conventional distributed methods	Privacy protection for that data in proposed distributed algorithm	Privacy protection for that data in conventional distributed methods
Power output or input ratio	●	✓	✓	✗
Heat output or input ratio	●	✓	✓	✗
Gas output or input ratio	●	✓	✓	✗
Power price	✓	✓	✗	✗
Heat price	✓	✓	✗	✗
Gas price	✓	✓	✗	✗

In accordance with the monotone-bounded convergence theorem and conclusions all above, we can prove that the power price is convergence. We can figure out the value of power price when it is convergence by the way that:

$$\begin{cases} \Pr p_{k+1} = \Pr p_k \times (1 - 0.2 \times w \times Psm), \\ \Pr p_{k+1} = \Pr p_k. \end{cases} \quad (34)$$

So,  $Psm = 0$ , the price of power will converge to a value that can make the power supply-demand balance. Similarly, the price of heat and gas will converge to a value that can reach the heat or gas supply-demand balance, too. The proving process of them are analogical to that of power, and we only need to change the types of energy. To sum up, after numerous times of iteration, all types of energy prices are converged and all kinds of energy are balanced between energy supply and energy demand. EI is stabilized.

The optimality of the convergence point in the annular directed distributed algorithm is proved below.

Similar to convergence proving, the attesting of optimality in energy management needs to prove optimality about power systems without energy conversion first.

$$\frac{\partial(W_{i,t})}{\partial(P_i^j)} = \Pr p - \frac{d(C(P))}{d(P)}. \quad (35)$$

Because  $C(P)$  is a convex function,  $d(C(P))/d(P)$  is an increasing function. Step 11 in the annular directed distributed algorithm requires all power-producing devices to choose operating conditions when  $d(C(P))/d(P) = \Pr p$ . At the convergence point, power supply-demand balance is

satisfied. We assume another operating condition of EI as device  $A$  produce  $\Delta P$  power less than its power-producing in the annular directed distributed algorithm. For maintaining power supply-demand balance, device  $B$  will produce  $\Delta P$  power more. Cost decrease in  $A$  is  $\Delta P \times \Delta C_A(\Delta P)$ .  $\Delta C_A(\Delta P)$  is backward difference gradient in the convergence point of device  $A$ . Analogically, cost decrease in  $B$  is  $\Delta P \times \Delta C_B(\Delta P)$ .  $\Delta C_B(\Delta P)$  is forward difference gradient in the convergence point of device  $B$ . Because all  $C(P)$  are convex functions,  $\Delta C_A(\Delta P) < \Pr p < \Delta C_B(\Delta P)$ . So, the convergence point is optimal for power without energy conversion. By the same token, the convergence point is optimal for heat and gas without energy conversion. And we should prove optimality among energy conversion.

Because  $w$  is a very small constant, energy price in a large number of iteration only changes a little. Hence, the speed of energy price changing is much lower than that of energy conversion changing so that we can ignore the change of energy price when we study energy conversion. If  $\eta_a^b \times \Pr b$  is more than  $\Pr a + \theta_a^b$ , due to (28), there is more and more energy that changes from  $a$  to  $b$  until  $\eta_a^b \times \Pr b$  is equal to  $\Pr a + \theta_a^b$ . Thereafter,  $\eta_a^b \times \Pr b$  is equal to  $\Pr a + \theta_a^b$  though the hole iteration. Whenever energy price changes a little, energy conversion will change at a far high speed to reach equality between  $\eta_a^b \times \Pr b$  and  $\Pr a + \theta_a^b$  and goes along with slowly energy price changing. That equality is still satisfied until convergence point. By the way, because of the difference between that two speeds, frequency about adjusting of  $dh$  is much less than that of  $r$ . So, Zeno behavior never happens in  $dh$ . However, the Zeno behavior never happens in  $r$ , either. And the reason for it will be described in this literature, too.



We assume another operating condition of EI as energy  $a$  transforms  $\Delta a$  energy less than its energy conversion in the annular directed distributed algorithm. For maintaining power supply-demand balance, energy management should produce  $\Delta a$  energy  $a$  less and produce  $\eta_a^b \times \Delta a$  energy more. The cost decrease in producing and transforming in  $a$  is  $\Delta a \times (\Delta C_a(\Delta a) + \theta_a^b)$ . And the cost increase in producing in  $b$  is  $\Delta a \times \eta_a^b \times \Delta C_b(\Delta a \times \eta_a^b)$ .  $\Delta C_a(\Delta a)$  and  $\Delta C_b(\Delta a \times \eta_a^b)$  are difference gradients. Because all  $C$  are convex functions,  $\Delta C_a(\Delta a) + \theta_a^b < \text{Pr}a + \theta_a^b = \eta_a^b \times \text{Pr}b < \Delta C_b(\Delta a \times \eta_a^b) \times \eta_a^b$ . So  $\Delta a \times (\Delta C_a(\Delta a) + \theta_a^b) < \Delta a \times \eta_a^b \times \Delta C_b(\Delta a \times \eta_a^b)$ , energy conversion in the convergence point is optimal. In addition, equal relations mentioned above do not consider the influence of constraint. So, it is no wonder that in reality EI project,

To sum up, the convergence point in the annular directed distributed algorithm has optimality.

Avoiding Zeno behavior of the annular directed distributed algorithm is proved below:

On account of the reason in the preceding part of this literature, Zeno behavior never happens in  $dh$ . But Zeno behavior in  $r$  still needs analysis.

If overshoot happens, energy overshoot and energy mismatch in the last time of iteration are all finite for the reason of if they are infinitely small we will regard them as zero and energy supply-demand are reached. (Both infinitely small and infinitely great are all infinite.) The adjusting of energy price can be calculated through linear or quadratic functions (all functions in this literature are linear or quadratic) by four fundamental rules, gradient rules, and inverse function rules from finite values (energy overshoot and energy mismatch in last time of iteration). Hence, they are finite, and so adjusting times of  $r$  in one or finite times of iteration is finite, thus Zeno behavior does not happen in  $r$  or  $dh$ .

To sum up, the annular directed distributed algorithm is not only optimal but also convergence. In addition, Zeno behavior never occurs in it.

## 5. Simulation Results

The framework of the EI system used to test the annular directed distributed algorithm containing 5 WEs and data of devices all above are exhibited in Appendix. In this article, if all the types of energy mismatches are less than 500kw, we think of the balance of energy-producing and energy-consuming as achieved and regard  $Psm$  as zero. After 42 times of iteration, that balance is reached. The simulation results are discoursed below

Figures 3–5 are prices of power, heat, and gas. Figures 6–8 are supply-demand mismatches of power, heat, and gas. The Zeno coefficient is times of  $r$  adjusting. It shows that after 42 times of the iteration, when the Zeno coefficient is 2, power, heat, and gas mismatch are all lower than 500kw. At this moment  $\text{kw} \cdot \text{h}$ , the power mismatch is 462kw less. The heat mismatch is 387kw more. And the gas mismatch is near zero in experimental precision. Comparing with traditional distributed algorithm 28 which needs hundreds of times to reach energy supply-demand balance, the annular

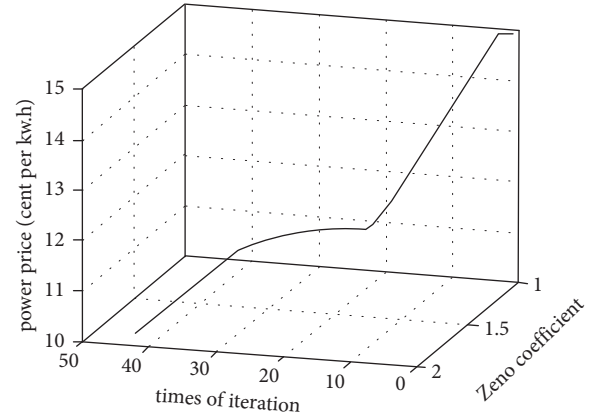


FIGURE 3: Power price.

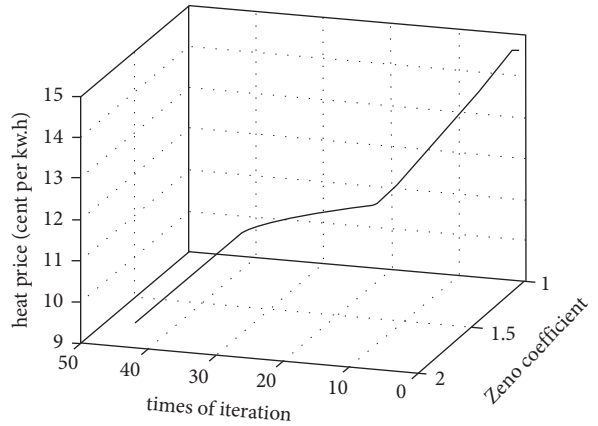


FIGURE 4: Heat price.

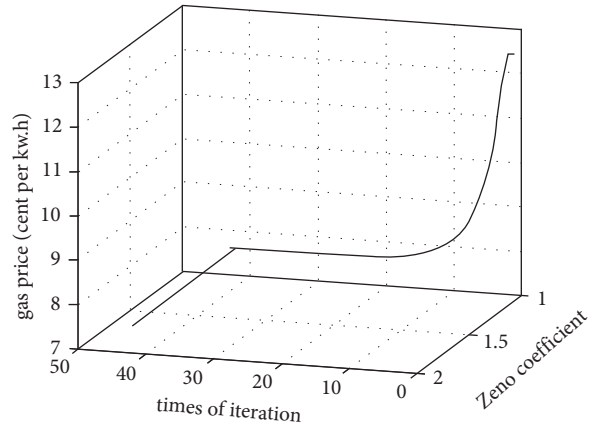


FIGURE 5: Gas price.

directed distributed algorithm is exceedingly quick. EI system should fix the prices of power heat and gas as 11 ¢ per  $\text{kw} \cdot \text{h}$ , 9 ¢ per  $\text{kw} \cdot \text{h}$ , and 8 ¢ per  $\text{kw} \cdot \text{h}$ . (Due to accuracy of USA dollars, retain prices to integral multiples.) Figures 9 and 10 are times of  $r$  and  $dh$  adjusting in each time of iteration. Times of those are no more than twice as they show. So, Zeno behavior does not appear. 11 and 12 are the

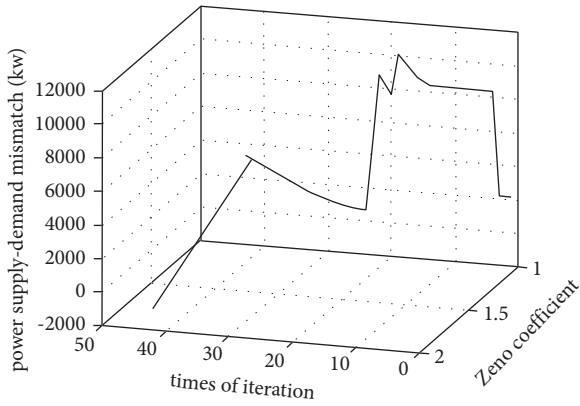


FIGURE 6: Power supply-demand mismatch.

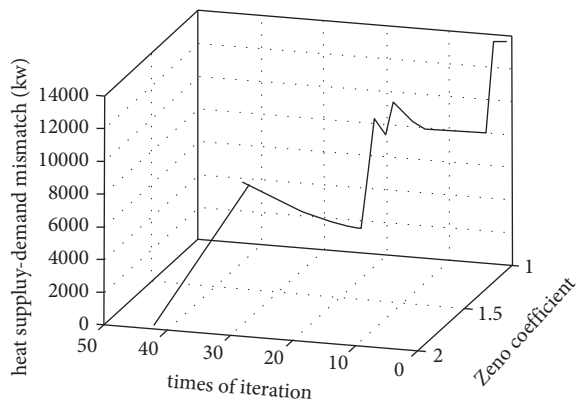


FIGURE 7: Heat supply-demand mismatch.

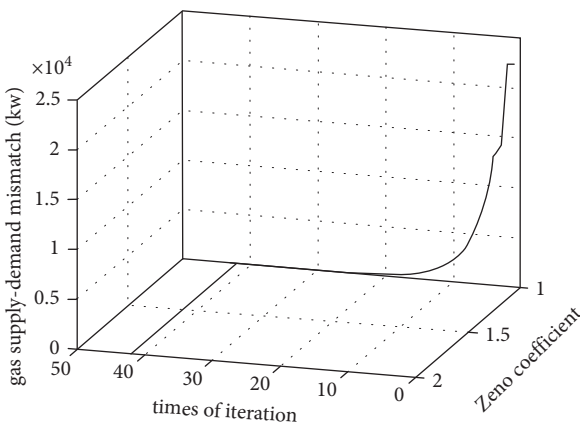


FIGURE 8: Gas supply-demand mismatch.

power-heat-gas mismatch in 100 times of  $w$ , and Figures 13–15 are the power-heat-gas mismatch in 0.01 times of  $w$ . They show that if the value of  $w$  is too large, the algorithm will vibrate seriously. If the value of  $w$  is too small, the algorithm will converge in a very slow speed. So, the algorithm in this article is very sensitive to the value of  $w$ . To this end, the plug and play performance of the proposed distributed method is low because if the EI framework and the energy load changes largely, it is very hard for us to

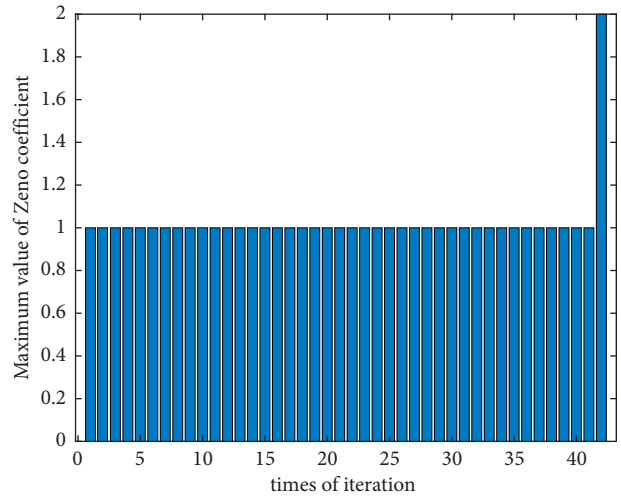


FIGURE 9: Maximum value of the Zeno coefficient.

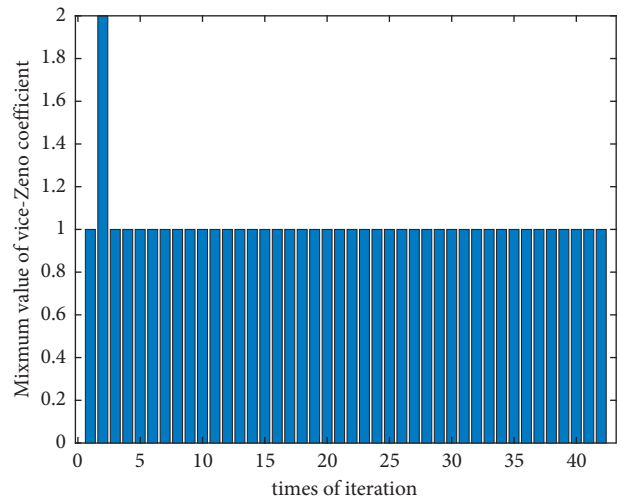


FIGURE 10: Maximum value of the vice-Zeno coefficient.

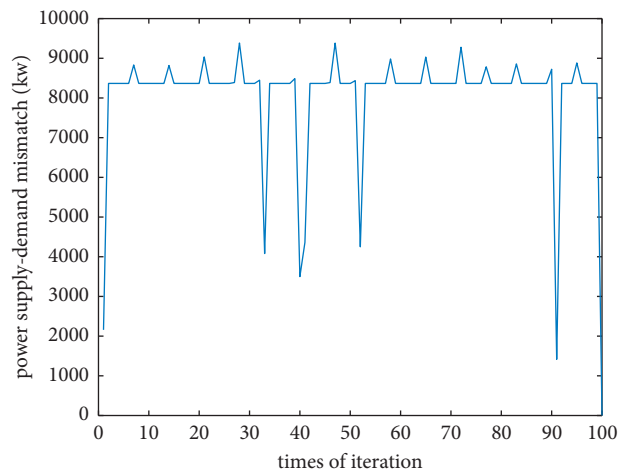
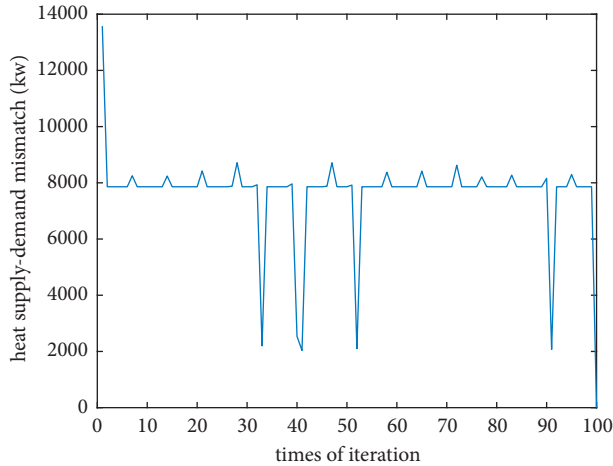
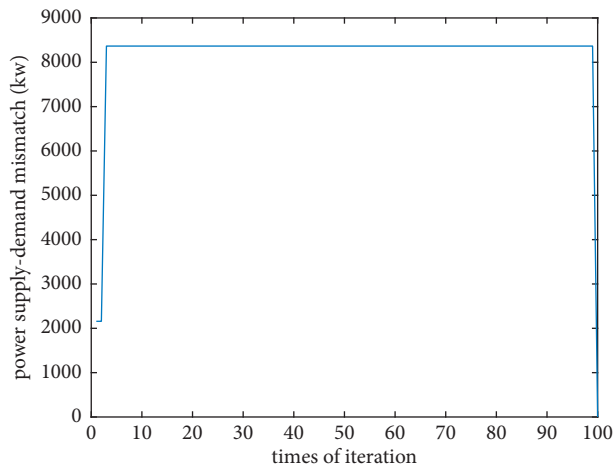
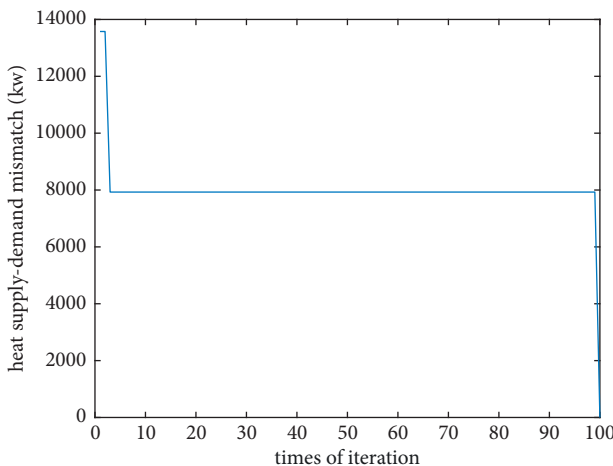
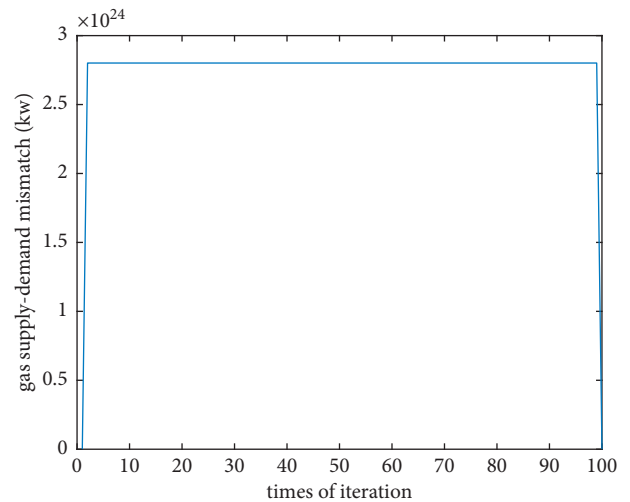


FIGURE 11: Power supply-demand mismatch (kw) in 100 times of  $w$ .

FIGURE 12: Heat supply-demand mismatch (kw) in 100 times of  $w$ .FIGURE 13: Power supply-demand mismatch (kw) in 0.01 times of  $w$ .FIGURE 14: Heat supply-demand mismatch (kw) in 0.01 times of  $w$ .FIGURE 15: Gas supply-demand mismatch (kw) in 0.01 times of  $w$ .

adjust  $w$ . What's more, the proposed method ignores energy transmitting cost so some areas which are hard to transmit energy are unsuitable for the proposed method. However, some areas require large demand of privacy protecting, so they must adopt the proposed method.

EI is a new energy system in scientists' conceive. Although EI has got large concern among researchers, there is not an unabridged EI system with a high permeability of renewable energy resources, a large scale of physical system, and a highly interconnected network among different kinds of energy nowadays because it has just been proposed. A lot of cases in articles which are imagined by authors may be absurd and unreasonable in actuality. The only thing we can know is the energy demand. We summarize various energy demands in the world in Table 4 and analyze if they are fit for the proposed algorithm (✓ for fit, ✗ for unfit). Because there are too many kinds of energy demand in the whole world, our work may be incomplete.

A1 is suitable for the proposed distributed method because the business competition in urban is sharp and the privacy protection demand is large. A2 is unsuitable for the proposed method because the energy load is changeable which cause great trouble of  $w$ . A3 is unsuitable for the both traditional and proposed method because the heat and gas transmitting is hard in that area. They need another method about heat and gas transmitting. A4 is suitable for the proposed method because the privacy protecting in that area is important due to political factors. A5 is unsuitable for the proposed method because the privacy protecting in that area is not important. A6 is suitable for the proposed method because the change of that area is very slow and the  $w$  is easy to choose. A7 is suitable for the proposed method because the business competition in that area is serious so the privacy protecting is important. A8 is suitable for the proposed method because the change of that area is very slow so the  $w$  is easy to choose. To sum up, the proposed method is suitable for some cases with high demand of privacy protecting and

TABLE 4: Application scenario analysis.

Serial number	Scene	Regional characteristics	Typical case	Fit for traditional distributed methods	Fit for the proposed distributed method
A1	Suburb type	Small area with low energy demand	Urban	✗	✓
A2	Seasonal switching type	Need heat in winter and cold in summer. The demand of power and gas is large.	Cities in Yangtze plain, middle and lower, China	✓	✗
A3	Cold plateau	The atmospheric pressure is low because of high altitude, and the temperature is cold for the same reason. All energy demands are low.	Qinghai-Tibet plateau, China	✗	✗
A4	Island (in sea)	Wind and petroleum are rich	Nansha six reefs, China	✗	✓
A5	Cold area	Heat load is high	Northeast, China	✓	✗
A6	Mountainous	Energy load is low. Wind and solar are rich.	Southwest, China	✗	✓
A7	High latitude port	DC load of ships is high. Heat load is high because the temperature is cold	Port cities in Northern Europe and North America	✗	✓
A8	Dispersing area	The natural gas is rich, and the energy load is dispersed	Northwest, China	✗	✓

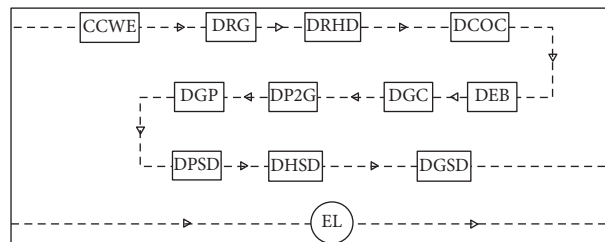


FIGURE 16: We-energy 1.

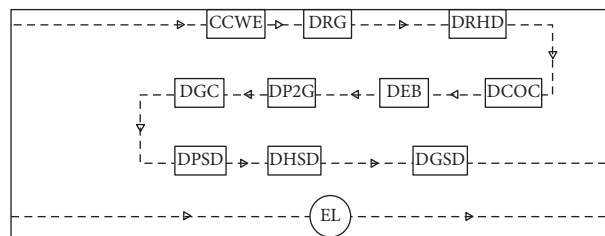


FIGURE 17: We-energies 2-5.

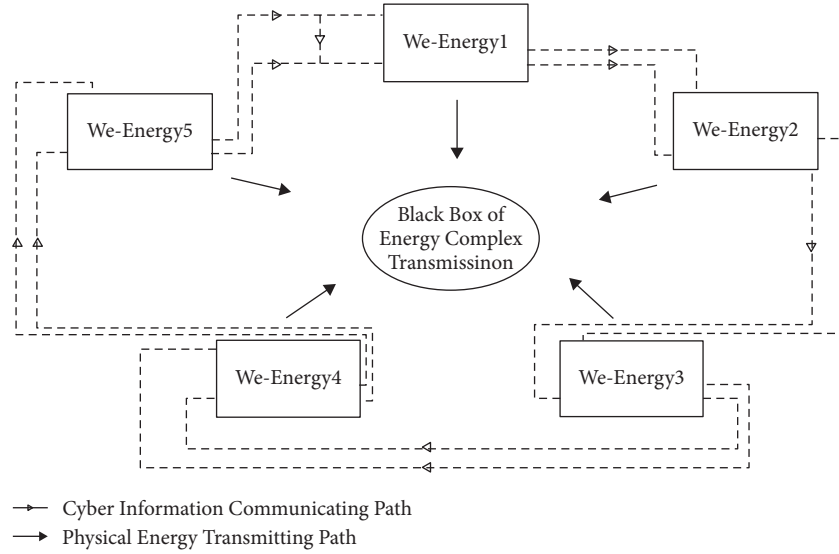


FIGURE 18: Energy internet.

TABLE 5: Data.

Distributed renewable generators and distributed renewable heat devices	$P_{it}^{wind}$ , ( $\times 10^3$ kw)	$P_{it}^{solar}$ , ( $\times 10^3$ kw)	$H_{it}^{solar}$ , ( $\times 10^2$ kw)	$P_{it}^{wind-min}$ , ( $\times 10^2$ kw)	$P_{it}^{wind-max}$ , ( $\times 10^4$ kw)	$P_{it}^{solar-min}$ , ( $\times 10^2$ kw)	$H_{it}^{solar-min}$ , ( $\times 10^2$ kw)	$H_{it}^{solar-max}$ , ( $\times 10^4$ kw)
WE1	3.9843	1.4254	0.4513	1.2182	5.2452	0.1420	1.1035	2.7131
WE2	4.5324	2.2871	0.2541	1.1546	2.6264	0.3197	1.3214	3.6157
WE3	0.5844	1.1250	2.2509	0.9137	4.2567	0.0984	2.3147	1.9548
WE4	1.6534	1.0070	0.0131	0.8954	4.3218	0.1247	1.2181	1.7496
WE5	1.2455	3.1543	0.3065	1.3193	3.2148	0.2214	1.3120	1.3427
Distributed coal or oil combined heat and power devices	$a_i^{DCOC}$ , ( $\times 10^{-4}$ )	$b_i^{DCOC}$ , ( $\times 10^{-3}$ )	$\alpha_i^{DCOC}$ , ( $\times 10^{-4}$ )	$\beta_i^{DCOC}$ , ( $\times 10^{-3}$ )	$c_i^{DCOC}$ , ( $\times 10^{-4}$ )	$\lambda_i^{DCOC}$ , ( $\times 10^2$ )	$d_i^{DCOC}$	$e_i^{DCOC}$
WE1	1.65	1.50	1.80	1.20	1.74	2.25	36.15	57.15
WE2	1.35	0.45	1.95	1.50	1.72	2.84	35.40	59.55
WE3	1.80	1.95	1.20	1.50	1.43	5.92	38.70	60.45
WE4	1.65	1.80	1.35	2.10	1.47	3.71	40.05	63.15
WE5	1.95	2.85	1.65	1.65	1.76	3.69	39.30	62.55
Distributed coal or oil combined heat and power devices	$f_i^{DCOC}$	$g_i^{DCOC}$	$h_i^{DCOC}$	$j_i^{DCOC}$	$\eta_i^{DCOC}$	$P_i^{DCOC-ramp}$ , (kw)	$P_{i,t-1}^{DCOC}$ , (kw)	
WE1	320355	488760	0.52	0.86	89%	1056	3908	
WE2	323760	479760	0.54	0.87	84%	987	3847	
WE3	305460	518805	0.51	0.91	91%	853	3691	
WE4	298095	482355	0.59	0.90	92%	964	4058	
WE5	277530	546315	0.58	0.88	95%	1208	4061	
Distributed gas producers	$a_{it}^{DGP}$ , ( $\times 10^{-4}$ )	$b_{it}^{DGP}$	$c_{it}^{DGP}$	$G_{it}^{DGP-min}$ (kw)	$G_{it}^{DGP-max}$ (kw)			
WE1	1.5	3.0360	1485	201.3	5941.40			

TABLE 5: Continued.

Distributed renewable generators and distributed renewable heat devices	$P_{i,t}^{wind}$ , ( $\times 10^3$ kw)	$P_{i,t}^{solar}$ , ( $\times 10^3$ kw)	$H_{i,t}^{solar}$ , ( $\times 10^2$ kw)	$P_{i,t}^{wind-min}$ , ( $\times 10^2$ kw)	$P_{i,t}^{wind-max}$ , ( $\times 10^4$ kw)	$P_{i,t}^{solar-min}$ , ( $\times 10^2$ kw)	$H_{i,t}^{solar-min}$ , ( $\times 10^2$ kw)	$H_{i,t}^{solar-max}$ , ( $\times 10^4$ kw)	
Distributed power to gas devices	$\eta_{i,t}^{DP2G}$	$\theta_{i,t}^{DP2G}$	$P_{i,t}^{DP2G-min}$ , (kw)	Initialized operating condition (kw)					
WE1	77%	0.03	520	520					
WE2	82%	0.02	610	610					
WE3	81%	0.04	710	710					
WE4	79%	0.01	610	610					
WE5	84%	0.02	600	600					
Distributed electric boiler	$\eta_{i,t}^{DEB}$	$\theta_{i,t}^{DEB}$	$P_{i,t}^{DEB-min}$ , (kw)	Initialized operating condition (kw)					
WE1	92%	0.02	980	980					
WE2	95%	0.04	720	720					
WE3	93%	0.01	840	840					
WE4	97%	0.03	1030	1030					
WE5	91%	0.05	790	790					
Distributed gas combined heat and power devices	$\theta_{i,t}^{DGC}$	$\eta_i^{DGC}$	$h_i^{DGC}$	$j_i^{DGC}$	Initialized condition	$G_{i,t}^{DGC-min}$ , (kw)			
WE1	0.03	83%	0.59	5.3120	750	750			
WE2	0.02	79%	0.55	5.2019	690	690			
WE3	0.05	82%	0.58	5.7187	840	840			
WE4	0.01	84%	0.57	5.2162	720	720			
WE5	0.04	86%	0.54	5.9146	710	710			
Distributed power storage devices	$a_i^{DPSD}$	$b_i^{DPSD}$	$\theta_{i,t}^{DPSD}$	$P_i^{in-DPSD}$ , (kw)	$P_i^{out-DPSD}$ , (kw)	$P_i^{min-S-DPSD}$ , (kw)	$P_i^{max-S-DPSD}$ , (kw)	$P_{i,t-1}^{S-DPSD}$ , (kw)	$\mu_i^{DPSD}$
WE1	1.12	154	0.15	432	567	271	1568	1100	625
WE2	1.09	136	0.13	459	614	226	1734	1025	629
WE3	0.93	127	0.17	503	412	191	1721	1328	735
WE4	0.82	198	0.21	441	450	140	1430	1327	577
WE5	1.33	121	0.11	404	442	142	1331	954	518
Distributed heat storage devices	$a_i^{DHSD}$	$b_i^{DHSD}$	$\theta_{i,t}^{DHSD}$	$H_i^{in-DHSD}$ , (kw)	$H_i^{out-DHSD}$ , (kw)	$H_i^{min-S-DHSD}$ , (kw)	$H_i^{max-S-DHSD}$ , (kw)	$H_{i,t-1}^{S-DHSD}$ , (kw)	
WE1	1.30	253	0.14	561	641	171	1765	1207	534
WE2	1.25	768	0.19	540	590	254	1583	1011	672
WE3	0.71	354	0.13	572	525	369	1852	1319	601
WE4	0.96	417	0.17	503	530	342	1754	1021	608
WE5	1.04	139	0.14	509	523	244	1543	1055	512
Distributed gas storage devices	$a_i^{DGSD}$	$b_i^{DGSD}$	$\theta_{i,t}^{DGSD}$	$G_i^{in-DHSD}$ , (kw)	$G_i^{out-DHSD}$ , (kw)	$G_i^{min-S-DGSD}$ , (kw)	$G_i^{max-S-DGSD}$ , (kw)	$G_{i,t-1}^{S-DGSD}$ , (kw)	$\mu_i^{DGSD}$
WE1	2.10	734	0.23	325	371	46	1206	435	542
WE2	2.86	261	0.14	317	384	71	1671	429	531
WE3	1.84	458	0.12	349	363	61	1087	456	568
WE4	2.10	430	0.21	401	312	82	960	463	591
WE5	1.61	419	0.19	366	350	69	1427	421	601
Energy load	$P_{i,t}^{EL}$ , ( $\times 10^4$ kw)	$H_{i,t}^{EL}$ , ( $\times 10^3$ kw)	$G_{i,t}^{EL}$ , (kw)	$\theta_{1,t}^{P-EL}$	$\theta_{1,t}^{H-EL}$	$\theta_{1,t}^{G-EL}$	$\theta_{2,t}^{P-EL}$	$\theta_{2,t}^{H-EL}$	$\theta_{2,t}^{G-EL}$
WE1	1.3790	6.9612	5640	2.8	2.6	2.1	1.0	1.0	2.7
WE2	2.3333	7.3429	6272	2.8	2.6	2.1	1.0	1.0	2.7
WE3	1.4900	7.0056	5080	2.8	2.6	2.1	1.0	1.0	2.7
WE4	1.4138	6.9752	6736	2.8	2.6	2.1	1.0	1.0	2.7
WE5	1.7618	7.1143	5592	2.8	2.6	2.1	1.0	1.0	2.7



some cases which change slowly. However, it is unsuitable for some cases with low demand of privacy protecting and some cases which change quickly.

## 6. Conclusions

Based on the traditional distributed and the alternating direction method of multipliers algorithm in energy market, this article proposed a new communicating and optimizing algorithm of energy management EI. EI in this algorithm communicates information in an annular way, which can not only greatly reduce communicating times, but also can protect the privacy data of all agents that can only be searched by itself. Compared with previous privacy protection in multiagent systems in which privacy data are transmitted to neighbor agents, privacy in this article is protected much more strongly. In addition, this article uses the subgradient method to quicken the annular directed distributed algorithm and solve the issue of astringency in energy transforming. Simulation results and theoretical identification containing the monotone-bounded convergence theorem, theory of limit, and contradiction have demonstrated the effectiveness of the proposed algorithm (see Table 5).

## Appendix

Figures 16 and 17 are structure of we-energy 1 and all others we-energy. Figure 18 is EI in simulation test platform of this article. CCWE is the control center of WE.

All data of the simulation test platform are in the chart

The price of coal or oil is 6 ¢ per kw · h. We initialize the prize of power, heat, and gas to 15 ¢ per kw · h.  $w$  is  $10^{-6}$  for power and heat and  $1 \cdot 5 \times 10^{-6}$  for gas.

## Data Availability

The authors confirm that all relevant data are included in the article.

## Conflicts of Interest

The authors declare that they have no conflicts of interest.

## References

- [1] A. Q. Huang, M. L. Crow, G. T. Heydt, J. P. Zheng, and S. J. Dale, "The future renewable electric energy delivery and management (FREEDM) system: the energy internet," *Proceedings of the IEEE*, vol. 99, no. 1, pp. 133–148, 2011.
- [2] T. Facchinetti and M. L. Della Vedova, "Real-time modeling for direct load control in cyber-physical power systems," *IEEE Transactions on Industrial Informatics*, vol. 7, no. 4, pp. 689–698, 2011.
- [3] H. M. Hussain, A. Narayanan, P. H. J. Nardelli, and Y. Yang, "What is energy internet? concepts, technologies, and future directions," *IEEE Access*, vol. 8, pp. 183127–183145, 2020.
- [4] D. Miyagi, R. Sato, N. Ishida et al., "Experimental research on compensation for power fluctuation of the renewable energy using the SMES under the state-of-current feedback control," *IEEE Transactions on Applied Superconductivity*, vol. 25, no. 3, pp. 1–5, June 2015.
- [5] S. Paul, T. Dey, P. Saha, S. Dey, and R. Sen, "Review on the development scenario of renewable energy in different country," in *Proceedings of the Innovations in Energy Management and Renewable Resources*, Kolkata, India, 2021.
- [6] B. Schfer, C. Beck, K. Aihara, D. Witthaut, and M. Timme, "Non-gaussian power grid frequency fluctuations characterized by Levy-stable laws and superstatistics," *Nature Energy*, vol. 3, pp. 119–126, 2018.
- [7] S. Hemamalini and S. P. Simon, "Maclaurin series-based lagrangian method for economic dispatch with valve-point effect," *IET Generation, Transmission & Distribution*, vol. 3, no. 9, pp. 859–871, 2009.
- [8] N. Zhang, Q. Sun, and L. Yang, "A two-stage multi-objective optimal scheduling in the integrated energy system with we-energy modeling," *Energy*, vol. 215, 2020.
- [9] B. Zakeri, G. C. Gissey, P. E. Dodds, and D. Subkhankulova, "Centralized vs. distributed energy storage – benefits for residential users," *Energy*, vol. 236, Article ID 121443, 2021.
- [10] Z. Tan, H. Zhong, Q. Xia, and C. Kang, "Non-iterative multi-area coordinated dispatch via condensed system representation," *IEEE Transactions on Power Systems*, vol. 36, 2020.
- [11] Z. Tan, H. Zhong, J. Wang, Q. Xia, and C. Kang, "Enforcing intra-regional constraints in tie-line scheduling: a projection-based framework," *IEEE Transactions on Power Systems*, vol. 34, no. 6, pp. 4751–4761, 2019.
- [12] A. A. Munshi and Y. A. R. I. Mohamed, "Unsupervised nonintrusive extraction of electrical vehicle charging load patterns," *IEEE Transactions on Industrial Informatics*, vol. 15, no. 1, pp. 266–279, 2019.
- [13] K. Anoh, S. Maharjan, A. Ikpehai, Y. Zhang, and B. Adebisi, "Energy peer-to-peer trading in virtual microgrids in smart grids: a game-theoretic approach," *IEEE Transactions on Smart Grid*, vol. 11, no. 2, pp. 1264–1275, 2020.
- [14] W. Hu, P. Wang, and H. Gooi, "Toward optimal energy management of microgrids via robust two-stage optimization," *IEEE Transactions on Smart Grid*, vol. 9, 2016.
- [15] M. Geidl, G. Koeppl, P. Favre-Perrod, B. Klockl, G. Andersson, and K. Frohlich, "Energy hubs for the future," *IEEE Power and Energy Magazine*, vol. 5, no. 1, pp. 24–30, 2007.
- [16] Y. Parag and B. K. Sovacool, "Electricity market design for the prosumer era," *Nature Energy*, vol. 1, no. 4, Article ID 16032, 2016.
- [17] L. Li and S. Zhang, "Peer-to-peer multi-energy sharing for home microgrids: an integration of data-driven and model-driven approaches," *International Journal of Electrical Power & Energy Systems*, vol. 133, Article ID 107243, 2021.
- [18] Q. Sun, R. Han, H. Zhang, J. Zhou, and J. M. Guerrero, "A multiagent-based consensus algorithm for distributed coordinated control of distributed generators in the energy internet," *IEEE Transactions on Smart Grid*, vol. 6, no. 6, pp. 3006–3019, 2015.
- [19] Q. Sun, *Energy internet and we-energy*, Springer-Verlag, Singapore, 2019.
- [20] Q. Sun, R. Fan, Y. Li, B. Huang, and D. Ma, "A distributed double-consensus algorithm for residential we-energy," *IEEE Transactions on Industrial Informatics*, vol. 15, no. 8, p. 1, 2019.
- [21] H. Zhang, Y. Li, D. W. Gao, and J. Zhou, "Distributed optimal energy management for energy internet," *IEEE Transactions on Industrial Informatics*, vol. 13, no. 6, pp. 3081–3097, Dec, 2017.

- [22] Y. Mi, X. Hao, Y. Liu et al., "Sliding mode load frequency control for multi-area time-delay power system with wind power integration," *IET Generation, Transmission & Distribution*, vol. 11, no. 18, pp. 4644–4653, 2017.
- [23] Y. Li, D. W. Gao, W. Gao, H. Zhang, and J. Zhou, "Double-mode energy management for multi-energy system via distributed dynamic event-triggered Newton-raphson algorithm," *IEEE Transactions on Smart Grid*, vol. 11, no. 6, pp. 5339–5356, 2020.
- [24] Y. Y. Liu, J. J. Slotine, and A. L. Barabási, "Controllability of complex networks," *Nature*, vol. 473, no. 7346, pp. 167–173, 2011.
- [25] C. Altafini, "A system-theoretic framework for privacy preservation in continuous-time multiagent dynamics," *Automatica*, vol. 122, 2020.
- [26] C. Altafini, "A dynamical approach to privacy preserving average consensus," in *Proceedings of the 2019 IEEE 58th Conference on Decision and Control (CDC)*, pp. 4501–4506, Nice, France, 2019.
- [27] X.-K. Liu, J.-F. Zhang, and J. Wang, "Differentially private consensus algorithm for continuous-time heterogeneous multi-agent systems," *Automatica*, vol. 122, Article ID 109283, 2020.
- [28] A. Cw, A. Zb, B. Qw et al., "Coordinated post-contingency dispatch of integrated energy system with multiple participants based on distributed energy trading—ScienceDirect," *International Journal of Electrical Power & Energy Systems*, vol. 130, 2021.
- [29] X. Zhang, T. Tan, B. Zhou, T. Yu, B. Yang, and X. Huang, "Adaptive distributed auction-based algorithm for optimal mileage based AGC dispatch with high participation of renewable energy," *International Journal of Electrical Power & Energy Systems*, vol. 124, Article ID 106371, 2021.
- [30] V. Mnih, K. Kavukcuoglu, D. Silver et al., "Human-level control through deep reinforcement learning," *Nature*, vol. 518, no. 7540, pp. 529–533, 2015.

## Research Article

# Situation Awareness of Electric Vehicle Charging Load Based on Random Forest Algorithm

Wen Bo, Donglai Wang , Yan Zhao, Quanzheng Li, and Zhen Zhang

Key Laboratory of Regional Multi-Energy System Integration and Control of Liaoning Province,  
Shenyang Institute of Engineering, Shenyang, Liaoning 110136, China

Correspondence should be addressed to Donglai Wang; [donglai.wang@hotmail.com](mailto:donglai.wang@hotmail.com)

Received 1 April 2022; Accepted 30 May 2022; Published 24 June 2022

Academic Editor: Qiuye Sun

Copyright © 2022 Wen Bo et al. This is an open access article distributed under the Creative Commons Attribution License, which permits unrestricted use, distribution, and reproduction in any medium, provided the original work is properly cited.

Due to the important characteristics of energy saving and carbon reduction, electric vehicles have attracted worldwide attention. It can be predicted that the power grid will be faced with the access problem of large-scale electric vehicles. In order to master the user behavior characteristics of electric vehicle load, it is necessary to establish the model based on electric vehicle charging behavior. In this paper, combined with the electric vehicle charging demand and the situational awareness results of the dispatchable resources in the station area, the characteristic indicators of the electric vehicle load are quantitatively analyzed. Situational prediction of electric vehicle load based on random forest algorithm is proposed, and the sample set is divided and trained. A simulation example is used to verify the effectiveness of the method provided in load forecasting.

## 1. Introduction

Energy crisis and climate warming have become the key problems that restrict the sustainable development of human society. Electric vehicles have significant advantages in alleviating global energy shortages and environmental pollution [1–3]. At the same time, distributed power generation, which is mainly composed of photovoltaic and wind power, develops rapidly [4]. However, the access of large-scale electric vehicles and the intermittence of renewable energy will aggravate the peak-valley difference of power grid load, making the operation of power grid more difficult to control [5, 6]. On the one hand, as a flexible load, the electric vehicle's off-driving charging time is usually longer than the time required for its battery to be fully charged. Orderly regulating the charging behavior of a large number of electric vehicles can not only avoid the impact of large-scale random access of electric vehicles to the power grid but also realize the peak load cutting and valley load filling, which is very important for the safe operation of the power grid in the future. It is of great significance to improve the economic benefits of the power grid [7–10]. On the other hand, due to the strong randomness at the moment when electric vehicles

connect and leave the power grid, the state of charge of the battery is uncertain, and the day-ahead scheduling process can not accurately predict the connection and departure of each electric vehicle in the future [11–13].

Short-term load forecasting is an important part of power system load forecasting, which mainly forecasts the load at any time in the future [14]. The factors that affect the accuracy of short-term load forecasting mainly include sudden weather changes, seasonal changes, dispatching plans, emergencies, large-scale social activities, and so on. Therefore, short-term load forecasting has randomness and uncertainty [15, 16]. However, in the process of random change, the load still has obvious periodicity in different periods, such as year, month, week, and day. Therefore, the short-term load variation comprehensively appears as a nonstationary random process in the time series [17, 18]. Accurate short-term load forecasting is of great significance to the economic dispatch of electric power dispatching departments, the control of unit allocation, and the current developing electric market [19].

The methods of early warning, decision making, and visualization in situational awareness technology play an important role in realizing the safe and stable operation of

smart grids. Reference [20] has designed a distribution network dispatching system based on situation awareness technology, which can flexibly detect and evaluate the running state of the distribution network. Reference [21] has already applied situational awareness to microgrid, and based on microgrid situational awareness, the situation leads to active decision. Reference [22] has proposed that the electric vehicle charging and discharging index is used for situational warning of the power supply capacity of the power distribution system. At present, the application of situational awareness in the distribution system is mainly aimed at the power supply and consumption early warning and monitoring of distribution network. However, the situation awareness of the distribution system to forecast and dispatch the charging load of electric vehicles has not been deeply developed.

In this paper, the basic user behavior characteristics of electric vehicle load are studied, and the charging behavior model of electric vehicle is established. The forecasting method of electric vehicle load based on random forest algorithm is put forward. The sample set is trained and compared with other methods in the field of short-term load forecasting. The validity and superiority of the random forest algorithm for electric vehicle load forecasting are verified, which can effectively improve the accuracy of electric vehicle charging load forecasting.

## 2. Modeling of Electric Vehicle Charging Behavior

*2.1. Electric Vehicle Charging Behavior Analysis.* After electric vehicles are connected to the power grid on a large scale, its charging load becomes an important factor that cannot be ignored in the power grid. Because the large-scale electric vehicle groups has certain aggregation characteristics, this paper takes the large-scale electric vehicle group as the research object and analyzes the charging demand of electric vehicles from the aspects of battery characteristics, charging time, mileage characteristics, and so on.

The characteristics of the battery mainly include battery capacity and the state of charge. The features include charging start time and charging duration. Driving features mainly include daily mileage and power consumption per kilometer of electric vehicles. The relationship between these 3 properties is as follows:

$$T_{\text{ch}} = \frac{Q_{\omega} \cdot d}{P_{\text{EV}}(k)} = \frac{Q_{\text{EV}} \cdot (1 - S_{\text{SOC}})}{P_{\text{EV}}(k)}, \quad (1)$$

where  $T_{\text{ch}}$  is the charging time in hours;  $Q_{\omega}$  is the electricity consumption per kilometer of the electric vehicle, in kilowatt-hours per kilometer;  $d$  is the mileage of the electric vehicle, in kilometers;  $P_{\text{EV}}(k)$  is the charging power in kilowatts;  $P_{\text{EV}}(k)$  is the battery capacity in kWh; and  $S_{\text{SOC}}$  is the battery state of charge, which is the ratio of the remaining battery power to the fully charged state.

The daily mileage of electric vehicles obeys a normal distribution, and its probability density function is as follows:

$$f(d) = \frac{1}{d\delta_d\sqrt{2\pi}} \exp\left[-\frac{(\ln d - \mu_d)^2}{2\delta_d^2}\right], \quad (2)$$

where  $\mu_d$  is the expected value of daily mileage, and  $\delta_d$  is the standard deviation of daily mileage. According to [23], it is advisable to take  $\mu_d = 3.2$  and  $\delta_d = 0.88$ .

The initial charging time of electric vehicles also has a certain normal distribution, and its probability density function is as follows:

$$f_{\text{car}}(t) = \frac{1}{t\delta_t\sqrt{2\pi}} \exp\left[-\frac{(\ln t - \mu_t)^2}{2\delta_t^2}\right], \quad (3)$$

where  $t$  is the initial charging time of each electric vehicle, and its value is in the range of [0, 1440] (24 h is divided into 1440 time periods, each of which is 1 minute);  $\mu_t$  represents the expected value of charging time; and  $\delta_t$  is the standard deviation of charging time. According to [23], it is advisable to take  $\mu_t = 17.6$  and  $\delta_t = 3.4$ .

*2.2. The Model of Single Electric Vehicle Charging Behavior.* It shows that the charging power of each electric vehicle is constant and continuously adjustable in each optimization period. The mathematical model of the charging behavior of a single electric vehicle is shown in

$$\left\{ \begin{array}{l} d_{\text{EV}}(t) = \eta \sum_{k=t_{\text{in}}}^t P_{\text{EV}}(k)\Delta t = d(t-1) + \eta P_{\text{EV}}(t)\Delta t, \\ d_{\text{min}}(t_{\text{out}}) = d_{\text{max}}(t_{\text{out}}) = D_{\text{expect}}, \\ d_{\text{min}}(t) \leq d_{\text{EV}}(t) \leq d_{\text{max}}(t), \\ P_{\text{max}}(t) = \frac{\min(P_{\text{EV,max}}, d_{\text{max}}(t) - d(t-1))}{\eta\Delta t}, \\ P_{\text{max}}(t) = \frac{\max(0, d_{\text{min}}(t) - d(t-1))}{\eta\Delta t}, \\ P_{\text{min}}(t) \leq P_{\text{EV}}(t) \leq P_{\text{max}}(t), \end{array} \right. \quad (4)$$

where  $d_{\text{EV}}(t)$  is the energy trajectory value of the electric vehicle at time  $t$ ;  $d_{\text{min}}(t)$  and  $d_{\text{max}}(t)$  are the lower and upper bounds of the energy trajectory  $d(t)$  at time  $t$ , respectively;  $\eta$  is the charging efficiency;  $P_{\text{EV}}(k)$  is the electric vehicle charging power at time  $k$  and remains constant during the period between time  $k$  and time  $k+1$ ;  $\Delta t$  is the time interval of the scheduling period;  $t_{\text{in}}$  and  $t_{\text{out}}$  are the access and departure times of the electric vehicle, respectively; that is, the electric vehicle is connected at time  $t_{\text{in}}$  and leaves at time  $t_{\text{out}}$ ;  $D_{\text{expect}}$  is the charging demand for electric vehicles;  $P_{\text{EV,max}}$  is the upper limit of the rated charging power of the electric vehicle battery;  $P_{\text{EV}}(t)$ ,  $P_{\text{max}}(t)$ , and  $P_{\text{min}}(t)$  are the charging power of the electric vehicle at time  $t$  and the maximum and minimum charging power limited by the energy boundary constraints, respectively. The schematic

diagram of the energy boundary model of a single electric vehicle is shown in Figure 1.

In Figure 1, it is assumed that the electric vehicle is connected at time  $t_{in}$  and left at time  $t_{out}$ . The curve  $abd$  is the upper bound  $d_{max}(t)$  of the energy boundary of the electric vehicle, which means that after the electric vehicle is connected to the power grid, it will be charged with the maximum charging power immediately until it reaches the user's expectation  $D_{expect}$ . The curve  $acd$  is the lower bound  $d_{min}(t)$  of the energy boundary of the electric vehicle, which means that the electric vehicle delays charging after it is connected to the power grid, until the user's expectation  $D_{expect}$  is reached at the time of departure. The slopes of  $ab$  and  $cd$  represent the increase in battery power per unit time according to the maximum charging power of the electric vehicle, that is,  $\eta P_{EV,max}$ .

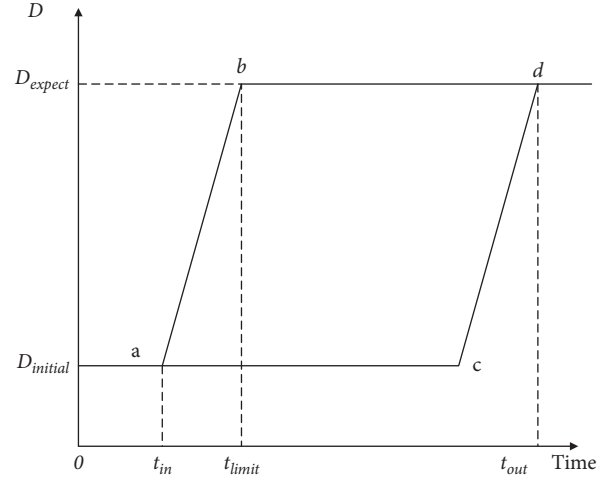


FIGURE 1: Energy boundary model of single electric vehicle.

**2.3. Cluster Equivalent Model for Electric Vehicles.** After the electric vehicles are connected to the power grid, the electric vehicles with the same departure time can be grouped into the same subcluster according to the charging parameters input by the owner. By superimposing the charging models belonging to the same subcluster, the equivalent charging model of a single subcluster can be obtained as follows:

$$\left\{ \begin{array}{l} d_{min,m}(t) \leq d_m(t) \leq d_{max,m}(t), \\ d_m(t) = \eta \sum_{k=1}^t P_m(k)\Delta t = d_m(t-1) + \eta P_m(t)\Delta t, \\ d_{min,m}(t) = \sum_{l=1}^{n_m} d_{min,m,l}(t), \\ d_{max,m}(t) = \sum_{l=1}^{n_m} d_{max,m,l}(t), \\ P_m(t) = \sum_{l=1}^{n_m} P_{EV,m,l}(t), \\ P_{max,m}(t) = \sum_{l=1}^{n_m} P_{EV,max,m,l}(t) \geq P_m(t), \end{array} \right. \quad (5)$$

where  $d_m(t)$  is the energy trajectory of subcluster  $m$  at time  $t$ .  $d_{min,m}(t)$  and  $d_{max,m}(t)$  are the lower and upper bounds of the energy trajectory of subcluster  $m$  at time  $t$ , respectively.  $P_m(t)$  is the total charging power of subcluster  $m$  at time  $t$ .  $P_{min,m}(t)$  and  $P_{max,m}(t)$  are the lower and upper limits of the charging power of subcluster  $m$  at time  $t$ , respectively.  $n_m$  is the number of electric vehicles belonging to subcluster  $m$  at time  $t$ .  $d_{min,m,l}(t)$ ,  $d_{max,m,l}(t)$  and  $P_{min,m,l}(t)$ ,  $P_{max,m,l}(t)$  are the lower and upper bounds of the energy trajectory and the lower and upper bounds of the charging power of the  $l$ -th electric vehicle of subcluster  $m$  at time  $t$ , respectively.

Because the electric vehicles belonging to the same subcluster will leave at the same time, the cluster charging model is equivalent to the single charging model; that is, the charging strategy of the subcluster meeting the cluster charging model must follow a certain energy allocation

mode. For the cluster charging amount set  $s = [s_1, s_2, \dots, s_t, \dots, s_T]$  that satisfies the cluster charging model, there must be at least one charging power distribution method so that all electric vehicles in the cluster are fully charged before leaving under the condition that the single charging model is satisfied. According to the cluster charging model, the following inequality holds for  $n = 1, 2, \dots, T$ .

$$\sum_{t=1}^n \sum_{l \in \{l|t_{out}=t\}} d_l \leq \sum_{t=1}^n s_t \leq \sum_{t=1}^n \sum_{l \in \{l|t_{in}=t\}} d_l, \quad (6)$$

where  $d_l$  is the charging power demand of the  $l$ -th vehicle.

First, when  $n = 1$ , the inequality is transformed into

$$\sum_{l \in \{l|t_{out}=1\}} d_l \leq s_1 \leq \sum_{l \in \{l|t_{in}=1\}} d_l. \quad (7)$$

Using the strategy of giving priority to charging the electric vehicles that leave first, the charging plan for all electric vehicles at departure time  $t_{out} = 1$  can be set as

$$P_{l1} = d_l, \quad (8)$$

so that it can be filled before leaving. Therefore, when  $n = 1$ , the proposition holds.

It is assumed that, for all time points  $m$ , the electric vehicles that leave before time point  $m$  can be fully charged within the cluster by adopting a strategy of charging the electric vehicles that leave first. That is, there is at least one charging plan set that satisfies the following equation:

$$\sum_{t=t_{in}}^{t_{out}} P_{lt} = d_l, \quad \forall l \in \{l|t_{out} \leq m\}, \quad (9)$$

$$P_{lt} \geq 0, \quad \forall t = t_{in}, \dots, t_{out}, \forall l \in \{l|t_{out} \leq m\}.$$

The result is as follows:

$$\sum_{t=1}^m \sum_{l \in \{l|t_{out}=t\}} d_l \leq \sum_{t=1}^m s_t, \quad (10)$$

TABLE 1: Classification rule of situation levels.

Situation levels	Situational range	Regional status	Detailed description
1	[0, 0.2)	Unobstructed	Resources can fully meet the charging needs of electric vehicles
2	[0.2, 0.4)	Basically unobstructed	The resources can basically meet the charging needs of electric vehicles, and occasionally, there is insufficient supply
3	[0.4, 0.6)	Light congestion	Under normal circumstances, the resources can meet the charging needs of electric vehicles, but sometimes there will be insufficient supply
4	[0.6, 0.8)	Moderate congestion	The resources can meet the charging needs of electric vehicles in most cases
5	[0.8, 1.0]	Serious congestion	Resources are basically unable to meet the needs of electric vehicles and other loads

where  $\sum_{t=1}^m s_t - \sum_{t=1}^m \sum_{l \in \{t_{out}=1\}} d_l$  represents the total amount of charge of the electric vehicle whose departure time is after the time point  $m$ . Due to the strategy of charging the electric vehicle that leaves first, once the electric vehicle at the departure time point  $m$  has been fully charged, the electric vehicle at the departure time point  $m+1$  will be preferentially arranged to be charged.

When

$$\sum_{t=1}^m s_t - \sum_{t=1}^m \sum_{l \in \{l_{out}=t\}} d_l \geq \sum_{t=1}^m \sum_{l \in \{l_{out}=m+1\}} d_l. \quad (11)$$

The electric vehicle whose departure time is  $m+1$  is charged, and the electric vehicle with departure time point  $m+2$  will be charged.

$$\sum_{t=1}^m s_t - \sum_{t=1}^m \sum_{l \in \{l_{out}=t\}} d_l < \sum_{l \in \{l_{out}=m+1\}} d_l. \quad (12)$$

Then, the electric vehicle with departure time point  $m+1$  will be charged, and the total amount of charging is  $\sum_{t=1}^m s_t - \sum_{t=1}^m \sum_{l \in \{l_{out}=t\}} d_l$ .

When  $n = m+1$ , because of

$$\sum_{t=1}^{m+1} \sum_{l \in \{l_{out}=t\}} d_l \leq \sum_{t=1}^{m+1} S_t, \quad (13)$$

it can be obtained as follows:

$$s_{m+1} \geq \sum_{l \in \{l_{out}=m+1\}} d_l - \left( \sum_{t=1}^m s_t - \sum_{t=1}^m \sum_{l \in \{l_{out}=t\}} d_l \right). \quad (14)$$

The above equations show that the charging plan  $s_{m+1}$  can meet the charging demand of the electric vehicle at the departure time point  $m+1$ .

$$\sum_{t=t_{in}}^{t_{out}} P_{lt} = d_l, \quad \forall l \in \{l | t_{out} \leq m+1\}, \quad (15)$$

$$P_{lt} \geq 0, \quad \forall t = t_{in}, \dots, t_{out}, \forall l \in \{l | t_{out} \leq m+1\}.$$

Because the upper and lower limits of the cluster charging power in the cluster charging mode will not exceed the sum of the upper and lower limits of all electric vehicles in the cluster, all charging strategies that meet the cluster

charging mode must have at least one power allocation method so that the charging amount of the cluster at the start and the single charging mode can meet.

### 3. Situational Awareness of Power Supply Resources for Electric Vehicles

*3.1. Situational Awareness Model of Electric Vehicle Power Supply Resources.* In the process of grid power resource scheduling, it is necessary to extract the relevant factors of electric vehicle demand change. Then, the situation is understood, the obtained information is integrated and classified, and finally, the situation is predicted, and the development trend is predicted and judged. In this way, the charging demand and power supply resources of electric vehicles can be accurately grasped, and the corresponding situation classification rules can be formulated so that the power supply resources can be reasonably allocated according to the real-time load status of the station area, as shown in Table 1.

The process of situational awareness mainly includes three parts: (1) extracting the characteristic parameters of situational awareness, preprocessing, and providing data support for situational understanding and prediction; (2) situational understanding, integrating, and classifying the obtained information; and (3) making predictions and judgments about the situation.

Based on the charging characteristics of the electric vehicle, the characteristic parameters of the situational awareness model are extracted, including the current charging state of electric vehicle, the charging start time, the charging time, and the charging pile usage interval time. We quantify the indicators and then get the situational awareness value, so as to reasonably dispatch the station resources. According to the mined indicators, the original data are collected, and the features are extracted to generate sample sets. If the total number of samples is  $n$  and the number of feature indicators is  $m$ , the sample matrix will be an  $m \times n$  matrix. Then, the training sample set is taken as the input, and the value corresponding to the sample matrix is taken as the training output, so as to train the integrated model.

*3.2. Prediction of Electric Vehicle Load Situation Based on Random Forest Algorithm.* In this section, a situation prediction model of electric vehicle power supply resources based on stochastic forest algorithm is proposed, and the



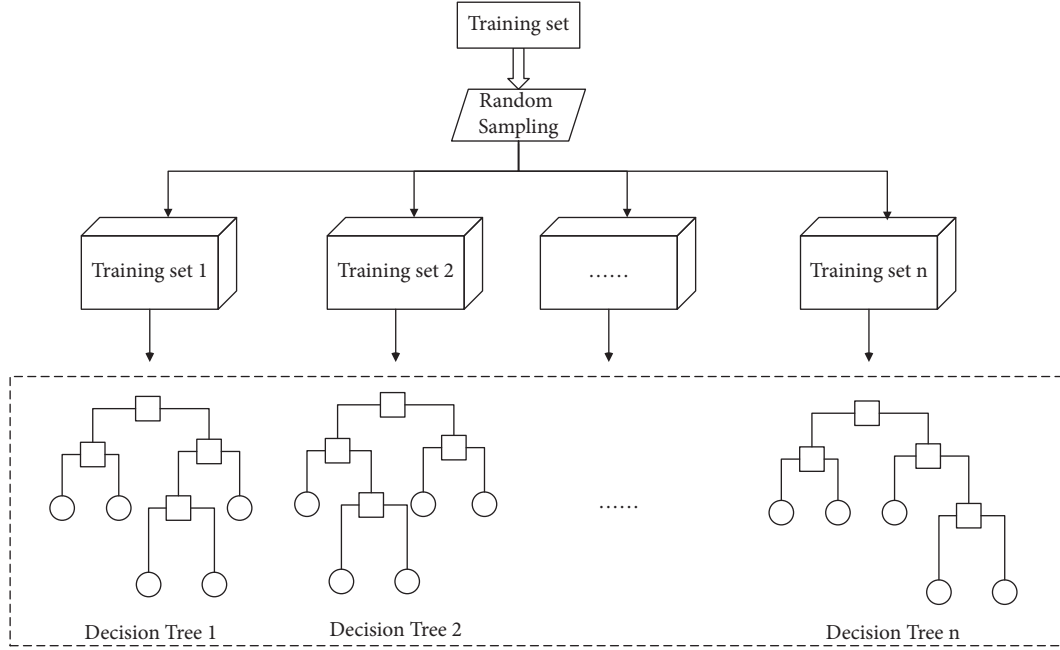


FIGURE 2: Random forest training process.

situation prediction of electric vehicle charging demand and regional power supply resources in the power supply station is made.

The decision tree of the random forest algorithm generally adopts the Classification and Regression Tree, which can effectively deal with large data samples and solve nonlinear problems. For classification problems, CART (Classification and Regression Tree) uses the Gini index as the attribute measure. The smaller the Gini coefficient is, the more accurate the classification effect will be. The Gini coefficient is defined as shown in

$$\text{Gini} = 1 - \sum_{i=1}^c [p(i|t)]^2, \quad (16)$$

where  $p(i|t)$  is the probability that the test variable  $t$  belongs to the sample of class  $i$ , and  $c$  is the number of samples. When  $\text{Gini} = 0$ , all samples belong to the same class.

$$\text{Gini}_A(C) = \frac{|C_1|}{C} \text{Gini}(C_1) + \frac{|C_2|}{C} \text{Gini}(C_2). \quad (17)$$

If the attribute satisfies a certain purity, the decision tree generation algorithm divides the sample into the left subtree; otherwise, it divides the sample into the right subtree. The CART decision tree generation algorithm selects the split attribute rules according to the principle of the smallest Gini index. Assuming that the attribute  $A$  in the training set  $C$  divides  $C$  into  $C_1$  and  $C_2$ , the Gini index of the given partition  $C$  is shown in

$$\text{Gini}_A(C) = \frac{|C_1|}{|C|} \text{Gini}(C_1) + \frac{|C_2|}{|C|} \text{Gini}(C_2). \quad (18)$$

For the regression problem, CART selects the optimal bisection cut point based on the sum of squared errors and

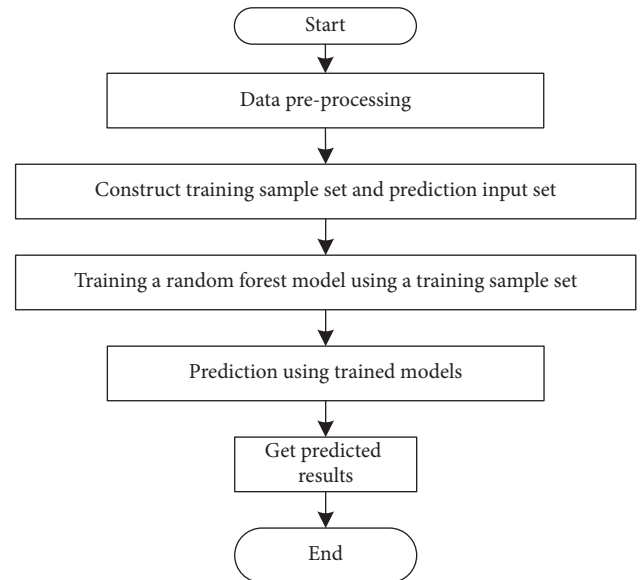


FIGURE 3: Forecasting process.

selects the optimal division attribute  $A$  and cut point  $c$ . The way to get it is as follows:

$$\min_{A,s} \left[ \min_{x_i \in R(A,s)} \sum (y_i - c_1)^2 + \min_{x_i \in R_2(A,s)} \sum (y_i - c_2)^2 \right]. \quad (19)$$

As an integrated algorithm based on decision trees, in the process of building a random forest model, different training sets are constructed to train each decision tree, thus increasing the difference between the classifiers and making the classification performance of random forest algorithm

surpass that of a single decision tree algorithm. Figure 2 shows the random forest training process. To reflect the randomness of the random forest model, the construction of the training set includes the following two key processes.

The random forest algorithm performs random sampling with replacement on the original training dataset. We construct a subdataset, the sample size of which is consistent with the original dataset. Samples in different subdatasets can be repeated, and samples in the same subdataset can be repeated. We generate a decision tree for each subset of data.

The splitting process of each decision tree in the random forest model only uses some of all the candidate features. The random forest algorithm first randomly selects a certain number of features from all the features to be selected and then uses the decision tree generation algorithm to select the optimal feature for splitting among the randomly selected features.

The specific implementation steps of the random forest algorithm are as follows:

- (a) Preprocess the data required for forecasting. And the missing data are filled in by linear interpolation. The training sample set is divided according to the needs of the prediction algorithm.
- (b) Training the random forest algorithm by using the training sample set. According to the parameter settings of the random forest algorithm, several decision trees are built, and the prediction model of the random forest is completed.
- (c) Use the characteristic data of the forecast samples to make the forecast. In the model, the characteristic data of the predicted samples will be followed by multiple decision tree prediction processes. The random forest algorithm will summarize and output the results to obtain the prediction results.

The flowchart of short-term electric vehicle charging load prediction based on random forest algorithm is shown in Figure 3.

At present, with the continuous improvement of electric vehicle data and other external data collection and storage level, there are many functions to choose from. Therefore, it is impossible to find all the features to participate in the fitting of the model, which may lead to problems such as overfitting of the model and reduce the accuracy of predictions. Therefore, considering the current research status of load forecasting, it is necessary to analyze the factors that affect the trip behavior of electric vehicles. This paper summarizes the following factors involved in the construction of feature engineering:

### 3.2.1. Historical Data of Electric Vehicle Charging Load.

The charging load of electric vehicles in the group also has the continuous characteristics of other conventional loads, and the historical load data closer to the predicted time can better reflect the load change trend. Of all the features, the historical data of load often have the greatest influence on the accuracy of the load model. The load history data of electric vehicle are selected as the input of the model, and the

built feature set determines the accuracy of the load forecasting model to a great extent.

**3.2.2. Meteorological Factor Data.** Meteorological factor data are temperature, humidity, and weather conditions. The influence of temperature and humidity on the behavior of electric vehicles is mainly reflected in the use of onboard air conditioners of electric vehicles, which will increase the power consumption of vehicles. Therefore, the influence reflected in the EV charging load is a delay in the falling time of the charging curve, which takes longer time to completely charge the EV battery. The weather often affects road conditions and driving behavior of electric vehicles. Vehicles that tend to drive in bad weather also consume more energy.

**3.2.3. Date Type.** The types of appointments are mainly divided into working days and weekends. In general, traffic congestion will be caused during peak hours on weekdays, which will affect the driving behavior of electric vehicles, increase the electricity consumption, and also affect the charging time of electric vehicles, thus affecting overall performance.

**3.2.4. Time Type.** The charging load of group electric vehicle, like the conventional load, has certain periodicity. Therefore, the difference of load capacity in this type at a certain time of day will not be particularly great. This is mainly due to the fact that the charging characteristics of group electric vehicles show a certain regularity. Therefore, the type of torque can also be used as an optional input feature.

## 4. Study Case and Simulation Results

In this paper, the charging piles in a certain area are selected as the simulation object. We assume that the number of electric vehicles connected to the charging station in this area is 300 and that the connected vehicles are only pure electric vehicles. The electric vehicle parameters use the data in Table 2. We assume an EV charging efficiency of 99%. The charging pile is an AC charging pile, and the power selection is set to 3.5 kW and 7 kW; the two are randomly generated with equal probability.

First of all, it is necessary to divide training data and prediction data. This paper selects the historical electric vehicle charging load data, meteorological data, date type data, and time type data of Shenyang City from November 15, 2021, to November 21, 2021, to construct the training sample set, forecast the load from November 22, 2021, to November 28, 2021, and compare the forecast results with the actual values to verify the effectiveness of the method.

The model input includes the following: load data at the moment before the time to be predicted, load data at the previous two moments, and load data at the same moment last week, temperature, humidity, wind direction, wind speed, weather condition information, date type, and time type.

TABLE 2: Pure electric power electric vehicle parameter model.

No.	Model name	Calibration mileage (km)	Battery capacity (kWh)	Power consumption per 100 kilometers (kWh/100 km)
1	BYD E9	506	64.8	15.8
2	Xiaopeng P5	460	55.9	14.6
3	WULING MINIEV	170	13.9	10.5
4	BJEV EC5	403	48	14.5
5	GAC AION S	410	58.8	13.9

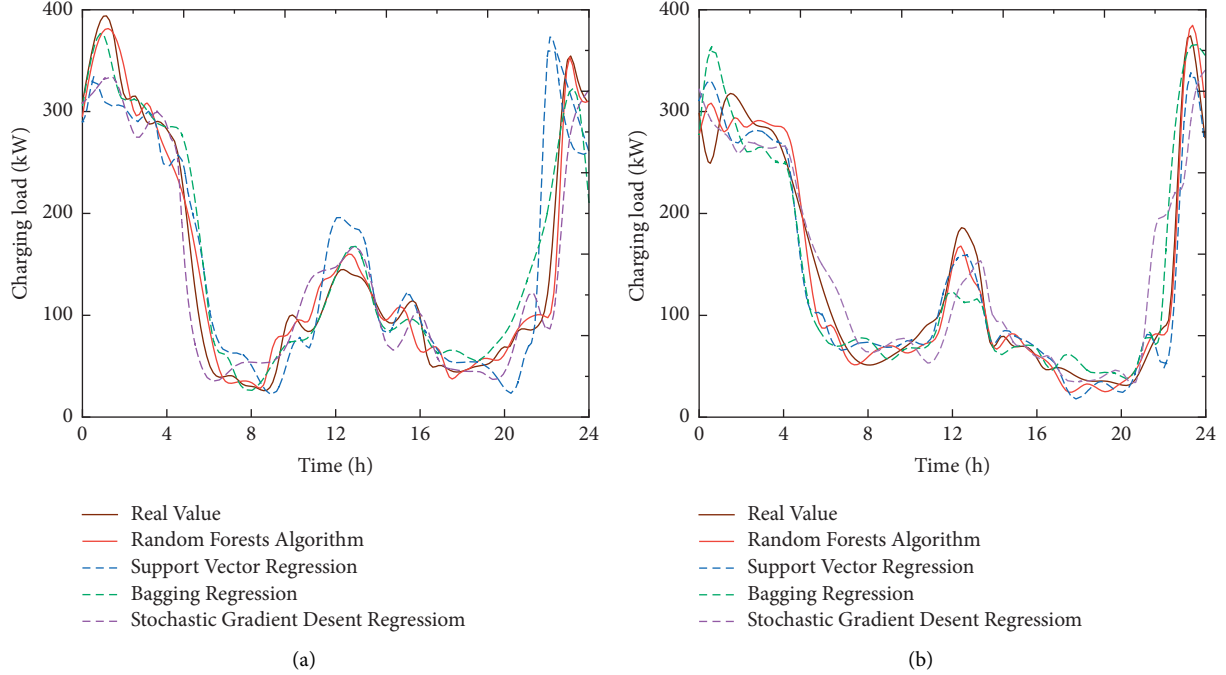


FIGURE 4: Forecasts for different time types. (a) Weekdays. (b) Weekends.

The linear interpolation method is used to preprocess the numerical anomaly data of time series. It is assumed that a few continuous data points show a linear variation. It mainly adopts the mean value of the nonmissing time series data before and after as the repair value of the missing data. It is suitable for scenes with high data acquisition quality and few missing values.

There are different processing methods for missing time series data in different positions, mainly including beginning and end missing and the middle missing. For the missing data in the first and last numbers, the nonmissing value closest to the first and last numbers will be used to fill in. The calculation formula is as follows:

$$\begin{aligned} a_1 &= a_2 = \dots = a_s, \\ a_N &= a_{N-1} = \dots = a_e, \end{aligned} \quad (20)$$

where  $a_s$  is the nonmissing value closest to the first position in the daily loading curve, and  $a_e$  is the nonmissing value closest to the last position.  $N$  is the data dimension of a single load data.

For the abnormal data of time series, this paper adopts the nearest-neighbor filling method. In the case of missing intermediate data, if single data are missing and the data of

its front and rear load point are known, the corresponding data can be filled by line interpolation; that is, the average value of the load value before and after the time is used for filling. If there are missing points, the linear expressions are calculated for the front and back nonmissing data points, and all the missing data points are calculated proportionally. The calculation formula is as follows:

$$a_x = a_m + \frac{a_n - a_m}{n - m} (x - m), \quad (21)$$

where  $a_x$  is the missing data, and  $a_m$  and  $a_n$  are the nearest nonmissing values before and after consecutive missing data.

Figure 4 shows the prediction results based on the random forest algorithm on weekdays and weekends. The trend in the figure can also see the travel habits of electric vehicles in this area. After 8:00 p.m., it gradually entered the charging peak, reached its peak around 11:00 p.m., and maintained a high level at around 5:00 a.m. Some vehicles have been charged, and the load begins to drop. It reaches a valley value around 8:00 a.m. and then continues to climb, with a small peak appearing at around 12:00 noon and then dropping.

In order to verify the effectiveness and superiority of the random forest algorithm for electric vehicle load forecasting,

TABLE 3: Forecasting error of each algorithm.

	Random forests algorithm	Support vector regression	Bagging regression	Stochastic gradient descend regression
MAPE	18.78%	29.92%	22.54%	30.85%
MSE	25.37	33.32	30.56	46.17

the other three algorithms are selected for forecasting, and the forecasting effect was compared with that of the random forest algorithm. They are support vector regression machine, Bagging regression machine, and stochastic gradient descent regression.

The prediction performance of the algorithm was evaluated using mean absolute percentage error (MAPE) and mean square error (MSE). The calculation formulas of MAPE and MSE are shown in following equations:

$$\delta = \frac{1}{N} \sum_{i=1}^N \left| \frac{P'_i - P_i}{P_i} \right| \times 100\%, \quad (i = 1, 2, \dots, N), \quad (22)$$

$$\varepsilon = \frac{1}{N} \sum_{i=1}^N (P'_i - P_i)^2, \quad (i = 1, 2, 3, \dots, N), \quad (23)$$

where  $P'_i$  is the predicted load value at the time  $i$  predicted by the algorithm.  $P_i$  is the actual load value at the time  $i$  moment of the day. The smaller  $\delta$  and  $\varepsilon$  are, the more accurate the prediction effect of the algorithm is.

Table 3 shows the statistics of load forecasting error of each forecasting algorithm. Among all experimental algorithms, the random forest algorithm has the smallest prediction error. It shows the effective load forecasting ability of electric vehicle. At the same time, horizontal comparison can be made, which shows that the method adopted in this paper can effectively improve the prediction accuracy of electric vehicles.

## 5. Conclusions

This paper analyzes the basic user behavior characteristics of electric vehicle load and establishes a single electric vehicle charging energy boundary model and a clustering classification model. A random forest algorithm-based electric vehicle load situation prediction method is proposed. The situational awareness results of the dispatchable resources in the power supply area are divided into sample sets and trained. Compared with other methods in the field of short-term load forecasting, the validity and superiority of the random forest algorithm for electric vehicle load forecasting are verified, and the charging performance and load forecasting accuracy of electric vehicles can be effectively improved. The following points can be explained by the simulation example.

- (a) According to the usage habits of electric vehicle users, the travel model of electric vehicles is established, and then, the mathematical model of charging behavior of electric vehicles clusters is established, and its correctness is proved. Aiming at the adverse impact of electric vehicle disorderly access on power grid dispatching, and considering the changing

characteristics of both the supply and demand sides, a situation awareness method is proposed to reasonably evaluate and forecast the power supply situation.

- (b) From a data-driven point of view, a method of electric vehicle load forecasting based on random forest algorithm is proposed, and the training set is constructed, which improves the accuracy of electric vehicle charging load forecasting. Moreover, the actual bearing capacity of the power supply area can also be taken into account while meeting the needs of users to the maximum extent.

## Data Availability

The data presented in this study are available on request from the corresponding author. The data are not publicly available due to the data use agreement.

## Conflicts of Interest

The authors declared that they have no conflicts of interest.

## Acknowledgments

This research was funded by Key R&D Program of Liaoning Province (2020JH2/10300101), Liaoning Revitalization Talents Program (XLYC1907138), the Key R&D Program of Shenyang (GG200252), and Liaoning PhD Initial Scientific Research Fund (2020-BS-179).

## References

- [1] S. R. Sinsel, R. L. Riemke, and V. H. Hoffmann, "Challenges and solution technologies for the integration of variable renewable energy sources—a review," *Renewable Energy*, vol. 145, pp. 2271–2285, 2020.
- [2] H.-I. Su and A. El Gamal, "Modeling and analysis of the role of energy storage for renewable integration: power balancing," *IEEE Transactions on Power Systems*, vol. 28, pp. 4109–4117, 2013.
- [3] L. Cozzi, T. Gould, S. Bouckaert et al., *World Energy Outlook 2020*, International Energy Agency, Paris, France, 2020.
- [4] S. Kim and J. Hur, "A probabilistic modeling based on Monte Carlo simulation of wind powered EV charging stations for steady-states security analysis," *Energies*, vol. 13, 2020.
- [5] M. P. Anand, B. Bagen, and A. Rajapakse, "Probabilistic reliability evaluation of distribution systems considering the spatial and temporal distribution of electric vehicles," *International Journal of Electrical Power & Energy Systems*, vol. 117, 2020.
- [6] M. Aziz, T. Oda, T. Mitani, Y. Watanabe, and T. Kashiwagi, "Utilization of electric vehicles and their used batteries for peak-load shifting," *Energies*, vol. 8, pp. 3720–3738, 2015.

- [7] Y. Wang and D. Infield, "Markov chain Monte Carlo simulation of electric vehicle use for network integration studies," *International Journal of Electrical Power & Energy Systems*, vol. 99, pp. 85–94, 2018.
- [8] Q. Dai, S. Duan, T. Cai, T. Chen, and L. Huang, "Cost-benefit model and its sensitivity analysis for battery charging and swapping station for electric vehicles," *Automation of Electric Power Systems*, vol. 38, pp. 41–47, 2014.
- [9] A. Colmenar-Santos, A. M. Muñoz-Gómez, E. Rosales-Asensio, and A. Lopez-Rey, "Electric vehicle charging strategy to support renewable energy sources in Europe 2050 low-carbon scenario," *Energy*, vol. 183, pp. 61–74, 2019.
- [10] R. Wang, Q. Sun, D. Ma, and Z. Liu, "The small-signal stability analysis of the droop-controlled converter in electromagnetic timescale," *IEEE Transactions on Sustainable Energy*, vol. 10, no. 3, pp. 1459–1469, 2019.
- [11] S. Deilami, A. S. Masoum, P. S. Moses, and M. A. S. Masoum, "Real-time coordination of plug-in electric vehicle charging in smart grids to minimize power losses and improve voltage profile," *IEEE Transactions on Smart Grid*, vol. 2, pp. 456–467, 2011.
- [12] K. Valentine, W. G. Temple, and K. M. Zhang, "Intelligent electric vehicle charging: rethinking the valley-fill," *Journal of Power Sources*, vol. 196, pp. 10717–10726, 2011.
- [13] R. Wang, Q. Sun, W. Hu, Y. Li, D. Ma, and P. Wang, "SoC-based droop coefficients stability region analysis of the battery for stand-alone supply systems with constant power loads," *IEEE Transactions on Power Electronics*, vol. 36, no. 7, pp. 7866–7879, 2021.
- [14] K. Wan and R. Liu, "Application of interval time-series vector autoregressive model in short-term load forecasting," *Power System Technology*, vol. 36, pp. 77–81, 2012.
- [15] H. Wang, J. Zhou, and K. Liu, "Summary of research on the short-term load forecasting method of the electric power system," *Electrical Automation*, vol. 37, pp. 1–3, 2015.
- [16] R. Wang, Q. Sun, P. Tu, J. Xiao, Y. Gui, and P. Wang, "Reduced-order aggregate model for large-scale converters with inhomogeneous initial conditions in DC microgrids," *IEEE Transactions on Energy Conversion*, vol. 36, no. 3, pp. 2473–2484, 2021.
- [17] N. Liao, Z. Hu, and Y. Ma, "Review of the short-term load forecasting methods of electric power system," *Power System Protection and Control*, vol. 39, pp. 147–152, 2011.
- [18] X. Huang, J. Chen, and Y. Chen, "Load forecasting method for electric vehicle charging station based on big data," *Automation of Electric Power Systems*, vol. 40, pp. 68–74, 2016.
- [19] W. Rui, S. Qiuye, Z. Pinjia, G. Yonghao, Q. Dehao, and W. Peng, "Reduced-order transfer function model of the droop-controlled inverter via Jordan continued-fraction expansion," *IEEE Transactions on Energy Conversion*, vol. 35, no. 3, pp. 1585–1595, 2020.
- [20] X. Zhou, M. Farivar, Z. Liu, L. Chen, and S. H. Low, "Reverse and forward engineering of local voltage control in distribution networks," *IEEE Transactions on Automatic Control*, vol. 66, pp. 1116–1128, 2021.
- [21] N. Eghtedarpour and E. Farjah, "Power control and management in a hybrid AC/DC microgrid," *IEEE Transactions on Smart Grid*, vol. 5, pp. 1494–1505, 2014.
- [22] W. Huang, Q. Liu, and S. Yang, "Security situation awareness based on power-supply ability model of active distribution system," *Electric Power Automation Equipment*, vol. 37, pp. 74–80, 2017.
- [23] H. Su, G. Wang, and L. Liu, "Ordered charging of electric vehicles based on time-space complementary," *Electrical Measurement & Instrumentation*, vol. 54, pp. 99–104, 2017.

## Research Article

# Energy Performance Contracting in a Supply Chain under Cap-and-Trade Regulation and Carbon Tax Policy

Chengzhen Meng,<sup>1</sup> Rong Zhang,<sup>2</sup> and Bin Liu <sup>3</sup>

<sup>1</sup>School of Economics and Management, Shanghai Maritime University, Shanghai 201306, China

<sup>2</sup>Research Center of Logistics, Shanghai Maritime University, Shanghai 201306, China

<sup>3</sup>Business School, University of Shanghai for Science and Technology, Shanghai 200093, China

Correspondence should be addressed to Bin Liu; [liubhnau@163.com](mailto:liubhnau@163.com)

Received 9 March 2022; Revised 11 May 2022; Accepted 13 May 2022; Published 8 June 2022

Academic Editor: B Rajanarayan Prusty

Copyright © 2022 Chengzhen Meng et al. This is an open access article distributed under the Creative Commons Attribution License, which permits unrestricted use, distribution, and reproduction in any medium, provided the original work is properly cited.

Energy performance contracting (EPC) is a new tool for supply chain members to cooperate in emission reduction. This paper investigates a two-tier supply chain composed of a supplier and a capital-constricted manufacturer with carbon reduction demand under different low-carbon policies (Cap-and-Trade Regulation and Carbon Tax Policy, respectively). The manufacturer is motivated to cooperate with the supplier to reduce carbon emissions through EPC services. Different from other research, the emission reduction decision maker of EPC services in this paper could be any supply chain member. The results show that cap-and-trade regulation and carbon tax policy have the same impact on the optimal pricing and emission reduction decisions in the monopoly supply chain, but the manufacturer's profit is higher under cap-and-trade regulation. And when the cost-sharing coefficient is within a low range, the emission reduction targets decided by the manufacturer are lower. Otherwise, the targets decided by the supplier are lower. Moreover, supply chain members can obtain higher profits when the reduction targets are determined by themselves, and supply chain coordination under different decision models could be realized through revenue sharing contracts. Considering the total profit of the supply chain, when the cost-sharing rate is within a low range, the supply chain can achieve a Pareto improvement if the supplier determines the emission reduction targets. Otherwise, the reduction targets decided by the manufacturer can realize a Pareto improvement.

## 1. Introduction

Chinese government proposed that carbon dioxide emissions should strive to achieve “carbon peak” in 2030 and “carbon neutrality” in 2060 on the 75<sup>th</sup> UN General Assembly. Cap-and-trade regulation and carbon tax policy are two effective low-carbon policies widely adopted by governments. Under the “double carbon” goal and low-carbon policies, to achieve both economic and environmental benefits, more and more manufacturing enterprises have increased their investment in carbon emission reduction. However, small and medium-sized enterprises may not be able to afford the high investment cost and can only choose to reduce production scales which damages the overall economic benefits of supply chain. Therefore, supply chain

members are motivated to help manufacturing enterprises to realize low-carbon production. Energy performance contracting (EPC) can be used as a financing mode to solve the above problem. For example, Siemens provides various modes of EPC services for its downstream manufacturers with limited funds and emission reduction needs to achieve environmental benefits [1]. Therefore, how to design an EPC project among supply chain members under the “double carbon” goal is very important.

At present, part of the research on EPC analyzes its implementation in the field of manufacturing [2], and is relatively rare in the context of supply chain [1]. On the other hand, the decider of the emission reduction targets in existing research on EPC is almost all the Energy Service Companies (ESCOs) which are the main investor of EPC



services [1–3]. However, under low-carbon policies, EPC clients with emission reduction demand have a better understanding of their own emission reduction needs and are closer to consumers with low-carbon preference. Therefore, it is also necessary to consider the clients to be the decision maker of EPC reduction targets in the context of low-carbon supply chain.

Based on the above discussion, this study establishes a two-echelon supply chain composed of a single supplier and a capital-constricted manufacturer with carbon reduction demand to explore the optimal emission reduction strategies and pricing decisions. Supply chain members are motivated to cooperate to reduce emissions through EPC services. The impact of different decision makers of EPC reduction targets and low-carbon policies are studied in this paper.

The main contributions of this work are as follows. Firstly, we consider the EPC implementation in the context of low-carbon supply chain which is rarely considered in existing research. Second, to the best of our knowledge, this is the first study to consider the manufacturer to be the decision maker of the reduction targets of EPC services. Finally, both cap-and-trade regulation and carbon tax policy are considered in this paper, and our study states the optimal decision maker of EPC reduction targets and the optimal reduction strategies and pricing decision under different circumstances.

The rest of this paper is organized as follows. Section 2 is the literature review. Section 3 describes the model and basic assumptions. Section 4 and section 5 discuss and obtain the equilibrium solutions when the reduction targets are decided respectively by the supplier and the manufacturer. Then, section 6 analyzes and compares the equilibrium results under different decision models. Moreover, it discusses the revenue sharing contracts to realize a Pareto improvement in the supply chain. And section 7 concludes this paper and proposes future research.

## 2. Literature Review

The research related to this study is mainly the research on low-carbon policies and EPC services. The research on low-carbon policies mainly focuses on the decision of supply chain emission reduction strategies under carbon trading regulation and carbon tax policy [4]. As an indirect mandatory measure, carbon trading regulation has an important impact on supply chain members' emission reduction decisions and supply chain operation decisions. Wang et al. [5] investigated the carbon reduction strategies and product recycle decisions under cap-and-trade regulation in a closed-loop supply chain. An et al. [6] developed a model composed of a finance-constrained manufacturer and a well-funded supplier and concluded the manufacturer's selection towards green credit financing and trade credit financing under different carbon caps. As for the carbon tax policy, Zhang et al. [7] considered that two manufacturers collaborated in core components' provision and competed in the final product market, and they need to decide to produce normal or low-carbon products. There are also many studies

comparing the above two carbon constraints. Zakeri et al. [8] analyzed the actual data from an Australian company to investigate the emission reduction decision and operation planning under these two policy schemes. Anand and Giraud-Carrier [9] developed an integrated production-pollution-abatement model of oligopolistic firms respectively under carbon trading and carbon tax policies and identified that these two low-carbon policies can replace each other to some extent. However, none of the above research has studied cooperative carbon reduction in the context of EPC projects.

The research on EPC mainly focuses on the implementation risks and obstacles [10–13], profit distribution [14] and building energy efficiency improvement [15, 16]. Liu et al. [3] explored the EPC contract design of building reconstruction under decentralized and centralized decision making, that is, the decisions on the distribution of EPC saving, contract term and project investment. Zhang et al. [2] compared the equilibrium solutions with or without EPC and with or without carbon trading respectively and found that the interaction between EPC and carbon trading regulation can reduce carbon emissions and increase corporate profits. Xu et al. [1] considered a two-echelon supply chain composed of a single supplier and two manufacturers with asymmetric funds and discussed the impact of the revenue sharing rates and variable cost coefficients on suppliers' profits, as well as which kind of manufacturers the supplier preferred to provide EPC services. However, the above literature does not consider that the manufacturer can also decide EPC's reduction targets, and only Xu et al. [1] considers the EPC service into a supply chain context.

The above literature studies the carbon reduction strategies of supply chain members and the design and implementation of EPC contracts from multiple perspectives. However, in the existing studies, few studies have considered EPC in a low-carbon supply chain and mostly consider the well-funded supplier as the decision maker of EPC reduction targets. However, the emission reduction targets decided by the manufacturer with emission reduction demand may be conducive to their collaborative management of carbon reduction and production. Hence, it is also necessary to consider that the manufacturer could be the decider of the EPC reduction target. This study considers the reduction targets can be decided by any supply chain member respectively under carbon trading regulation and carbon tax policy, discusses the impact of different low-carbon policies and different decision makers of reduction targets on the optimal pricing and reduction decision.

## 3. The Basic Model and Assumptions

This paper considers a two-echelon supply chain composed of a single supplier and a capital-constricted manufacturer with carbon reduction demand. The supplier is a Stackelberg leader and provides raw materials to the manufacturer who produces and sells the final products to consumers. Besides, the supplier can also provide EPC services to the

manufacturer as an ESCO to realize low-carbon production referring to the example of Siemens [1]. Facing various low-carbon policies, the capital-constrained manufacturer is also motivated to cooperate with its well-funded supplier to reduce emissions. The supply chain structure is shown in Figure 1.

Without loss of generality, the carbon emission of unit product produced by the manufacturer before the implementation of EPC is standardized to 1. The carbon reduction target  $e$  ( $0 < e < 1$ ) of EPC contract is determined by the manufacturer or the supplier. Therefore, the total emission reduction cost is  $k(1-e)^2/2$ , in which  $k$  ( $k > 0$ ) represents the carbon abatement cost coefficient. In the shared savings EPC, the manufacturer bears the total reduction cost in proportion  $\theta$  ( $0 < \theta < 1$ ) and shares the EPC savings in proportion  $\lambda$  ( $0 < \lambda < 1$ ) with its supplier.

Based on the previous researches [17–19], the market demand of the final products has a linear relationship with the retail price and reduction target, which can be described as  $q = 1 - bp + \delta(1 - e)$ , in which  $b$  ( $b > 0$ ) denotes the price-sensitive coefficient,  $p$  is the retail price of the final products and  $\delta$  ( $\delta > 0$ ) denotes the low-carbon preference of consumers.

This paper mainly considers two low-carbon policies: cap-and-trade regulation and carbon tax policy. Under the cap-and-trade regulation, the government allocates a certain carbon quota  $\phi$  to each enterprise. When the carbon emission generated in the process of production is higher than  $\phi$ , the enterprise needs to purchase the excessive quota from the carbon trading market at a certain price  $p_e$ . Conversely, the enterprise can sell the remaining quota to the carbon trading market at the same price  $p_e$ . Under the carbon tax policy, the government charges manufacturing enterprises' per unit of carbon emissions at a certain tax rate  $t$ .

To sum up, this paper totally considers four kinds of decision models which are summarized in Table 1. The decision on the reduction target of the EPC service takes precedence over the pricing decision. Therefore, as is shown in Figure 2, in the Stackelberg game model, the decision-making consequence is that one of the supply chain members firstly decides the reduction target  $e$ , and then the supplier decides the wholesale price  $w$ , and finally, the manufacturer determines the retail price  $p$ .

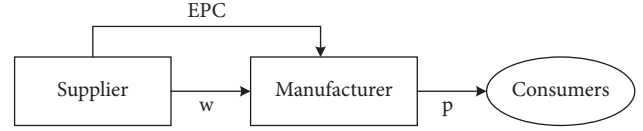


FIGURE 1: Supply chain structure.

TABLE 1: Four decision models.

EPC reduction target decision maker	Cap-and-trade regulation	Carbon tax policy
The supplier	Model SE	Model ST
The manufacturer	Model ME	Model MT

Superscript SE, ME, ST, MT are used to represent the equilibrium solutions of corresponding decision models. The following obtains and analyzes the equilibrium solution of each decision model respectively, and finally derives the optimal decision-making strategy through comparative analysis.

#### 4. EPC Carbon Reduction Target Determined by the Supplier

EPC carbon reduction target decided by the supplier is a commonly used decision-making method in existing research. As the ESCO of EPC service, the supplier needs to trade off its investment and share revenue of EPC savings when determining the emission reduction target. The following respectively discuss the game models under cap-and-trade regulation and carbon tax policy.

**4.1. Carbon Trading Regulation-Model SE.** Under carbon trading regulation, the manufacturer will sell its remaining quota to the carbon trading market when  $\phi - e^{SE}q^{SE} > 0$ , and will purchase excessive quota when  $\phi - e^{SE}q^{SE} < 0$ . The EPC savings in Model SE is  $p_e q^{SE} (1 - e^{SE})$ , and the supplier's share revenue of the savings is  $\lambda p_e q^{SE} (1 - e^{SE})$ . The investment of emission abatement borne by the manufacturer is  $(k\theta/2)(1 - e^{SE})^2$ , and that borne by the supplier is  $(k(1 - \theta)/2)(1 - e^{SE})^2$ . Therefore, the profit functions of the supplier and the manufacturer can be described as

$$\begin{aligned} \pi_s^{SE} &= w^{SE} q^{SE} - \frac{k(1-\theta)}{2} (1 - e^{SE})^2 + \lambda p_e q^{SE} (1 - e^{SE}), \\ \pi_m^{SE} &= (p^{SE} - w^{SE}) q^{SE} - \frac{k\theta}{2} (1 - e^{SE})^2 - \lambda p_e q^{SE} (1 - e^{SE}) - (e^{SE} q^{SE} - \phi) p_e. \end{aligned} \quad (1)$$

Using the backward induction method, the equilibrium solution of the Model SE is existing when  $B_e > 0$ ,  $k > ((1 + \delta)A_e)/4bF$  and  $kB_e^2 [2bkF^2 - \theta A_e^2] + 2\phi p_e (\Delta - A_e^2)^2 > 0$  and is shown in Table 2. All the proofs are shown in Appendix.

**4.2. Carbon Tax Policy-Model ST.** Under carbon tax policy, the government taxes per unit carbon emission of the manufacturer at a certain tax rate  $t$ . The EPC savings in Model ST is  $tq^{ST} (1 - e^{ST})$ , and the manufacturer shares a

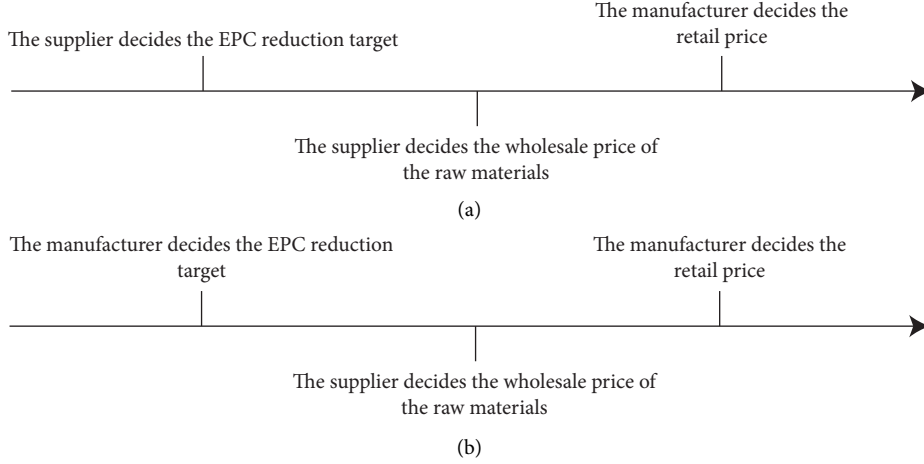


FIGURE 2: Game sequence of all decision models.

TABLE 2: Equilibrium solutions of Model SE and Model ST.

	Model SE	Model ST
$P$	$(kF(bp_e + 3) - p_e(1 + \delta)A_e)/(\Delta - A_e^2)$	$((kF(bt + 3) - t(1 + \delta)A_t)/\Delta - A_t^2)$
$E$	$((\Delta - (1 + \delta)A_e)/\Delta - A_e^2)$	$((\Delta - (1 + \delta)A_t)/\Delta - (1 + \delta)A_t)$
$W$	$((B_e(2kF - \lambda p_e A_e))/\Delta - A_e^2)$	$((B_t(2kF - \lambda t A_t))/\Delta - A_t^2)$
$\pi_s$	$(kFB_e^2/2(\Delta - A_e^2))$	$(kFB_t^2/2(\Delta - A_t^2))$
$\pi_m$	$((kB_e^2[2bkF^2 - \theta A_e^2])/2(\Delta - A_e^2) + \phi p_e)$	$((kB_t^2[2bkF^2 - \theta A_t^2])/2(\Delta - A_t^2))$

Where  $\Delta = 4bk(1 - \theta)$ ,  $F = 1 - \theta$ ,  $A_e = bp_e + \delta$ ,  $A_t = bt + \delta$ ,  $B_e = 1 - bp_e$  and  $B_t = 1 - bt$ .

portion of the savings  $\lambda t q^{ST}(1 - e^{ST})$  to the supplier. The manufacturer also bears a portion of the total investment of EPC  $(k\theta/2)(1 - e^{ST})^2$ . Therefore, the profit functions of the

supplier and the manufacturer in Model ST can be obtained as

$$\pi_s^{ST} = w^{ST} q^{ST} - \frac{k(1 - \theta)}{2}(1 - e^{ST})^2 + \lambda t q^{ST}(1 - e^{ST}), \quad (2)$$

$$\pi_m^{ST} = (p^{ST} - w^{ST})q^{ST} - \frac{k\theta}{2}(1 - e^{ST})^2 - \lambda t q^{ST}(1 - e^{ST}) - t e^{ST} q^{ST}. \quad (3)$$

Using the backward induction method, the equilibrium solution of the Model ST is existing when  $B_t > 0$  and  $k > \max\{((1 + \delta)A_t)/4bF, (\theta A_t^2/2bF^2)\}$  and is shown in Table 2.

## 5. EPC Carbon Reduction Target Determined by the Manufacturer

This section considers the optimal pricing and reduction decision when the emission reduction targets are decided by

the manufacturer. It is also a decision-making method rarely considered in current research. The reduction and pricing strategies of supply chain members are also discussed under two low-carbon policies.

5.1. Carbon Trading Regulation-Model ME. The profit functions of the supplier and the manufacturer in Model ME can be obtained as follows.

$$\pi_s^{ME} = w^{ME} q^{ME} - \frac{k(1 - \theta)}{2}(1 - e^{ME})^2 + \lambda p_e q^{ME}(1 - e^{ME}), \quad (4)$$

$$\pi_m^{ME} = (p^{ME} - w^{ME})q^{ME} - \frac{k\theta}{2}(1 - e^{ME})^2 - \lambda p_e q^{ME}(1 - e^{ME}) - (e^{ME} q^{ME} - \phi)p_e.$$

It can be found that the profit functions of the supplier and the manufacturer in Model ME are the same as that of Model SE. Because Model ME and Model SE are both developed under carbon trading regulation, and the only difference between them is the calculations in backward induction method because of the different decider of the reduction targets. Using the backward method, the

equilibrium solution of the Model ME is existing when  $B_e > 0$  and  $k > \max\{(FA_e^2/16b\theta^2), ((1 + \delta)A_e/8b\theta)\}$  and is shown in Table 3.

5.2. *Carbon Tax Policy-Model MT.* Facing carbon tax policy, the profit functions in Model MT can be described as.

$$\begin{aligned}\pi_s^{MT} &= w^{MT} q^{MT} - \frac{k(1-\theta)}{2}(1-e^{MT})^2 + \lambda t q^{MT}(1-e^{MT}), \\ \pi_m^{MT} &= (p^{MT} - w^{MT})q^{MT} - \frac{k\theta}{2}(1-e^{MT})^2 - \lambda t q^{MT}(1-e^{MT}) - t e^{MT} q^{MT}.\end{aligned}\quad (5)$$

The profit functions of the supplier and the manufacturer are the same as equation (2) and (3) for the same reasons as above. And the optimal solution of Model MT is existing when  $B_t > 0$  and  $k > \max\{(FA_t^2/16b\theta^2), ((1 + \delta)A_t/8b\theta)\}$  and is shown in Table 3.

### Proposition 1

- (i) In addition to the manufacturer's profit, when  $p_e = t$ , the equilibrium solutions obtained under two different low-carbon policies are the same when the EPC carbon reduction targets are both decided by the same player.
- (ii)  $\pi_m^{SE} - \pi_m^{ST} = \pi_m^{ME} - \pi_m^{MT} = \phi p_e$ .

Comparing the equilibrium solutions of the above four decision-making models in Table 2 and Table 3, when the carbon trading price is equal to the carbon tax rate, the equilibrium solutions are similar under two low-carbon policies if the reduction targets are decided by the same supply chain members. That is, these two low-carbon policies have the same impact on the decision making of supply chain members when the EPC reduction targets are determined by the same supply chain member. The only difference is the manufacturer's profit, which is higher under carbon trading regulation. This conclusion is similar to that of Anand and Giraud-Carrier [9]. To facilitate comparison and discussion, the following analysis takes the carbon tax policy as an example, and the conclusion is also valid under carbon trading regulation.

## 6. Analysis and Comparison

This section firstly analyses the impact of the cost-sharing rate  $\theta$  on decision making, and then compares the optimal equilibrium solutions and profits in different decision models. Finally, we figure out the optimal reduction and pricing strategies of supply chain members under different circumstances.

### 6.1. The Impact of the Cost-Sharing Rate $\theta$ on Emission Reduction Targets and Optimal Retail Prices

**Proposition 2.** When  $B_t > 0$  and  $k > \max\{((1 + \delta)A_t/4bF), (\theta A_t^2/2bF^2), (FA_t^2/16b\theta^2), ((1 + \delta)A_t/8b\theta)\}$ ,

- (i)  $(\partial e^{ST^*}/\partial\theta) < (0\partial e^{MT^*}/\partial\theta) > 0$ ;
- (ii) If  $0 < \delta < (bt/3)$ ,  $(\partial p^{ST^*}/\partial\theta) < 0$ ,  $(\partial p^{MT^*}/\partial\theta) > 0$ , if  $\delta > (bt/3)$ ,  $(\partial p^{ST^*}/\partial\theta) > 0$ ,  $(\partial p^{MT^*}/\partial\theta) < 0$ .

Proposition 2 indicates that (i) the impact of the cost-sharing rate on emission reduction targets is opposite in different decision models. That is, the increase in the cost-sharing rate decreases the reduction target in Model ST, while increases the target in Model MT. This is because a higher  $\theta$  means a higher proportion of reduction cost borne by the manufacturer and a lower the proportion borne by the supplier. Therefore, with the increase of  $\theta$ , the supplier prefers to take more emission abatement effort to obtain a higher profit from sharing revenue of EPC savings. While in Model MT, the capital-constricted manufacturer has to increase its target to reduce total emission reduction cost.

Proposition 2 (ii) demonstrates that the impact of the cost-sharing rate on the optimal retail prices will be influenced by the low-carbon preference of consumers and is also opposite in different decision models. When  $\delta$  is within a low range (i.e.  $0 < \delta < (bt/3)$ ), the optimal retail price decreases with  $\theta$  in Model ST, while increases with  $\theta$  in Model MT. When  $\delta$  is relatively high (i.e.  $\delta > (bt/3)$ ), the results are opposite.

This is because when  $\delta$  is within a low range ( $0 < \delta < (bt/3)$ ), the product demand will be lightly influenced by the reduction of unit carbon emission and significantly affected by the retail price according to the demand function. Therefore, the manufacturer prefers to set a lower retail price in Model ST to earn more profits from sales revenue and EPC savings with the increase of  $\theta$ . When  $\delta$  is relatively high, the reduction of unit carbon emission has a significant impact on demand, therefore the manufacturer can also obtain high demand even if the retail price is higher.

While in Model MT, when  $\delta$  is within a low range, with the increase of  $\theta$ , the demand will lightly decrease because of the increase of the target which enable the manufacturer to lightly increase the retail price to earn more profits from sales revenue. When  $\delta$  is relatively high, the demand will significantly decrease with the increase of  $\theta$ . As a result, the manufacturer has to decrease the retail price to ensure the demand.

TABLE 3: Equilibrium solutions of Model ME and Model MT.

	Model ME	Model MT
$p$	$((2k\theta(bp_e + 3) - p_e(1 + \delta)A_e)/8bk\theta - A_e^2)$	$((2k\theta(bt + 3) - t(1 + \delta)A_t)/8bk\theta - A_t^2)$
$E$	$((8bk\theta - (1 + \delta)A_e)/8bk\theta - A_e^2)$	$((8bk\theta - (1 + \delta)A_t)/8bk\theta - A_t^2)$
$w$	$((B_e(4k\theta - \lambda p_e A_e))/8bk\theta - A_e^2)$	$((B_t(4k\theta - \lambda t A_t))/8bk\theta - A_t^2)$
$\pi_s$	$((kB_e^2(16bk\theta^2 - FA_e^2))/2(8bk\theta - A_e^2)^2)$	$((kB_t^2(16bk\theta^2 - FA_t^2))/2(8bk\theta - A_t^2)^2)$
$\pi_m$	$((k\theta B_e^2)/2(8bk\theta - A_e^2)) + \phi p_e$	$((k\theta B_t^2)/2(8bk\theta - A_t^2))$

Where  $F = 1 - \theta$ ,  $A_e = bp_e + \delta$ ,  $A_t = bt + \delta$ ,  $B_e = 1 - bp_e$  and  $B_t = 1 - bt$ .

**6.2. Comparative Analysis of Different Decision-Making Methods.** This section compares and analyzes the equilibrium solutions obtained in Model ST and Model MT and discusses the strategy choice of the decider of the EPC reduction target in different circumstances.

### 6.2.1. The Comparison of the Reduction Targets of the EPC Service

**Proposition 3.** When  $B_t > 0$  and  $k > \max\{((1 + \delta)A_t/4bF), (\theta A_t^2/2bF^2), (FA_t^2/16b\theta^2), ((1 + \delta)A_t/8b\theta)\}$ , if  $0 < \theta < (1/3)$ ,  $e^{ST^*} > e^{MT^*}$ , if  $(1/3) < \theta < 1$ ,  $e^{ST^*} < e^{MT^*}$ .

Proposition 3 shows that the reduction targets will be influenced by the cost-sharing rate. When  $\theta$  is within a low range ( $0 < \theta < (1/3)$ ), the reduction target is lower in Model MT, that is, the manufacturer prefers to take more emission abatement effort than the supplier. Otherwise ( $(1/3) < \theta < 1$ ), the target is lower in Model ST.

The reason is that the supplier will bear most of reduction cost when  $\theta$  is relatively low ( $0 < \theta < (1/3)$ ), which induces the supplier to place a higher reduction target to reduce the cost and encourages the manufacturer to set a lower target to earn more profits from sales revenue and carbon tax savings.

When  $\theta$  is within a high range, both supply chain members will take opposite reduction decisions. The capital-constricted manufacturer has to set a higher target because of the high sharing rate, and the supplier prefers to lower the target to earn more profits from sharing revenue of EPC savings and wholesale revenues.

### 6.2.2. The Comparison of the Optimal Wholesale Prices

**Proposition 4.** The supplier's optimal wholesale prices in different decision models will be jointly affected by the EPC savings sharing rate  $\lambda$ , the cost-sharing rate  $\theta$  and the consumers' low-carbon preference  $\delta$ , and the comparison results are shown in Table 4.

Proposition 4 indicates that when the sharing rate  $\lambda$  is within a low range (i.e.  $0 < \lambda < (1/2)$ ), the optimal wholesale prices will be affected by the cost-sharing rate  $\theta$ . When  $\theta$  is low (i.e.  $0 < \theta < (1/3)$ ), the wholesale price is higher in Model MT. Otherwise (i.e.  $(1/3) < \theta < 1$ ), it is higher in Model ST. The reason is that the supplier cannot obtain higher revenue from offering EPC service if the sharing rate is low. According to Proposition 3, the lower reduction target increases the final product demand and therefore enable the

supplier to set a higher wholesale price to maximizing its profit from selling raw products.

When  $\lambda$  is relatively high (i.e.  $(1/2) < \lambda < 1$ ), the wholesale prices will be jointly affected by the cost-sharing rate and consumers' low-carbon preference. If both  $\theta$  and  $\delta$  are within a low or high range (i.e.  $(1 - 3\theta)[\delta - bt(2\lambda - 1)] > 0$ ), the wholesale price in Model MT is higher. Conversely, the wholesale price in Model ST is higher. This is because the product demand will be jointly affected by the reduction target and retail price referring to the demand function. If  $\theta$  and  $\delta$  are both within a low or high range, product demand is higher in Model MT. As a result, the supplier can set a higher wholesale price to earn more profits from selling raw materials as well as sharing revenue of EPC. The reason is similar in Model ST if one parameter is high while the other is low.

### 6.2.3. The Comparison of the Optimal Retail Prices

**Proposition 5.** When  $B_t > 0$  and  $k > \max\{((1 + \delta)A_t/4bF), (\theta A_t^2/2bF^2), (FA_t^2/16b\theta^2), ((1 + \delta)A_t/8b\theta)\}$ ,

- (i) When  $0 < \delta < (bt/3)$ , if  $0 < \theta < (1/3)$ ,  $p^{ST^*} > p^{MT^*}$ , if  $(1/3) < \theta < 1$ ,  $p^{ST^*} < p^{MT^*}$ ;
- (ii) When  $\delta > (bt/3)$ , if  $0 < \theta < (1/3)$ ,  $p^{ST^*} < p^{MT^*}$ , if  $(1/3) < \theta < 1$ ,  $p^{ST^*} > p^{MT^*}$ .

Proposition 5 shows that the optimal retail prices under two models will be jointly affected by the cost-sharing rate and consumers' low-carbon preference. When  $\theta$  and  $\delta$  are both within a high or low range (i.e.  $(1 - 3\theta)(bt - 3\delta) > 0$ ), the retail price is higher in Model ST. Otherwise, it is higher in Model MT.

The reason is that when  $\delta$  is within a low range ( $0 < \delta < (bt/3)$ ), the retail price will significantly influence the demand. As a result, the manufacturer will set a higher retail price for the decision model with higher reduction target to reduce demand and thus reduce the cost of carbon tax. When  $\delta$  is relatively high (i.e.  $\delta > (bt/3)$ ), the manufacturer prefers to set a higher retail price for the decision model with lower reduction target to earn more profits from sales revenue and savings revenue of EPC service.

### 6.2.4. The comparison of the profits of the supplier, the manufacturer and the supply chain

**Proposition 6.** When  $B_t > 0$  and  $k > \max\{((1 + \delta)A_t/4bF), (\theta A_t^2/2bF^2), (FA_t^2/16b\theta^2), ((1 + \delta)A_t/8b\theta)\}$ ,

TABLE 4: The comparison results of the supplier's optimal wholesale prices in different decision models.

Sharing rate of EPC service	Cost-sharing rate	Consumers' low-carbon preference	Comparison results
$0 < \lambda < (1/2)$	$0 < \theta < (1/3)$		$w^{ST^*} < w^{MT^*}$
	$(1/3) < \theta < 1$		$w^{ST^*} > w^{MT^*}$
$(1/2) < \lambda < 1$	$0 < \theta < (1/3)$	$0 < \delta < bt(2\lambda - 1)$	$w^{ST^*} < w^{MT^*}$
		$\delta > bt(2\lambda - 1)$	$w^{ST^*} > w^{MT^*}$
	$(1/3) < \theta < 1$	$0 < \delta < bt(2\lambda - 1)$	$w^{ST^*} > w^{MT^*}$
		$\delta > bt(2\lambda - 1)$	$w^{ST^*} < w^{MT^*}$

TABLE 5: Profits of supply chain members after coordination.

	$0 < \theta < ((8bk - A_t^2)/16bk)$	$((8bk - A_t^2)/16bk) < \theta < 1$
$\pi_s$	$((kFB_t^2)/2(\Delta - A_t^2)) - f_1$	$((kFB_t^2)/2(\Delta - A_t^2))$
$\pi_m$	$((k\theta B_t^2)/2(8bk\theta - A_t^2))$	$((k\theta B_t^2)/2(8bk\theta - A_t^2)) - f_2$

Where  $\Delta = 4bk(1 - \theta)$ ,  $F = 1 - \theta$ ,  $A_t = bt + \delta$ ,  $B_t = 1 - bt$ ,  $f_1 = ((bk^2 A_t^2 B_t^2 (1 - 3\theta)^2)/(8bk\theta - A_t^2)(\Delta - A_t^2)^2)$ ,  $f_2 = ((2bk^2 A_t^2 B_t^2 (1 - 3\theta)^2)/(\Delta - A_t^2)(8bk\theta - A_t^2)^2)$ .

- (i)  $\pi_s^{ST^*} > \pi_s^{MT^*}$ ,  $\pi_m^{ST^*} < \pi_m^{MT^*}$ ;  
(ii) When  $0 < \theta < ((8bk - A_t^2)/16bk)$ ,  $\pi_{sc}^{ST^*} > \pi_{sc}^{MT^*}$ , when  $((8bk - A_t^2)/16bk) < \theta < 1$ ,  $\pi_{sc}^{ST^*} < \pi_{sc}^{MT^*}$ .

Proposition 6 (i) shows that in decentralized decision model, rational decision makers aim at maximizing their own profits and can always obtain a higher profit when the reduction target is made by themselves. That is, both supply chain members both prefer to determine the reduction target by themselves. This is because the decision of reduction targets determines the total reduction cost and further influences the demand and all price decisions, and ultimately affects the profits of supply chain members.

Proposition 6 (ii) demonstrates that if the cost-sharing rate is within a low range ( $0 < \theta < ((8bk - A_t^2)/16bk)$ ), the total profit is higher in Model ST. Otherwise (i.e.  $((8bk - A_t^2)/16bk) < \theta < 1$ ), the total profit in Model MT is higher. That is, the total profit of supply chain is higher in the decision model which decision maker of reduction target bears a higher proportion of emission reduction costs.

This is because a lower range of  $\theta$  results in a lower reduction target and a higher sales revenue in Model MT. However, higher sales revenue cannot compensate for the higher cost of emission reduction and carbon tax. Therefore, the total profit is higher in Model ST when  $\theta$  is within a low range. The reason is similarly when  $\theta$  is relatively high. Proposition 6 (ii) also means that for the total profit of supply chain, the lower the emission reduction targets are not the better.

Considering the total profit of supply chain, the supply chain coordination under different decision models can be realized through the revenue sharing contracts. Therefore, when  $\pi_{sc}^{ST^*} > \pi_{sc}^{MT^*}$ , Pareto improvement can be realized in the supply chain when the reduction target is determined by the supplier. And the revenue sharing contract needs to satisfy  $\pi_m^{ST^*} + f_1 \geq \pi_m^{MT^*}$  and  $\pi_s^{ST^*} - f_1 \geq \pi_s^{MT^*}$ . When  $\pi_{sc}^{ST^*} < \pi_{sc}^{MT^*}$ , supply chain achieves a Pareto improvement when the target is decided by the manufacturer. And the revenue sharing contract needs to satisfy  $\pi_s^{MT^*} + f_2 \geq \pi_s^{ST^*}$  and  $\pi_m^{MT^*} - f_2 \geq \pi_m^{ST^*}$ . The profits of supply chain members after coordination are shown in Table 5.

## 7. Conclusion and Discussions

Under the background of the capital-constrained manufacturer's demand for emission reduction, considering two different low-carbon policies, this paper studies the selection of the decision maker of emission reduction target in a two-tier supply chain to realize cooperative carbon reduction through EPC services. Respectively obtains the equilibrium solutions of four decision models with backward induction approach, analyzes the impact of the emission reduction cost-sharing rate on the optimal reduction targets and retail prices, and compares the equilibrium solutions and profits in different decision models.

This research finds that, the cap-and-trade regulation and carbon tax policy have the same impact on the optimal pricing and emission reduction decision in the monopoly supply chain, but the manufacturer's profit is higher under cap-and-trade regulation. Furthermore, when the cost-sharing coefficient is within a low range, the emission reduction targets decided by the manufacturer are lower. Otherwise, the targets decided by the supplier are lower. Meanwhile, supply chain members can obtain higher profit when the reduction targets are determined by themselves, and supply chain coordination under different decision models could be realized through revenue sharing contracts. Based on the overall profit of the supply chain, when the cost-sharing rate is within a low range, the supply chain can achieve a Pareto improvement if the supplier determines the emission reduction targets. When the cost-sharing coefficient is relatively high, the reduction targets decided by the manufacturer can realize a Pareto improvement.

This study also has a lot to expend. For example, this paper only considers a simple supply chain structure composed by a single supplier and a single manufacturer. In practical, a large scale supplier has multiple small and medium-sized downstream manufacturers. What will the pricing and emission reduction of supply chain members be when the supply chain structure is more complex? It can also consider two competing supply chains to compare the optimal pricing and reduction decision with and without EPC.

## Appendix

### A. Proof of the equilibrium solution of Model SE

Using the backward induction approach, the manufacturer decides the retail price firstly,

$$\frac{\partial \pi_m^{SE}}{\partial p} = 1 + \delta(1 - e) - 2bp + b[w + (e + \lambda - e\lambda)p_e]. \quad (A.1)$$



Make it equal to 0, and we get  $p^{SE} = (1 + \delta(1 - e) + b[w + (e + \lambda - e\lambda)p_e]/2b)$ . And  $(\partial^2 \pi_m^{SE}/\partial p^2) = -2b < 0$ , which means  $\pi_m^{SE}$  is a concave function with respect to  $p^{SE}$ . Substituting  $p^{SE}$  into  $\pi_m^{SE}$  and  $\pi_s^{SE}$ , the supplier decides the wholesale price,

$$\frac{\partial \pi_s^{SE}}{\partial w} = 1 + \delta(1 - e) - 2bw - bp_e[2\lambda(1 - e) + e]. \quad (\text{A.2})$$

Also make it equal to 0, and we get  $w^{SE} = (1 + \delta(1 - e) - bp_e[2\lambda(1 - e) + e]/2b)$ . Also substituting  $w^{SE}$  into  $\pi_m^{SE}$  and  $\pi_s^{SE}$ .

Finally, the supplier decides the reduction target,

$$\frac{\partial \pi_s^{SE}}{\partial e} = \Delta - (1 + \delta)A_e - (\Delta - A_e^2)e. \quad (\text{A.3})$$

The corresponding Hessian Matrix is

$$H_1(w, e) = \begin{bmatrix} -b & \frac{[\delta + bp_e(1 - 2\lambda)]}{2} \\ \frac{[\delta + bp_e(1 - 2\lambda)]}{2} & \lambda p_e[\delta + bp_e(1 - \lambda)] - kF \end{bmatrix}. \quad (\text{A.4})$$

It is easily to check that  $H_1(w, e)$  is a negative definite matrix when  $k > (A_e^2/4bF)$ . Let  $(\partial \pi_s^{SE}/\partial e) = 0$ , we can get  $e^{SE*} = (\Delta - (1 + \delta)A_e/\Delta - A_e^2)$ . Substituting  $e^{SE*}$  back into  $p^{SE}$ ,  $w^{SE}$ ,  $\pi_s^{SE}$  and  $\pi_m^{SE}$ , we can get the equilibrium solutions and the optimal profits of supply chain members. In order to satisfy the conditions of  $0 < e^{SE*} < 1$  and  $\pi_m^{SE} > 0$ , we have  $B_e > 0$ ,  $\Delta > (1 + \delta)A_e$  and  $kB_e^2[2bkF^2 - \theta A_e^2] + 2\phi p_e(\Delta - A_e^2)^2 > 0$ .

## B. Proof of the equilibrium solution of Model ST

The game sequence of Model ST is similar to Model SE. Firstly, the manufacturer decides the retail price,

$$\frac{\partial \pi_m^{ST}}{\partial p} = 1 + \delta(1 - e) - 2bp + b[w + (e + \lambda - e\lambda)t]. \quad (\text{B.1})$$

Make it equal to 0, and we get  $p^{ST} = (1 + \delta(1 - e) + b[w + (e + \lambda - e\lambda)t]/2b)$ . And  $(\partial^2 \pi_m^{ST}/\partial p^2) = -2b < 0$ , which means  $\pi_m^{ST}$  is a concave function with respect to  $p^{ST}$ . Substituting  $p^{ST}$  into  $\pi_m^{ST}$  and  $\pi_s^{ST}$ .

Then, the supplier decides the wholesale price,

$$\frac{\partial \pi_s^{ST}}{\partial w} = 1 + \delta(1 - e) - 2bw - bt[2\lambda(1 - e) + e]. \quad (\text{B.2})$$

Also make it equal to 0, and we can get  $w^{ST} = (1 + \delta(1 - e) - bt[2\lambda(1 - e) + e]/2b)$ . Also substituting  $w^{ST}$  into  $\pi_m^{ST}$  and  $\pi_s^{ST}$ .

Finally, the supplier decides the reduction target,

$$\frac{\partial \pi_s^{ST}}{\partial e} = \Delta - (1 + \delta)A_t - (\Delta - A_t^2)e. \quad (\text{B.3})$$

The corresponding Hessian Matrix is

$$H_2(w, e) = \begin{bmatrix} -b & \frac{[\delta + bt(1 - 2\lambda)]}{2} \\ \frac{[\delta + bt(1 - 2\lambda)]}{2} & \lambda t[\delta + bt(1 - \lambda)] - k(1 - \theta) \end{bmatrix}. \quad (\text{B.4})$$

It is easily to check that  $H_2(w, e)$  is a negative definite matrix when  $k > (A_t^2/4bF)$ . Let  $(\partial \pi_s^{ST}/\partial e) = 0$ , we can get  $e^{ST*} = (\Delta - (1 + \delta)A_t/(\Delta - A_t^2))$ . Substituting  $e^{ST*}$  back into  $p^{ST}$ ,  $w^{ST}$ ,  $\pi_s^{ST}$  and  $\pi_m^{ST}$ , we can get the equilibrium solutions and the optimal profits of supply chain members. In order to satisfy the condition of  $0 < e^{ST*} < 1$  and  $\pi_m^{ST} > 0$ , we have  $B_t > 0$  and  $k > \max\{(1 + \delta)A_t/4bF, (\theta A_t^2/2bF^2)\}$ .

## C. Proof of the equilibrium solution of Model ME

The only difference between Model SE and Model ME is the decider of the reduction target. Therefore, the solving process of the first two stages is similar to Model SE. After solving  $p^{ME}$  and  $w^{ME}$  which are similar to  $p^{SE}$  and  $w^{SE}$  respectively, the manufacturer finally decides the reduction target,

$$\frac{\partial \pi_m^{ME}}{\partial e} = 8bk\theta - (1 + \delta)A_e - (8bk\theta - A_e^2)e. \quad (\text{C.1})$$

The corresponding Hessian Matrix is  $H_3(p, e) = \begin{bmatrix} -2b & ((bp_e - 3\delta)/2) \\ ((bp_e - 3\delta)/2) & \delta p_e - k\theta - (\delta^2/b) \end{bmatrix}$ . It is easily to check that  $H_3(p, e)$  is a negative definite matrix when  $k > (A_e^2/8b\theta)$ . Let  $(\partial \pi_m^{ME}/\partial e) = 0$ , we can get  $e^{ME*} = ((8bk\theta - (1 + \delta)A_e)/8bk\theta - A_e^2)$ . Substituting  $e^{ME*}$  back into  $p^{ME}$ ,  $w^{ME}$ ,  $\pi_s^{ME}$  and  $\pi_m^{ME}$ , we can get the equilibrium solutions and the optimal profits of supply chain members. In order to satisfy the conditions of  $0 < e^{ME*} < 1$  and  $\pi_s^{ME} > 0$ , we have  $B_e > 0$  and  $k > \max\{(FA_e^2/16b\theta^2), (1 + \delta)A_e/8b\theta\}$ .

## D. Proof of the equilibrium solution of Model MT

The solving process of the first two stages is similar to Model ST. After solving  $p^{MT}$  and  $w^{MT}$  which are similar to  $p^{ST}$  and  $w^{ST}$  respectively, the manufacturer finally decides the reduction target,

$$\frac{\partial \pi_m^{MT}}{\partial e} = 8bk\theta - (1 + \delta)A_t - (8bk\theta - A_t^2)e. \quad (\text{D.1})$$

The corresponding Hessian Matrix is  $H_4(p, e) = \begin{bmatrix} -2b & ((bt - 3\delta)/2) \\ ((bt - 3\delta)/2) & \delta t - k\theta - (\delta^2/b) \end{bmatrix}$ . It is easily to check that  $H_4(p, e)$  is a negative definite matrix when  $k > (A_t^2/8b\theta)$ . Let  $(\partial \pi_m^{MT}/\partial e) = 0$ , we can get  $e^{MT*} = ((8bk\theta - (1 + \delta)A_t)/8bk\theta - A_t^2)$ . Substituting  $e^{MT*}$  back into  $p^{MT}$ ,  $w^{MT}$ ,  $\pi_s^{MT}$  and  $\pi_m^{MT}$ , we can get the equilibrium solutions and the optimal profits of supply chain members. In order to satisfy the

conditions of  $0 < e^{MT^*} < 1$  and  $\pi_s^{MT} > 0$ , we have  $B_t > 0$  and  $k > \max\{(FA_t^2/16b\theta^2), ((1 + \delta)A_t/8b\theta)\}$ .

## E. Proof of Proposition 1

When  $p_e = t$ , besides the profit of the manufacturer, it is easily to figure out that the equilibrium solutions of Model SE is similar to those in Model ST, and the equilibrium solutions of Model ME is also similar to those in Model MT.

As for the manufacturer's profit, it is higher under cap-and-trade regulation than under carbon tax policy, and the difference equals to the product of the manufacturer's initial carbon quota  $\phi$  and the carbon trading price  $p_e$ .

## F. Proof of Proposition 2

When  $B_t > 0$  and  $k > \max\{((1 + \delta)A_t/4bF), (\theta A_t^2/2bF^2), (FA_t^2/16b\theta^2), ((1 + \delta)A_t/8b\theta)\}$

$$(i) (\partial e^{ST^*}/\partial\theta) = -(4bkA_tB_t/(\Delta - A_t^2)^2) < 0, (\partial e^{MT^*}/\partial\theta) = (8bkA_tB_t/(8bk\theta - A_t^2)^2) > 0$$

$$(ii) \text{ We have } (\partial p^{ST^*}/\partial\theta) = (-kA_tB_t(bt - 3\delta)/(\Delta - A_t^2)^2). \text{ When } bt - 3\delta > 0, \text{ i.e. } 0 < \delta < (bt/3), (\partial p^{ST^*}/\partial\theta) < 0, \text{ when } bt - 3\delta < 0, \text{ i.e. } \delta > (bt/3), (\partial p^{ST^*}/\partial\theta) > 0.$$

We also have  $(\partial p^{MT^*}/\partial\theta) = (2kA_tB_t(bt - 3\delta)/(8bk\theta - A_t^2)^2)$ . When  $bt - 3\delta > 0$ , i.e.  $0 < \delta < (bt/3)$ ,  $(\partial p^{MT^*}/\partial\theta) > 0$ , when  $bt - 3\delta < 0$ , i.e.  $\delta > (bt/3)$ ,  $(\partial p^{MT^*}/\partial\theta) < 0$ .

## G. Proof of Proposition 3

When  $B_t > 0$  and  $k > \max\{((1 + \delta)A_t/4bF), (\theta A_t^2/2bF^2), (FA_t^2/16b\theta^2), ((1 + \delta)A_t/8b\theta)\}$ ,  $e^{ST^*} - e^{MT^*} = (4bkA_tB_t(1 - 3\theta)/(\Delta - A_t^2)(8bk\theta - A_t^2))$ . It is easily to figure out that when  $0 < \theta < (1/3)$ ,  $e^{ST^*} > e^{MT^*}$ , when  $(1/3) < \theta < 1$ ,  $e^{ST^*} < e^{MT^*}$ .

## H. Proof of Proposition 4

When  $B_t > 0$  and  $k > \max\{((1 + \delta)A_t/4bF), (\theta A_t^2/2bF^2), (FA_t^2/16b\theta^2), ((1 + \delta)A_t/8b\theta)\}$ ,  $w^{ST^*} - w^{MT^*} = -(2kA_tB_t(1 - 3\theta)[\delta + bt(1 - 2\lambda)]/(\Delta - A_t^2)(8bk\theta - A_t^2))$ . It is easily to figure out that when  $0 < \lambda < (1/2)$ ,  $\delta + bt(1 - 2\lambda) > 0$ . Therefore, if  $0 < \theta < (1/3)$ ,  $w^{ST^*} < w^{MT^*}$ , if  $(1/3) < \theta < 1$ ,  $w^{ST^*} > w^{MT^*}$ .

When  $(1/2) < \lambda < 1$ , if  $0 < \theta < (1/3)$  and  $0 < \delta < bt(2\lambda - 1)$ , we have  $w^{ST^*} < w^{MT^*}$ , if  $0 < \theta < (1/3)$  and  $\delta > bt(2\lambda - 1)$ , we have  $w^{ST^*} > w^{MT^*}$ . If  $(1/3) < \theta < 1$  and  $0 < \delta < bt(2\lambda - 1)$ ,  $w^{ST^*} > w^{MT^*}$ , if  $(1/3) < \theta < 1$  and  $\delta > bt(2\lambda - 1)$ ,  $w^{ST^*} < w^{MT^*}$ .

## I. Proof of Proposition 5

When  $B_t > 0$  and  $k > \max\{((1 + \delta)A_t/4bF), (\theta A_t^2/2bF^2), (FA_t^2/16b\theta^2), ((1 + \delta)A_t/8b\theta)\}$ ,  $p^{ST^*} - p^{MT^*} = kA_tB_t(1 - 3\theta)(bt - 3\delta)/(\Delta - A_t^2)(8bk\theta - A_t^2)$ . When  $(1 - 3\theta)(bt - 3\delta) > 0$ ,  $p^{ST^*} > p^{MT^*}$ , when  $(1 - 3\theta)(bt - 3\delta) < 0$ ,  $p^{ST^*} < p^{MT^*}$ . Therefore, when  $0 < \delta < (bt/3)$ , if

$0 < \theta < (1/3)$ ,  $p^{ST^*} > p^{MT^*}$ , else  $p^{ST^*} < p^{MT^*}$ . When  $\delta < (bt/3)$ , if  $0 < \theta < (1/3)$ ,  $p^{ST^*} < p^{MT^*}$ , else  $p^{ST^*} > p^{MT^*}$ .

## J. Proof of Proposition 6

When  $B_t > 0$  and  $k > \max\{((1 + \delta)A_t/4bF), (\theta A_t^2/2bF^2), (FA_t^2/16b\theta^2), ((1 + \delta)A_t/8b\theta)\}$ .

$$(i) \pi_s^{ST^*} - \pi_s^{MT^*} = 2bk^2A_t^2B_t^2(1 - 3\theta)^2/(\Delta - A_t^2) \\ (8bk\theta - A_t^2)^2 > 0, \pi_m^{MT^*} - \pi_m^{ST^*} = bk^2A_t^2B_t^2(1 - 3\theta)^2/ \\ (8bk\theta - A_t^2)(\Delta - A_t^2)^2 > 0;$$

$$(ii) \pi_{sc}^{MT^*} - \pi_{sc}^{ST^*} = bk^2A_t^2B_t^2(1 - 3\theta)^2[A_t^2 - 8bk(1 - 2\theta)]/ \\ (8bk\theta - A_t^2)^2(\Delta - A_t^2)^2. \text{ If } A_t^2 - 8bk(1 - 2\theta) > 0, \\ \pi_{sc}^{MT^*} > \pi_{sc}^{ST^*}, \text{ else } \pi_{sc}^{ST^*} > \pi_{sc}^{MT^*}. \text{ Let } A_t^2 - 8bk(1 - \\ 2\theta) = 0, \text{ we can get } \theta_1 = (8bk - A_t^2/16bk). \text{ And} \\ \text{according to } H_2(w, e), \text{ we have } k > (A_t^2/4bF), \text{ i.e.} \\ (A_t^2/4bk) < F = 1 - \theta < 1. \text{ Therefore, it is easily to} \\ \text{check that } 8bk > A_t^2, \text{ i.e. } \theta_1 > 0. \text{ As a result, if} \\ 0 < \theta < ((8bk - A_t^2)/16bk), \pi_{sc}^{MT^*} - \pi_{sc}^{ST^*} < 0, \text{ and if} \\ ((8bk - A_t^2)/16bk) < \theta < 1, \pi_{sc}^{MT^*} - \pi_{sc}^{ST^*} > 0.$$

## Data Availability

All data included in this study are available upon request by contact with the corresponding author.

## Conflicts of Interest

All authors declare no possible conflicts of interest.

## Acknowledgments

The authors gratefully acknowledge the support from the National Science Foundations of China through grant number 71971134.

## References

- [1] S. Xu, L. Fang, and K. Govindan, "Energy performance contracting in a supply chain with financially asymmetric manufacturers under carbon tax regulation for climate change mitigation," *Omega*, vol. 106, Article ID 102535, 2022.
- [2] Q. Zhang, L. Wang, and D. Q. Zhou, "Remanufacturing under energy performance contracting-an alternative insight from sustainable production," *Environmental Science and Pollution Research*, vol. 27, no. 32, pp. 40811-40825, 2020.
- [3] H. M. Liu, X. Y. Zhang, and M. Y. Hu, "Game-theory-based analysis of energy performance contracting for building retrofits," *Journal of Cleaner Production*, vol. 231, pp. 1089-1099, 2019.
- [4] P. Zhou and W. Wen, "Carbon-constrained firm decisions: from business strategies to operations modeling," *European Journal of Operational Research*, vol. 281, no. 1, pp. 1-15, 2020.
- [5] Z. R. Wang and Q. H. Wu, "Carbon emission reduction and product collection decisions in the closed-loop supply chain with cap-and-trade regulation," *International Journal of Production Research*, vol. 59, no. 14, pp. 4359-4383, 2021.
- [6] S. An, B. Li, D. Song, and X. Chen, "Green credit financing versus trade credit financing in a supply chain with carbon emission limits," *European Journal of Operational Research*, vol. 292, no. 1, pp. 125-142, 2021.

- [7] H. Q. Zhang, P. Li, H. Zheng, and Y. X. Zhang, "Impact of carbon tax on enterprise operation and production strategy for low-carbon products in a co-opetition supply chain," *Journal of Cleaner Production*, vol. 287, Article ID 125058, 2021.
- [8] A. Zakeri, F. Dehghanian, B. Fahimnia, and J. Sarkis, "Carbon pricing versus emissions trading: a supply chain planning perspective," *International Journal of Production Economics*, vol. 164, pp. 197–205, 2015.
- [9] K. S. Anand and F. C. Giraud-Carrier, "Pollution regulation of competitive markets," *Management Science*, vol. 66, no. 9, pp. 4193–4206, 2020.
- [10] P. Bertoldi and B. Boza-Kiss, "Analysis of barriers and drivers for the development of the ESCO markets in Europe," *Energy Policy*, vol. 107, pp. 345–355, 2017.
- [11] M. Garbuzova-Schlifter and R. Madlener, "AHP-based risk analysis of energy performance contracting projects in Russia," *Energy Policy*, vol. 97, pp. 559–581, 2016.
- [12] P. Principi, R. Fioretti, A. Carbonari, and M. Lemma, "Evaluation of energy conservation opportunities through energy performance contracting: a case study in Italy," *Energy and Buildings*, vol. 128, pp. 886–899, 2016.
- [13] T. C. Shang, L. Yang, P. H. Liu, K. T. Shang, and Y. Zhang, "Financing mode of energy performance contracting projects with carbon emissions reduction potential and carbon emission ratings," *Energy Policy*, vol. 144, Article ID 111632, 2020.
- [14] T. C. Shang, K. Zhang, P. H. Liu, Z. W. Chen, X. P. Li, and X. Wu, "What to allocate and how to allocate? -Benefit allocation in shared savings energy performance contracting projects," *Energy*, vol. 91, pp. 60–71, 2015.
- [15] P. P. Xu, E. H. W. Chan, H. J. Visscher, X. L. Zhang, and Z. Z. Wu, "Sustainable building energy efficiency retrofit for hotel buildings using EPC mechanism in China: analytic network process (ANP) approach," *Journal of Cleaner Production*, vol. 107, pp. 378–388, 2015.
- [16] S. N. Zheng, P. P. Xu, and H. J. Wu, "Study on the governance of energy performance contracting projects in building," in *Proceedings of the 20th International Symposium on Advancement of Construction Management and Real Estate*, pp. 1135–1146, Berlin, Germany, May 2017.
- [17] P. Y. Cheng, G. X. Ji, G. T. Zhang, and Y. Y. Shi, "A closed-loop supply chain network considering consumer's low carbon preference and carbon tax under the cap-and-trade regulation," *Sustainable Production and Consumption*, vol. 29, pp. 614–635, 2022.
- [18] L. C. Sun, X. X. Cao, M. Alharthi, J. J. Zhang, F. Taghizadeh-Hesary, and M. Mohsin, "Carbon emission transfer strategies in supply chain with lag time of emission reduction technologies and low-carbon preference of consumers," *Journal of Cleaner Production*, vol. 264, Article ID 121664, 2020.
- [19] D. Wu, J. H. Chen, P. Li, and R. J. Zhang, "Contract coordination of dual channel reverse supply chain considering service level," *Journal of Cleaner Production*, vol. 260, Article ID 121071, 2020.

## Research Article

# Wearable Mixed Energy Management System Based on Power Trajectory Tracking

Shijun Shen,<sup>1</sup> Chaofan Wang,<sup>1</sup> Chuan Lu,<sup>2</sup> Wei Zheng,<sup>3</sup> and Dawei Gong <sup>1</sup>

<sup>1</sup>University of Electronic Science and Technology of China, Chengdu 611731, China

<sup>2</sup>Science and Technology on Reactor System Design Technology Laboratory, Nuclear Power Institute of China, Chengdu 610213, China

<sup>3</sup>Science and Technology on Thermal Energy and Power Laboratory, Wuhan Second Ship Design and Research Institute, Wuhan 430064, China

Correspondence should be addressed to Dawei Gong; pzhzhx@126.com

Received 30 March 2022; Accepted 21 April 2022; Published 1 June 2022

Academic Editor: Qiuye Sun

Copyright © 2022 Shijun Shen et al. This is an open access article distributed under the Creative Commons Attribution License, which permits unrestricted use, distribution, and reproduction in any medium, provided the original work is properly cited.

With more and more extensive research and application of wearable devices, their continuous working time has become a prominent problem which is increasingly concerned. Within the limitations of existing battery technology, environmental energy harvesting can be used to enhance the continuous working time of wearable devices. To solve this problem, this paper designs a collection system for heat energy and radiofrequency (RF) energy in the environment. This system designs a thermoelectric collector based on thermoelectric generation, an RF energy collector based on a rectifier antenna, and a mixed energy collection controller based on power trajectory tracking. This system can generate power according to the temperature difference between environment and human body and RF energy in the environment. This system uses the heart rate sampling algorithm to accurately collect the required voltage and current information while saving system energy consumption. The maximum power output algorithm based on power trajectory tracking keeps the maximum power output of the energy collection system at all times. In this paper, two kinds of environmental energy models and a mixed energy acquisition system model are established by MATLAB. After setting reasonable environmental conditions, we get the results to verify the rationality and effectiveness of this environment energy collection system.

## 1. Introduction

As the material basis of human production, energy has been playing an important role in the development of human society. The energy collection technology is to collect the energy lost in the environment and convert it into direct current energy through conversion, storage, and other means, which can be used by electronic devices. This way is undoubtedly the greatest extent to reduce the waste of energy and greatly improve the energy's utilization, which has a decisive significance to solve the energy problem.

As we know, wearable electronic devices generally have the following two characteristics. Firstly, the energy demand is generally small. Secondly, its power supply equipment replacement is relatively complex, which means we have to

face the problems to apply a power module that can work for a long time. With the development of technology, the wearable energy collection system can be divided into two directions. Firstly, the volume of energy acquisition systems will be reduced smaller and smaller to eventually integrate it into the energy modules in wearable electronic devices. Another one is to continuously optimize the energy collection system, design its own storage module, collect and store the environment energy, and unify the management.

A large number of scientific researchers are exploring the perfect combination of wearable and energy collection in those two ways mentioned above. Georgia Institute of Science and Technology, the Wang Zhonglin team from the Institute of Chinese Academy of Sciences, and the H. Alshareef research team from King Abdullah University

of Science and Technology (KAUST) have designed a bracelet that combines the energy collection and storage inside the device to provide sustainable energy for the wearable devices [1]. At the same time, Cheng Jianli, Wang Bin, and others from the Institute of Chemical Materials of China Engineering and Physics Institute have designed a fiber optic capacitor shown in Figure 1, which has 5.1% energy conversion efficiency and is of great significance to the energy supply for the wearable electronic equipment [2].

By looking for energy collection devices that are more efficient and applicable to the wearable electronic equipment, the Takao Someya team from Tokyo University and the Japan Institute of Physical Chemistry and Research has designed a superflexible organic solar cell that is 13% efficient in transferring energy, and the solar cells are still able to maintain a good device performance after multiple stretching tests [3]. Professors Pietro Cataldi and Mario Caironi from the Institute of Science and Technology in Italy have designed a planar flexible thermoelectric device with good flexibility and washing stability, which provides a profound meaning for the development of wearable thermoelectric devices [4]. Professor Yanliang Zhang from the University of Notre Dame Aerospace and Mechanical Engineering has designed a flexible thermoelectric acquisition unit through its improved 3D printing technology, which can show a high power density of  $7.65 \text{ mw/cm}^2$  under the temperature gradient of 60 k, which is a great help for the application of thermoelectric collectors used in wearable products. A flexible 3D fabric was developed by Professor Zhi Chunyi from the City University of Hong Kong and Hu Hong from the Hong Kong Institute of Science and Technology, which can be able to provide energy to the electronic devices by friction. A yarn-based triboelectric nanogenerator for energy acquisition was prepared by Xiong Pu, Weiguo Hu, and Zhonglin Wang from the Beijing Institute of Nanoenergy and Systems, Chinese Academy of Sciences [5]. The research group of Professor Hu Chenguo from Chongqing University and Professor Guo Hengyuan from Beijing Institute of Nanoenergy and Nanosystems, Chinese Academy of Sciences, used traditional weaving techniques to produce self-charging energy fabrics for collecting human movement energy with the characteristics of mass production [6].

In energy storage of wearable electronic devices, the research team led by Associate Professor Chunyi Zhi of the City University of Hong Kong has built a set of evaluation standards for energy storage devices of wearable devices by analyzing the flexibility, tensile, and wearability of flexible energy storage devices [7], which provides a direction for the development of wearable energy memory to a certain extent. A flexible fiber membrane lithium-sulfur battery was designed by the research group of Professors Yan Wei and Yu Shujiang from Xi'an Jiaotong University and Xi Kai and Vasant Kumar from the University of Cambridge [8]. Jianli Cheng, Bin Wang from the Institute of Chemical Materials, CaEP, and Jun Lu from Argonne National Laboratory together designed a high flexibility fiber Li-CO<sub>2</sub> battery [9]. Chen et al. from the Department of Materials, ETH Zurich, made a highly elastic thin-film cell [10]. A sodium ion

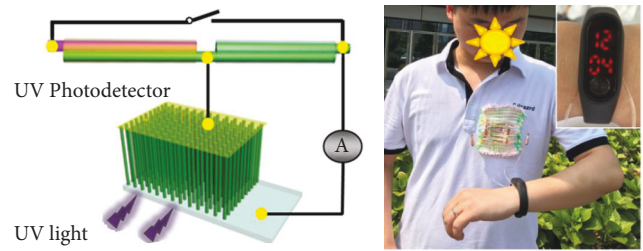


FIGURE 1: Fiber optic containers and energy collecting bracelets.

battery with high conductivity, high mechanical strength, and high flexibility was prepared by Professor Junmin Yan's research group from Jilin University using industrial wastewater and waste cotton fabric [11]. The research team of Professor Geng Fengxia from Suzhou University prepared a high magnification flexible thin-film electrode battery by using two-dimensional materials [12] and so on.

As RF energy collecting, it is found that researchers basically collect frequency bands around 1.8 GHz, 2.1 GHz, 2.3 GHz, 2.4 GHz, 2.5 GHz, 3.3 GHz, 3.8 GHz, 5.2 GHz, and 5.5 GHz (mainly WIFI frequency band and WIMAX frequency band). Meanwhile, the current research directions of researchers mainly include the following: (1) trying different flexible materials to prepare multiband antenna models; (2) trying to use metamaterial technology to improve the gain of RF energy collection antenna [13–17]. Although there is no flexible RF energy collector that is fully applicable and has reached the application level at present, as the attempt in literature, the flexible RF energy collector suitable for wearable devices will one day become a product and appear in people's life [18].

At present, conclusively, there are two ways in most researches on maximum power output algorithm of energy acquisition. First, add the DC-DC function after each energy acquisition module to increase the output voltage value and use some algorithm like MPPT (Maximum Power Point Tracking) to control the energy discharging [19]. Second, add only one DC-DC module after several energy modules and use the passive mode (only the energy module with the highest voltage value can discharge) to supply the energy power to load. The first method leads to a high loss of environmental energy in multiple DC-DC stages, reducing the utilization of hard-won environmental energy. For the second method, the discharging power of the energy module passively selected is not necessarily the maximum; that is to say, the energy module with the maximum discharging power cannot discharge, resulting in energy waste.

Based on the circuit topology of the second way (only one DC-DC module), this paper uses the power trajectory tracking algorithm to actively supply the energy power to load. Compared with passive discharge, the active discharge method can effectively improve the utilization of environmental energy.

This paper analyzes the architecture of mixed environment energy collection system, then, respectively, analyzes and establishes the models of thermoelectric collector and RF energy collector, and makes the physical objects of these two collectors at last in Section 2. It designs a heart rate

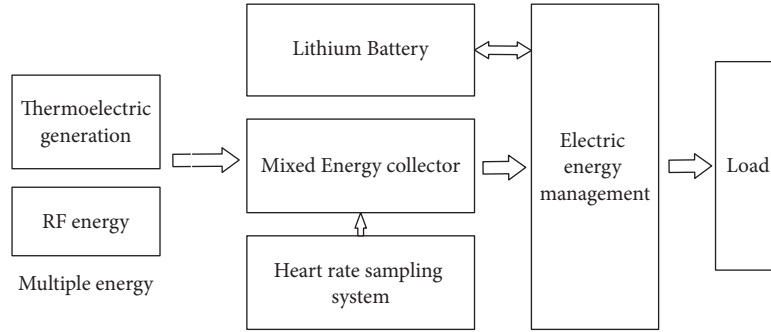


FIGURE 2: Wearable device environmental energy acquisition and management system.

sampling algorithm to accurately collect the required environmental energy voltage and current information in Section 3, establishes an energy management model with the maximum power output algorithm based on power trajectory tracking and simulates it in Section 4, and at last sets an experiment to verify the effect of this energy collection system in Section 5.

## 2. Analysis and Design of Mixed Energy System

Contraposing the actual environment of human activities, the energy source of the wearable energy acquisition system includes heat energy (for the temperature difference between the human body and the environment) and radiofrequency energy (for the external environment of human beings).

Due to the uncertainty and weakness of environmental energy, we still use lithium battery as the main power supply of wearable devices and the two mixed energies as supplementary power.

It is well known that environmental energy can easily change according to environmental conditions. In the case of poor environmental conditions, the energy output is extremely weak, so it is needless to detect the port voltage of the environmental energy module. The port voltage has to be detected when the environmental conditions become better, or the energy module has stored enough output energy. Therefore, this paper adds a heart rate sampling system for the environmental energy module to avoid invalid real-time voltage or current detection and accurately collect the port voltage value on the premise of saving energy.

To effectively improve the utilization rate of environmental energy, this paper designs a mixed energy collector. The energy collector will control the sampling sequence of the heart rate sampling system and control the environment energy supplied to the load or charging the battery efficiently. The block diagram of wearable environmental energy collection system designed in this paper is shown in Figure 2.

**2.1. Thermoelectric Energy Collection.** The basic principle of thermoelectric energy collector is the same as that of thermoelectric power generation, which is to connect two kinds of semiconductor thermoelectric materials, *N*-type and *P*-type, in series with the conductive plate with good thermal conductivity and conductivity and then fix them on

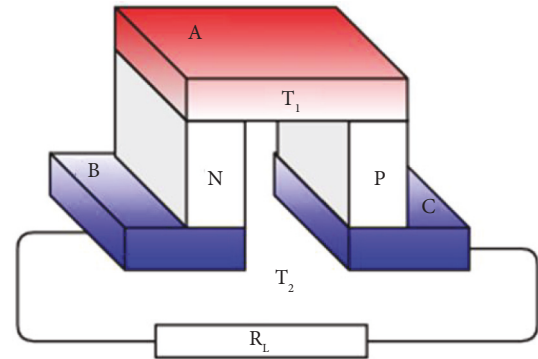


FIGURE 3: Structure drawing of monomer thermogenerator.

the ceramic plate with good thermal conductivity, and then it can get the thermoelectric power generation or thermoelectric energy collection.

In practical application, the hot side of the thermoelectric material slice is closely connected with the heat source, and the temperature of the cold side is reduced as far as possible by means of heat dissipation so that the temperature difference is formed on both sides of the device. According to the Seebeck effect, a voltage will be generated in the loop, and a current will flow through the load. In order to achieve the required power, usually in practical applications, 18–128 groups of monomers are arranged in series or parallel to form thermoelectric devices.

**2.1.1. Thermoelectric Model Analysis.** Thermoelectric devices will be evaluated using the following parameters to design and implement efficient hardware thermoelectric systems.

**(1) Output Power of Thermocouple.** As shown in Figure 3, the thermocouple arrangement structure is generally adopted in the basic units of thermoelectric power generation elements. According to the Seebeck effect, when the temperature at both sides of the element is  $T_1, T_2$ , and  $T_1 > T_2$ , the voltage in the loop is [20, 21]

$$U = \alpha(T_1 - T_2). \quad (1)$$



Due to the internal resistance  $r$  of the thermoelectric element itself, only part of the voltage generated by the thermoelectric element is loaded onto the load resistance  $R_L$ . That is, the voltage presented on the load resistance ( $R_L$ ) at this time is the actual output voltage of the thermoelectric device, which is usually expressed as

$$V_{\text{out}} = \alpha(T_1 - T_2) \frac{R_L}{R_L + r} = \frac{m\alpha(T_1 - T_2)}{1 + m}. \quad (2)$$

In the above formula, the ratio of load resistance to internal resistance is expressed as  $m$ . Furthermore, the loop current can be expressed by the following formula:

$$I = \alpha \frac{(T_1 - T_2)}{R_L + r}. \quad (3)$$

Through the above expressions of voltage and current, the output power of the temperature difference generator can be calculated as follows:

$$P = \frac{\alpha^2 (T_1 - T_2)^2 R_L}{(R_L + r)^2} = \frac{m}{(1 + m)^2} \cdot \frac{\alpha^2 (T_1 - T_2)^2}{r}. \quad (4)$$

When  $m = R_L/r = 1$ , that is, when the load resistance value is equal to the internal resistance value of the thermoelectric element, its output power is the maximum, and the maximum value is [22]

$$P_{\text{max}} = \frac{\alpha^2 (T_1 - T_2)^2}{4r} = \frac{\alpha^2 \Delta T^2}{4r}. \quad (5)$$

(2) *Power Generation Efficiency of Thermoelectric Generator.* In order to investigate the power generation efficiency of thermoelectric elements, the total heat  $Q_h$  absorbed from the heat source needs to be considered first.  $Q_h$  is composed of joule heat, heat conduction, and Partie heat, which can be expressed as

$$Q_h = \alpha T_1 I - \frac{1}{2} I^2 r + \lambda (T_1 - T_2), \quad (6)$$

where  $\lambda$  is the thermal conductivity of thermocouple material and Seebeck coefficient between  $\alpha$  and two materials ( $P$ - and  $N$ -type semiconductor) can be expressed as follows:

$$\alpha = \alpha_P - \alpha_N. \quad (7)$$

Thus, the power generation efficiency of thermoelectric generator can be obtained:

$$\eta = \frac{P_0}{Q_h} = \frac{\alpha^2 (T_2 - T_1)^2 R_L / (R_L + r)^2}{\alpha T_2 I - (1/2) I^2 r + \lambda (T_2 - T_1)}. \quad (8)$$

Arrange it again:

$$\eta = \left( \frac{T_2 - T_1}{T_2} \right) \left[ \frac{m}{(1 + m) - (T_2 - T_1/T_2) + (1 + m)^2 / ZT_2} \right], \quad (9)$$

where  $Z$  is the optimal value coefficient of the material,  $Z = \alpha^2 / RK$ .

When  $d_\eta/d_m = 0$ , which also is  $m = (1 + Z\bar{T})^{1/2}$ , the output efficiency of the thermoelectric generator is the highest, where  $\bar{T}$  represents the average temperature between the cold side and the hot side of the thermoelectric element; namely,

$$\bar{T} = \frac{(T_2 + T_1)}{2}. \quad (10)$$

Thus, the maximum efficiency can be expressed as follows:

$$\eta_{\text{max}} = \frac{T_2 - T_1}{T_2} \cdot \frac{\sqrt{(1 + Z\bar{T})} - 1}{\sqrt{(1 + Z\bar{T})} + T_1/T_2}. \quad (11)$$

2.1.2. *Thermoelectric Module Design.* According to previous studies, the circuit model of thermoelectric module is shown in Figure 4:

$$R_{\text{TEG}} = \frac{R_{\text{TE}} + R_S}{R_{\text{TE}} \cdot R_S}. \quad (12)$$

Then, the basic relationship can be obtained from the above model:

$$\Delta T_{\text{TEG}} = \frac{R_{\text{TEG}}}{R_{\text{thA}} + R_{\text{thB}} + R_{\text{TEG}}} \cdot \Delta T. \quad (13)$$

From the above analysis, it can be seen that the difference between human body temperature and ambient temperature ( $\Delta T$ ) is obviously larger than the difference between the cold side and hot side ( $\Delta T_{\text{TEG}}$ ) of the thermoelectric element ( $TEG$  element); that is, the actual temperature difference ( $\Delta T_{\text{TEG}}$ ) between the two sides of the thermoelectric device is relatively small. Meanwhile, the parallel structure of multiple thermocouples inside  $TEG$  makes its thermal resistance smaller [23–26]. As a result, the temperature difference in the environment is much greater than the temperature difference applied to the thermoelectric element. However, it should also be noted that some phenomena in the external environment (such as air flow) can make the heat exchange on the  $TEG$  surface more active because thermal resistance  $R_{\text{thA}}$  is affected by thermal radiation and thermal convection between the thermoelectric element and the external environment; that is, when wind flows on the surface of  $TEG$  in the environment, its value will be greatly reduced. Therefore, the performance of  $TEG$  is closely related to the external environment.

To explore the performance of thermoelectric elements more definitively, we can make the following assumptions. Assuming that the number of thermocouples contained in  $TEG$  is  $N$ , the Seebeck coefficient of thermoelectric materials is  $\alpha$ , the temperature difference between the two surfaces of  $TEG$  is  $\Delta T_{\text{TEG}}$ , and the voltage generated by  $TEG$  is  $V_T$ ; the following relation can be obtained:

$$V_T = N \cdot \alpha \cdot \Delta T_{\text{TEG}}. \quad (14)$$

A simplified electrical model is constructed with  $TEG$  components as the source, and its basic style is shown in Figure 5.  $TEG$  is equivalent to a series of voltage source  $V_T$  and

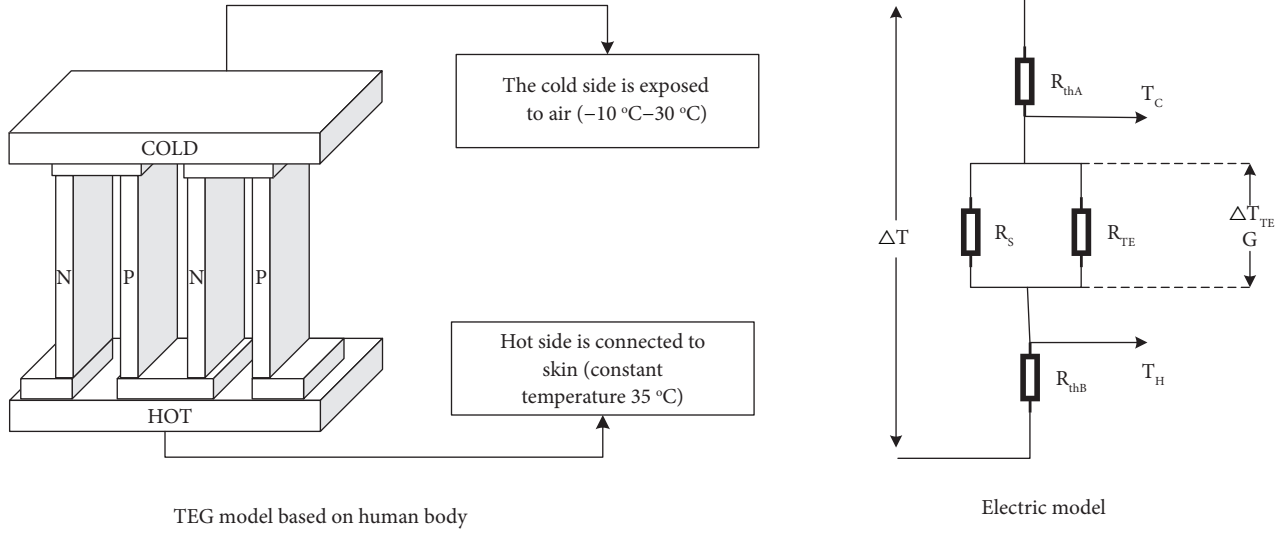


FIGURE 4: TEG model and electrical model based on human body.

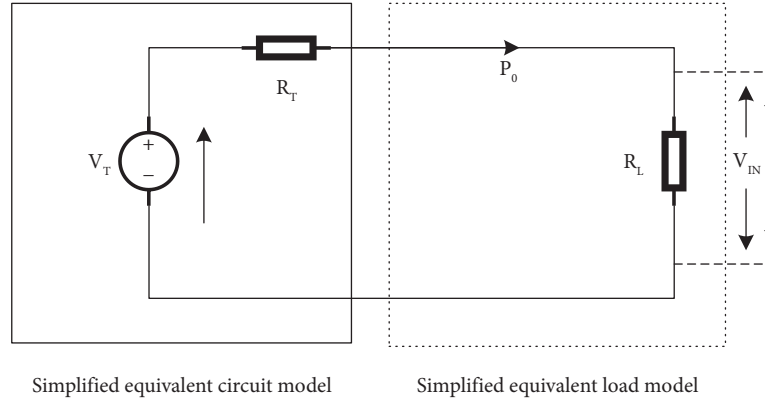


FIGURE 5: Equivalent electrical model of TEG.

internal resistance  $R_T$ , and the external circuit is replaced by resistance  $R_L$ . Meanwhile, the value of the output power  $P_O$  of the thermoelectric element depends on its internal equivalent resistance  $R_T$  and the resistance  $R_L$  of the external load circuit. Based on basic circuit principles, the output power  $P_O$  of a thermoelectric element can be expressed as follows:

$$P_O = \frac{V_T^2}{(R_L + R_T)^2} \cdot R_L. \quad (15)$$

According to the basic properties of the above equation, the power curve of TEG can be basically expressed as a quadratic function. When the external resistance  $R_L$  is equal to the internal resistance  $R_T$  of the TEG element, the maximum power point can be obtained, which could be expressed as

$$P_O = P_M = \frac{V_T^2}{4R_T}. \quad (16)$$

**2.1.3. Thermoelectric Module Design.** There are many factors that affect the performance of thermoelectric acquisition

devices. To select suitable thermoelectric devices, it is necessary to comprehensively analyze the advantages of thermoelectric materials, the shape of thermocouple arms, and the structure of thermoelectric devices.

In order to build thermoelectric devices with better performance, *N*-type and *P*-type materials can be added to semiconductor materials to make them have similar advantages. Such processing technology is also relatively simple and easy to implement. At the same time, the physical size (geometric size) of thermocouple also affects the energy conversion efficiency of thermoelectric devices. In general, when the two materials of the galvanic arm have different optimal values, their geometric dimensions are usually different.

In this paper, thermoelectric devices with conventional longitudinal structure are selected. To closely combine wearable characteristics with its structure, 3D printing technology is used to design the structure as shown in Figure 6(a). Through reasonable placement, the thermoelectric generator perfectly reflects the wearable characteristics. Figure 6 shows a thermoelectric generator connecting to the mixed energy collector designed in this paper.

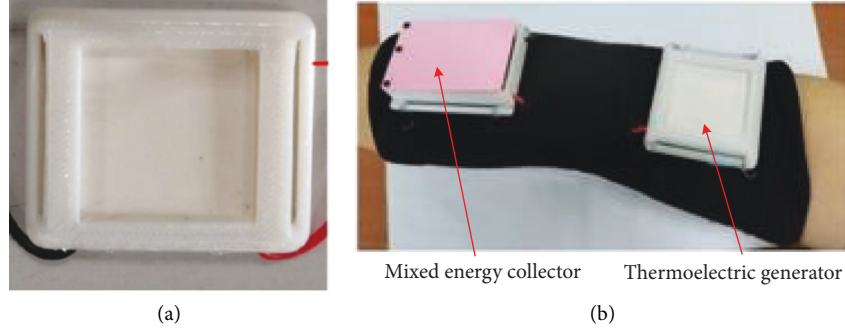


FIGURE 6: Thermoelectric collection module: (a) 3D shell and (b) connection of thermoelectric generator and mixed energy collector.

## 2.2. RF Energy Collection

*2.2.1. Analysis of RF Energy Collection Model.* RF energy collection can avoid the influence of harsh environment and light and is more stable than solar energy and wind energy.

Since the RF energy used in this paper belongs to the energy that exists in the environment and may be transmitted by multiple signal sources with uncertain transmission power, the RF energy collector shall consist of at least two parts, a receiving antenna and a filter rectifier circuit. Receiving antenna is the first device to receive RF energy from space to the circuit, and its performance determines the effect of RF energy collector. The parameters of the receiving antenna are resonance frequency, bandwidth, return loss, receiving efficiency, and so on. The larger the harmonic frequency bandwidth is, the more environmental RF energy can be received, and the higher the efficiency of the receiving antenna is, the higher the efficiency of receiving RF energy is.

For RF energy receiving antenna models in space, we usually have Free Space model, Dual Ray Ground model, and Rayleigh model.

(1) *Free Space Model.* According to the Friis equation, the power that an energy receiver can receive is

$$P_R = \frac{P_T G_T G_R \lambda^2}{(4\pi d)^2 L}, \quad (17)$$

where  $P_T$  is the transmitting power of the transmitter,  $G_T$  is the transmitting antenna gain of the transmitter,  $G_R$  is the receiving antenna gain of the energy receiver,  $\lambda$  is the wavelength of RF signal, and  $d$  is the distance between the transmitting antenna and the receiving antenna.

(2) *Dual Ray Ground Mode.* As RF signals reach the receiving antenna through a direct path and a reflected path, respectively, the power obtained by the energy collection antenna from the energy transmitter is as follows:

$$P_R = P_T G_T G_R \frac{h_t^2 h_r^2}{d^4}, \quad (18)$$

where  $P_T$  is the transmitting power of the transmitter,  $G_T$  is the transmitting antenna gain of the transmitter,  $G_R$  is the receiving antenna gain of the energy receiver,  $h_t$  is the height

TABLE 1: Radiofrequency signal bands in the environment.

Mobile operators	Frequency band (MHz)	Tower signal (G)
China Mobile (TD-LTE)	2320–2370	4
China Unicom (TD-LTE)	2300–2320	4
China Telecom (CDMA2000)	2110–2125	3

of the transmitting antenna,  $h_r$  is the height of the receiving antenna, and  $d$  is the distance between the transmitting antenna and receiving antenna.

(3) *Rayleigh Model.* Rayleigh model stipulates that the received power obtained by the energy collection antenna from energy transmitters is (the power that relay nodes/secondary users can receive from RF signals transmitted from source nodes/primary users)

$$P_R = P_R^{\text{det}} \times 10^L \times \log(1 - \text{unif}(0, 1)), \quad (19)$$

where  $L = -\alpha \log_{10}(d/d_0)$  is the path loss factor of the radio channel,  $d_0$  is the reference distance,  $P_R^{\text{det}}$  is the accepted power calculated by a deterministic model, and  $\text{unif}(0, 1)$  is the random number generated between 0 and 1.

In the assumption of this paper, the radiofrequency energy in space is radiated by multiple energy sources. The power of the radiation energy source and radiation direction and the distance between the radiation antenna and the receiving antenna are uncertain. Therefore, the Rayleigh model is more consistent with the actual situation in this paper.

We use the Rayleigh model as a reference for modeling and analysis, which can better simulate the characteristics of RF energy in this paper.

*2.2.2. Design of RF Energy Collection Module.* RF energy collector usually consists of three parts: a receiving antenna, a rectifier, and a voltage doubling circuit. The collector needs to be measured by working bandwidth, return loss, efficiency, gain, and input impedance. Combined with the measurement standards and based on the actual application scenarios, this paper will design an energy collection antenna that can collect RF energy in the environment and is suitable for wearable.

TABLE 2: Basic parameters of a receiving antenna.

Parameters	Parameters range	
Working frequency range	2.1 GHz (2.1–2.125 GHz)	2.3 GHz (2.3–2.37 GHz)
Return loss	2.1 GHz (-10 dB)	2.3 GHz (-10 dB)
Gain	2.1 GHz (1.50 dB)	2.3 GHz (3.0 dB)
Impedance characteristic	$(40-60) + (-10-10) j$	

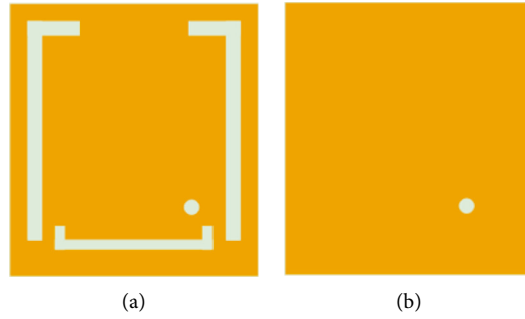


FIGURE 7: Antenna basic shape diagram: (a) front side and (b) back side.

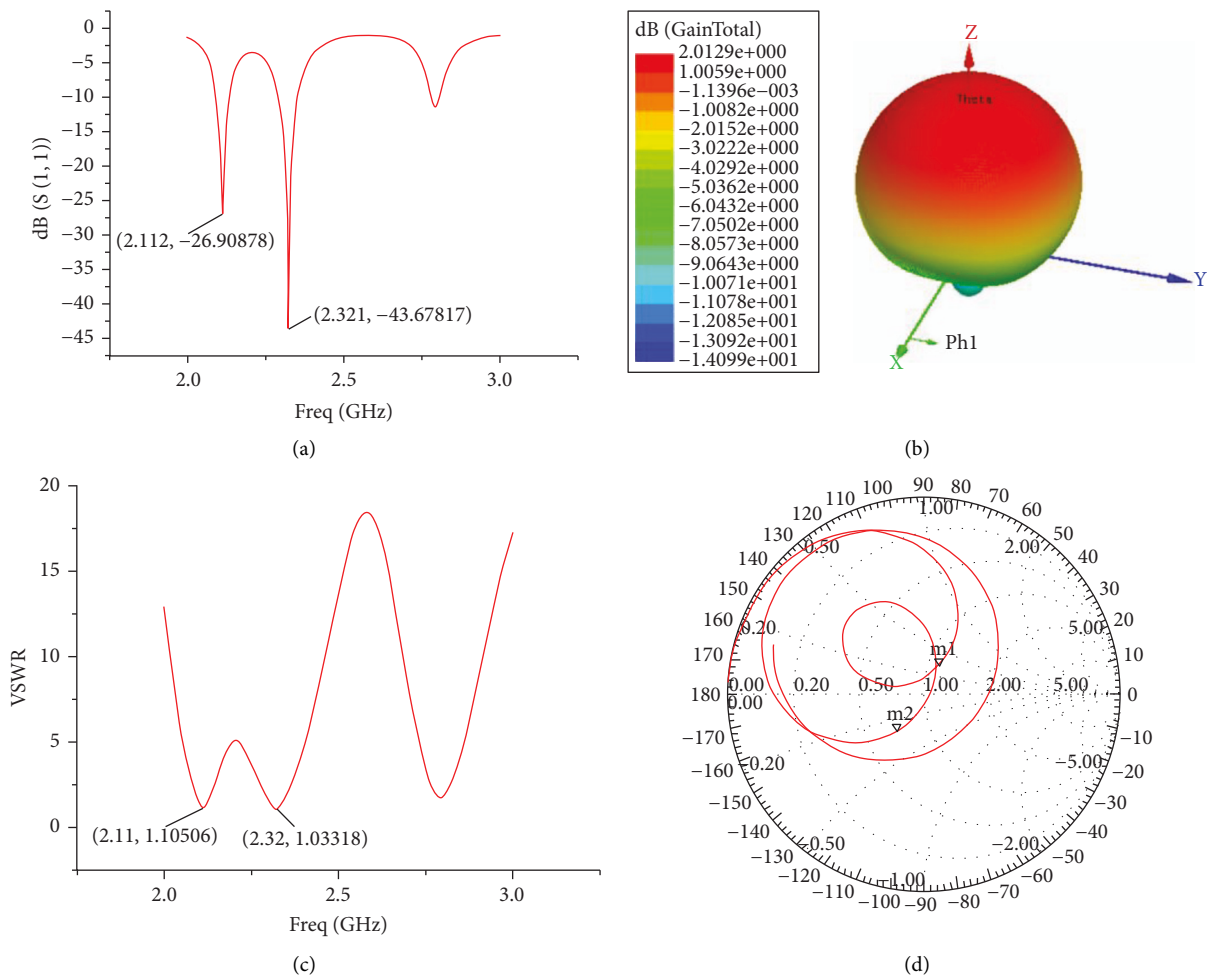


FIGURE 8: Antenna simulation results: (a) antenna return loss, (b) antenna radiation patterns, (c) antenna standing wave ratio, and (d) Smith chart.

For the selection of frequency band, considering the frequency band of the signal transmission tower of China mobile operators, which is shown in Table 1, the 3G (near 2.1 GHz) and 4G (near 2.3 GHz) signals in the environment are taken as the final target frequency band for collection.

Normally, the return loss  $S_{11}$  and gain value are more important in the antenna index. Therefore, the antenna designed in this paper has basically defined the above parameters, and the specific requirements are shown in Table 2.

The basic structure of the antenna is designed by HFSS software in this paper. Firstly, the basic size of the antenna is calculated according to the plate medium coefficient and antenna formula. Secondly, in order to get a broadband antenna, a slot is needed on the back of the antenna. Finally, to save the cost, this paper uses the common RF4 plate to design and simulate the antenna.

With the help of 3D electromagnetic simulation software HFSS, according to the conventional calculation formula of microstrip antenna size, L slot's characteristics on the back, FR4 plate parameters, the expected antenna operating frequency, and so on, the antenna structure is designed as shown in Figure 7.

After a long time of calculation with HFSS, the antenna's  $S_{11}$  return loss, radiation patterns, standing wave ratio, and Smith chart are obtained as shown in Figure 8.

From Figure 8(a), we can see that it has a good return loss of  $S_{11}$  at frequencies 2.1 GHz and 2.3 GHz. The antenna standing wave ratio is very closely equal to 1 at 2.1 GHz and 2.3 GHz, which is shown in Figure 8(c). And the Smith chart in Figure 8(d) represents the impedance characteristics of antenna. The antenna in this paper is linearly polarized because there is only pole at "m1."

The antenna layout is slightly arranged in the software Altium Designer for processing, and the physical antenna made of FR4 plate is shown in Figure 9.

The high-frequency AC energy received by RF antennas cannot be supplied directly to electronic devices. That means it is necessary to design a reasonable rectifier circuit matching the antenna to convert the high-frequency electromagnetic energy into DC energy (RF-DC), which can ultimately be provided to the electronic equipment load. The process is shown in Figure 10. RF receiving antenna and rectifying circuit are collectively called RF energy rectifying antenna.

The rectifier circuit is the core component of the rectifier antenna, which is generally divided into series type, parallel type, single-stage voltage doubling type, Greinacher type, and bridge rectifier type according to its way to access a circuit. Through analyzing and comparing the above structures, it is found that the overall effect of half-wave rectification is better than full-wave rectification when the input power is low. Therefore, this paper designed a first-order voltage doubling rectifier circuit using the half-wave rectification, which is suitable for RF energy collection antenna.

Using HFSS software to design the impedance matching circuit, input filter part, rectifier part, and output filter and then optimizing the rectifier circuit according to the desired rectification efficiency and rectification voltage, this paper

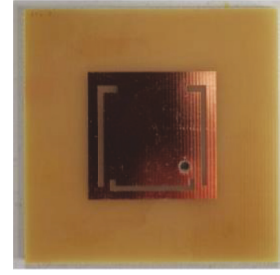


FIGURE 9: Physical antenna made of FR4 plate.

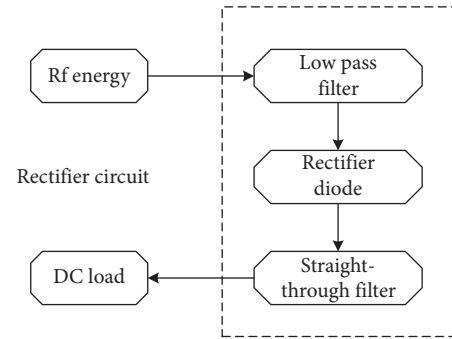


FIGURE 10: Basic diagram for RF-DC.

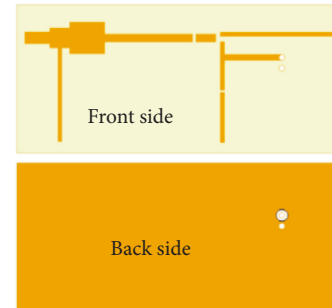


FIGURE 11: Voltage doubling rectifying circuit model.

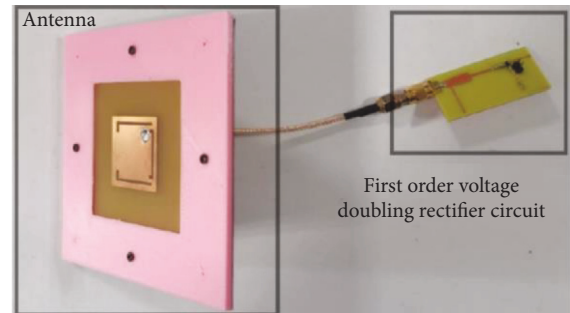


FIGURE 12: Material object of rectifying antenna.

got a voltage doubling rectifying circuit model shown in Figure 11. After making the rectifier circuit with FR4 plate, we connect the antenna and rectifier circuit together through the coaxial line, which is shown in Figure 12.

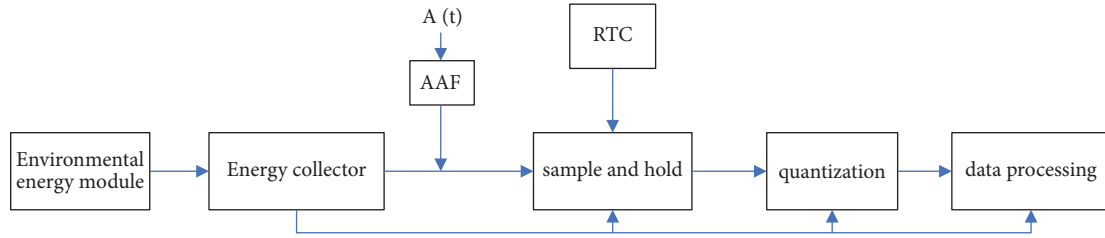


FIGURE 13: Structural diagram of heart rate sampling system.

### 3. Heart Rate Sampling System

Environmental energy is characterized by instability and weakness. When an energy module is in an unfriendly environment, it is very likely that the module will not be output. If the port voltage of each energy module is collected in real time without judgment, the additional system power consumption will be increased.

Therefore, according to the characteristics of environmental energy, this paper designed a heart rate sampling system driven by an environmental energy module. The sampling sequence obtained by the system can be approximated to a nonuniform sampling sequence, which is analyzed by combining the theory of nonuniform sampling and restored by the nonuniform sampling reconstruction method.

The heart rate sampling system based on environmental energy collection is shown in Figure 13. As the controller of the system, the energy collector also needs to control the heart rate sampling system, while the sampling system is controlled by the output voltage of the environmental energy module.

$A(t)$  is the sampled signal. The discontinuous energy generated by the environmental energy drives the sampling device to perform the sampling work; at the same time, the sampling sequence is thus obtained. The discontinuous energy replaces the continuous energy supply in the existing traditional sampling system to finish the original signal's sampling.

The RTC is used to record the time of the sampling site, and its primary responsibility is to provide an accurate time baseline.

Due to the instability of environmental energy, the sampling system is prone to power failure. Therefore, a low-power power failure storage system "sample and hold" is designed in this paper.

### 4. Energy Management Model and Simulation

In most environmental energy collection circuit topologies, a DC-DC is configured for each energy collection module, which greatly increases the overall energy consumption of the system and reduces the energy utilization efficiency. The traditional environmental energy collection circuit is shown in Figure 14.

Therefore, this paper designs an energy collection and management module with only one DC-DC and only one environmental energy output at the same time. In order to ensure the maximum environmental energy will be output,

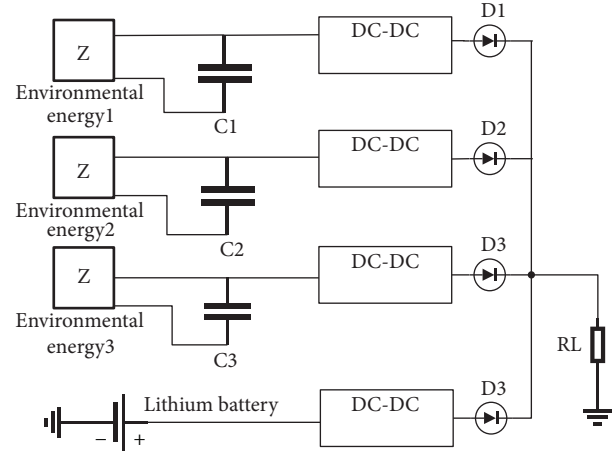


FIGURE 14: Traditional environmental energy collection circuit diagram.

we should know which one is maximum, which means we should establish a dynamic model of load to confirm the maximum energy at every "current time" [27].

This paper presents an energy management circuit topology and its algorithm, which is called power trajectory tracking for the first time. Its circuit topology is shown in Figure 15.

It can be seen that there is only one DC-DC module in this circuit topology, and all energy sources (except batteries) use the same DC-DC, which can effectively reduce the loss of environmental energy in the conversion process. However, the problem caused by this topology is that energy sources with different port voltages cannot output their energy at the same time. Only one energy can be output at a time, and other energies are temporarily stored by the ultracapacitors.

During the operation of this circuit, two (or more) energies may complete storing and need to discharge to the load or to the battery. According to previous studies, the order of energy release is generally determined according to the current voltage of the energy module; that is, the one with the highest voltage is the first to discharge. However, due to the randomness of environmental energy and the functional difference of different energy modules, the power released by the energy module with a high voltage value is not necessarily the maximum (the discharge current needs to be considered).

Assume that the voltage and discharging power per unit time of two energy modules are  $V_1$  and  $V_2$  and  $P_1$  and  $P_2$ ,



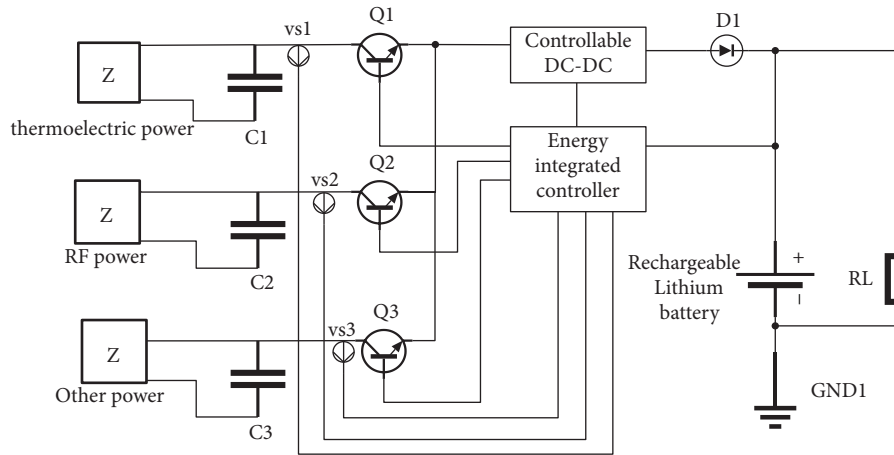


FIGURE 15: Energy management circuit topology. C1, C2, and C3 are ultracapacitors, VS1, VS2, and VS3 are voltage sensors of the heart rate sampling system, Q1, Q2, and Q3 are three controllable audions, and D1 is a single guided diode.

respectively. Even  $V1 > V2$ , but  $P2 > P1$  may occur. In view of this situation, in order to effectively improve the energy utilization, the maximum power control strategy based on power trajectory tracking is proposed for the first time in this paper.

The maximum power control strategy based on power trajectory tracking is to control the discharge sequence of the energy module in a sufficiently small period to ensure the environmental energy discharge with the maximum power output capacity at the moment, that is, to ensure the maximum energy obtained by the load at the moment. Based on this, the flow diagram of this energy management system is designed as shown in Figure 16.

To effectively improve the efficiency of DC-DC, this paper sets a voltage threshold, and only the energy module that meets the threshold is allowed to output electric energy.

In order to ensure that the energy module with the highest power discharges at any time, we must know the discharge capacity of all energy modules. Therefore, we need to measure the discharge power of all energy modules in different environments, synthesize the power curve and save them, and form a large database of power curves at last.

This means that we need to track the power curve in the current environment, similar to the trajectory tracking strategy of robotic devices [28–30].

In a real system, how to define different environments is an issue to consider. After studying enough environmental energy collection modules, it is found that the port voltage of the energy module has a certain proportional relationship with the external environment. Therefore, the control strategy in this paper stipulates that those different environmental energies are determined by different energy module port voltages.

Therefore, the above description can be summarized as follows: we need to measure the discharge power of all energy modules under different initial voltages, form and save power curves under different initial voltages, and form a large database of power curves under different initial port voltages.

The procedure power track tracking of all power modules that meet the voltage threshold is as follows:

- (1) Measure the port voltage of all energy modules by the heart rate sampling system and open the energy modules meeting the voltage threshold 100 times in turn to obtain 100 power points of different energy modules.
- (2) Fit the measured power points into P-t curves using genetic algorithm.
- (3) Select a small unit time, calculate the power integral value in unit time according to this curve, save this power integral value, and form a large database of power integral values in unit time under different energy modules and different voltage values.

Next, we will choose the power module with the maximum power integral value at the current time to discharge to the load. During the discharge process, check whether the voltage of each energy module has a voltage mutation or whether the terminal voltage of the new energy module meets the voltage threshold. If no, perform the previous discharge sequence. If yes, check whether the power curve of the energy module at the current voltage is stored in the power curve database. If not, it is necessary to collect the power values of 100 energy modules that meet the requirements again and fit them into P-t curves, integrate them again, and save and update the large database again. However, if the data exists in the database, the energy module to discharge at the next moment can be determined directly according to the integral value of power per unit time saved in the big data.

The power integral large database saves the power integral values of different energy modules in a microperiod under certain environmental conditions. Any change in the output power of an energy module due to environmental changes will be measured again and saved. That is, the database can self-update, self-preserve, and self-learn according to the measurement system and according to the learning results to determine the discharge sequence of energy modules. The above process shows that the longer the system runs, the larger its database will be, but the more efficient its execution will be.

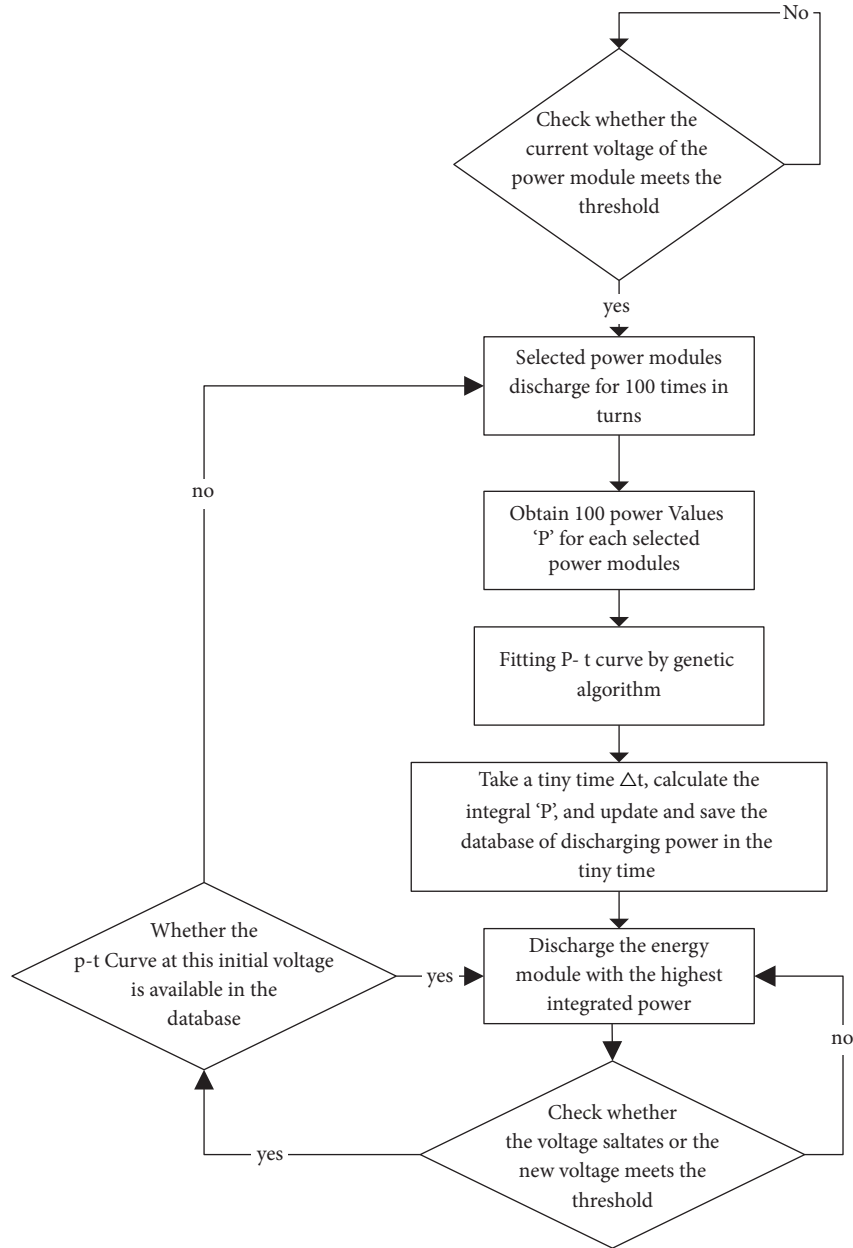


FIGURE 16: Flow diagram of maximum power control strategy based on power trajectory tracking.

The database does not use the original discharge power curve of the energy module (which can be obtained from the factory manual of the energy acquisition module) but uses the power curve synthesized by the real-time measuring system as a reference, which effectively avoids the error between the original power curve and the actual power curve caused by the decrease of the hardware working efficiency.

To sum up, the system can always maintain the maximum power output, effectively improve the utilization of environmental mixed energy, and improve the endurance of wearable devices.

In order to verify the effectiveness of the algorithm, a mixed environmental energy collection and management system model was established in Simulink, as shown in Figure 17.

Models ① and ② are RF energy collection and thermoelectric energy collection as clearly shown in Figures 18(a) and 18(b). To increase the output power of the thermoelectric collector, the temperature of the hot side is assumed to be 329 degrees Fahrenheit, and the cold side temperature is varied by the following formula:

$$T_c = (0.5 * t^{(1/8)} + 1) * \cos(0.5 * t) + 325, \quad (20)$$

where  $T_c$  is the cold side temperature.

Model ③ is the mixed energy collection controller within the heart rate sampling system algorithm and the maximum power control algorithm based on power trajectory tracking.

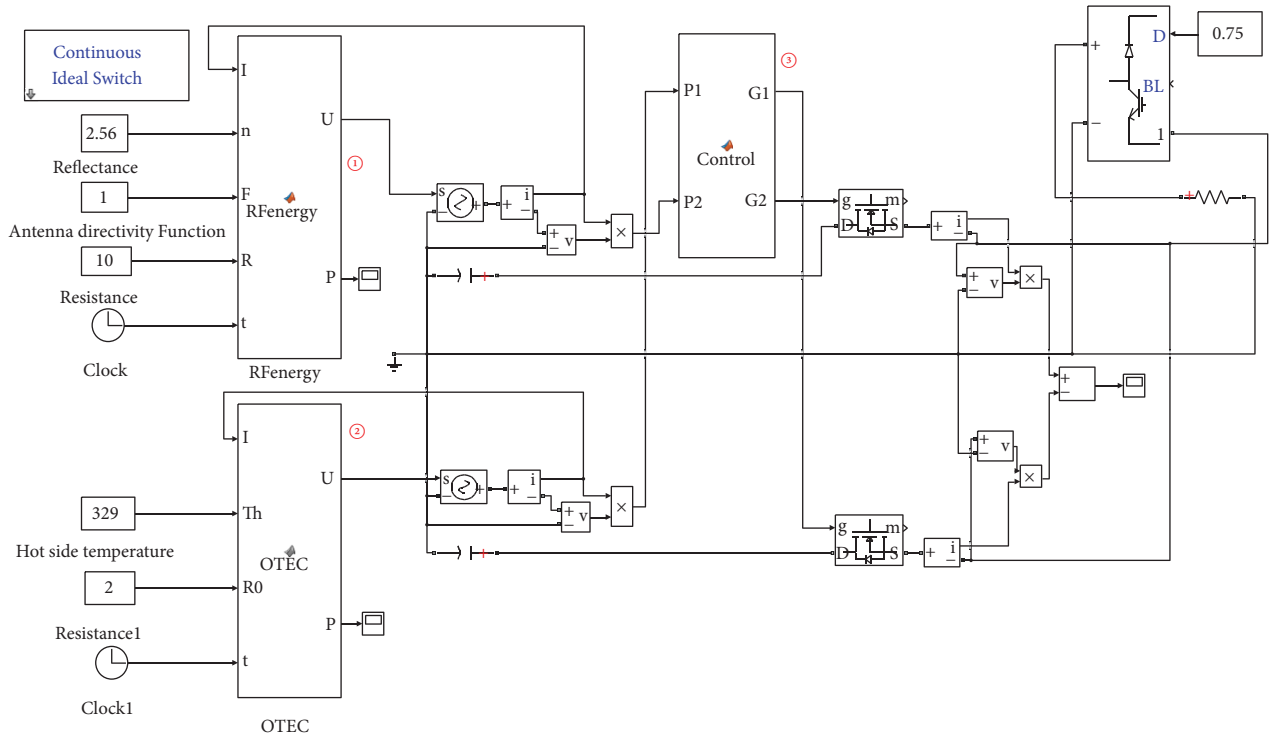


FIGURE 17: Mixed environmental energy collection and management system model.

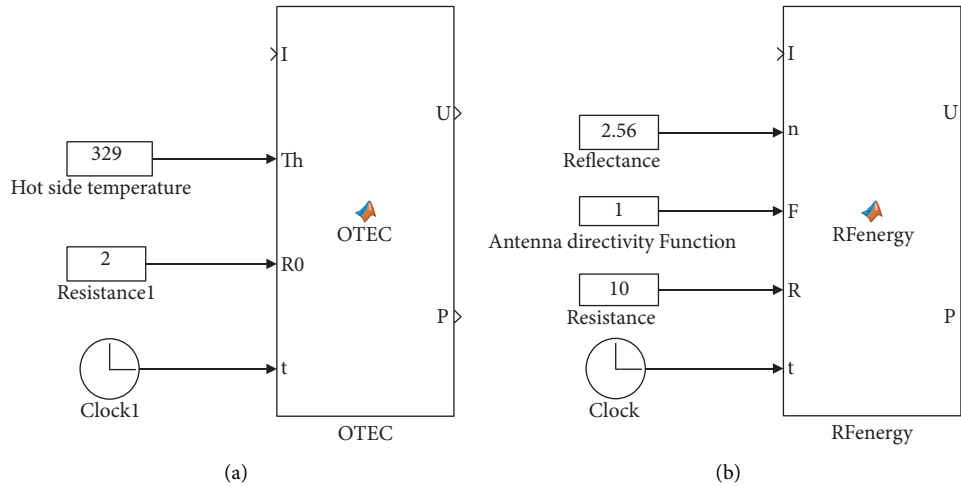


FIGURE 18: Thermoelectric and RF energy modules established in Simulink: (a) thermoelectric module and (b) RF energy module.

In the experiment, the RF energy module will collect the radiation energy from a router. Assume that the radiated power of the router changes to 1 W–3 W (randomly) and the RF energy collection circuit is placed in the far-field area of the router with a distance of 10 cm.

The output power curve was obtained as shown in Figures 19(a) and 19(b), under the condition of fixed load and randomly input within the preset interval.

According to the assumed power output curves of the two environmental energy modules, combined with the circuit topology and maximum power control strategy based on power trajectory tracking of this paper, the MATLAB simulation results are shown in Figure 20.

In Figure 20, we can see that the output power curve of the system is similar to Sine. Its highest point was 8.2 W (appeared at  $t=6.3$  s), and its lowest point was 4 W (appeared at  $t=12.8$  s). The sum of the two inputs in Figure 19 is 8.4 W when  $t=6.3$  s and 4.15 W when  $t=12.8$  s. By comparing the two sets of data, it is proved that the energy utilization ratio of the circuit topology combined with the maximum power algorithm is 97% at the maximum power and 96% at the minimum power. The simulation results show that the maximum power algorithm can keep high environmental energy utilization of the system.

The unreleased energy in the system is stored in the ultracapacitors and released only after the maximum power

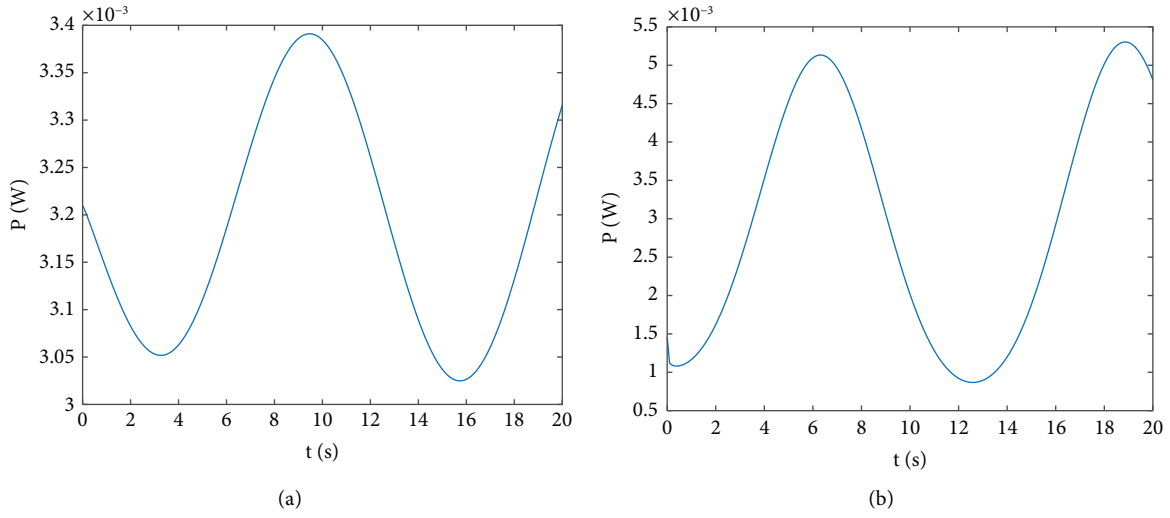


FIGURE 19: Simulated output power in MATLAB: (a) output power of RF energy module and (b) output power of thermoelectric module.

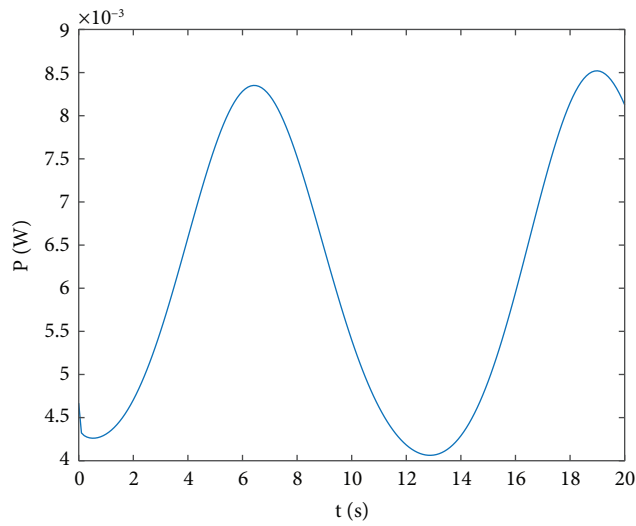


FIGURE 20: Simulated cure of maximum power control strategy based on power trajectory tracking.

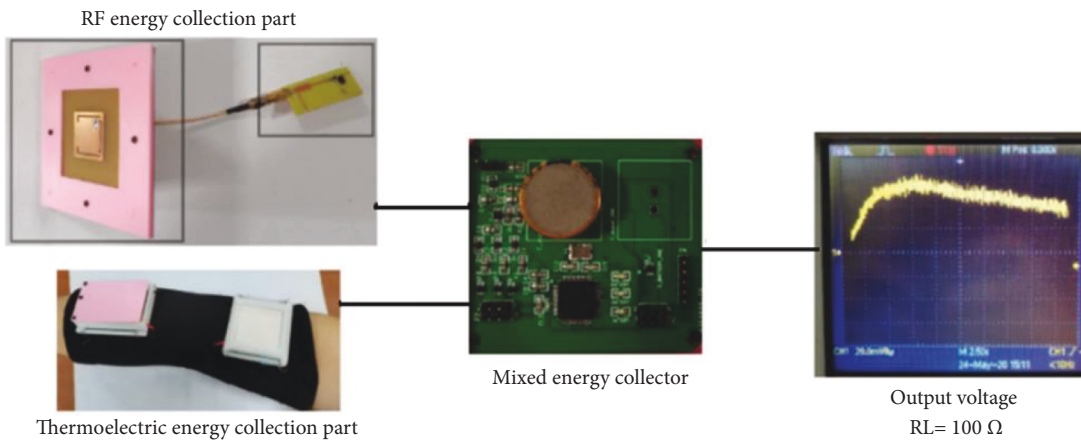


FIGURE 21: Test wiring diagram and output results.

TABLE 3: Power measurement on load.

Power	Time					
	0 s	1 s	2 s	3 s	4 s	5 s
Power of thermoelectric energy	0.11 mw	0.32 mw	0.49 mw	0.52 mw	0.48 mw	0.46 mw
Power of RF energy	0.29 mw	0.3 mw	0.31 mw	0.28 mw	0.29 mw	0.28 mw
Power of mixed energy (power of load)	0.39 mw	0.59 mw	0.77 mw	0.79 mw	0.72 mw	0.72 mw

condition is met. The smaller the minimum time  $\Delta t$  in the system is, the better the system control effect is. However, calculating the integral under too small  $\Delta t$  will occupy a lot of computing resources and increase the energy consumption of the system. Therefore,  $\Delta t = 0.1$  ms is adopted in this paper.

## 5. Experimental Tests

In this paper, a real mixed energy control circuit is designed according to the circuit topology in the figure, using  $100 \Omega$  resistance as the load. In order to accurately verify the output effect of environmental energy, lithium batteries were not used in this experiment.

After testing the output curve of a single energy module, try to keep the environmental conditions unchanged (according to the theory of air flow rate and heat transfer, air flow has a great impact on the thermoelectric module, so it is difficult to ensure the condition's consistency).

We use the oscilloscope to observe the power curve on the load and set the oscilloscope time axis (horizontal axis) to 0.5 s one grid. The test result is shown in Figure 21.

In an effort to keep the environmental conditions of the single module measurement and the system measurement constant, the output power measured on the load is shown in Table 3.

There will be a measurement error due to measurement accuracy, environmental conditions, and so on. As shown in Table 3, the mixed energy management system ensures the high efficiency of environmental energy output through the method of maximum power control strategy based on power trajectory tracking.

## 6. Conclusions

In this paper, the model of thermoelectric collector and RF energy collector and the management model of two kinds of mixed energy are established by MATLAB. The discharge sequence of two kinds of energy modules is controlled by heart rate acquisition algorithm and power trajectory tracking algorithm. Simulink is used to simulate the above-mixed energy management model and maximum power trajectory tracking algorithm. Based on the simulation results, a mixed energy collection and management system is designed, and the effectiveness of the maximum power trajectory tracking algorithm is verified by experiments.

In the following research process, this paper will set more rigorous environmental conditions, use more environmental energy modules of different power levels, optimize control strategies, optimize experimental testing methods, and so on

in order to achieve a better maximum power output effect of environmental energy.

## Data Availability

All data included in this study are available upon request by contact with the corresponding author.

## Conflicts of Interest

The authors declare that there are no conflicts of interest regarding the publication of this paper.

## Acknowledgments

This work was supported by the National Natural Science Foundation of China (61803285 and 62001332) and the National Defense Pre-Research Foundation of China (H04W201018).

## References

- [1] M. He, Y.-J. Lin, C.-M. Chiu et al., "A flexible photo-thermoelectric nanogenerator based on  $\text{MoS}_2$ /PU photothermal layer for infrared light harvesting," *Nano Energy*, vol. 49, 2018.
- [2] P. Cataldi, M. Cassinelli, A. José et al., "Green biocomposites for thermoelectric wearable applications," *Advanced Functional Materials*, 2019.
- [3] C. Dun, W. Kuang, N. Kempf, M. Saeidi-Javash, D. J. Singh, and Y. Zhang, "3D printing of solution-processable 2D nanoplates and 1D nanorods for flexible thermoelectrics with ultrahigh power factor at low-medium temperatures," *Advanced Science*, vol. 6, no. 23, Article ID 1901788, 2019.
- [4] Z. Wang, Z. Ruan, W. S. Ng et al., "Integrating a triboelectric nanogenerator and a zinc-ion battery on a designed flexible 3D spacer fabric," *Small Methods*, vol. 2, no. 10, 2018.
- [5] Z. Ren, Z. Qiao, H. Wang et al., "Wearable and self-cleaning hybrid energy harvesting system based on micro/nano-structured haze film," *Nano Energy*, vol. 67, Article ID 104243, 2019.
- [6] J. Qi, A. C. Wang, W. Yang et al., "Hydrogel-based hierarchically wrinkled stretchable nanofibrous membrane for high performance wearable triboelectric nanogenerator," *Nano Energy*, vol. 67, Article ID 104206, 2020.
- [7] X. Chen, H. Huang, L. Pan, T. Liu, and M. Niederberger, "Fully integrated design of a stretchable solid-state lithium-ion full battery," *Advanced Materials*, vol. 31, no. 43, Article ID 1904648, 2019.
- [8] Y.-h. Zhu, S. Yuan, D. Bao et al., "Decorating waste cloth via industrial wastewater for tube-type flexible and wearable sodium-ion batteries," *Advanced Materials*, vol. 29, no. 16, Article ID 1603719, 2017.
- [9] H. Tang, W. Li, L. Pan et al., "A robust, freestanding MXene-sulfur conductive paper for long-lifetime Li-S batteries,"

- Advanced Functional Materials*, vol. 29, no. 30, Article ID 1901907, 2019.
- [10] K. Chen, H. Huang, L. Pan, T. Liu, and M. Niederberger, "Fully integrated design of a stretchable solid-state Lithium-Ion full battery," *Advanced Materials*, vol. 31, no. 43, Article ID 1904648, 2019.
- [11] J. Wu, K. Jiang, G. Li, Z. Zhao, Q. Li, and F. Geng, "Molecularly coupled two-dimensional titanium oxide and carbide sheets for wearable and high-rate quasi-solid-state rechargeable batteries," *Advanced Functional Materials*, vol. 29, no. 30, Article ID 1901576, 2019.
- [12] M. K. Hota, Q. Jiang, Z. Wang, Z. L. Wang, K. N. Salama, and H. N. Alshareef, "Integration of electrochemical micro-supercapacitors with thin film electronics for on-chip energy storage," *Advanced Materials*, vol. 31, no. 25, Article ID 1807450, 2019.
- [13] M. Karaaslan, M. Bagmanci, E. Unal, O. Akgol, O. Altintas, and C. Sabah, "Broad band metamaterial absorber based on wheel resonators with lumped elements for microwave energy harvesting," *Optical and Quantum Electronics*, vol. 50, no. 5, 2018.
- [14] M. Bagmanci, M. Karaaslan, O. Altintas, F. Karadag, E. Tetik, and M. Bakir, "Wideband metamaterial absorber based on CRRs with lumped elements for microwave energy harvesting," *Journal of Microwave Power & Electromagnetic Energy*, vol. 52, no. 1, pp. 45–59, 2018.
- [15] A. Galoic, B. Ivsic, D. Bonefacic, and J. Bartolic, "Wearable energy harvesting using wideband textile antennas," in *Proceedings of the 2016 10th European Conference on Antennas and Propagation (EuCAP)*, Davos, Switzerland, April 2016.
- [16] H. Li, Z. Tang, Z. Liu, and C. Zhi, "Evaluating flexibility and wearability of flexible energy storage devices," *Joule*, vol. 3, no. 3, pp. 613–619, 2019.
- [17] J. Wang, G. Yang, J. Chen et al., "Flexible and high-loading lithium-sulfur batteries enabled by integrated three-in-one fibrous membranes," *Advanced Energy Materials*, vol. 9, no. 38, Article ID 1902001, 2019.
- [18] X. Li, J. Zhou, J. Zhang et al., "Bamboo-like nitrogen-doped carbon nanotube forests as durable metal-free catalysts for self-powered flexible Li-co 2 batteries," *Advanced Materials*, vol. 31, no. 39, Article ID 1903852, 2019.
- [19] N. Zhang and X. Zhang, "Asymmetric ring millimeter wave microstrip antenna based on communication satellite," *Foreign Electronic Measurement Technology*, vol. 32, no. 6, pp. 79–82, 2013.
- [20] J. O. Mcspadden, L. Lu Fan, and K. Kai Chang, "Design and experiments of a high-conversion-efficiency 5.8-GHz rectenna," *IEEE Transactions on Microwave Theory and Techniques*, vol. 46, no. 12, pp. 2053–2060, 1998.
- [21] V. Marian, C. Vollaie, and B. Allard, "Low power rectenna topologies for medium range wireless energy transfer," in *Proceedings of the European Conference on Power Electronics & Applications*, IEEE, Lille, France, 2011.
- [22] A. Dolgov, R. Zane, and Z. Popovic, "Power management system for online low power RF energy harvesting optimization," *IEEE Transactions on Circuits and Systems I: Regular Papers*, vol. 57, no. 7, pp. 1802–1811, 2010.
- [23] F. Jia, *Study on Preparation and Related Mechanism of Thermoelectric Materials and Micro Thermoelectric Generator Based on Electrochemical Technology*, Tianjin University, Tianjin, China, 2006.
- [24] I. Boniche and D. P. Arnold, "Micromachined radial thermoelectric modules for power generation using hot gas streams," *Journal of Microelectromechanical Systems*, vol. 20, no. 2, pp. 512–521, 2011.
- [25] Z. Wang, *Power Electronics*, China Machine Press, Beijing, China, 2011.
- [26] Z. Cao, C. Wang, M. Yuan, J. Luo, and J. Zhang, "Research status and development trend of environmental energy acquisition technology," *Journal of Nanjing University of Posts and Telecommunications*, vol. 36, no. 4, pp. 1–10, 2016.
- [27] X. Dai, S. Song, W. Xu, Z. Huang, and D. Gong, "Modal space neural network compensation control for Gough-Stewart robot with uncertain load," *Neurocomputing*, vol. 449, pp. 245–257, 2021.
- [28] C. Yang, D. Huang, W. He, and L. Cheng, "Neural control of robot manipulators with trajectory tracking constraints and input saturation," *IEEE Transactions on Neural Networks and Learning Systems*, vol. 32, no. 9, pp. 4231–4242, 2021.
- [29] C. Yang, C. Chen, W. He, R. Cui, and Z. Li, "Robot learning system based on adaptive neural control and dynamic movement primitives," *IEEE Transactions on Neural Networks and Learning Systems*, vol. 30, no. 3, pp. 777–787, 2019.
- [30] G. Peng, C. L. P. Chen, and C. Yang, "Neural networks enhanced optimal admittance control of robot-environment interaction using reinforcement learning," *IEEE Transactions on Neural Networks and Learning Systems*, pp. 1–11, 2021.



## Research Article

# Robust Low-Carbon Discrete Berth Allocation under Uncertainty

Feifei Yu <sup>1</sup>, Qihe Shan <sup>1</sup>, Yang Xiao <sup>2</sup>, and Fei Teng <sup>3</sup>

<sup>1</sup>Navigation College, Dalian Maritime University, Dalian 116026, China

<sup>2</sup>Department of Computer Science, The University of Alabama, Tuscaloosa, AL, USA

<sup>3</sup>College of Marine Electrical Engineering, Dalian Maritime University, Dalian 116026, China

Correspondence should be addressed to Qihe Shan; shanqihe@dlnu.edu.cn

Received 19 December 2021; Accepted 18 April 2022; Published 1 June 2022

Academic Editor: Sitharthan R

Copyright © 2022 Feifei Yu et al. This is an open access article distributed under the Creative Commons Attribution License, which permits unrestricted use, distribution, and reproduction in any medium, provided the original work is properly cited.

A robust discrete berth allocation method under a low-carbon target is proposed in this study, considering the uncertainty of vessels' arrival time and handling time. According to the actual situation of port operations, a bilevel, biobjective model is established to minimize both average carbon emission and the range of carbon emission during the berthing period. A set of alternative berth allocation schemes, namely, the set of Pareto solutions, are obtained by a heuristic algorithm based on a genetic algorithm. The effectiveness of the proposed method is verified by simulation.

## 1. Introduction

With the intensification of energy shortage and global warming, “low carbon” and “energy-saving and emission reduction” have gradually become the keywords in various fields. As a significant contributor to carbon emissions, port consumes great quantities of energy, and its CO<sub>2</sub> emissions, accounting for about 3% of the total anthropogenic CO<sub>2</sub> emissions, [1] must be taken seriously. In this case, reducing carbon emissions in the port area is important under the “dual carbon targets,” officially put forward by China in 2020. At present, China's ports mainly carry out emission reduction in structural and technical energy conservation methods to build green ports [2–4]. However, the carbon emission generated in the process of berthing is also a significant amount, which makes it a noteworthy means to reduce port carbon emissions from the perspective of berth allocation [5].

In recent years, many research results have been obtained in the field of berth allocation. According to spatial attributes, the berth allocation problem (BAP) can be divided into continuous berth allocation problem and discrete berth allocation problem. Continuous berth regards the wharf coastline as a continuous whole, and vessels can dock at any coastline position. Frojan et al. [6] study the continuous berth allocation problem in the case of multiple

terminals in a port and establish a model comprehensively considering four costs, including anchorage waiting for cost and delayed departure compensation. Chen and Huang [7] establish a dynamic continuous berth allocation model in which a penalty cost function is proposed by considering vessel departure delay and berth deviation distance. Carlos [8] studies the dynamic allocation of continuous berths and proposes a mixed-integer model to minimize the travel distance of forklifts and cranes in container operation, which was solved by a heuristic algorithm. The discrete berth is to cut the continuous coastline into individual berths, and each berth can only park one vessel at the same time. For the discrete case, Cordeau et al. [9] discuss the dynamic scheduling problem with the time window and present a tabu search heuristic together with two types of formulation. Sun et al. [10] study the influence of tide on discrete berth allocation from two aspects of the water level change in tide and the variance of vessel arrival time. Arram et al. [11] apply a bird mating optimizer algorithm, which can effectively explore and use the search space to find the global solution for solving the discrete berth allocation problem. On the other hand, according to temporal attributes, berth allocation problems can be divided into static BAP and dynamic BAP. Static BAP assumes that all vessels have arrived at the port and can berth immediately before the start of the scheduled cycle. The static model is generally applicable to

the scheduling of large-area detention of vessels caused by extreme weather, [12] which is difficult to play a role in the normal production operation. Dynamic BAP means that vessels will arrive in succession during the implementation of berth scheduling. It is more in line with the actual arrival situation of vessels and can well simulate the specific constraints. [13] Therefore, the research on the dynamic BAP model is much more extensive. Comprehensively considering the actual and urgent requirements of ports for reducing carbon emissions, this study conducts the study on the discrete and dynamic berth allocation problem under a low-carbon target to be close to the real port.

With the prevalence of “low-carbon” and the proposal of “dual-carbon targets,” mounting research is conducted on berth allocation with low-carbon targets. Zhao et al. [14] establish a joint berth-quay scheduling model under the strategies of variable arrival time and constant arrival time to minimize the carbon emissions of the whole terminal and the fuel consumption and the departure delay. Using port shore power technology, Peng et al. [15] propose a cooperative optimization method to minimize total cost and air pollution, in which different pollutants are uniformly expressed as economic penalties by levying an environmental tax. Wang et al. [16] consider the joint scheduling of berth, wharf crane, and yard truck and establish a multi-objective model to minimize the total carbon emission in the port area, the average waiting time, and departure delay [17] of each vessel in the port. However, the premise of optimization and scheduling in the above literature is that the vessel can arrive at a planned accurate time, ignoring various uncertain factors in the process of vessel berthing in real-life scenarios, such as arrival delay, handling delay, and equipment failure.

More and more scholars have begun to notice and study the uncertainty in berth allocation in recent years [18]. Sheikholeslami and Ilati [19] propose a new port berth allocation model, which considers the destructive impact of the tide on the berth plan and the uncertainty of ship arrival time to generate an effective berth allocation plan. Umang et al. [20] study the BAP in case of interruption caused by uncertain arrival time and handling time and propose an intelligent greedy algorithm, together with an optimal recovery algorithm based on set partition. Some scholars also began to combine berth scheduling with shore bridge schedules. Liang et al. [21] study the joint scheduling problem of berth and quay crane under the environment of random vessel arrival time and handling time and reduce uncertain factors’ influence by adding delay time. Considering the uncertainty of vessel arrival and the fluctuation of container handling rate of terminal crane, Iris and Lam [22] propose an active baseline plan with reactive recovery cost, which aims to develop a recoverable robust optimization method for the weekly berth and terminal crane planning. In actual working conditions, these uncertainties not only bring great hidden dangers to the operation of the wharf but also seriously strike the reliability of its operation plan, resulting in the fluctuation of terminal carbon emissions in a large range, which is not conducive to the accounting and treatment of terminal pollution [23]. However, limited

research studies have considered the impact of these uncertainties on port carbon emissions. Therefore, it is of great practical significance to consider the uncertainty when studying the berth allocation with the low-carbon target in actual working conditions.

The innovations of this study are as follows:

- (1) A discrete berth allocation problem is studied, which focuses on the objective of low-carbon emission in the port. Under the dual-carbon targets, the main sources of the carbon emission in the port are analyzed and the calculation formulas are given. A bilevel, biobjective model is established to reduce the average carbon emission and the range of carbon emission.
- (2) The impact of uncertainty on berth allocation of a low-carbon target is considered in the model for the first time to improve the robustness. The arrival time and handling time of the vessels are set to be uncertain and modeled as time windows. A heuristic algorithm based on a genetic algorithm is used to solve this problem, and its effectiveness is verified by simulation.

The rest of the study is structured as follows. Section 2 analyzes the carbon emission of the port area and establishes a bilevel, biobjective model. Section 3 explains the solution algorithm. In Section 4, an example is applied to verify the effectiveness of the algorithm by comparing it to two commonly used berth allocation policies under uncertainty. Conclusions and possible research directions in the future are noted in Section 5.

## 2. A Bilevel, Biobjective Model

The carbon emissions in the port area originate from two aspects: the portland area and the port water area.

In the portland area, the carbon emissions mainly come from the cargo handling equipment at the core of the port terminal, such as the shore bridge, container truck, and yard bridge. These types of equipment will produce a large amount of CO<sub>2</sub> in the process of providing services to berthing vessels. However, in recent years, to achieve the “dual-carbon targets,” the construction of a zero-carbon wharf has been continuously promoted. On October 17, 2021, the world’s first “smart zero-carbon” terminal was put into operation in Tianjin Port. The wharf loading and unloading equipment, horizontal transportation equipment, and production auxiliary equipment are powered by electricity, and 100% of the energy consumption comes from the “wind, light, and storage integration system.” At the same time, advanced energy-monitoring technology is adopted to carry out real-time statistical analysis on various energy consumption of the wharf to ensure zero carbon emission. In addition to all electric-driven facilities and equipment in the port area, for “large emitters” such as vessels, Tianjin Port has built an onshore power system at the wharf front. After the vessel lands, it will supply power to the vessel through the onshore power system to realize zero-emission during vessel berthing operation. Therefore, with the continuous

construction of green ports, all carbon emissions in the port area will come from the water area in the future.

While the carbon emissions in the port water area are mainly generated by berthing vessels, during berth scheduling, the port arranges the berthing time and berthing position of the vessels according to the relevant information provided by them to determine the berth scheduling table. After arrival, the vessel waits at the anchorage first. Once the allocated berth is free, it can sail to the berth through the channel and receive berthing services. Since the vessels can be connected to the shore power system during berthing operation, the carbon emission of the vessels in port is equivalent to the carbon emission of waiting in anchorage and navigation in the channel. When the vessel is sailing in the port, the main engine and auxiliary engine operate together. The main engine is used as the propulsion power device, and the auxiliary engine generates power to meet the power demand in the vessel. The power of the main engine is usually more than ten times that of the auxiliary engine. While the vessel is waiting at the anchorage, the main engine is turned off, and the auxiliary engine is used to generate power. Therefore, the carbon emission of navigation in the port accounts for the main part of the total carbon emission of the vessel.

For the carbon emission during navigation, Hughes [24] proposed the famous ‘‘cubic law,’’ that is, the fuel consumption of the vessel is positively correlated with the cubic of its navigation speed. The fuel consumption  $f_i$  of vessel  $i$  per sailing day can be expressed as follows:

$$f_i = r_i^1 + r_i^0 \cdot v_i^3, \quad (1)$$

where  $v_i$  represents the speed adopted by the vessel  $i$ , and  $r_i^0$  and  $r_i^1$  represent the skill coefficient of the driver and fuel consumption of the auxiliary engine per sailing day [25].

Then, the fuel consumption  $F_i$  in the process of entering the berth through the channel of length  $l$  can be calculated as follows:

$$F_i = \frac{1}{24} \cdot f_i \cdot \frac{l}{v_i} = \frac{l}{24} \cdot \left( r_i^1 \cdot \frac{1}{v_i} + r_i^0 \cdot v_i^2 \right). \quad (2)$$

When minimizing the fuel consumption, there is an optimal sailing speed  $v_i^*$ , which can be derived by the following:

$$v_i^* = \left( \frac{r_i^1}{2r_i^0} \right)^{1/3}. \quad (3)$$

If  $v_i \in [\underline{v}_i, \overline{v}_i]$ , but  $v_i^*$  is not in this value interval, the smallest  $F_i$  is taken at the lower bound or the upper bound. In this study, we assume that the optimal sailing speed  $v_i^*$  is within the speed range of vessel  $i$ . The CO<sub>2</sub> emissions of vessel  $i$  while sailing,  $C_i$ , can be further calculated by [26].

$$C_i = EF_1 \cdot F_i, \quad (4)$$

where  $EF_1$  is the emission factor of CO<sub>2</sub> while sailing.

As for the carbon emission during the waiting period at the anchorage, the vessel shuts down the main engine and uses the auxiliary engines to generate electricity to meet the

TABLE 1: Carbon emission factor.

	EF <sub>1</sub> (kg/kw-fuel)	EF <sub>2</sub> (kg/kw-fuel)
Emission factor	3.11	0.683

power demand inside the vessel. The CO<sub>2</sub> emission of vessel  $i$  during this period,  $Q_i$  is calculated by [27].

$$Q_i = PO_i \cdot LF_i \cdot EF_2 \cdot EN_i \cdot AC_i, \quad (5)$$

where  $PO_i$  is the rated power of auxiliary engines of vessel  $i$  during waiting;  $LF_i$  is the load ratio of auxiliary engines of vessel  $i$ ;  $EF_2$  is the CO<sub>2</sub> emission factor during the waiting period;  $EN_i$  is the number of auxiliary engines working on vessel  $i$ ; and  $AC_i$  is the auxiliary engines' continuous working time, that is waiting time of vessel  $i$ .

The reference values of CO<sub>2</sub> emission factors when sailing and waiting are shown in Table 1 [14].

Since the emission of vessels sailing in the port accounts for the main part of the total carbon emission, the vessel speed can be directly taken as its optimal speed  $v^*$ , under the goal of reducing the total carbon emission of the port. Then, the total carbon emission of the port area during berth scheduling,  $P$ , is presented as follows:

$$P = \sum_i C_i + \sum_i Q_i = 3.11 \cdot \frac{l}{24} \cdot \sum_i \left( r_i^1 \cdot \frac{1}{v_i^*} + r_i^0 \cdot v_i^{*2} \right) + 0.683 \cdot \sum_i PO_i \cdot LF_i \cdot EN_i \cdot (st_i - A_i), \quad (6)$$

where  $A_i$  is the arrival time of vessel  $i$ , that is, the time from the waters outside the port to the anchorage;  $st_i$  is the start time of vessel  $i$ , that is, the time of vessel  $i$  starting from the anchorage to the berth.

A container port with  $n$  vessels and  $m$  berths is assumed. The relevant notation is presented in Table 2. The solution to the berth allocation problem will include the berth allocation information and service order information of each vessel. So a berth schedule can be described by  $S(X, Y)$ , where  $X$  indicates the assignment of vessels to berths and  $Y$  indicates the service order.

In this study, it is assumed that the arrival time and handling time of the vessel are uncertain, and the time windows are given in advance. The vessel  $i$  arrives within  $[A_i^l, A_i^u]$  and has different handling time windows at different berths due to yard position and other factors.  $A$  and  $C$  contain the arrival and handling time windows of all vessels. For a given berth schedule  $S$ ,  $st_i$  can be determined by  $A$  and  $C$ . Because of the uncertainty of  $A$  and  $C$ ,  $st_i$  is also uncertain, which will lead to lower and upper bounds of the value of  $P$ . So we take the average total carbon emissions as an optimization objective function in equation (7). However, scheduling solely based on the average total carbon emissions might lead to a high range of total carbon emissions, which will result in weak robustness of the berthing schedule [28]. To deal with this problem, we construct the model as a biobjective optimization problem, introducing the minimum range of total carbon emissions as another objective function. So the model can be described as follows:

TABLE 2: Notation.

Sets	
$I = \{1, \dots, n\}, i \in I$	The set of $n$ vessels
$J = \{1, \dots, m\}, j \in J$	The set of $m$ berths
Parameters	
$A_i$	Arrival time of vessel $i$
$A_i^l$	Lower bound of $A_i$
$A_i^u$	Upper bound of $A_i$
$A$	$n$ vector of $A_i$ values
$c_{ij}$	Handling time of vessel $i$ at berth $j$
$c_{ij}^l$	Lower bound of $c_{ij}$
$c_{ij}^u$	Upper bound of $c_{ij}$
$C$	$n \times m$ matrix of $c_{ij}$ values
$l$	Length of port channel
$t_i$	Tonnage of vessel $i$
$T_j$	Tonnage of berth $j$
$v_i^*$	Optimal speed of vessel $i$
$M$	A large positive number
Decision variables	
$x_{ij}$	Binary variable, 1 if vessel $i$ is allocated to berth $j$
$X$	$n \times m$ matrix of $x_{ij}$ values
$y_{ab}$	Binary variable, 1 if $x_{aj} = x_{bj} = 1$ and $b$ is immediately serviced after $a$
$Y$	$n \times n$ matrix of $y_{ab}$ values
$st_i$	Start time of vessel $i$ from the anchorage to the berth
$ft_i$	Service finish time of vessel $i$
Auxiliary variable	
$z_i$	An auxiliary variable limiting the start time of vessel $i$

$$f_1: \min_{X,Y} \left[ \frac{1}{2} \left( \max_{C,A} P + \min_{C,A} P \right) \right], \quad (7)$$

$$f_2: \min_{X,Y} \left( \max_{C,A} P - \min_{C,A} P \right), \quad (8)$$

$$\text{s.t. } A_i^l \leq A_i \leq A_i^u, \quad (9)$$

$$c_{ij}^l \leq c_{ij} \leq c_{ij}^u, \quad (10)$$

$$\sum_{j \in J} x_{ij} = 1, \quad (11)$$

$$st_i \geq A_i, \quad (12)$$

$$st_b \geq st_a + \frac{l}{v_a^*} + \sum_{j \in J} x_{aj} c_{aj} - M(1 - y_{ab}), \quad (13)$$

$$T_j \geq t_i - M(1 - x_{ij}). \quad (14)$$

Constraints (9) and (10) specify the lower and upper bounds of the vessel's arrival time and handling time, respectively. Constraint (11) indicates that each vessel can only select one berth. Constraint (12) indicates that the start time is later than the arrival time. Constraint (13) restricts that only when the previous vessel finishes its handling operation, the latter vessel can start to the berth, and constraint (14) restricts the vessel to be serviced only in berths that meet the tonnage requirement.

In both definitions of the two objective functions, the maximum and minimum values of total carbon emissions need to be calculated. To solve this bilevel optimization problem, we refer to the hierarchical optimization method proposed by Golias [29]. Since the value of  $P$  depends on  $C$  and  $A$ , let  $[C^{\max}, A^{\max}]$  ( $S$ ) and  $[C^{\min}, A^{\min}]$  ( $S$ ) be the arrival time and handling time for  $\max P$  and  $\min P$ , respectively, under the schedule  $S$ . So the problem can be described as follows:

$$f_3: \max_{C,A} P = P_{C^{\max}, A^{\max}}, \quad (15)$$

$$\text{or } \min_{C,A} P = P_{C^{\min}, A^{\min}}.$$

s.t. equations (9)–(14).

$$z_i \in \{0, 1\}, \quad (16)$$

$$A_i - st_i + M(1 - z_i) \geq 0, \quad (17)$$

$$\sum_{a \in I, a \neq i} y_{ai} \cdot \left( st_a + \frac{l}{v_a^*} \right) + \sum_{j \in J, a \in I, a \neq i} c_{aj} x_{aj} y_{ai} - A_i \leq M(1 - z_i), \quad (18)$$

$$A_i - \left[ \sum_{a \in I, a \neq i} y_{ai} \cdot \left( st_a + \frac{l}{v_a^*} \right) + \sum_{j \in J, a \in I, a \neq i} c_{aj} x_{aj} y_{ai} \right] \leq M z_i. \quad (19)$$

Constraint (16) shows that  $z_i$  is an auxiliary variable with a value of 0 or 1. Constraints (17)–(19) ensure that the start

time of the vessel is the larger of its arrival time and the finish time of the previous vessel at the berth.

Then, the original biobjective, bilevel optimization problem can be reorganized as follows:

$$f_1: \min_{X,Y} \left[ \frac{1}{2} \left( P_{C^{\max}, A^{\max}} + P_{C^{\min}, A^{\min}} \right) \right], \quad (20)$$

$$f_2: \min_{X,Y} \left( P_{C^{\max}, A^{\max}} - P_{C^{\min}, A^{\min}} \right).$$

### 3. A Genetic Algorithm for BAP

Considering that the berth scheduling problem is a classical NP-hard problem with high computational complexity and is difficult to be solved by an accurate algorithm, we use a heuristic algorithm based on a genetic algorithm to obtain the solution under double objectives. The flow of the algorithm is roughly as follows: first, the representation of chromosomes is determined and the population is initialized; then, the objective functions corresponding to chromosomes are evaluated; the operations of selection, crossover, and mutation are carried out; and when the termination conditions are met, the iteration ends. The specific steps are described next.

**3.1. Chromosome Representation and Population Initialization.** For the berth scheduling problem, a chromosome represents a scheduling scheme, which includes the service berth and service order of each vessel. In this study, we use an integer to encode chromosomes, where the numbers represent the vessels and the berths are separated. An example is given in Figure 1 for a problem instance with seven vessels and three berths. This chromosome indicates that in the first berth, the service is carried out in the order of vessel 1-2; in the second berth, the order is vessel 3-4-5; and in the third berth, the order is vessel 6-7.

In addition, due to constraint (14), the berthing positions of some chromosomes are not compliant, so we need to obtain a list to specify the berths that each vessel can choose. Then, we randomly generate 100 chromosomes that meet the constraints according to this list. The process of generating the initial population is described in the following procedures, where  $B_i$  represents the optional berth list of vessel  $i$ , and  $ch$  and  $chs$  represent a chromosome and a chromosome set, respectively.

- 0: For  $i = 1: n$ 
  - 1: For  $j = 1: m$ 
    - 2: If  $T_j \geq t_i$ ;  $B_i$  append  $j$
    - 3: End
  - 4: End
- 5: End
- 0: Set  $L = \{1, 2, \dots, n\}$
- 1: For  $k = 1: \text{population}$ 
  - 2: Shuffle  $L$

	Berth 1		Berth 2			Berth 3	
Vessel	1	2	3	4	5	6	7

FIGURE 1: An example of a chromosome.

- 3: Set  $ch$  an empty chromosome with  $m$  berths
- 4: For  $i = 1: n$ 
  - 5: Randomly choose a berth from  $B_{L_i}$
  - 6: append  $L_i$  to the chosen berth of  $ch$
  - 7: End
- 8:  $chs$  append  $ch$
- 9: End
- 10: Return  $chs$ .

**3.2. Objective Function Evaluation.** To evaluate the given chromosome, we need to calculate the values of the two objective functions. According to the model established above, to calculate the values of  $f_1$  and  $f_2$ , we need to obtain  $[C^{\min}, A^{\min}](S)$  and  $[C^{\max}, A^{\max}](S)$  first, using the minimum search heuristic and maximum search heuristic methods in reference [29].

Minimum search heuristic (MISH) plans the arrival time and handling time of each vessel through the given time windows, which will affect the start time of the vessel, to minimize the value of total carbon emissions under the given chromosome. In this way,  $[C^{\min}, A^{\min}](S)$  is calculated. The procedure is as follows:

For each berth  $j$ :

- 0: Set  $ft_0 = 0$
- 1: For  $i = 1: n$ 
  - 2: Set  $c_{ij} = c_{ij}^l$
  - 3: If  $i = 1$  or  $ft_{i-1} \leq A_i^l$ ; set  $A_i = A_i^l$ ; set  $st_i = A_i$ ; set  $ft_i = st_i + l/v_i + c_{ij}$
  - 4: Elseif  $ft_{i-1} > A_i^u$ ; set  $A_i = A_i^u$ ; set  $st_i = A_i$ ; set  $ft_i = st_i + l/v_i + c_{ij}$
  - 5: Elseif  $A_i^u > ft_{i-1} > A_i^l$ ; set  $A_i = ft_{i-1}$ ; set  $st_i = A_i$ ; set  $ft_i = st_i + l/v_i + c_{ij}$
  - 6: End
- 7: End
- 8: Set  $C^{\min} = c_{ij}$ ; Set  $A^{\min} = A_i$
- 9: Return  $C^{\min}, A^{\min}$ .

Similar to MISH, maximum search heuristic is used to determine the arrival time and handling time  $[C^{\max}, A^{\max}](S)$  by the following procedure:

- 0: Set  $ft_0 = 0$
- 1: For  $i = 1: n$ 
  - 2: Set  $c_{ij} = c_{ij}^u$
  - 3: If  $i = 1$  or  $ft_{i-1} \leq A_i^l$ ; set  $A_i = A_i^u$ ; set  $st_i = A_i$ ; set  $ft_i = st_i + l/v_i + c_{ij}$
  - 4: Else; set  $A_i = A_i^l$ ; set  $st_i = ft_{i-1}$ ; set  $ft_i = st_i + l/v_i + c_{ij}$



- 5: End
- 6: End
- 7: Set  $C^{max} = c_{ij}$ ; Set  $A^{max} = A_i$
- 8: Return  $C^{max}$ ,  $A^{max}$ .

**3.3. Pareto Front (PF) Selection and Improvement.** When the genetic algorithm is used to solve the biobjective optimization problem, the concept of Pareto must be introduced. Pareto solutions are also called nondominated solutions. When there are multiple targets, due to the conflict and incompatibility between them, one solution is the best on one target and maybe the worst on other targets. While improving any objective function, these solutions that will inevitably weaken at least one other objective function are called nondominated solutions or Pareto solutions. The set of optimal solutions of a set of objective functions is called Pareto optimal set, and the surface formed by the optimal set in space is called the Pareto front. Pareto improvement, referring to a change that makes at least one target better without deteriorating any other target, is used to describe the optimization direction of this optimal set.

In this study, a berth schedule is included in the Pareto optimal set if there is no other schedule that can improve both objectives at the same time. When the chromosomes of the previous generation are not eliminated after PF selection, it means that there is no Pareto improvement. The process of PF selection and improvement judgment is described in the following procedure, where  $lb$  is the lower bound,  $ub$  is the upper bound, and  $ace$  and  $rce$  are the average and the range of carbon emission of the schedule.

- 0: Set change = False
- 1: For  $ch$  in  $ch$  s:
  - 2: Set  $lb = \text{mish}(ch)$ ; Set  $ub = \text{mash}(ch)$
  - 3:  $ace$  append  $(lb + ub)/2$ ;  $rce$  append  $(ub - lb)$
- 4: End
- 5:  $i = 1$
- 6: While  $i < |LS|$ 
  - 7: Set  $j = i + 1$
  - 8: While  $j \leq |LS|$ 
    - 9: If  $ace_i = ace_j$  and  $rce_i = rce_j$  and  $chs_i$  equals  $chs_j$  or  $ace_i < ace_j$  and  $rce_i \leq rce_j$  or  $ace_i \leq ace_j$  and  $rce_i < rce_j$ 
      - 10:  $LS = LS - \{(ace_j, rce_j, chs_j)\}$ ; go to step 8
      - 11: Elseif  $ace_i > ace_j$  and  $rce_i \geq rce_j$  or  $ace_i \geq ace_j$  and  $rce_i > rce_j$ 
        - 12: If  $i < \text{pre\_size}$ ; change = True
        - 13: End
        - 14:  $LS = LS - \{(ace_i, rce_i, chs_i)\}$ ; go to step 6
    - 15: End
    - 16: Set  $j = j + 1$
  - 17: End
  - 18: Set  $i = i + 1$

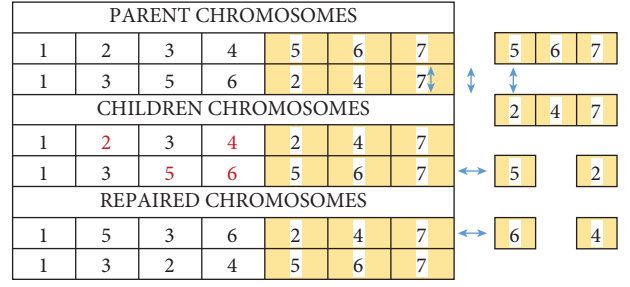


FIGURE 2: An example to illustrate chromosome crossover.

- 19: End
- 20: Return change.

**3.4. Crossover and Mutation.** To generate new chromosomes, we perform crossover and mutation operations. We adopt the method of partial-mapped crossover, and the parent chromosomes are crossed as shown in Figure 2. Since some genes will be repetitive, conflict detection needs to be carried out to repair the children's chromosomes. A mapping relationship is established according to the exchanged two sets of genes. All conflicting genes are transformed through the mapping relationship to form a new pair of conflict-free genes, finally obtaining the repaired chromosomes. Due to the influence of the berth restriction list, we need to further adjust the chromosomes of offspring.

The crossover operation is achieved by the following procedure.

- 0: Set L1 the array representation of parent\_ch1; Set L2 the array representation of parent\_ch2
- 1: Randomly choose an index  $lk$  as the cross point of L1 and L2
- 2: Set  $L3 = L1[1: lk] + L2[lk:]$ ; Set  $L4 = L2[1: lk] + L1[lk:]$
- 3: Set L5 a copy of L3; Set L6 a copy of L4;
- 4: Set  $i = 1$
- 5: while  $i < lk$ 
  - 6: For  $j = lk: |L5|$ 
    - 7: if  $L5_i = L5_j$ 
      - 8: Set  $L5_i = L4_j$ ; go to step 5
  - 9: End
- 10: End
- 11: Set  $i = i + 1$
- 12: End
- 13: Set  $i = 1$
- 14: while  $i < lk$ 
  - 15: For  $j = lk: |L6|$ 
    - 16: if  $L6_i = L6_j$ 
      - 17: Set  $L6_i = L3_j$ ; go to step 14
  - 18: End
- 19: End
- 20: Set  $i = i + 1$



21: End

22: Return L5 and L6.

The mutation operation is performed according to the two types illustrated in Figure 3. Insert mutation is to randomly select a vessel and randomly insert it into any other optional position. Swap mutation is to randomly select two vessels and exchange their positions. Note that the mutated chromosomes must still meet the constraints. The chromosome after insert or swap operation needs to be checked whether the berth assigned to each vessel is an accessible berth according to the berth list in 3.1. If not, the vessel will be randomly assigned to any berth it can go to according to the list to ensure that the chromosome still meets the constraints. The adjusted chromosome enters the next iteration as the mutated offspring.

**3.5. Termination.** When PF is not improved for 500 consecutive iterations or the CPU running time reaches 10 minutes, the algorithm ends.

#### 4. Numerical Example

In this study, a numerical example of 20 vessels with four berths at a container port is used for simulation. The vessel information in Table 3 refers to the data in reference [30]. The planning period is set to 24 hours. In this period, the vessels dynamically arrive from zero time and wait for berthing 60 nautical miles away from the port. We assume that the vessel works with a single auxiliary engine during the waiting period. The expected handling time of each vessel at different berths is assumed according to the tonnage and location of the berth, together with the number of containers of the vessel. The upper bound of the handling time window floats from 20% to 40% based on the expected handling time and is randomly generated according to a uniform distribution. The lower bound is lowered according to the same rule.

We apply the algorithm in Section 4 to this example and get a Pareto set as shown in Figure 4. Each point represents a berth allocation solution, the abscissa represents the average carbon emission value of the solution, and the ordinate represents the carbon emission range value of the solution. The boundary formed by these solutions is the Pareto front.

In this set of solutions, we choose the scheme with the lowest average total carbon emission as the solution to the problem. The berthing schedule is shown in Table 4, including the berth and service order of each vessel. The average total carbon emission of this scheduling scheme is 65199.2 kg under the set uncertainty, and the range of carbon emission is 51609.4 kg.

In practice, the port can select the desired berth allocation scheme in the set of solutions according to the specific needs and other considerations. For example, a port requires that the maximum carbon emission generated during the dispatching period shall not exceed 90000 kg. According to formulas (7) and (8), we know that the maximum carbon emission of a scheduling scheme,  $\max P$ , can be calculated by  $f_1$  and  $f_2$  as follows:

INSERT Mutation							
Before	1	2	3	4	5	6	7
After	1	2	5	3	4	6	7
SWAP Mutation							
Before	1	2	3	4	5	6	7
After	1	5	3	4	2	6	7

FIGURE 3: An example to illustrate chromosome mutation.

TABLE 3: Arrival vessel data.

Vessel number	$A_i^l$	$A_i^u$	$r_i^0$	$r_i^1$ (t/day)	Number of containers
1	0	1.5	0.09	1.7	200
2	0.7	2.3	0.11	2.2	1330
3	2.4	2.9	0.12	2.0	420
4	3	4.2	0.11	1.9	210
5	4.5	6	0.09	1.9	105
6	7.4	8.3	0.13	2.0	632
7	8	8.9	0.12	1.7	112
8	9.3	10	0.10	2.1	857
9	10.4	11	0.09	2.0	100
10	11.5	12.3	0.08	2.0	672
11	12.8	13.6	0.16	2.0	832
12	13.9	15.1	0.08	2.1	1080
13	14.9	16.3	0.08	1.8	475
14	16.4	17.1	0.11	1.7	153
15	17.7	19.3	0.10	1.8	390
16	18	19.1	0.09	1.8	400
17	19	19.7	0.12	1.7	207
18	20.9	22	0.10	1.9	590
19	22.5	23.5	0.11	2.2	555
20	22.7	23.4	0.09	1.8	369

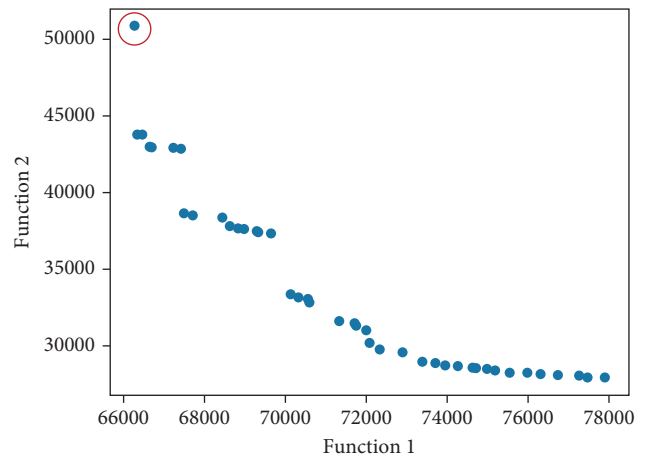


FIGURE 4: Pareto front.

TABLE 4: Final berth schedule.

Berth 1	Vessel 2	Vessel 8	Vessel 14	Vessel 19	Vessel 10
Berth 2	Vessel 3	Vessel 11	Vessel 16	Vessel 20	Vessel 13
Berth 3	Vessel 5	Vessel 6	Vessel 12	Vessel 18	Vessel 1
Berth 4	Vessel 4	Vessel 7	Vessel 9	Vessel 15	Vessel 17

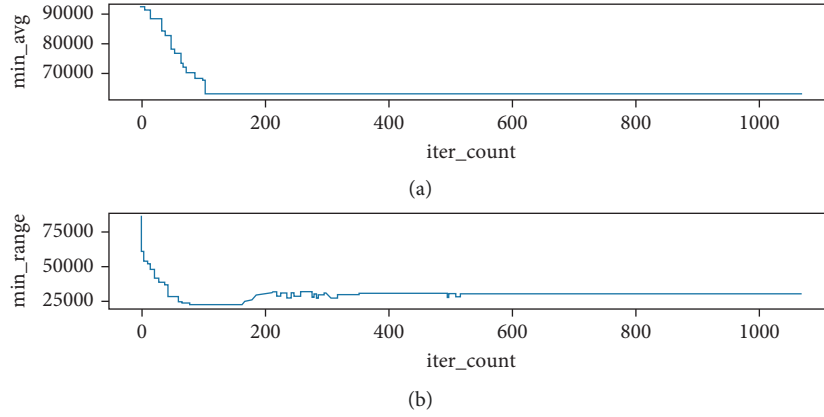


FIGURE 5: The downward trend of the two objective functions.

TABLE 5: Results of three strategies.

	Average	Range
FCFS-S	92245.1	84957
FCFS-F	115235.7	99793
PF solution	65199.2	51609.4

$$\max P = \frac{1}{2} (2f_1 + f_2). \quad (21)$$

At this time, the maximum carbon emission of the selected scheme is 91003.9 kg, which does not meet the carbon emission limit of the port. Therefore, it is necessary to reselect the qualified scheme on the Pareto front.

The downward trend of the two objective functions is described in Figure 5, in which the abscissa represents the number of iterations, and the ordinate represents the smallest objective function value in the PF obtained in each iteration. Both graphs show a downward trend on the whole, while Figure b shows a small increase. It is because that when the population number is controlled to 100 and the ranking is mainly based on  $f_1$ , the solution with small  $f_2$  value of the previous generation may be deleted, increasing the smallest  $f_2$  in the PF of the next generation. Both objective functions have been greatly optimized through the heuristic algorithm.

To evaluate the berth scheduling strategy proposed in this study, we compare the results with the other two commonly used strategies under uncertainty: the first come, first served with an early start (FCFS-S) strategy and first come, first served with early finish (FCFS-F) strategy [29]. The FCFS-S strategy means that the first-arriving vessel selects the berth that can serve it first according to the current berth state and selects the berth with a shorter handling time when the service start time is the same. Similarly, the FCFS-F strategy means that the first-arriving vessel selects the berth to leave first after the operation.

The two objective function values of the solutions obtained by the three strategies are listed in Table 5. The average total carbon emission of the PF solution decreased by 29.3% compared with the value of 92245.1 kg under the FCFS-S strategy and 43.4% compared with the value of 115235.7 kg under the FCFS-F strategy. The range of the

total carbon emission of the PF solution decreased by 39.2% and 48.3%, respectively, compared to 84957 kg of FCFS-S and 99793 kg of FCFS-F. It can be seen that the performance of the proposed method is much better than the other two commonly used strategies, and both average and range values have been greatly optimized.

## 5. Conclusions and Future Research

The carbon emission during vessel berthing is the main source of port carbon emissions. A good berth allocation schedule can effectively reduce the carbon emission of the port by planning the berthing process of vessels. In this study, a robust discrete allocation method under a low-carbon target has been proposed. The established model has considered the impact of uncertain arrival time and handling time on the scheduling table, which has been quantified as the maximum and minimum carbon emission of the scheduling scheme. While minimizing the total average carbon emission, the robustness of berth allocation has been taken into consideration to make the carbon emission of the scheduling scheme fluctuate in a small range. Also, this study has introduced the second objective function of the range value of carbon emission and established a hierarchical biobjective model. The maximum and minimum of the scheduling scheme have been searched by two heuristic methods. The model has been solved by a heuristic algorithm based on a genetic algorithm and applied to a problem example. The effectiveness has been illustrated by comparing the simulation results with those obtained by the FCFS-S and FCFS-F strategies.

The research of this study is based on the discrete berth so that that future research will be extended to the continuous berth allocation problem. In addition, the uncertainty of arrival time and handling time considered in this study is directly modeled as a given time window. The internal variation characteristics of the uncertainty need to be further studied.

## Data Availability

The data used to support the findings of this study are available from the corresponding author upon request.

## Conflicts of Interest

The authors declare that they have no conflicts of interest.

## References

- [1] L. Wang, C. Peng, W. Shi, and M. Zhu, "Carbon dioxide emissions from port container distribution: spatial characteristics and driving factors," *Transportation Research Part D: Transport and Environment*, vol. 82, Article ID 102318, 2020.
- [2] L. Jin, G. Huang, C. Min, B. Huang, H. Wang, and X. Wang, "Energy consumption measurement and analysis for electricity changed from oil of rubber-tyred gantry crane," *Hoisting and Conveying Machinery*, 2015.
- [3] B. Huang, Y. Li, F. Zhan, Q. Sun, and H. Zhang, "A distributed robust economic dispatch strategy for integrated energy system considering cyber-attacks," *IEEE Transactions on Industrial Informatics*, vol. 18, no. 2, pp. 880–890, 2022.
- [4] Q. Sun, R. Fan, Y. Li, B. Huang, and D. Ma, "A distributed double-consensus algorithm for residential we-energy," *IEEE Transactions on Industrial Informatics*, vol. 15, no. 8, p. 1, 2019.
- [5] Y. Allahviridizadeh, M. P. Moghaddam, and H. Shayanfar, "A survey on cloud computing in energy management of the smart grids," *International Transactions on Electrical Energy Systems*, vol. 29, no. 10, 2019.
- [6] P. Frojan, J. F. Correcher, R. Alvarez-Valdes, G. Koulouris, and J. M. Tamarit, "The continuous Berth allocation problem in a container terminal with multiple quays," *Expert Systems with Applications*, vol. 42, no. 21, pp. 7356–7366, 2015.
- [7] L. Chen and Y. Huang, "A dynamic continuous Berth allocation method based on genetic algorithm," in *Proceedings of the 2017 3rd IEEE International Conference on Control Science and Systems Engineering (ICCSSE)*, pp. 770–773, Beijing, China, 2017.
- [8] Carlos, Arango, Pablo et al., "Simulation-optimization models for the dynamic berth allocation problem," *Computer-Aided Civil and Infrastructure Engineering*, vol. 28, no. 10, pp. 769–779, 2013.
- [9] J.-F. Cordeau and G. P. L. Laporte, "Models and tabu search heuristics for the berth-allocation problem," *Transportation Science*, vol. 39, no. 4, pp. 526–538, 2005.
- [10] S. W. Sun, B. Yang, H. U. Zhi-Hua, L. Center, and S. M. University, "Research on discrete berth allocation under tidal influence at container terminal," *Journal of Hefei University of Technology*, vol. 37, no. 4, pp. 486–492, 2014.
- [11] A. Arram, M. Z. A. Nazri, M. Ayob, and A. Abunadi, "Bird mating optimizer for discrete Berth allocation problem," in *Proceedings of the 2015 International Conference on Electrical Engineering and Informatics (ICEEI)*, pp. 450–455, Denpasar, Indonesia, 2015.
- [12] S. Emde, N. Boysen, and D. Briskorn, *The Berth Allocation Problem with Mobile Quay Walls: Problem Definition, Solution Procedures, and Extensions*, Publications of Darmstadt Technical University, Darmstadt, Germany, 2014.
- [13] S. W. Lin and C. J. Ting, "Solving the dynamic Berth allocation problem by simulated annealing," *Engineering Optimization*, vol. 46, 2013.
- [14] H. Zhao, X. L. Han, L. Center, and S. M. University, "Berth and quay crane scheduling based on variable arrival time of ship," *Journal of Guangxi University*, vol. 41, no. 6, 2016.
- [15] Y. Peng and M. X. H. W. Dong, "Cooperative optimization of shore power allocation and berth allocation: a balance between cost and environmental benefit," *Journal of Cleaner Production*, vol. 279, Article ID 123816, 2021.
- [16] T. Wang, M. Li, and H. Hu, "Berth allocation and quay crane-ward truck assignment considering carbon emissions in port area," *International Journal of Shipping and Transport Logistics*, vol. 11, no. 2/3, p. 216, 2019.
- [17] Y. Wu and J. Dong, "Local stabilization of continuous-time T-S fuzzy systems with partly measurable premise variables and time-varying delay," *IEEE Transactions on Systems, Man, and Cybernetics: Systems*, vol. 51, no. 1, pp. 326–338, 2021.
- [18] C. Deng, C. Wen, J. Huang, X.-M. Zhang, and Y. Zou, "Distributed observer-based cooperative control approach for uncertain nonlinear MASs under event-triggered communication," *IEEE Transactions on Automatic Control*, vol. 67, no. 5, pp. 2669–2676, 2022.
- [19] A. Sheikholeslami and R. Ilati, "A sample average approximation approach to the Berth allocation problem with uncertain tides," *Engineering Optimization*, vol. 50, 2018.
- [20] N. Umang, M. Bierlaire, and A. L. Erera, "Real-time management of berth allocation with stochastic arrival and handling times," *Journal of Scheduling*, vol. 20, no. 1, pp. 67–83, 2017.
- [21] C. Liang, W. Yu, L. Center, and S. M. University, "Simultaneous Berth and quay crane scheduling under uncertainty environments in container terminals," *Computer Engineering and Applications*, vol. 53, no. 7, 2017.
- [22] Ç. Iris and J. S. L. Lam, "Recoverable robustness in weekly berth and quay crane planning," *Transportation Research Part B: Methodological*, vol. 122, pp. 365–389, 2019.
- [23] M. A. Ebrahim, M. Becherif, and A. Y. Abdelaziz, "PID-/FOPID-based frequency control of zero-carbon multisources-based interconnected power systems underderegulated scenarios," *International Transactions on Electrical Energy Systems*, vol. 31, no. 2, 2020.
- [24] C. Hughes, *Ship Performance: Technical Safety Environmental and Commercial Aspects*, Lloyd's of London Press, London, UK, 1996.
- [25] R. Wang, Q. Sun, W. Hu, Y. Li, D. Ma, and P. Wang, "SoC-based droop coefficients stability region analysis of the battery for stand-alone supply systems with constant power loads," *IEEE Transactions on Power Electronics*, vol. 36, no. 7, pp. 7866–7879, 2021.
- [26] Y. Du, Q. Chen, X. Quan, L. Lei, and R. Y. K. Fung, "Berth allocation considering fuel consumption and vessel emissions," *Transportation Research Part E: Logistics and Transportation Review*, vol. 47, no. 6, pp. 1021–1037, 2011.
- [27] Q.-M. Hu and Z.-H. Y. Hu, "Berth and quay-crane allocation problem considering fuel consumption and emissions from vessels," *Computers & Industrial Engineering*, vol. 70, pp. 1–10, 2014.
- [28] Q. Sun, B. Wang, X. Feng, and S. Hu, "Small-signal stability and robustness analysis for microgrids under time-constrained DoS attack and a mitigation adaptive secondary control method," *Science China Information Sciences*.
- [29] M. Golias and I. D. E. G. Portal, "Robust berth scheduling at marine container terminals via hierarchical optimization," *Computers & Operations Research*, vol. 41, pp. 412–422, 2014.
- [30] X. Wang, S. Liu, R. Zhang, and J. Wang, "Integrated berth and quay crane allocation multi-objective algorithm for container terminal," *Journal of System Simulation*, vol. 30, no. 3, 2018.

## Research Article

# Resilience Assessment for Microgrid with Pre-Position and Reconfiguration of Emergency Distribution Generations under Natural Hazard

Hongtao Lei <sup>1,2</sup>, Shengjun Huang <sup>1,2</sup>, Yajie Liu <sup>1,2</sup> and Tao Zhang <sup>1,2</sup>

<sup>1</sup>College of Systems Engineering, National University of Defense Technology, Changsha, Hunan 410073, China

<sup>2</sup>Hunan Key Laboratory of Multi-Energy System Intelligent Interconnection Technology, Changsha, Hunan 410073, China

Correspondence should be addressed to Hongtao Lei; hongtaolei@aliyun.com

Received 3 March 2022; Revised 23 March 2022; Accepted 30 March 2022; Published 15 April 2022

Academic Editor: Qiuye Sun

Copyright © 2022 Hongtao Lei et al. This is an open access article distributed under the Creative Commons Attribution License, which permits unrestricted use, distribution, and reproduction in any medium, provided the original work is properly cited.

Recently, increasing the number and severity of the natural hazards requires the resilience assessment and enhancement of the power system, especially the microgrid system. The emergency distribution generations have great potential to enhance the resilience of microgrid against blackouts under the emergency environment. This paper investigates the resilience assessment of the microgrid system under natural hazard, where emergency distribution generations are firstly pre-positioned on system nodes and then reconfigured after system damage occurs. A new resilience metric index and an efficient approximation computation method are provided for the resilience assessment of the focused problem. A new pre-position strategy and a new reconfiguration strategy on emergency distribution generations are proposed for the microgrid system emergency restoration under natural hazard. Also, a framework of resilience assessment is provided for problem-solving. The results of extensive experiments on the modified IEEE 30-Bus system and modified IEEE 118-Bus system confirm the effectiveness of the resilience assessment methodology and the superiority of proposed restoration strategies.

## 1. Introduction

Due to a lot of the blackouts caused by natural hazards, the resilience of power systems has become a focusing point in society nowadays. As a smart terminal end of the power grid, the microgrid system provides the services of power supply for domestic and industrial customers, and the resilience of microgrid closely corresponds to the quality of services for the customers. However, the extreme disruptions under natural hazards, which lead to line failure, equipment damage, infrastructure destruction, and so on, would result in large-scale outages and loss of health and wealth. For example, in the US, natural hazards cause about 25 to 70 billion dollars to cost annually [1]. Therefore, it is necessary to assess and improve the power system resilience under natural hazards, especially for the microgrid system.

In the literature, Holling [2] firstly introduced the concept of resilience from a view of the ecological system, where it defined the resilience of the ecological system as its

ability to move away from equilibria for disturbances. Then, a lot of research works on resilience in the social system [3], engineering system [4], and so on have been triggered. Like Mili et al. [5], in this work, we consider resilience as the ability of a system, where the system performance degrades for unexpected extreme disturbances and the system could recover its function through emergency restoration actions once the disturbances cease. Since the focus on the resilience of power system to extreme events is increasing, it is important to develop the related quantitative approaches and metrics for the measure of resilience. Several resilience metrics have been provided in [6–12]. Bruneau et al. [7] introduced a “resilience triangle” to assess seismic resilience of community system, where the resilience can be computed as the integral of degraded system performance with time after disruptions [13]. Ouyang and Duenas-Osorio [11] proposed the time-dependent resilience metrics for urban infrastructure systems. Also, Panteli et al. [12] proposed a “resilience trapezoid” metric concept, during which authors



extended the “resilience triangle” to fix the different phase measure of system resilience for the disruption. Lei et al. [14] proposed a two-stage dispatch framework consisting of pre-positioning and real-time allocation for dispatching mobile emergency generators as distributed generators in distribution systems to restore critical loads by forming multiple microgrids. Ti et al. [15] provided a cyber-physical power system resilience assessment framework that considered the space-time metrics of disasters. A state-of-the-art review of existing research on the study of grid resilience for definitions, frameworks, quantitative assessment methodologies, and enhancement strategies has been presented by Jufri et al. [10]. Also, an overview of the assessment metrics of the concept of resilience in electrical grids was given by Dehghani et al. [8], who explained the metrics that have been presented in various researches and compared these metrics from different aspects in order to determine the most comprehensive metric.

For microgrid, Amirioun et al. [16] presented a microgrid proactive management framework to cope with adverse impacts of extreme windstorms, and the proposed method considered the benefit of network reconfiguration, generation reschedule, backup generation capacity, and so on. Amirioun et al. [6] provided a quantitative framework for assessing the system resilience in response to high-impact low-probability windstorms, where the proposed framework jointly employs fragility curves of overhead distribution branches and windstorm profile to quantify the degradation in microgrid performance. Hussain et al. [17] reviewed the formation and strategy of microgrids for resilience enhancement and provided future directions for resilience-oriented operation methods. Nelson et al. [18] developed a statistical framework to quantify resilience of grid-connected microgrids to ensure critical loads served during islanding scenarios, and Markov chains were used to evaluate microgrid transition states for the quantified resilience. Ibrahim and Alkhrabat [9] introduced a set of metrics that are utilized for resiliency quantification of microgrid systems, such as level of resilience, level of performance reduction, and recovery time.

In summary, the aforementioned work focuses on either power system’s (or microgrid) general resilience assessment or enhancement method under extreme disturbances, where the system resilience assessment and enhancement problems are considered simultaneously. However, different from the above research work, (1) we consider the resilience assessment for the microgrid with system emergency restoration under natural hazard, where the resilience emergency enhancement strategies in the predisturbance and restoration phases are incorporated into the resilience assessment progress; (2) we extend the system resilience metric of microgrid with consideration of the supplied load demand importance and propose an efficient approximation computation method for the resilience metric index based on the system emergency restoration strategy; (3) we also provide a new pre-position strategy and a new reconfiguration strategy on emergency distribution generations for microgrid system restoration, considering the flexibility and practicability of microgrid restoration action under the

emergency environment. So, the main contributions of this paper are summarized as follows:

- (i) To the best of our knowledge, the emergency system restoration with distribution generation has never been considered in the resilience assessment for the microgrid under natural hazard. This gap is filled by this paper.
- (ii) In this new problem, the emergency distribution generations are pre-positioned and reconfigured on the microgrid nodes for emergency system restoration. A new resilience metric index with the integration of load demand importance and system resilience is provided for the resilience assessment of the proposed problem. An efficient approximation computation method is presented for the proposed resilience metric index, based on the system restoration strategy.
- (iii) A new pre-position strategy and a new reconfiguration strategy for emergency distribution generations are proposed for the improvement of system resilience and performance at the stage of system restoration. An assessment framework of the focused problem is also provided for the problem-solving.
- (iv) The effectiveness of the resilience assessment methodology and the superiority of the restoration strategies are demonstrated in the extensive experiments on the modified IEEE 30-Bus system and modified IEEE 118-Bus system.

The remainder of the paper is structured as follows. Section 2 describes the focused problem and provides the resilience metric for this paper. Section 3 presents the fragility modeling under hazard, the emergency system restoration with distribution generation pre-position and reconfiguration, the computation of resilience metric under emergency system restoration, and the assessment framework for the methodology. Results of simulation experiments are discussed in Section 4. Section 5 concludes the paper.

## 2. Problem Description and Resilience Metric

The focused issue is to assess the system resilience for the microgrid under hazard, where emergency distribution generations are pre-positioned and reconfigured on microgrid nodes for the emergence system restoration. There exist two stages for the system restoration: (1) the distribution generations are first pre-positioned on nodes as backups before the hazard event; (2) after the hazard occurs, the pre-positioned generations are reconfigured to the suitable nodes for maximal system resilience and performance.

The hazard, for example, windstorm, earthquake, flood, and so on, causes the performance of the microgrid system to be degraded by destroying its elements such as transmission lines, electric transformers, and plants. Since the repair for the destroyed elements of the power system

requires the collection of equipment resources and repair crews, it usually needs to be implemented for several hours (or even several days) after the hazard happens, which may lead to the huge cost of economy and health. Therefore, the emergency distribution generations, such as microturbine and mobile energy storage system, are pre-positioned and reconfigured on microgrid nodes, respectively, before and after the hazard for rapid and efficient system restoration.

In this paper, there exist a microgrid node set  $N = \{1, \dots, i, \dots, n\}$  and a distribution generation set  $M = \{1, \dots, k, \dots, m\}$ , where  $m < n$  and distribution generation  $k$  has capacity  $G_k$ . The concerned conceptual resilience curve is shown in Figure 1. The microgrid states include six states, which are the predisturbance state  $[t_0, t_e]$ , the degradation state  $[t_e, t_{de}]$ , the degraded state  $[t_{de}, t_{re}]$ , the restoration state  $[t_{de}, t_{res}]$ , the restored state  $[t_{res}, t_{ir}]$ , and the infrastructure recovery state  $[t_{ir}, t_{pir}]$ . In Figure 1, a hazard event happens at  $t_e$ , which results in the performance degradation of the microgrid in  $[t_e, t_{de}]$ . After the event, the damage and consequences are identified to preserve the optimal operation of the microgrid system in  $[t_{de}, t_{re}]$ , and the performance of the microgrid stays at a postevent degraded level  $Q_{de}$ .

During the restoration progress of  $[t_{re}, t_{res}]$ , the pre-positioned or reconfigured emergency distribution generations are sequentially added to the microgrid for rapid and efficient energy supplying, considering the system stability and demand of critical loads. After the emergency system restoration, the performance of the microgrid will be improved to an upgraded level  $Q_{re}$ . The level  $Q_{re}$  could be higher or less than the predisturbance system performance level  $Q_0$ , which depends on the system restoration actions and the capacities of emergency distribution generations. Note that, for convenience and simplicity, we believe that, at each “pre-” or “-ed” state in Figure 1, the microgrid system will achieve optimal stable performance under its situation.

In Figure 1, we consider three cases for the value of upgraded level  $Q_{re}$ , described as  $C_0$  “ $C_0$ ,” “ $C_1$ ,” and “ $C_2$ ,” respectively. The remarkable unsatisfied demands have been considered at the predisturbance state, and enough emergency distribution generations have been added at the restoration state in the case of  $C_2$  “ $C_2$ ,” so it obtains a final performance higher than that of the predisturbance state. The microgrid system remains at the upgraded level  $Q_{re}$  for the emergency restoration actions in  $[t_{res}, t_{ir}]$ . Then, the infrastructure recovery will be implemented from  $t_{ir}$  to  $t_{pir}$ . This paper focuses on period horizon  $T$  from  $t_e$  to  $t_{ir}$ , which involves the degradation state, degraded state, restoration state, and restored state.

System resilience is a system’s ability to prepare for and adapt to changing conditions and withstand and recover rapidly from disruptions [19]. And the load shedding has been widely considered as the disturbance which directly impacts the system restoration process [20]. The microgrid system performance can be defined as the load demand supplied at the period horizon  $T$ , and then the microgrid system resilience in this work is quantified based on the

percentage of the met demand with consideration of the supplied load weight as follows:

$$R = \frac{\int_{t_e}^{t_{ir}} \sum_{i \in N} w_i q_i^1(t) dt}{\int_{t_e}^{t_{ir}} \sum_{i \in N} w_i q_i^0(t) dt} \quad (1)$$

$$= \frac{\int_{t_e}^{t_{ir}} \sum_{i \in N} w_i q_i^1(t) dt}{\sum_{i \in N} w_i q_i^0 T},$$

where  $N$  is the node set of the microgrid system,  $q_i^0$  is the supplied load at node  $i$  in  $[t_0, t_e]$ ,  $q_i^1(t)$  is the supplied load at node  $i$  in  $[t_e, t_{ir}]$ , and  $w_i$  is the weight of supplied load at node  $i$ . We can record  $\sum_{i \in N} w_i q_i^0$  as  $Q_i^0$  and  $\sum_{i \in N} Q_i^0 = Q_0$ , where the “weighted” supplied loads are considered as the “weighted” performance of the microgrid system at the predisturbance state. Also,  $Q_{re}$  and  $Q_{de}$  are the “weighted” performance of the microgrid system at their states.  $\sum_{i \in N} w_i q_i^1(t)$  can be noted as  $Q^1(t)$  and  $\sum_{i \in N} Q_i^1(t) = Q^1(t)$ . However,  $Q^1(t)$  equals  $Q_{de}$  and  $Q_{re}$ , respectively, at the degraded state and the restored state, and the value depiction of  $Q^1(t)$  at the degradation state and restoration state, respectively, corresponds to the descent curve and ascent curve. Then, formula (1) can be changed to

$$R = \int_{t_e}^{t_{ir}} \frac{Q^1(t) dt}{Q_0 T}$$

$$= \frac{\left( \int_{t_e}^{t_{de}} Q^1(t) dt + Q_{de} (t_{re} - t_{de}) + \int_{t_{re}}^{t_{res}} Q^1(t) dt + Q_{re} (t_{ir} - t_{res}) \right)}{Q_0 T} \quad (2)$$

In formula (2), two terms “ $\int_{t_e}^{t_{de}} Q^1(t) dt$ ” and “ $\int_{t_{re}}^{t_{res}} Q^1(t) dt$ ” are not easy to be computed. Referring to Panteli et al. [12] and Panteli et al. [21], we approximate “ $\int_{t_e}^{t_{de}} Q^1(t) dt$ ” as the sum of corresponding “triangle” and “rectangle” areas in Figure 1,

$$\int_{t_e}^{t_{de}} Q^1(t) dt = \frac{(t_{de} - t_e)(Q_0 - Q_{de})}{2 + (t_{de} - t_e)Q_{de}} \quad (3)$$

The term “ $\int_{t_{re}}^{t_{res}} Q^1(t) dt$ ” corresponds to the performance area of the microgrid system at the restoration state. For the stability of the microgrid system, we assume in the system restoration process that the pre-positioned and reconfigured emergency distribution generations are sequentially added to the system at each time interval  $\Delta t$ . The position and addition sequence of emergency distribution generations are important for system resilience assessment and affect the computation of “ $\int_{t_{re}}^{t_{res}} Q^1(t) dt$ ” “ $\int_{t_{re}}^{t_{res}} Q^1(t) dt$ .” We will discuss them in detail in Sections 3.2 and 3.3.

The values of  $Q_0$  “ $Q_0$ ,” “ $Q_{de}$ ,” and “ $Q_{re}$ ” can be easily obtained by an optimal power flow (OPF) approach [22] based on the states of the microgrid system, where the focus of this work is on developing and illustrating a novel and specific resilience assessment methodology. It is worth mentioning that, based on the above discussion of computation and description of Figure 1, the value of the system



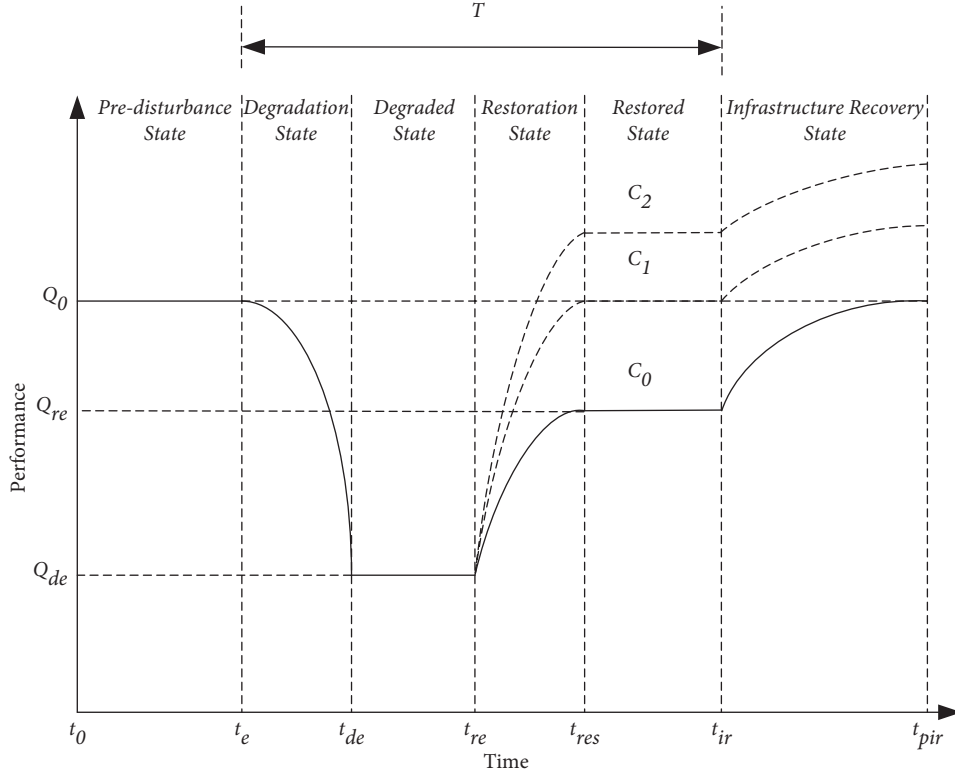


FIGURE 1: A conceptual resilience curve with a disturbance event and emergency restoration.

resilience metric “ $R$ ” could be equal to 1, less than 1, or larger than 1.

### 3. Assessment Methodology for the Microgrid under Hazard

In this section, we provide an assessment methodology for the microgrid system with pre-position and reconfiguration of emergency distribution generations under hazard.

**3.1. Fragility Modeling under Hazard.** The fragility describes the failure of a structure or structural component of the focused system, conditional on a loading that relates to the potential intensity of a hazard [23]. The wind storm has been recognized to cause the highest percentage of failure in power infrastructure among hazards [24]. Therefore, we use it to model the fragility of the microgrid system under hazard, where the fragility modeling for other hazards is similar. Since the microgrid is geographically small, wind storm passes through the system within a few minutes, and we only consider the transmission line failure in the fragility modeling of the microgrid for simplicity. Like Panteli et al. [12]; Panteli et al. [23]; Panteli et al. [21]; Fu et al. [25]; and Amiroun et al. [6], we use the fragility curve that presents the failure probability of transmission line as a function of hazard intensity (e.g., wind speed) to model the fragility of transmission lines in microgrid system. We also apply the fragility curve shown in Figure 2, as Panteli et al. [12], with the following constraint. where  $P_k(V)$  is the failure probability of transmission lines as a function of wind speed  $V$  at

simulation iteration  $k$ ,  $V_{\text{critical}}$  is the wind speed value at which the failure probability of lines can be discerned, and  $V_{\text{collapse}}$  is the wind speed value when the failure of lines will certainly occur. For each transmission line, a uniformly distributed random number  $u \in (0, 1)$  will be generated to check the failure of the line in each simulation iteration. If  $P_k(V) > u$ , the transmission line is not failed; otherwise, the transmission line is destroyed by the wind storm.

$$P_k(V) = \begin{cases} 0, & \text{if } V < V_{\text{critical}}, \\ P(V), & \text{if } V_{\text{critical}} \leq V < V_{\text{collapse}}, \\ 1, & \text{if } V \geq V_{\text{collapse}}, \end{cases} \quad (4)$$

**3.2. Pre-Position and Reconfiguration of Emergency Distribution Generations under Emergency System Restoration.** In this work, the emergency system restoration actions with emergency distribution generations are run at two stages. The emergency distribution generations are firstly pre-positioned on microgrid nodes for backups at the first stage. Then, after system damage occurs, some emergency distribution generations are reconfigured to suitable nodes with the aim of maximization of system resilience and performance at the second stage. The pre-positions of emergency distribution generations sharply impact the restored level  $Q_{re}$  and system resilience metric of the microgrid. Considering formulas (1) and (2), we propose the following pre-position strategy for the emergency system restoration of the microgrid.

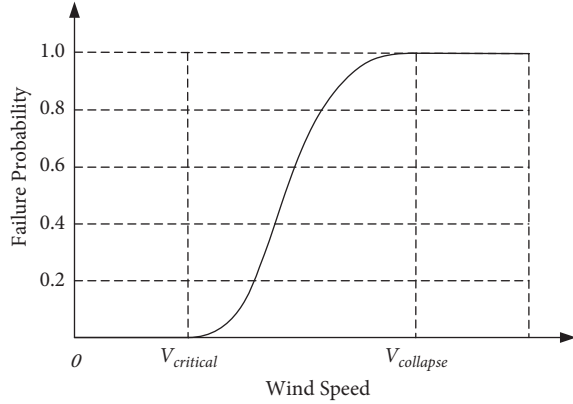


FIGURE 2: Fragility curve of transmission lines with failure probability as a function of wind speed.

*Definition 1.* The pre-position of distribution generation is defined by the following steps. Firstly, the nodes of the microgrid are sorted in descending order of the value of  $w_i q_i^0$ . Then, the emergency distribution generations are sorted in descending order of the value of  $G_k$ . Finally,  $m$  emergency distribution generations are mapped to be pre-positioned on the previous  $m$  nodes of the microgrid system.

Following the above pre-position strategy, the emergency distribution generations are inclined to be pre-positioned at the first stage on these nodes, where it has the larger weighted load demand value. At the second stage, since the damage of wind storm is uncertain, it is necessary to adjust and reconfigure the pre-positioned emergency distribution generations for better system resilience and performance. For simplicity, we assume that the pre-positioned distribution generation can be reconfigured only once, and each node can be located with two emergency distribution generations at most. So, we provide the following reconfiguration strategy.

*Definition 2.* Based on the damaged transmission lines and pre-positioned emergency distribution generations, the power output of distribution generation  $k$  pre-positioned on node  $j$  and shed loads on node  $i$  can be determined, respectively, as  $q_{k,j}^1$  and  $\Delta d_i$ , after optimizing the power flow of the damaged microgrid system at the first stage. Distribution generation  $k$  can be reconfigured to node  $z$  at the second stage as follows:

$$z = \begin{cases} \arg_i \max_{i \in RN} q_{k,i}^1 & \text{if } RN \neq \emptyset, \\ j, & \text{if } RN = \emptyset \end{cases} \quad (5)$$

where

$$RN = \{i | q_{k,i}^1 = \min\{G_k, \Delta d_i\}, q_{k,i}^1 > q_{k,j}^1\}. \quad (6)$$

According to this reconfiguration strategy, the reconfiguration node for the pre-positioned distribution generation is chosen with a maximum of generation power output at those nodes, where it obtains larger generation power output in comparison to that at the pre-position node. If there exists

no such node, the pre-positioned distribution generation will stay at the pre-position node.

We note that although this work focuses on the microgrid system, for the high dimensional power system, the dimensionality reduction method is an effective way to prepare for the restoration strategy design, such as reduced-order aggregate model for large-scale converters with inhomogeneous initial conditions in DC microgrids and reduced-order transfer function model of the droop-controlled inverter via Jordan continued-fraction expansion.

*3.3. Computation of Resilience Metric under Emergency System Restoration.* As mentioned above, the microgrid system under hazard is restored by the emergency restoration actions, where the emergency distribution generations are pre-positioned and reconfigured within two stages. This certainly affects the resilience assessment for the microgrid at the focused states, where the core issue is the computation of resilience metric under the system emergency restoration.

Assume that the performance of the microgrid system reduces to degraded level  $Q_{de}$  at the degraded state. After the pre-position and reconfiguration of emergency distribution generations, the restored system performance level  $Q_{re}$  can be actually determined by the OPF approach from a system view. However, the startup sequence of the pre-positioned and reconfigured emergency distribution generations still affects the resilience assessment metric of the system restoration. With consideration of system stability, the pre-positioned and reconfigured emergency distribution generations are sequentially started for energy supply at the beginning of each time interval  $\Delta t$ . Then, the upgraded curve in Figure 1 at the restoration state will be changed to the “staircase” curve as shown in Figure 3.

Considering the system resilience metric in formulas (1) and (2), if the pre-positioned and reconfigured distribution generation on the node with the higher value of “weighted” power demand obtains an earlier start, it will prompt the higher system performance with the above “staircase” curve and lead to the higher resilience metric under system emergency restoration. So, we provide the following startup strategy for the pre-positioned and reconfigured emergency distribution generations.

*Definition 3.* The startup sequence of emergency distribution generations is defined by the following steps. Firstly, the microgrid nodes with the pre-positioned and reconfigured emergency distribution generations are sorted in descending order of their values of  $w_i q_{k,i}^1$ . Then, the emergency distribution generations are sequentially started by the order of the nodes at the beginning of each time interval  $\Delta t$ .

Therefore, in order to compute the formulas in Section 3, we propose the following proposition.

**Proposition 1.** Assume that the time of restoration state  $[t_{re}, t_{res}]$  is divided into  $m+1$  time intervals as  $\{\Delta t, \dots, \Delta t, \Delta t_1\}$  and  $m\Delta t + \Delta t_1 = t_{res} - t_{re}$ . During each of precious  $m$  time intervals, the system performance is upgraded  $w_i \Delta q_{k,i}^1$  ( $i \in N, k \in \tilde{M}$ ) by the started pre-positioned (or

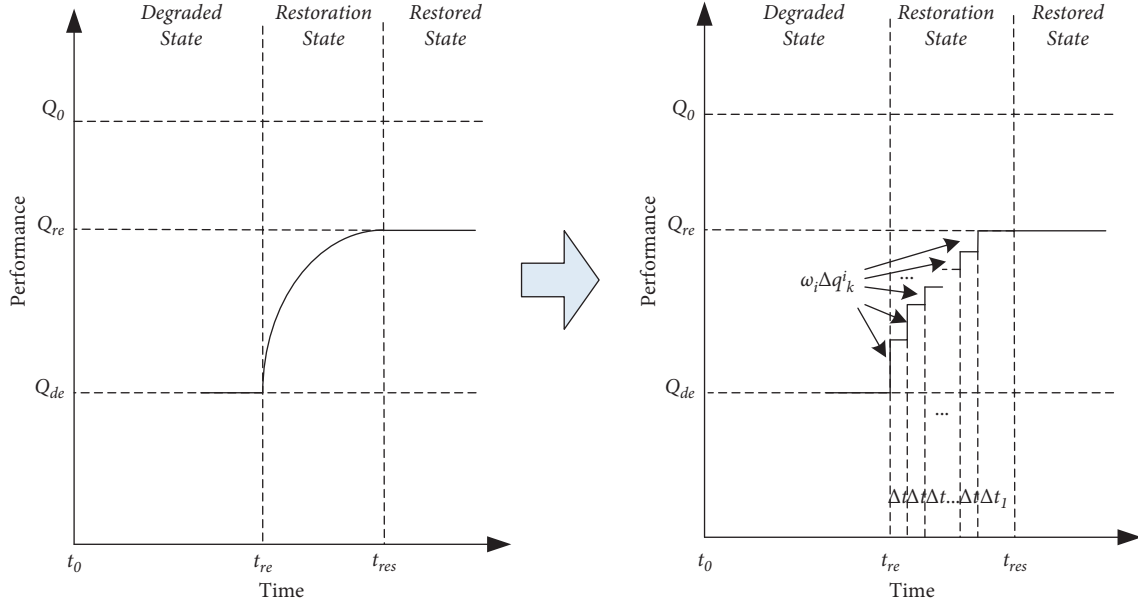


FIGURE 3: Performance curve of restoration state changed as a staircase.

reconfigured) distribution generation  $k$  on node  $i$ , where  $\hat{M}$  is the new distribution generation set of startup based on Definition 3 and  $Q_{de} + \sum_{k=1}^m \omega_i \Delta q_{k,i}^1 = Q_{re}$ . Then,  $\int_{t_{re}}^{t_{res}} Q^1(t) dt$  in formula (2) can be computed as

$$\int_{t_{re}}^{t_{res}} Q^1(t) dt = Q_{de} m \Delta t + \sum_{k=1}^m \left( \sum_{z=1}^{z=k} \omega_i \Delta q_{z,i}^1 \Delta t \right) + Q_{re} \Delta t_1. \quad (7)$$

*Proof.* As in Figure 3,  $\int_{t_{re}}^{t_{res}} Q^1(t) dt$  represents the computation of the area between system performance curve of restoration state and time axis. At the right of formula (7),  $Q_{de} m \Delta t$  means the computation of the area between “ $Q_{de}$ ” line and time axis at the precious  $m \Delta t$  time intervals,  $\sum_{k=1}^m (\sum_{z=1}^{z=k} \omega_i \Delta q_{z,i}^1 \Delta t)$  represents the computation of the area between system performance curve of restoration state and “ $Q_{de}$ ” line at precious  $m \Delta t$  time intervals, and  $Q_{re} \Delta t_1$  is the computation of the area between “ $Q_{re}$ ” line and time axis at  $\Delta t_1$  time interval. So, these three areas constitute the focused area between system performance curve of restoration state and time axis.  $\square$

**3.4. Assessment Framework for the Microgrid System with Emergency Restoration.** The proposed resilience assessment framework for the microgrid with distribution generation pre-position and reconfiguration under natural hazard (wind storm) is shown in Figure 4.

*Step 1.* Input the initial parameters and settings of the microgrid system, and use the OPF approach to assess the predisturbance system performance level  $Q_0$ .

*Step 2.* Utilize the fragility model to assess the state of the microgrid system under scenarios of a natural hazard (wind storm).

*Step 3.* Compute the postevent degraded system performance level  $Q_{de}$  by the OPF approach.

*Step 4.* Utilize the system restoration model to obtain the pre-position, reconfiguration, and startup sequence of emergency distribution generations, according to Definitions 1, 2, and 3.

*Step 5.* Compute the restored system performance level  $Q_{re}$  by the OPF approach for the microgrid at the restoration state.

*Step 6.* Compute the resilience metric of the microgrid system at the focused states following formulas (2), (3), and (7), and obtain the result of resilience assessment for the proposed problem.

## 4. Experiments

In this section, the simulation experiments for the assessment framework of the proposed approach are implemented on the modified IEEE 30-Bus system and the modified 118-Bus system. The experiments have been executed on a laptop with Intel Core i7 CPU@4 GHz and 32 GB RAM. The resilience assessment progress and the optimal power flow for the microgrid with pre-position and reconfiguration of emergency distribution generations have been solved using MATLAB software and YALMIP package.

### 4.1. Case I: Modified IEEE 30-Bus System

**4.1.1. Experiment Setup.** The proposed approach and metric are first tested based on the IEEE 30-Bus system. We design the experiments as follows. The parameters and the values used in the experiments are summarized in Table 1.

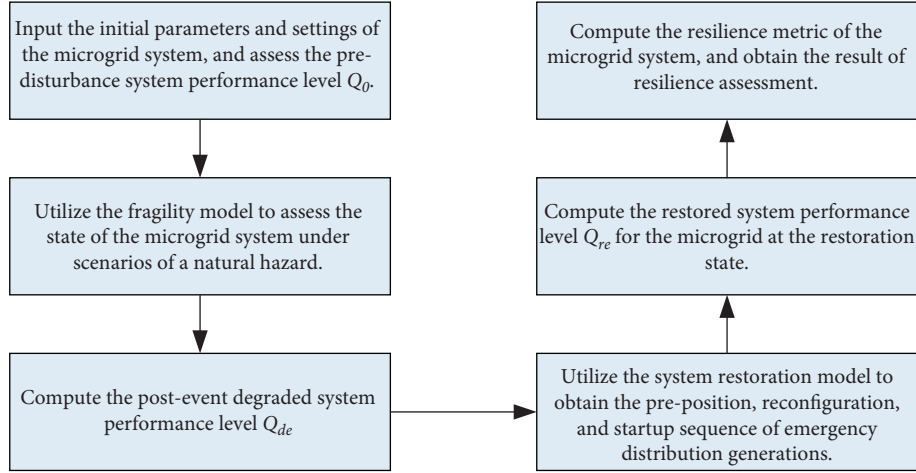


FIGURE 4: Resilience assessment framework for the microgrid system with emergency restoration.

TABLE 1: Parameters for modified IEEE 30-Bus system experiments.

Parameter	Value, (fixed)-(varied)
Number of damaged lines	(8)-(4, 6, 8, 10, 12)
Times of original fixed generation capacity	(1)-(1/4, 1/2, 1, 2, 4)
Number ( $m$ ) of emergency distribution generations	(4)
Set of distribution generation capacity	(50, 20, 20, 10) KWh
Set of load weight	(1, 2, 3)
$t_{de} - t_e$	(1) h
$t_{re} - t_{de}$	(2) h
$t_{ir} - t_{res}$	(3) h
$t_{res} - t_{re}$	(2) h
$\Delta t$	(15) min
$\Delta t_1$	(1) h

(1) *Damaged Transmission Lines.* The damaged transmission lines in the experiments are generated according to Section 3.1. As in Table 1, the number of damaged lines varies from 4 to 12, and different damaged lines are generated. When the other parameter is focused, the number of damaged lines is fixed at 8, and the same damaged lines are used in the experiment.

(2) *Fixed Generations and Emergency Distribution Generations.* In order to investigate the effect of original generations in the IEEE 30-Bus system for the resilience assessment of microgrid under natural hazard, we have changed the capacity value from 1/4 to 4 times of that of fixed generation in the IEEE 30-Bus system. The number  $m$  of emergency distribution generations is set as 4, and the capacity of 4 emergency distribution generations is, respectively, set as {50, 20, 20, 10}. We note that it is noneconomic and unnecessary to prepare the emergency distribution generations whose ability covers all the system demands. As common, we set fewer emergency distribution generations whose capacity value is larger or smaller than the average demand value of the test system case and more emergency distribution generations whose capacity value is around the average demand value.

(3) *Load Weight.* The weight of loads in the IEEE 30-Bus system is randomly generated from the set {1, 2, 3}, which means the loads are classified into three levels by their importance.

(4) *Time Length in the Focused Resilience Assessment States.* For convenient computation, we set the time length of the degradation state  $[t_e, t_{de}]$ , the degraded state  $[t_{de}, t_{re}]$ , the restoration state  $[t_{re}, t_{res}]$ , and the restored state  $[t_{res}, t_{ir}]$ , as 1 h, 2 h, 3 h, and 2 h, respectively. The time interval  $\Delta t$  is set as 15 min, and  $\Delta t_1$  is then set as 1 h according to Proposition 1.

(5) *Comparing System Restoration Strategies.* In the experiments, we have also provided three system restoration strategies for comparison as follows:

- (i) *Strategy I (No-Restoration Strategy).* This strategy implements no restoration action and just runs the optimal power flow on the damaged system.
- (ii) *Strategy II (Pre-Position Strategy).* It focuses on the pre-position of emergency distribution generations in the system as Definition 1 and then optimizes the power flow of the damaged system with emergency distribution generations.
- (iii) *Strategy III (Pre-Position Reconfiguration Strategy).* It first determines the pre-position of emergency distribution generations following Definition 1, then reconfigures the positioned emergency distribution generations according to Definition 2 after the damage of the system occurs, and finally optimizes the system power flow. This strategy is the proposed strategy of this paper.

4.1.2. *Experimental Result.* In this section, we present the experimental results for the resilience and performance assessment for the microgrid under natural hazard and the comparison among the different system restoration strategies. Table 2 provides the resilience and performance assessment result, and Figure 5 shows an illustrated result

TABLE 2: Resilience and performance assessment result with 8 damaged lines and original generations on the modified IEEE 30-Bus system.

	Normal	Strategy I	Strategy II	Strategy III
Optimal running weighted loads	389.4	326.4	350.4	378.9
Resilience metric	—	0.8483	0.9066	0.9432

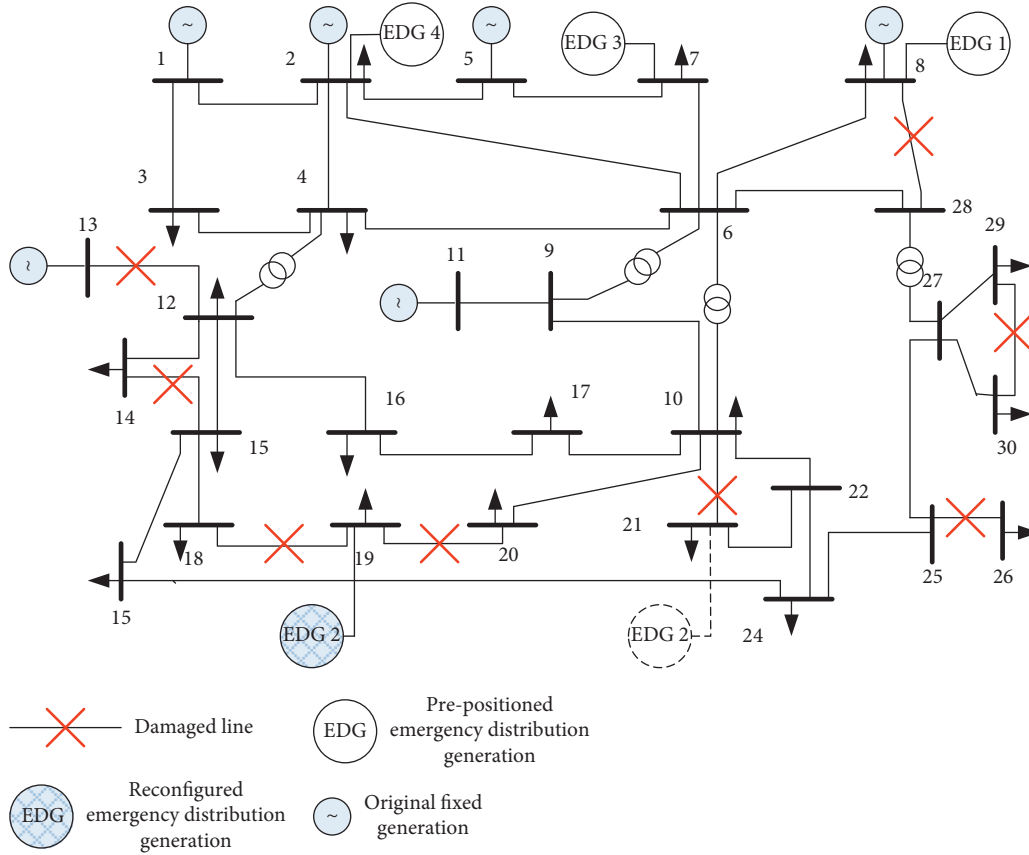


FIGURE 5: Illustrated restoration result under strategy III on the modified IEEE 30-Bus system.

under the proposed restoration strategy (strategy III) on the modified IEEE 30-Bus system when the number of damaged lines is set as 8 and the original fixed generations are used.

Figure 6 shows the results of optimal running weighted load and resilience metric when the same 8 damaged lines are used, and the capacities of fixed generations in the IEEE 30-Bus system are changed from 1/4 to 4 times of the original data. Figure 7 shows the results of optimal running weighted load and resilience metric when the original data of generations is used and the number of damaged lines varies from 4 to 12. Note that the “Normal” in Figures 6 and 7 means the results of optimal running weighted load and resilience metric when there is no damage in the microgrid system for a “Normal” state.

We can clearly see from Figures 6 and 7 that the optimal running weighted load of the microgrid system increases following the improvement of the capacity of fixed generations and decreases following the increment of the number of damaged lines; the resilience metric of the system with restoration actions decreases following the improvement of the capacity of fixed generations and the

increment of the number of damaged lines, respectively. Particularly, when the capacity of fixed generation is not enough for power demand, the number of damaged lines is relatively larger, and the emergency distribution generations are sufficient, the reasonable restoration strategy provides a significant effect on the optimal running weighted load and system resilience metric value. This is the reason why the value of loads in Figure 6(a) under “Normal” case is smaller than strategy III at 1/4 and 1/2, and the resilience of the system decreases as the capacity of the fixed generations increases in Figure 6(b). This also confirms the effectiveness of the proposed resilience metric on the microgrid with emergency restoration under natural hazard. We can find that, based on the experiments of the modified IEEE 30-Bus system, the proposed strategy (strategy III) provides the highest value of optimal running weighted load and resilience metric when the number of damaged lines and the times of fixed generation capacity is changed, respectively. And this verifies the superiority of the proposed system restoration strategy in comparison with the other two restoration strategies.



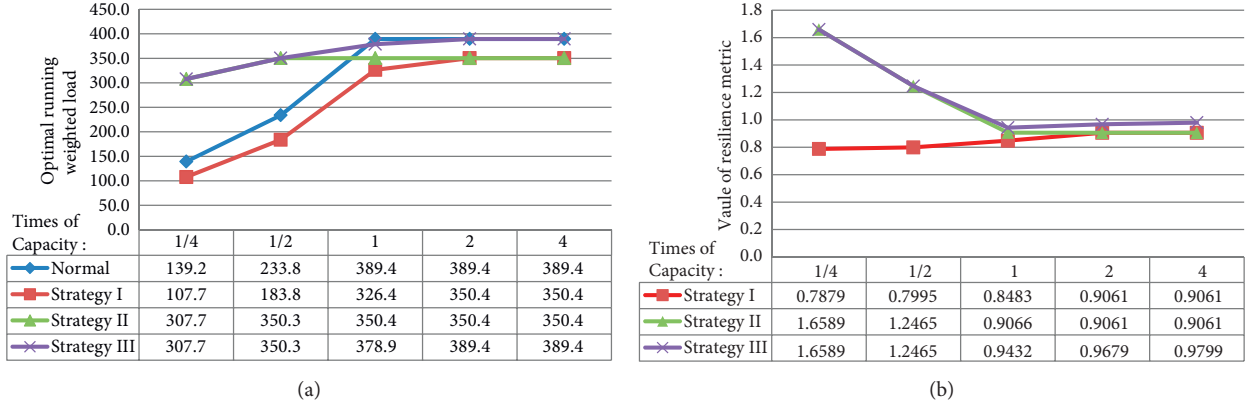


FIGURE 6: Results on modified IEEE 30 bus system with varied generation capacities.

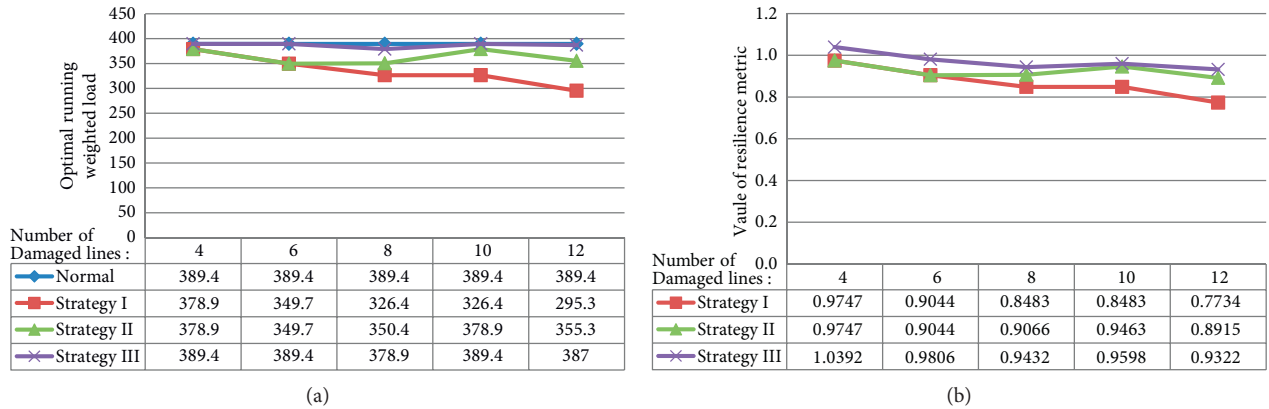


FIGURE 7: Results on modified IEEE 30 bus system with varied damaged lines.

## 4.2. Case II: Modified IEEE 118-Bus System

4.2.1. *Experiment Setup.* We have also tested the proposed approach and resilience metric based on the IEEE 118-Bus system. The parameters and the values used in the experiments of this section are presented in Table 3.

Like those experiment setups on the modified IEEE 30-Bus system, we have used similar settings of “load weight” and “comparing system restoration strategies” in this section. But there exist some differences: (1) the number of damaged lines varies from 10 to 40; (2) the number of emergency distribution generations is set as 10, and the capacity of 10 emergency distribution generations is, respectively, set as {100, 80, 80, 80, 50, 50, 50, 50, 20, 20}; (3) since the number of emergency distribution generations is increased to 10, the value of “ $t_{res} - t_{re}$ ” is increased to 3 h and the value of “ $\Delta t_1$ ” is changed as 0.5 h. Note that, as the setting of the experiment on the modified IEEE 30-Bus system, we set fewer emergency distribution generations with a larger or smaller capacity value than the average demand value of the test system case and more emergency distribution generations with the capacity value around the average demand value.

4.2.2. *Experimental Result.* Table 4 provides the performance and resilience assessment result, and Figure 8 presents an

TABLE 3: Parameters for modified IEEE 118-Bus system experiments.

Parameter	Value (fixed)–(varied)
Number of damaged lines	(20)–(10, 15, 20, 30, 40)
Times of original fixed generation capacity	(1)–(1/4, 1/2, 1, 2, 4)
Number ( $m$ ) of emergency distribution generations	(10)
Set of distribution generation capacity	(100, 80, 80, 80, 50, 50, 50, 50, 20) KWh
Set of load weight	(1, 2, 3)
$t_{de} - t_e$	(1) h
$t_{re} - t_{de}$	(2) h
$t_{ir} - t_{res}$	(3) h
$t_{res} - t_{re}$	(3) h
$\Delta t$	(15) min
$\Delta t_1$	(0.5) h

illustrated result under strategy III on the modified IEEE 118-Bus system when the number of damaged lines is set as 20 and the original fixed generation data is used.

Figure 9 provides the results of the optimal running weighted load and system resilience metric when the similar 20 damaged lines are used and the capacities of generations in the IEEE 118-Bus system are changed from 1/4 to 4 times



TABLE 4: Resilience and performance assessment result with 20 damaged lines and original generations on modified IEEE 118-Bus system.

	Normal	Strategy I	Strategy II	Strategy III
Optimal running weighted loads	1293	1293	2483	2733
Resilience metric	—	1.0000	1.5682	1.6434

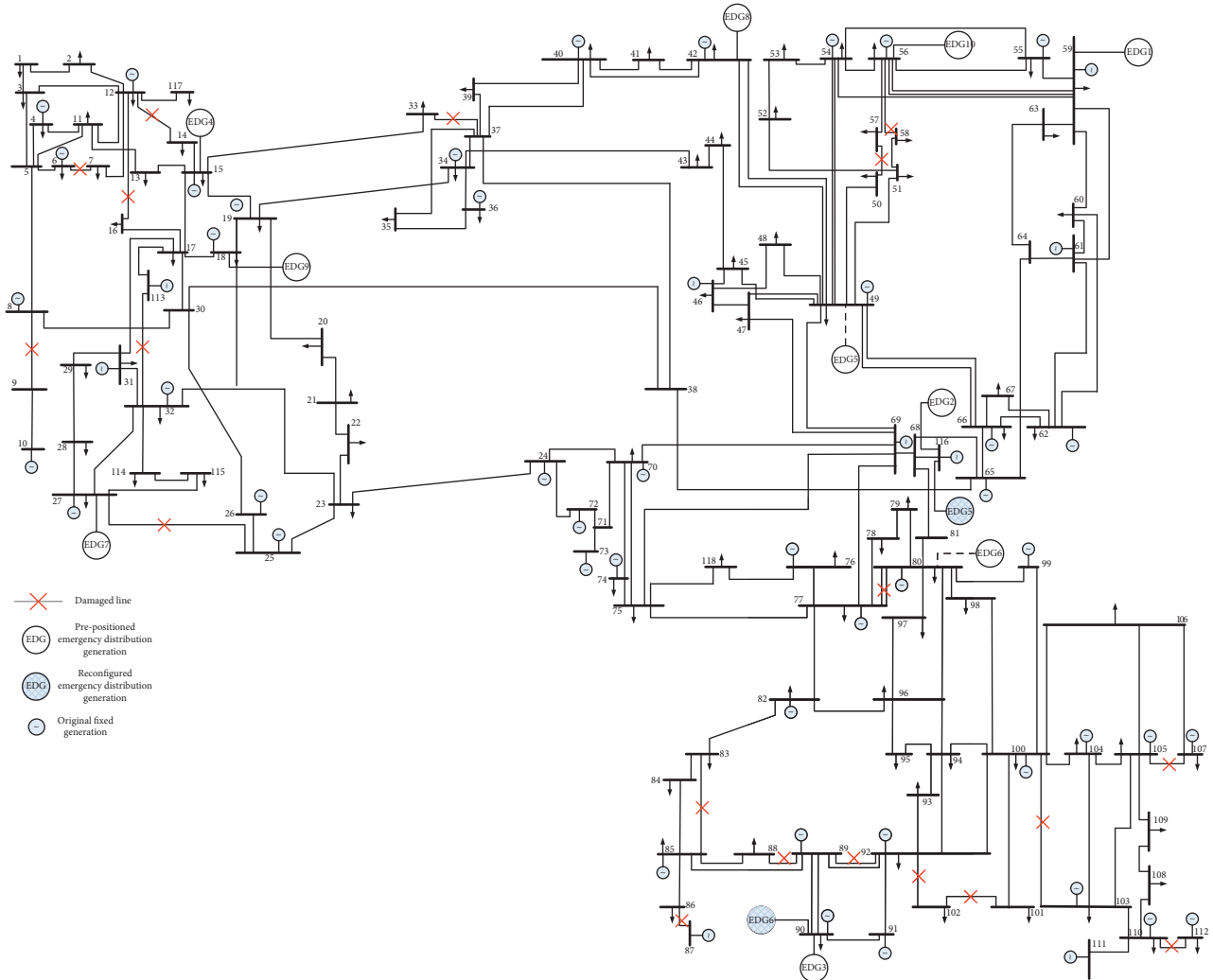


FIGURE 8: Illustrated restoration result under strategy III on modified IEEE 118-Bus system.

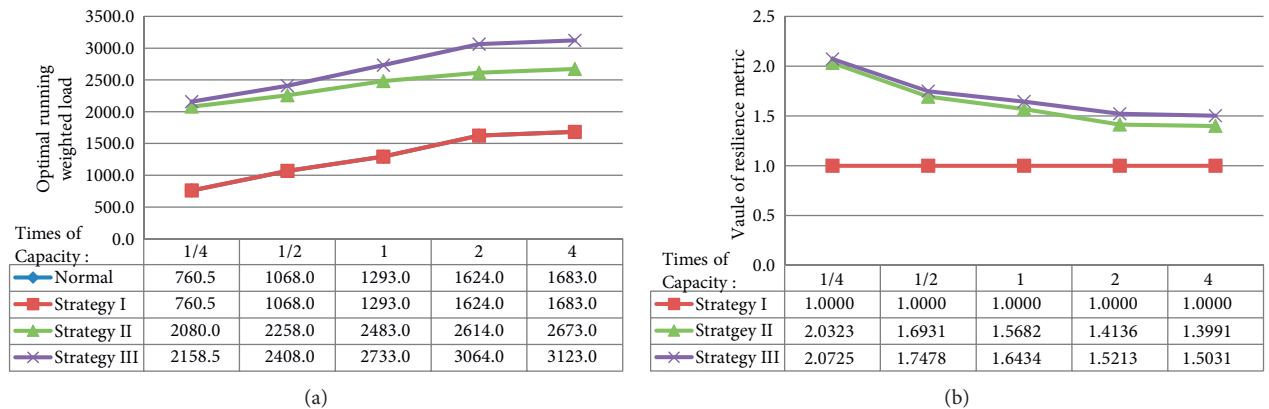


FIGURE 9: Results on modified IEEE 118 bus system with varied generation capacities.

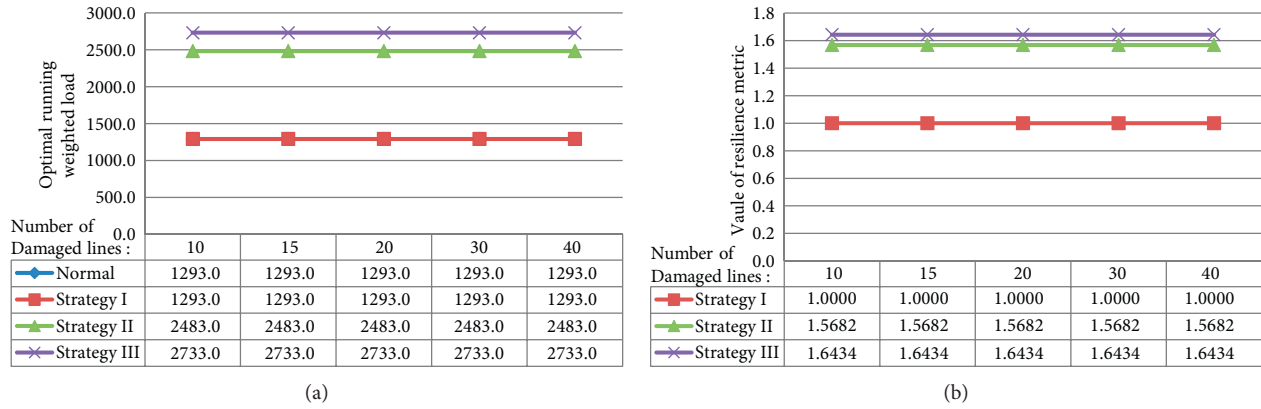


FIGURE 10: Results on modified IEEE 118 bus system with varied damaged lines.

of the original data. Figure 10 gives the results of the optimal running weighted load and system resilience metric when the original data of fixed generations is used and the number of damaged lines varies from 10 to 40.

From Table 4 and Figures 9 and 10, we can observe that the proposed restoration strategy also provides the highest value of optimal running weighted load and system resilience at these experiments based on the modified IEEE 118-Bus system. And we can see that the value of the system resilience metric is equal to 1 when there exists no restoration action by the generations under “strategy I.” This is because there are 54 fixed generations distributed at the system with 118 buses in the original data, and these distributed generations can provide enough energy supply for the buses when the damage occurs. We can also find that the value of the system resilience metric is larger than 1 under “strategy II” and “strategy III,” and this is because more energy can be supplied by suitably positioned generations, and more resiliency can be obtained by the microgrid system. Note that since there are 54 generations distributed at the 118 buses in the original data, it can achieve a “stable state” of optimal running weighted load and system resilience metric though the number of damaged lines is changed from 10 to 40 at the experiments as in Figure 10.

## 5. Conclusion

This paper introduces and solves the microgrid system resilience assessment under natural hazard, where the emergency distribution generations are pre-positioned and reconfigured on microgrid nodes for system emergency restoration. We provide a resilience metric index and an approximation computation method for the system resilience assessment, a pre-position strategy and a reconfiguration strategy of emergency distribution generations for the microgrid system restoration, and a framework of resilience assessment for problem-solving. The effectiveness of the resilience assessment methodology and the superiority of proposed restoration strategies are, respectively, verified with extensive experiments.

Since we focus on the resilience metric computation and the emergency restoration strategy of microgrid under

natural hazard in this work, two directions will be considered in our future work. First, we intend to propose the mathematical formation of the multistage resilience assessment of microgrid with system emergency restoration under natural hazard. Secondly, we would like to apply our method for the resilience assessment of the sea island microgrid system, where a seasonal natural disaster occurs frequently.

## Data Availability

The data used to support the findings of this study are available from the corresponding author upon request.

## Conflicts of Interest

The authors declare that they have no conflicts of interest.

## Acknowledgments

This work was partly supported by the Chinese National Natural Science Foundation under Grants 61973310, 71901210, and 72071205. This support was greatly appreciated.

## References

- [1] R. J. Campbell and S. Lowry, “Weather-related power outages and electric system resiliency,” in *Proceedings of the Congressional Research Service*, Library of Congress, Washington, DC, USA, August 2012.
- [2] C. S. Holling, “Resilience and stability of ecological systems,” *Annual Review of Ecology and Systematics*, vol. 4, no. 1, pp. 1–23, 1973.
- [3] C. Folke, “Resilience: the emergence of a perspective for social-ecological systems analyses,” *Global Environmental Change*, vol. 16, no. 3, pp. 253–267, 2006.
- [4] R. Francis and B. Bekera, “A metric and frameworks for resilience analysis of engineered and infrastructure systems,” *Reliability Engineering and System Safety*, vol. 121, pp. 90–103, 2014.
- [5] L. Mili, K. Triantis, and A. Greer, “Integrating community resilience in power system planning,” *Power Engineering*:

- Advances and Challenges, Part B: Electrical Power*, CRC Press, Boca Raton, FL, USA, 2018.
- [6] M. H. Amirioun, F. Aminifar, H. Lesani, and M. Shahidehpour, "Metrics and quantitative framework for assessing microgrid resilience against windstorms," *International Journal of Electrical Power and Energy Systems*, vol. 104, pp. 716–723, 2019.
  - [7] M. Bruneau, S. E. Chang, R. T. Eguchi et al., "A framework to quantitatively assess and enhance the seismic resilience of communities," *Earthquake Spectra*, vol. 19, no. 4, pp. 733–752, 2003.
  - [8] A. Dehghani, M. Sedighzadeh, and F. Haghjoo, "An overview of the assessment metrics of the concept of resilience in electrical grids," *International Transactions on Electrical Energy Systems*, vol. 31, no. 12, Article ID e13159, 2021.
  - [9] M. Ibrahim and A. Alkhraibat, "Resiliency assessment of microgrid systems," *Applied Sciences*, vol. 10, no. 5, p. 1824, 2020.
  - [10] F. H. Jufri, V. Widiputra, and J. Jung, "State-of-the-art review on power grid resilience to extreme weather events: definitions, frameworks, quantitative assessment methodologies, and enhancement strategies," *Applied Energy*, vol. 239, pp. 1049–1065, 2019.
  - [11] M. Ouyang and L. Dueñas-Osorio, "Time-dependent resilience assessment and improvement of urban infrastructure systems," *Chaos*, vol. 22, no. 3, pp. 033122–033123, 2012.
  - [12] M. Panteli, P. Mancarella, D. N. Trakas, E. Kyriakides, and N. D. Hatziargyriou, "Metrics and quantification of operational and infrastructure resilience in power systems," *IEEE Transactions on Power Systems*, vol. 32, no. 6, pp. 4732–4742, 2017.
  - [13] M. Bruneau and A. Reinhorn, "Exploring the concept of seismic resilience for acute care facilities," *Earthquake Spectra*, vol. 23, no. 1, pp. 41–62, 2007.
  - [14] S. Lei, J. Wang, C. Chen, and Y. Hou, "Mobile emergency generator pre-positioning and real-time allocation for resilient response to natural disasters," *IEEE Transactions on Smart Grid*, vol. 9, no. 3, pp. 2030–2041, 2018.
  - [15] B. Ti, G. Li, M. Zhou, and J. Wang, "Resilience assessment and improvement for cyber-physical power systems under typhoon disasters," *IEEE Transactions on Smart Grid*, vol. 13, no. 1, pp. 783–794, 2022.
  - [16] M. H. Amirioun, F. Aminifar, and H. Lesani, "Resilience-oriented proactive management of microgrids against windstorms," *IEEE Transactions on Power Systems*, vol. 33, no. 4, pp. 4275–4284, 2018.
  - [17] A. Hussain, V.-H. Bui, and H.-M. Kim, "Microgrids as a resilience resource and strategies used by microgrids for enhancing resilience," *Applied Energy*, vol. 240, pp. 56–72, 2019.
  - [18] J. Nelson, N. G. Johnson, K. Fahy, and T. A. Hansen, "Statistical development of microgrid resilience during islanding operations," *Applied Energy*, vol. 279, Article ID 115724, 2020.
  - [19] T. T. Dan and W. T. P. Wang, "A more resilient grid: the us department of energy joins with stakeholders in an r & d plan," *IEEE Power and Energy Magazine*, vol. 13, no. 3, pp. 26–34, 2015.
  - [20] Z. Bie, Y. Lin, G. Li, and F. Li, "Battling the extreme: a study on the power system resilience," *Proceedings of the IEEE*, vol. 105, no. 7, pp. 1253–1266, 2017.
  - [21] M. Panteli, D. N. Trakas, P. Mancarella, and N. D. Hatziargyriou, "Power systems resilience assessment: hardening and smart operational enhancement strategies," *Proceedings of the IEEE*, vol. 105, no. 7, pp. 1202–1213, 2017.
  - [22] R. D. Zimmerman, C. E. Murillo-Sánchez, and R. J. Thomas, "MATPOWER: steady-state operations, planning, and analysis tools for power systems research and education," *IEEE Transactions on Power Systems*, vol. 26, no. 1, pp. 12–19, 2011.
  - [23] M. Panteli, C. Pickering, S. Wilkinson, R. Dawson, and P. Mancarella, "Power system resilience to extreme weather: fragility modeling, probabilistic impact assessment, and adaptation measures," *IEEE Transactions on Power Systems*, vol. 32, no. 5, pp. 3747–3757, 2017.
  - [24] L. McColl, E. J. Palin, H. E. Thornton, R. A. Betts, K. Mylne, and M. H. S. David, "Assessing the potential impact of climate change on the UK's electricity network," *Climatic Change*, vol. 115, no. 3, pp. 821–835, 2012.
  - [25] G. Fu, S. Wilkinson, R. J. Dawson et al., "Integrated approach to assess the resilience of future electricity infrastructure networks to climate hazards," *IEEE Systems Journal*, vol. 12, no. 4, pp. 3169–3180, 2018.